University of Strathclyde
Department of Mechanical Engineering

Coupled Thermo-Mechanical Modelling of Friction Stir Welding

Hongjun Li

A thesis presented in fulfilment of the requirements for the degree of Doctor of Philosophy

2008

THESIS
CONTAINS
CD/DVD

Copyright statement

Acknowledgements

First and foremost I would like sincerely to express my gratitude to my principal supervisor **Dr Donald Mackenzie**, Head of Mechanical Engineering Department, for his expert advice, continuous assistance and support in all aspect of my research since I came to Glasgow. I was given plenty of opportunities to present my work in UK, European and international conferences and attend training in summer schools. All the experiences will be no doubt beneficial to my future career.

I would also like to thank **Dr Robert Hamilton**, my second supervisor for his help and encouragement.

I was luckily awarded the Overseas Research Students Awards by Universities UK, which covered my tuition fees and the International Research Scholarship by Strathclyde University, which provided the living costs. Without these funding, this thesis would not have been possible.

Thanks must be given to my colleagues and staff in Mechanical Engineering Department, **Dr Jim Wood, Dr Tugrul Comlekci, Dr David Nash, Prof. Jim Boyle ...** for their help.

Thanks also must go to my friends in Glasgow, **Di Zhu, Wendan Wang, Wei Zhang, Ying Zhang, Ke Wang ...** We have shared all the highs and lows during our study at Strathclyde University.

Last but not least I would like to thank my **parents** for their understanding, patience and endless encouragement. This thesis will be a special gift to them and make them proud, although they may not understand what's written in it.

Abstract

Friction Stir Welding (FSW) is a new welding technique for joining and processing metals. The object of this thesis is to develop the numerical models based on scientific knowledge and to provide a useful tool for predicting field variables and understanding the FSW process at a fundamental level.

The thesis is focused on developing a continuum solid mechanics-based, fully coupled thermo-mechanical numerical model of FSW using the finite element method to simulate coupling between the welding tool movement, material deformation and movement, energy dissipation and heat transfer in the welding system. The model can simulate the whole welding process. Similar models in literature can only simulate the plunge stage. At the end of plunge stage, the mesh pattern is kept unchanged and used at the beginning of traverse stage. The tool travel speed is ramped to its normal speed from zero in the initial 0.2 second of the traverse stage. The model is able to give detailed simulation of transient thermal response, material flow, residual stress and strain, etc. Material movement is visualized by defining tracer particles at the locations of interest. The numerically computed material flow patterns are in very good agreement with the general findings in experiments. The model used for investigating the tool geometry effect predicted a maximum temperature close to the melting point. It was found in the tool shape effect study that, in plunge stage, the tool radius has a much more significant effect on tool reaction force, heat generation than the shoulder surface angle.

To circumvent the complexity and computational cost of the fully coupled model, a simplified thermo-mechanical finite element model is developed. The heat source is applied externally rather than computed, in the model, from plastic deformation and friction. This model cannot be used to investigate the tool stirring in material or the interaction between the tool and workpiece but is able to predict the temperature, stress and deformation in the workpiece. The model is shown to predict a temperature history in good agreement with experimentally measured results.

Contents

Nomenclature

$\mathbf{a}$	Acceleration vector (m/s^2)
$\mathbf{B}_{MeshM}$	Matrix of mesh motion parameters
c	Specific heat (J/kgK)
c_d	Dilatational wave speed determined by effective Lamé's constants $\hat{\lambda}$ and $\hat{\mu}$
d_{clear}	Clearance between surfaces
$\mathbf{d}$	Nodal position
e_I	Internal energy density
f	Arbitrary function
$\mathbf{f}$	Load vector
$\mathbf{f}_{in}$	Elementary internal force matrix
$\mathbf{f}_{ext}$	Elementary external force matrix
$\dot{f}$	Time derivative of an arbitrary function
$\mathbf{g}$	Body force per unit mass (m/s^2)
h_{fc}	Convection film coefficient
h_{fr}	Radiation film coefficient
k_{gap}	Gap conductance
l	Element length (m)
$\mathbf{m}$	Elementary mass matrix
$\mathbf{n}$	Unit outward vector
p	Hydrostatic pressure
$p_{contact}$	Contact pressure
q_{hg}	Heat generation rate per unit volume (J/m^3)

$\mathbf{q}$	Heat flux vector (W/m^2)
s_{en}	Density of entropy
t	Time (s)
$\mathbf{u}$	displacement vector (m)
$\mathbf{x}$	Position vector
$\mathrm{x, y, z}$	Position coordinates (m)

$\mathbf{C}$	Heat capacity matrix
E	Young's modulus
E_I	Internal energy (J)
E_K	Kinetic energy (J)
E_W	Work of external and internal forces (J)
$\mathbf{F}_{in}$	Assembled internal force matrix
$\mathbf{F}_{ext}$	External force matrix
J_1, J_2, J_3	Invariants of the deviatoric stress tensor
$\mathrm{H_c}$	Boundary convection matrix
K	Thermal conductivity (J/msK)
$\mathbf{K}$	Stiffness matrix
$\mathbf{K}_k$	Thermal conductivity matrix
$L_{\min}$	Smallest element dimension in the mesh (m)
$\mathbf{M}$	Assembled mass matrix
N	Shape function
Q	Heat input (J)
$\dot{Q}_A$	Rate of heat added to the control volume (J/s)
$\mathbf{I}$	Identity matrix
S	Surface of control volume
S	Deviatoric stress tensor
S_{en}	Entropy of the system

$\mathbf{S}_B$	Boundary heat flux vector
$\mathbf{S}_h$	Boundary convection vector
$\mathbf{S}_Q$	Heat generation vector
T	Temperature (K)
V	Volume (m^3)
$\mathbf{V}$	velocity vector (m/s)

Greek letter

$\boldsymbol{\alpha}_{MeshM}$	Vector of mesh motion parameters
ε	Strain
$\boldsymbol{\varepsilon}$	Strain tensor
$\dot{\varepsilon}$	Strain rate
$\dot{\varepsilon}^{el}$	Elastic strain rate
$\dot{\varepsilon}^{pl}$	Plastic strain rate
$\dot{\varepsilon}^{cl}$	Creep strain rate
$\bar{\varepsilon}^{pl}$	Equivalent plastic strain
ϕ	Element variable
$\boldsymbol{\Phi}$	Surface tractions
$\lambda_{\max}$	Largest eigenvalue in the system of equations of the thermal solution response
μ_k	Kinetic friction coefficient
μ_s	Static friction coefficient
ν	Poisson's ratio
ρ	Density (kg/m^3)
$\boldsymbol{\sigma}$	Stress tensor (N/m^2)
σ_y	Yield stress (N/m^2)

$\bar{\sigma}$	Equivalent stress
ς	Thermal diffusivity of the material, $k/_{\rho c}$ (m^2/s)
τ	Shear stress (N/m^2)
υ	Velocity vector (m/s)
ω_{max}	Highest frequency in the system of equations of the mechanical solution response
Δx	Node distance
Ψ	Free energy

Abbreviations

ALE	Arbitrary Lagrangian and Eulerian formulation
CFD	Computational fluid dynamics
MWR	Method of weighted residuals
FEM	Finite element method
FDM	Finite difference method
FSW	Friction stir welding
FSP	Friction stir processing
FV	Finite volume method

List of Figures

List of Tables

Chapter 1
Introduction

1.1 Background

The presence of welded joints in most fabricated structures introduces local areas of weakness due to geometric discontinuity, stress concentration, altered material microstructure, increased corrosion, etc. A great deal of research has been directed at improving joining technology over the past few decades. One of the most significant recent developments has been the introduction of the solid state welding process Friction Stir Welding (FSW), (a subcategory of friction welding, which has been used since the 1950s), patented in 1991 by Thomas et al. [1, 2].

FSW is a new technique for joining and processing metals, in which a rotating tool traverses the weld seam, heating and rotationally displacing the local material to form a solid state welded joint. Since its inception, FSW has attracted worldwide interest. The first commercial application of this technique was in a few Scandinavian companies [3] and the Boeing company [4]. It is now widely used in a wide range of manufacturing industries. In the automotive industry, for example, FSW is used for a variety of components by major companies such as BMW, Land Rover, Ford and Mazda.

Despite the rapid development of FSW and interest from industry, technology transfer into main stream industry is somewhat high risk, due to a lack of understanding of the fundamental FSW material transport mechanism and the influence that tool design and welding parameters have on ultimate weld properties [5]. Extensive research has been carried out to study the heat evolution, material flow, microstructure evolution, processes optimization, effect of tool geometry and welding parameters, weld properties, etc. A more detailed illustration of current popular research areas is shown in Figure 1.1.

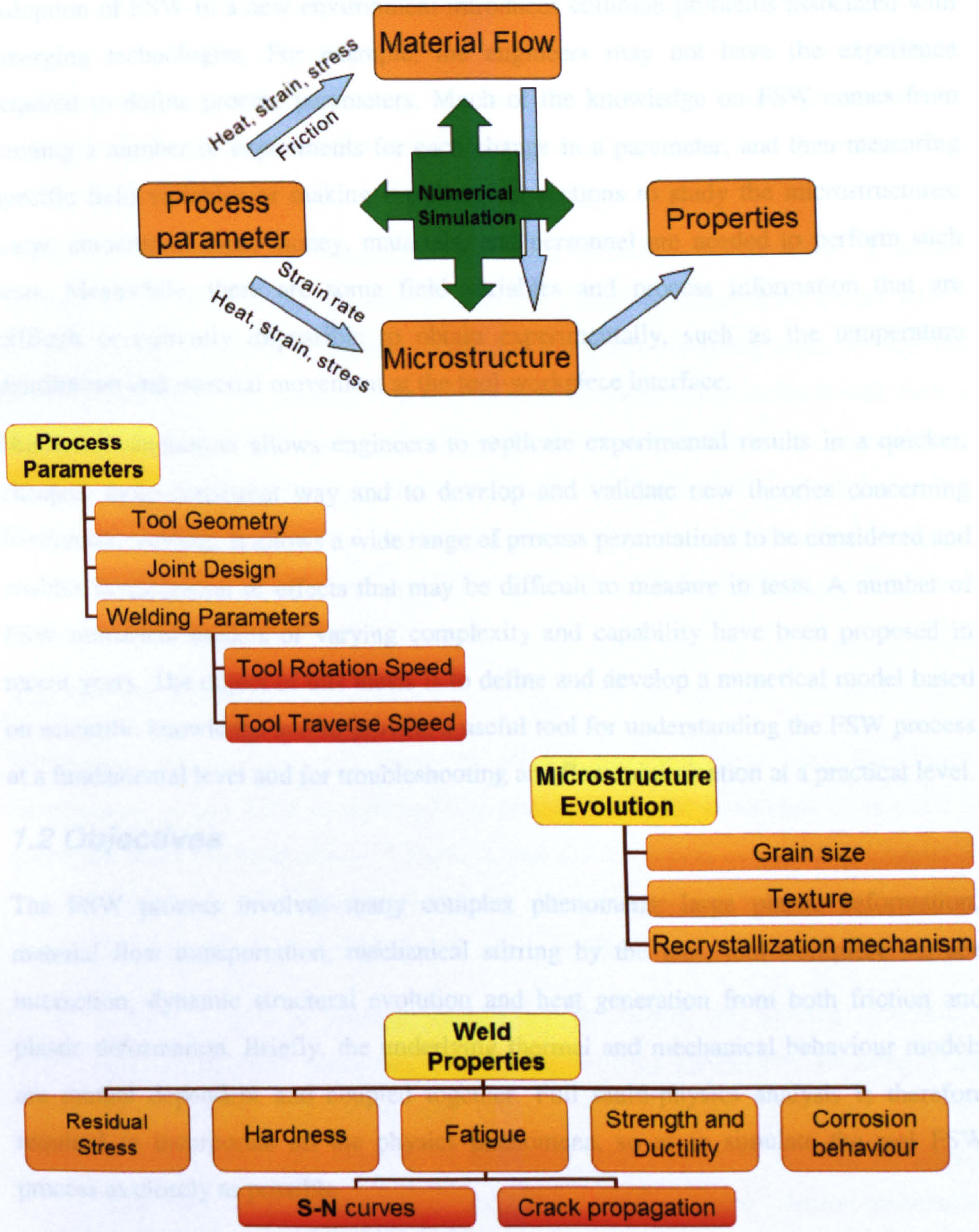

Figure 1.1 Main research areas around friction stir welding process

Adoption of FSW in a new environment introduces common problems associated with emerging technologies. For example, the engineers may not have the experience required to define process parameters. Much of the knowledge on FSW comes from running a number of experiments for each change in a parameter, and then measuring specific field variables or making metallurgical sections to study the microstructures. Large amounts of time, money, materials, and personnel are needed to perform such tests. Meanwhile, there are some field variables and process information that are difficult or currently impossible to obtain experimentally, such as the temperature distribution and material movement at the tool-workpiece interface.

Numerical simulation allows engineers to replicate experimental results in a quicker, cheaper, more consistent way and to develop and validate new theories concerning friction stir welding. It allows a wide range of process permutations to be considered and enables investigation of effects that may be difficult to measure in tests. A number of FSW numerical models of varying complexity and capability have been proposed in recent years. The object of this thesis is to define and develop a numerical model based on scientific knowledge and to provide a useful tool for understanding the FSW process at a fundamental level and for troubleshooting and flaw minimization at a practical level.

1.2 Objectives

The FSW process involves many complex phenomena: large plastic deformation, material flow transportation, mechanical stirring by the tool, tool-workpiece surface interaction, dynamic structural evolution and heat generation from both friction and plastic deformation. Briefly, the underlying thermal and mechanical behaviour models are mutual dependent ,and coupled together. Full multi-physics analysis is therefore required to incorporate all the physics phenomena, so as to simulate the real FSW process as closely as possible

The principal objective of the reported research is to define and develop a continuum solid mechanics-based, fully coupled thermo-mechanical numerical model of friction stir welding (FSW) using the finite element method to tackle the issues of coupling between the welding tool movement, material deformation and movement, energy dissipation and heat transfer in the welding system. The model is able to give detailed simulation of transient thermal response, material flow, residual stress and strain, etc. The developed model is used to carry out parametric studies on the effect of process parameters, in particular the tool shape, on the resulting tool reaction force, heat generation and temperature distributions, etc.

Due to the complexity and computational cost of the fully coupled model, a second objective of the research is to develop a simplified thermo-mechanical FE model, where the heat source is applied externally rather than computed internally from friction and plastic deformation. The stirring effect of the tool is not included in the model. Hence the model is mainly used to predict temperature, stress and workpiece deformation but can not be used to produce any material movement information. The simplified model has more potential in practical industrial application, where the temperature and residual stress distributions are the most significant quantities and they can be provided in a cheaper and faster way by simplified models.

1.3 Thesis Layout

The structure of the thesis can simply be divided into three parts: basic knowledge, development of new FSW models and conclusion. The basic knowledge component is presented in the literature review, Chapter 2, and the theoretical background, Chapter 3. The new numerical FSW models are defined and developed in Chapter 4, a simplified thermo-mechanical model, and Chapter 5, a fully coupled thermo-mechanical model.

- Chapter 2 gives a detailed introduction to friction stir welding technology, considering FSW principals, tool design, welding parameters, advantages and disadvantages, application and Friction Stir Welding Processing (FSWP). Previous associated research is discussed with respect to thermal modelling, simplified thermo-mechanical modelling, and coupled thermo-mechanical modelling and material flow modelling.
- Chapter 3 provides the fundamental theories required for the numerical FSW modelling. It considers solution methods for partial differential equations,

followed by three general domain discretization techniques: Eulerian, Lagrangian and Arbitrary Lagrangian and Eulerian formulations (ALE). Mathematical models of heat transfer, metal mechanics and thermo-mechanical systems are then introduced. The finite element formulation for coupled thermo-mechanical analysis is addressed using two approaches: implicit and explicit analyses. Metal plasticity is discussed separately from metal mechanics, where mass, linear momentum and energy conservation laws are considered. Finally, the equations governing surface interactions are presented.

- Chapter 4 details development of a simplified thermo-mechanical FE model. First the methodology of thermal modelling and mechanical modelling is discussed. A novel heat source algorithm is then described through equations and flow charts. Finally two experimental results from the literature are used to validate the numerically predicted temperature and stresses distributions.
- Chapter 5 defines three fully coupled thermo-mechanical FE models of different complexity and details their development and implementation. Advanced Finite Element models encapsulating various aspects associated with the FE model such as contact modelling, material modelling and meshing techniques are discussed in detail. The initial model has a geometry size of the same order as experiment specimens. The model quality and problems occurred during analysis are then assessed. Based on the evaluation of the initial model, an improved model is presented but with a much smaller size. The simulation results including temperature, stress, strain, heat generation and material movement are provided to investigate the coupled thermo-mechanical behaviour of FSW. Towards the end of this chapter the effects of tool geometry (shoulder surface angle and pin radius) on tool reaction force, reaction moment, frictional and plastic energy dissipation, temperature field and weld zone are studied.
- Chapter 6 presents concluding remarks and proposes future work.

1.4 References

[1] W.M. Thomas, E.D. Nicholas, J.C. Needham, M.G. Murch, P. Temple-Smith, C.J. Dawes, Friction stir butt welding, International Patent Application number PCT/GB92/02203; GB Patent Application number 9, 125, 978.8, 1991; US Patent number 5,460,317, 1995.

[2] W.M. Thomas, E.D. Nicholas, J.C. Needham, M.G. Murch, P. Temple-Smith, C.J. Dawes, Improvements relating to friction welding, International Patent Classifications 23K 20/12, B29C 65/06,1993.

[3] Knipstrom, KE and Pekkari, B., "A novel joining process - Friction Stir Welding" Svetsaren, No. 1-2, Vol. 52, pp. 49-52, 1997

[4] M., Johnsen, "Friction Stir Welding Takes Off at Boeing", *Welding Journal*, February, pp 35-39, 1999.

[5] Pedro Vilaca, Luisa Quintino , Jorge F. dos Santos, iSTIR-Analytical thermal model for friction stir welding, *Journal of Materials Processing Technology*, volume 169, pp. 452–465, 2005

Chapter 2

Literature Review

This chapter presents a detailed introduction to friction stir welding technology. Previous works are discussed with respect to thermal modelling, simplified thermo-mechanical modelling, and coupled thermo-mechanical modelling and material flow modelling. The microstructure modelling is not included in the literature review.

2.1 Friction Stir Welding Technology

2.1.1 Principle of Friction Stir Welding

Friction Stir Welding (FSW) is a solid state joining process that can be considered to be a special subset of Friction Welding. A basic FSW arrangement is shown in Figure 2.1. The two plates to be joined are firmly clamped together and no relative movement is allowed during the welding process. A non-consumable rotating tool with a specially designed pin and shoulder is mounted in a stiff spindle which rotates and translates the tool. There are four main stages in the welding stages: plunge, dwell, travel and pull-out.

Initially, the tool is rotated at a specified speed with zero translational velocity. The tool is then *plunged* normally into the joint between the abutting plates. Frictional heat is produced between the rotating tool pin and the plates, heating and hence softening the material, allowing the tool to maintain sinking without significantly increased resistant force from the plate materials. The tool continues plunging until the shoulder comes into full contact with the top surfaces of the plates.

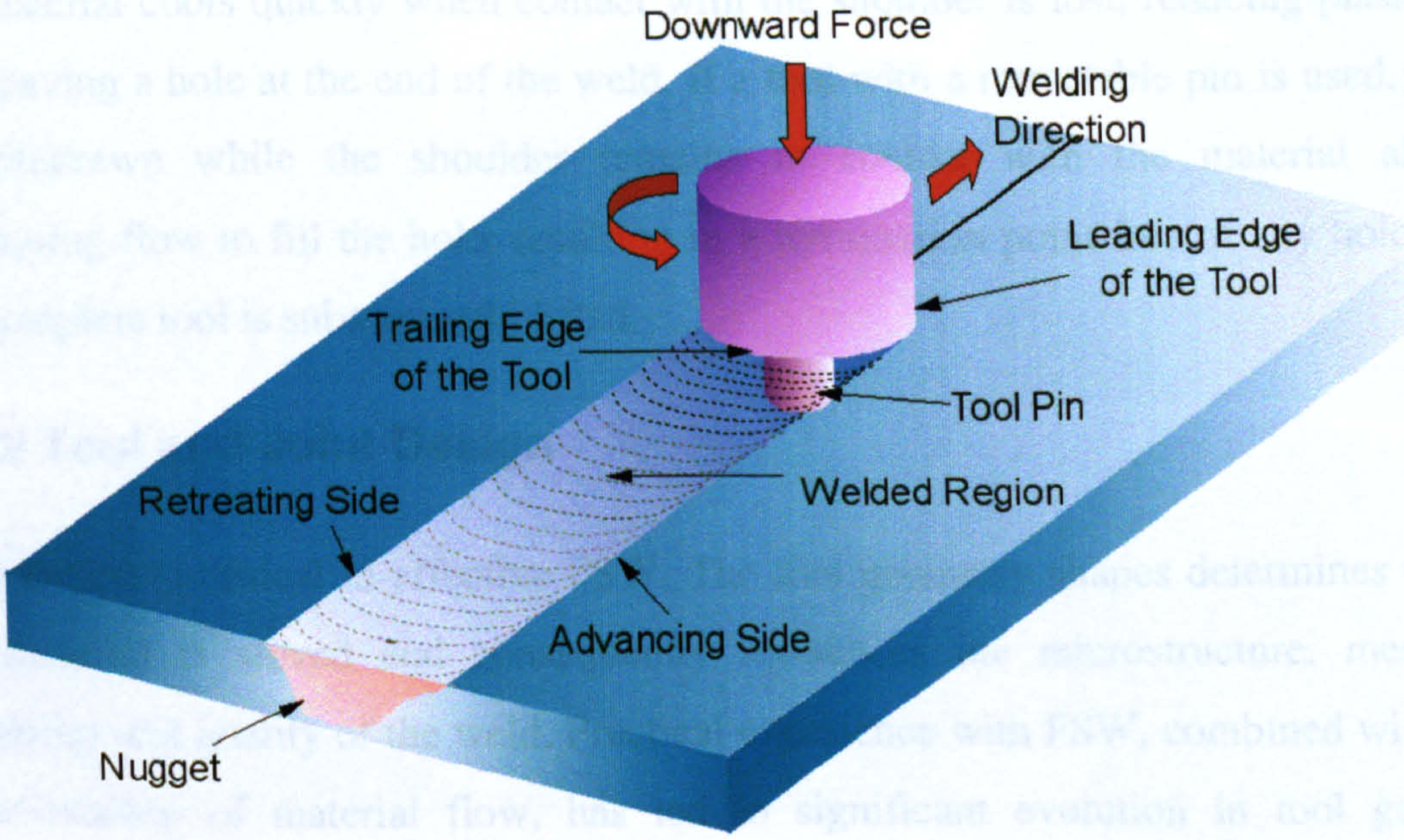

Figure 2.1 Schematic illustration of Friction Stir Welding.

In the *dwell* stage, the position of the tool at the end of plunge stage is maintained without changing the rotation speed. Additional heat is generated from the shoulder-plate interface, raising the temperature of the material in contact with the tool close to its melting point. After an appropriate dwell time, the material reaches a state in which it flows or *stirs* in a stable manner. Dwell time is crucial for the success of the subsequent stage and is a function of plate thickness, material properties and other welding parameters.

In the travel stage, the tool is traversed along interface between the plates. The softened material at the leading edge of the tool is stirred or extruded by the rotating tool and deposited at the trailing edge. Extensive plastic deformation in a confined region leads to intimate contact between the materials on either side of the joint, resulting in a strong metallurgical bond. The shape of the tool creates high hydrostatic pressure along the joint line, resulting in consolidation of the material.

When the specified length of weld has been formed, the process is terminated by stopping the forward movement and lifting the tool. If the entire tool is lifted in one step, the material cools quickly when contact with the shoulder is lost, reducing plastic flow and leaving a hole at the end of the weld. If a tool with a retractable pin is used, the pin is withdrawn while the shoulder remains in contact with the material allowing continuing flow to fill the hole, resulting in a termination point free of any holes when the complete tool is subsequently lifted.

2.1.2 Tool and Joint Design

Tool design is critical to effective FSW. The tool geometry shapes determines the way the material is stirred and consequently influences the microstructure, mechanical properties and quality of the weld. Practical experience with FSW, combined with better understanding of material flow, has led to significant evolution in tool geometry. Basically, the tool consists of two parts: the pin and the shoulder. Figure 2.2 illustrates the evolution of the tool using five selected typical tools. Initially, the tool pin had a smooth cylindrical surface. This is easy to manufacture but weld productivity (relatively low translation speed) and quality is relatively poor. A few defects such as void and lack-of-penetration could occur. More complex features such as threads and flutes were later added to the tool pin. These features are believed to reduce welding force and enable easier flow of plasticized material. Two examples are the Whorl^{TM} and the MXTriflute^{TM} developed by Thomas et al. [2.1]. Pins for both of these tools are shaped as a frustum that displaces less material than a cylindrical tool of the same root diameter. The Whorl^{TM} tool uses a tapered pin with re-entrant features or a variable pitch thread and the MXTriflute^{TM} design has a complex system of three tapering, threaded re-entrant flutes. These features increase the depth of penetration and the plate thickness that can be welded, particularly in lap welds. Later designs include the Flared-Trifute^{TM}, with the flute lands flared out, and the A-skew^{TM}, with the pin axis being slightly inclined to the axis of machine spindle [2.2–2.4].

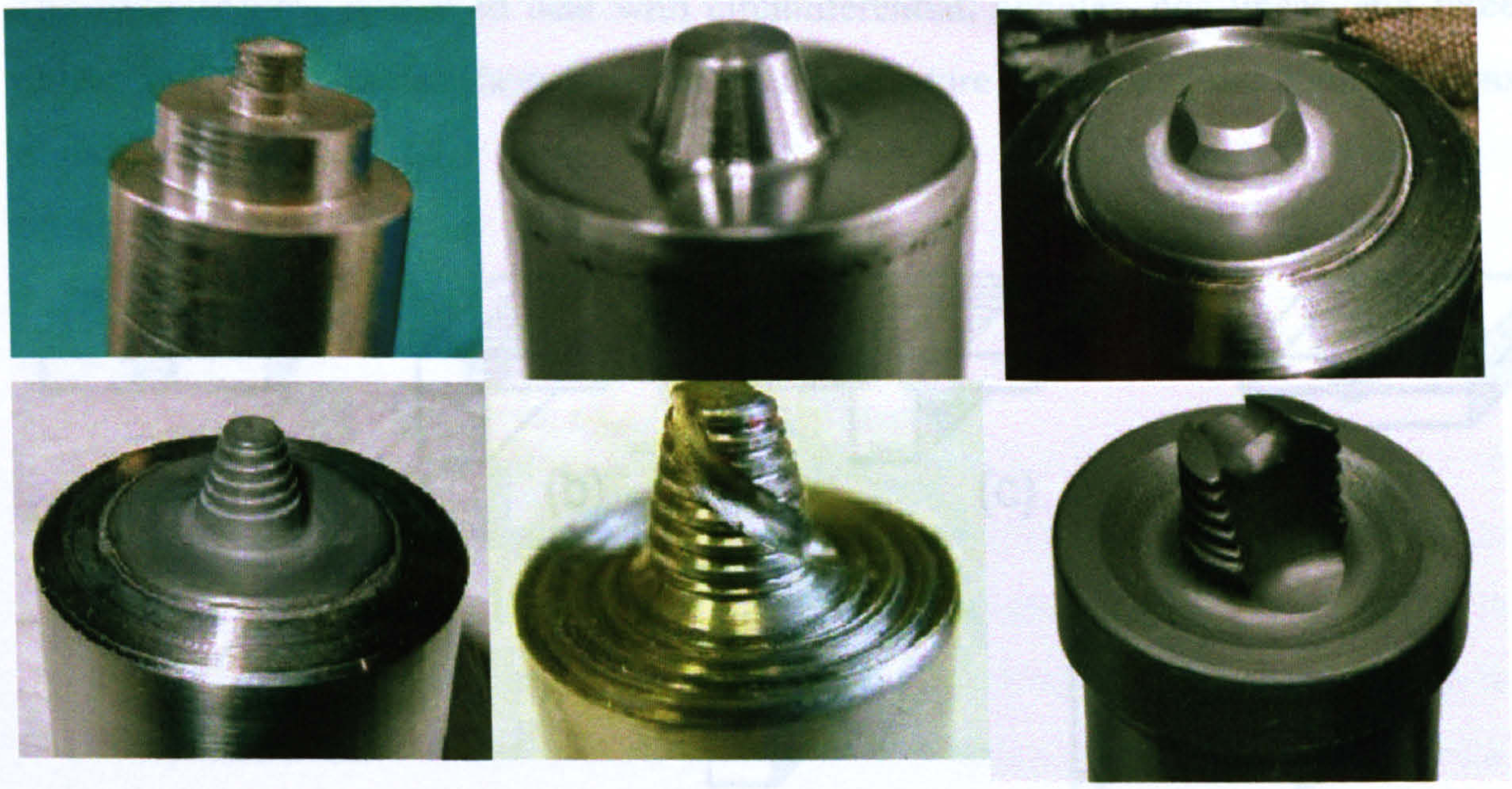

Figure 2.2 Typical FSW tools [2.6].

Various shoulder profiles have been designed to suit different materials and conditions, as shown in Figure 2.3. These shoulder profiles act as an escape volume for the material displaced by the pin, entrap plasticized material within special re-entrant features and provide additional movement of material in the interface between the shoulder and plates. In addition, more heat will be generated with the increased contact area between shoulder and workpiece.

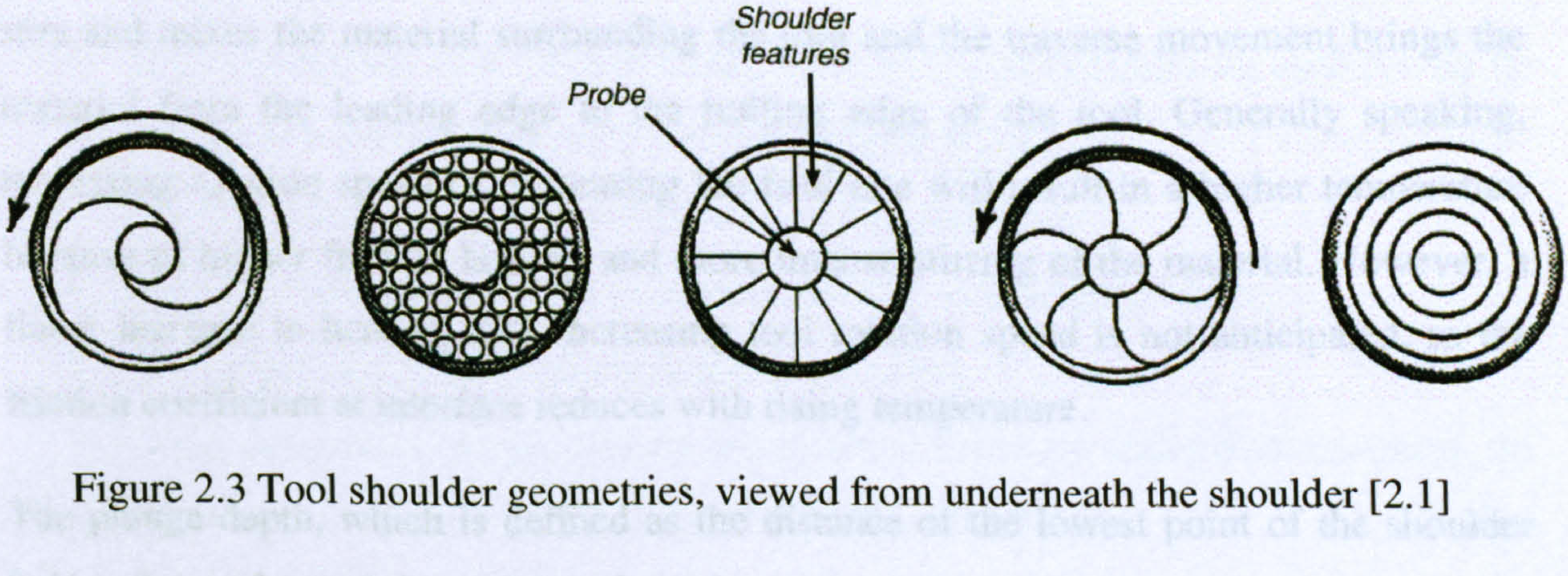

Figure 2.3 Tool shoulder geometries, viewed from underneath the shoulder [2.1]

The FSW process is able to deal with circumferential, annular, non-linear, and three dimensional welds and has been used for the manufacture of various joint configurations, as presented in Figure 2.4.

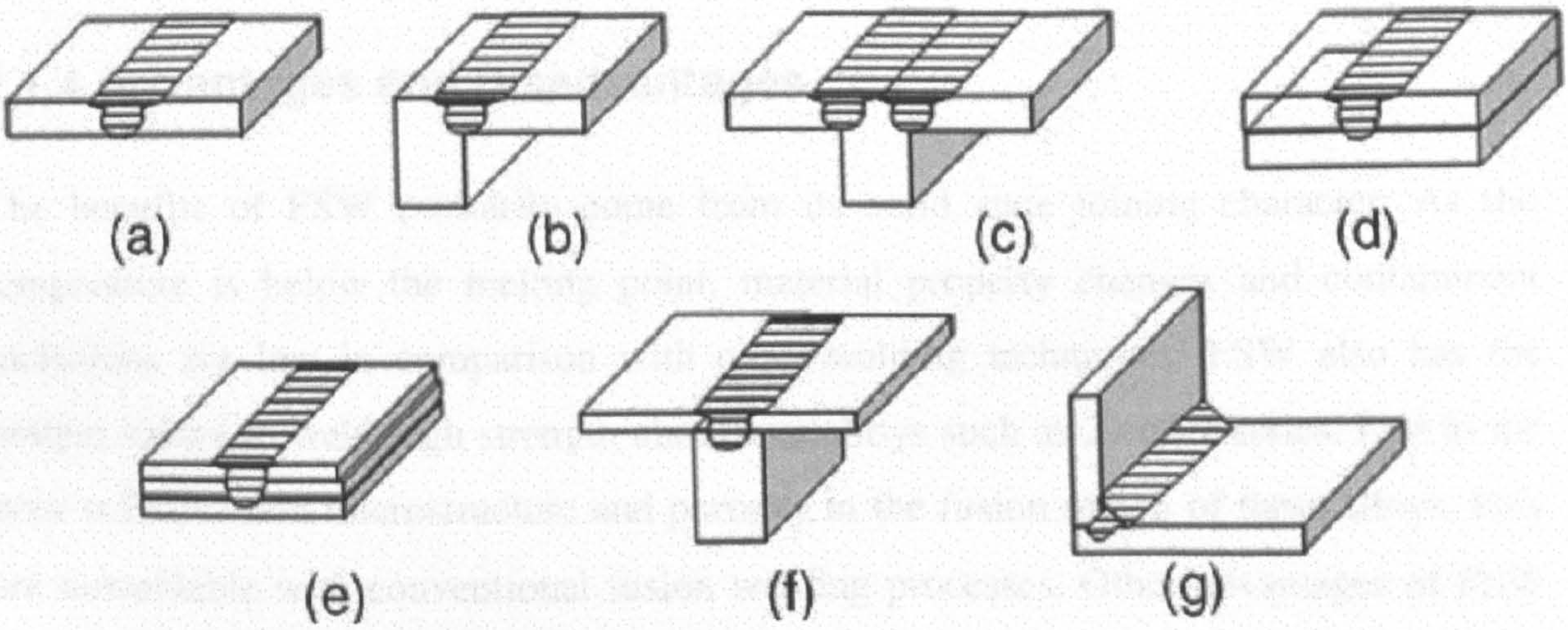

Figure 2.4 Joint configurations for friction stir welding: (a) square butt, (b) edge butt, (c) T butt joint, (d) lap joint, (e) multiple lap joint, (f) T lap joint, and (g) fillet joint. [2.5]

2.1.3 Welding Parameters

In FSW there are two important welding parameters that control the movement of the tool: tool rotation and feed speeds. Well chosen combinations of these two speeds for a specific material can lead to enhanced productivity and weld quality. The tool rotation stirs and mixes the material surrounding the tool and the traverse movement brings the material from the leading edge to the trailing edge of the tool. Generally speaking, increasing rotation speed or decreasing the feed rate will result in a higher temperature because of higher friction heating and more intense stirring of the material. However, a linear increase in heating with increasing tool rotation speed is not anticipated, as the friction coefficient at interface reduces with rising temperature.

The plunge depth, which is defined as the distance of the lowest point of the shoulder below the surface of the welded plate, is another critical parameter for ensuring weld quality, [2.7]. If the depth is too small, inadequate pressure is exerted on the material while too large a depth will result in excessive flash and affect the surface finish of the weld. The tool or spindle is often tilted by a small angle towards the opposite direction of welding to increase the time for which the material at the bottom of the pin experiences high temperature and improve the quality of the weld.

2.1.4 Advantages and Disadvantages

The benefits of FSW primarily come from its solid state joining character. As the temperature is below the melting point, material property changes and contaminant inclusions are low in comparison with other welding techniques. FSW also has the unique ability to weld high strength aluminum alloys such as 2 and 7 series. Due to the poor solidification microstructure and porosity in the fusion region of these alloys, they are unweldable with conventional fusion welding processes. Other advantages of FSW are summarized below [2.8] [2.9]:

- Relative low distortion, even in long welds
- Good mechanical properties as proven by fatigue, tensile and bend tests
- Improved safety due to the absence of toxic fumes or the spatter of molten material
- No porosity and Low shrinkage
- Can operate in all positions (horizontal, vertical, etc), as there is no weld pool
- Energy efficient
- Non-consumable tool - conventional steel tools can typically be used for up to 1000m of weld length in 6000 series aluminum alloys
- No filler wire or no gas shielding for welding aluminum
- Easily automated on simple milling machines - lower set-up costs
- No welder certification required and less training
- Generally good weld appearance and minimal thickness under/over-matching, no grinding, brushing or pickling required in mass production
- Relative low environmental impact

The main disadvantage of FSW lies in the large forces required to press and translate the tool. As a result, the work-pieces must be tightly clamped and equipment must have enough rigidity to ensure process accuracy. Other disadvantages such as the exit hole left at the end of each weld, limited material application, relative low welding speed, not portable, tool worn out quickly when welding hard materials, high cost of backing plate when welding curved surfaces, wider weld seam, difficulties with thickness variations welds can be solved with the development of welding techniques.

2.1.5 Application

FSW was originally used to weld high strength aluminums. Recently, it has been applied to join other materials including copper, bronze, lead, magnesium, thermoplastic resin, zinc, titanium and steel. Furthermore, FSW is capable of joining dissimilar materials, for instance, aluminum-lithium and aluminum metal matrix composites.

Application of FSW has spread rapidly and touches almost all industrial sectors [2.10]. In the aerospace industry, friction stir welding has been replacing riveting where possible, thus reducing manufacturing costs and weight [2.11-2.12]. Various components and structures have been welded successfully: wings, fuselages, empennages, fuel tanks and military and scientific rockets. In the shipbuilding and marine industries, applications include panels for decks, sides, bulkheads and floors, hulls, helicopter landing platforms offshore accommodation, masts and booms for sailing boats, refrigeration plant, etc. In the land transportation industry, potential and existing applications are wheel rims, truck bodies, tail lifts for lorries, mobile cranes, thin armor plate vehicles, caravans, buses and airfield transportation vehicles, motorcycle and bicycle frames. It is clear that the FSW has been widely accepted and made a significant impact in manufacturing.

2.1.6 Friction Stir Processing

Friction Stir Processing (FSP) is an emerging processing technique based on the basic concept of FSW [2.13]. It is a friction stir welding process intended to alter the workpiece's microstructure rather than to join plates. It provides a generic tool for localized microstructural modification and manufacturing. FSP can be used to remove casting defects, refine microstructures and improve the mechanical properties. Current important applications include producing fine grain materials with superplasticity performance [2.14], surface composite, homogenization of nanophase aluminum alloys and metal matrix composites.

2.2 Thermal Modelling for Friction Stir Welding

The temperature history during the FSW has a direct impact on the microstructure of the weld, such as grain size, grain boundary character, coarsening and dissolution of precipitates, and consequently influences mechanical properties of the weld [2.5]. Therefore, a good understanding of temperature distribution helps in evaluating the quality of the weld. In the case of welding high melting temperature alloys, for example the nickel alloys, titanium alloys and carbon steels, the temperature profile in the tool is valuable in predicting the fatigue life of the tool [2.15]. Thermal modeling provides an alternative method of obtaining temperature profiles to experiments and testing and has been the focus of much research in the last few years.

2.2.1 Analytical Thermal Model

The FSW process depends on the heat generated to soften the material around the tool. The heat generation mainly comes from interfacial friction and plastic energy dissipation during plastic flow deformation. But the ratio between them is still under augument and not defined. Preliminary thermal modelling of the FSW process was analytical and based on some fundamental assumptions of heat generation. The first analysis was presented by Gould, etc [2.16]. In their model, only the heat generated by the friction between the tool shoulder and the workpiece was considered. To calculate this heating, a line contact in the form of a ring (rather than a surface contact) was assumed between the tool shoulder and the workpiece.

The model is based on the Rosenthal Equation 2.1, originally derived for Arc Welding [2.17]. The Rosenthal equation describes the quasi-steady state temperature distribution for a moving point heat source of a constant velocity. In a cylindrical coordinate system, Figure 2.5, the temperature, T, at a point $P(r, \theta, z)$ on the workpiece as a result of a point heat source at $P'(R,\alpha,0)$ on the contact ring, i.e. $R=R_{shoulder}$, is expressed as

$$T = T_0 + \frac{\dot{Q}}{2\pi k\sqrt{r_0^2 + z_0^2}} \exp\left[-\frac{V}{2\varsigma}\left(w_0 + \sqrt{r_0^2 + z_0^2}\right)\right] \tag{2.1}$$

where $\dot{Q}$ is the heat generation rate, k thermal conductivity and $\varsigma = {k}/{cp}$, thermal diffusivity. Other terms are defined as

$$r_0^2 = R^2 + r^2 - 2Rr\cos(\alpha - \theta) \tag{2.2}$$

$$w_0 = r\cos\theta - R\cos\alpha \tag{2.3}$$

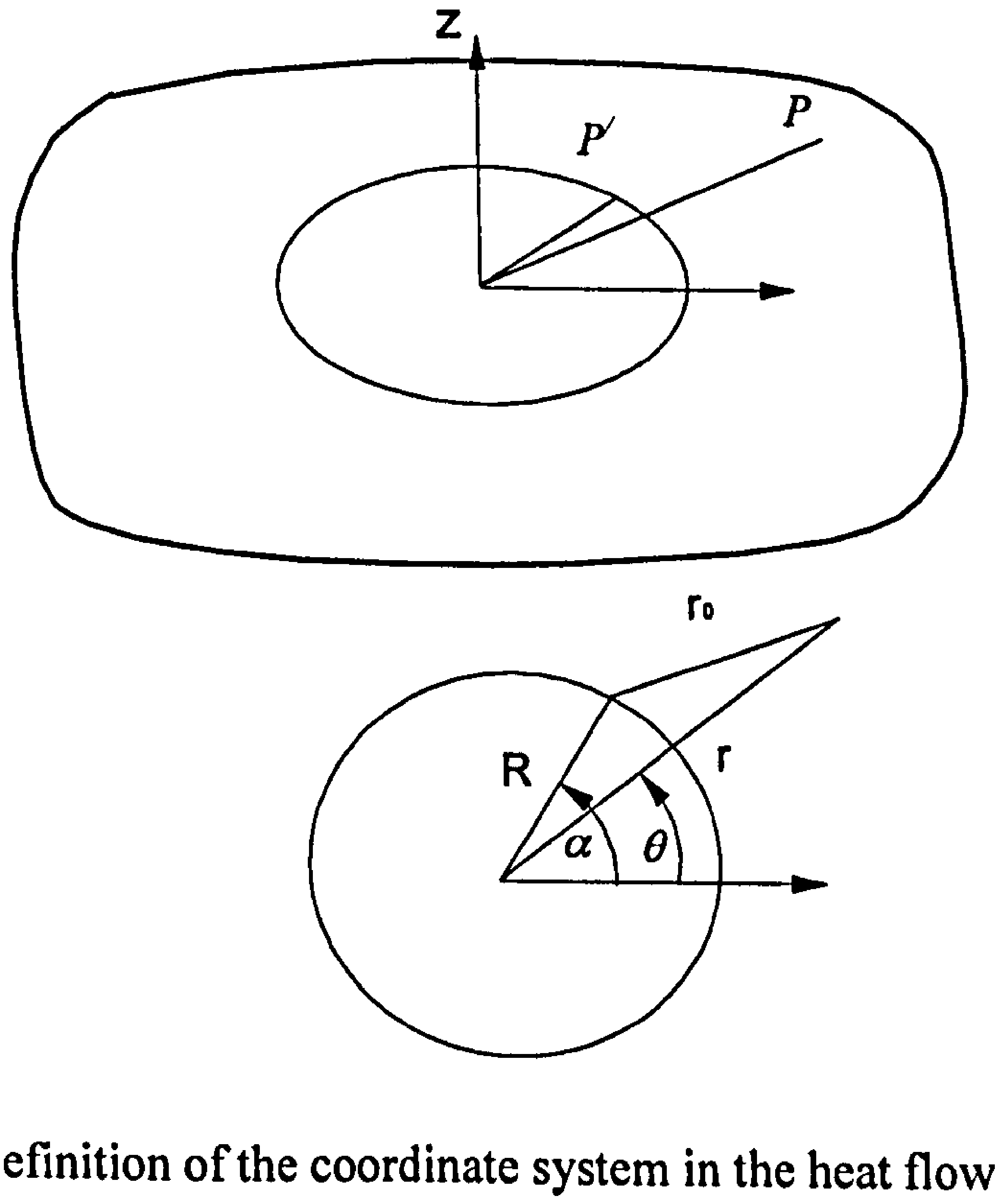

Figure 2.5 Definition of the coordinate system in the heat flow model [2.16].

The heat generation rate can be expressed as

$$\dot{Q} = \mu FnRd\alpha \tag{2.4}$$

where n is the rotation speed of the tool, μ the friction coefficient and F the downward force of the tool.

The final equation of the heat flow model can be obtained by integrating over the whole circle

$$T = T_0 + \int_{-\pi}^{\pi} \frac{\mu FnR \cdot \exp\left[-\frac{V}{2\varsigma}\left(w_0 + \sqrt{r_0^2 + z_0^2}\right)\right]}{2\pi k} d\alpha$$

$$= T_0 + \frac{\mu Fn}{2\pi k} \int_{-\pi}^{\pi} \frac{\exp\left[-\frac{VR}{2\varsigma}\left(\frac{r}{R}\cos\theta - \cos\alpha + \sqrt{1 + \left(\frac{r}{R}\right)^2 + \left(\frac{z}{R}\right)^2 - 2\frac{r}{R}\cos(\alpha - \theta)}\right)\right]}{\sqrt{1 + \left(\frac{r}{R}\right)^2 + \left(\frac{z}{R}\right)^2 - 2\frac{r}{R}\cos(\alpha - \theta)}} d\alpha$$

(2.5)

A Romberg numerical integration scheme embedded into an MS Excel spreadsheet was used to solve the integral in (2.5).

Another analytical thermal model recently presented by Vilaca, etc [2.18] was also based on the Rosenthal equation. A moving point power source was located at the mid-thickness of the plate, corresponding to the centre of the recrystallized zone. Two particular effects of the FSW process were superimposed on the Rosenthal equation:

1. One directly into the thermal field of the work-piece under the shoulder, owing to the friction between the tool and work-piece.
2. The other, due to the different heat flow distribution for hot and cold FSW conditions.

The asymmetric temperature distribution at the vicinity of the shoulder comes from the combination of the rotating and translation of the FSW tool. Figure 2.6 illustrates the velocity field on the tool. The strategy to formulate the asymmetric temperature distribution on the vicinity of the shoulder periphery is schematically shown in Figure 2.7.

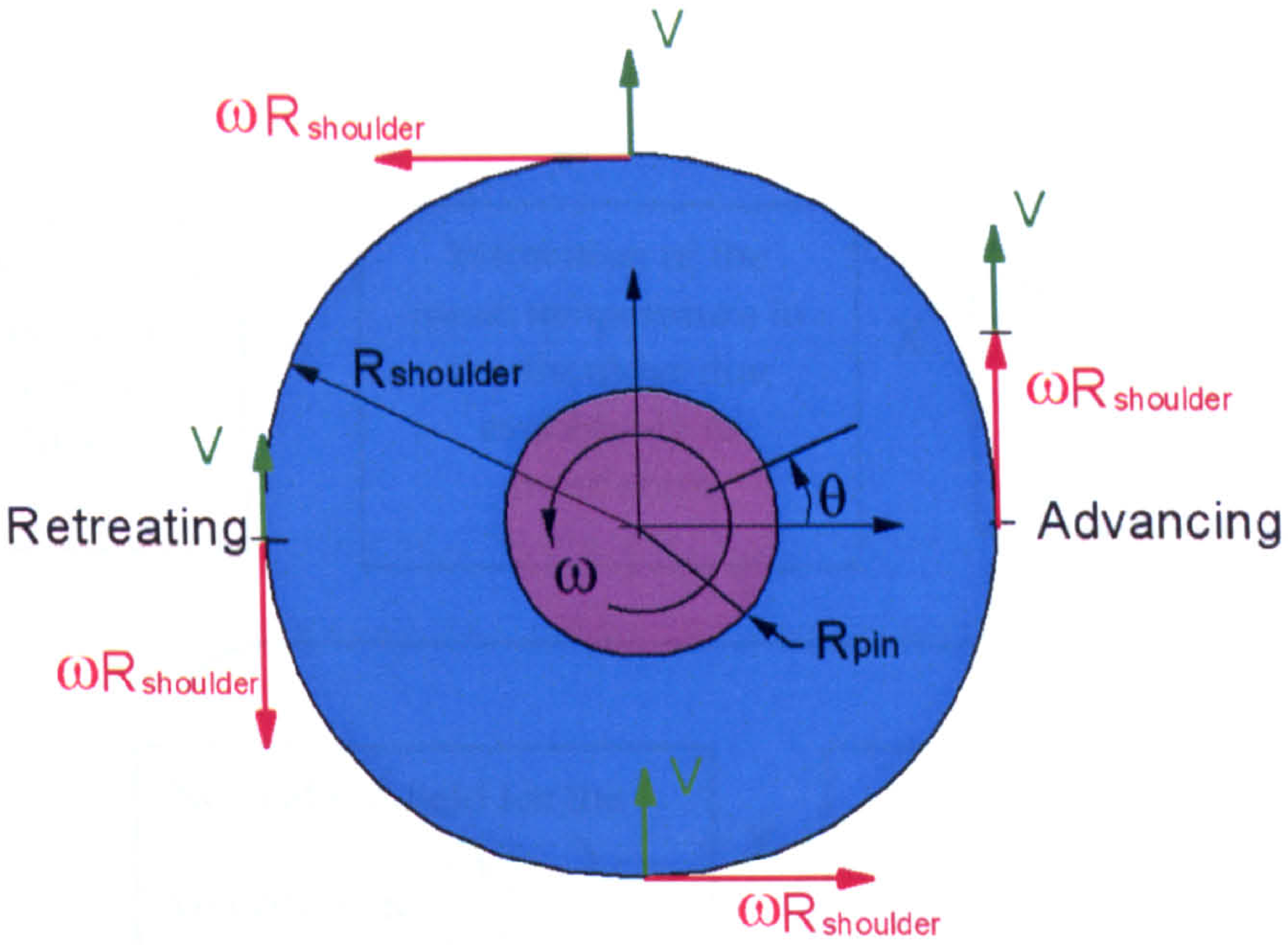

Figure 2.6 Velocity field on the tool.

To estimate the temperature due only to the translation movement, Equation 2.6, which is frequently applied in the field of tribological bimetallic contacts, was used [2.20], [2.21].

$$T_V = \frac{\gamma_{parts} \mu F V}{\pi k \left(R_{shoulder} - R_{pin} \right)} \tag{2.6}$$

where γ_{parts} is the portition of the total heat dissipated to the parts during FSW process, μ the friction coefficient, and F the downward force applied to the tool.

Equation 2.7 represents the normalised field for the velocity ratio at the shoulder periphery.

$$V_{norm}\left(r = R_{shoulder}, \theta\right) = \frac{\sqrt{\left(\omega R_{shoulder}\right)^2 + 2V \cdot \omega R_{shoulder} \cos\theta + V^2} - \omega R_{shoulder}}{\sqrt{\left(\omega R_{shoulder}\right)^2 + 2V \cdot \omega R_{shoulder} + V^2} - \omega R_{shoulder}} \qquad (2.7)$$

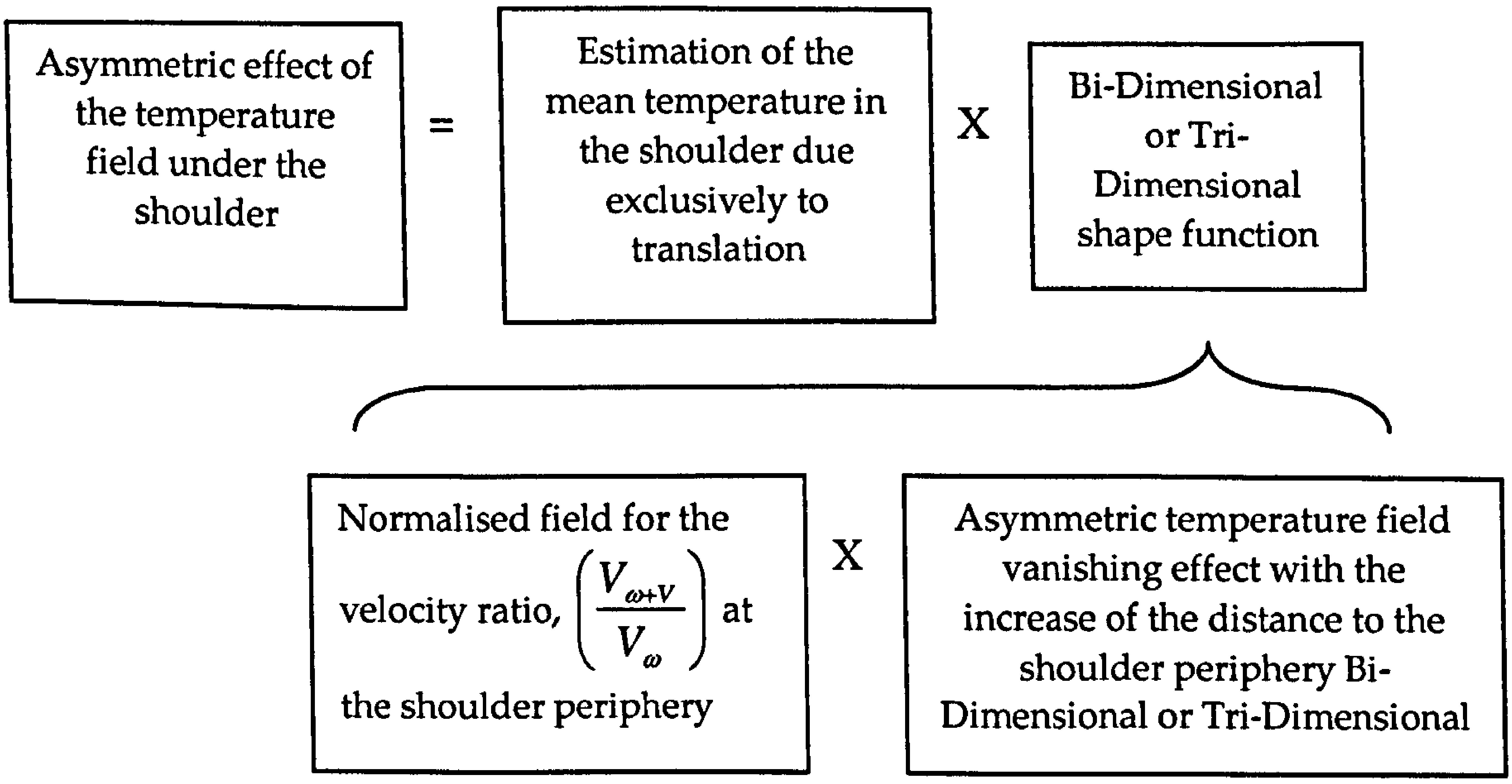

Figure 2.7 Strategic plans for establish the thermal asymmetric effect under the shoulder.

The function simulating vanish effect of the thermal asymmetric effect with increase of distance from the shoulder periphery is expressed as

$$Ef_{vanish}\left(r, \theta, z\right) = \begin{cases} \exp\left[C_{red}\left(\frac{R_{shoulder}^2 - r^2}{R_{shoulder}^2} - 5\frac{z}{g}\right)\right] & \Leftrightarrow 3D\ Heat\ Flux \\ \exp\left(C_{red}\frac{R_{shoulder}^2 - r^2}{R_{shoulder}^2}\right) & \Leftrightarrow 2D\ Heat\ Flux \end{cases}$$

(2.8)

where C_{red} is the tuning constant of the vanish effect (typically: $1 \le C_{red} \le 3$).

According to Figure 2.6, combining Equations 2.6, 2.7 and 2.8 leads to the final expression for the asymmetric thermal effect,

$$T_{Asym}(r,\theta,z)=\frac{\gamma_{parts}\mu FV}{\pi k\left(R_{shoulder}-R_{pin}\right)}\frac{\sqrt{\left(\omega R_{shoulder}\right)^2+2V\cdot\omega R_{shoulder}\cos\theta+V^2}-\omega R_{shoulder}}{\sqrt{\left(\omega R_{shoulder}\right)^2+2V\cdot\omega R_{shoulder}+V^2}-\omega R_{shoulder}}$$

$$\times\begin{cases}\exp\left[C_{red}\left(\frac{R_{shoulder}^2-r^2}{R_{shoulder}^2}-5\frac{z}{g}\right)\right] & \Leftrightarrow 3D\ Heat\ Flux\\ \exp\left(C_{red}\frac{R_{shoulder}^2-r^2}{R_{shoulder}^2}\right) & \Leftrightarrow 2D\ Heat\ Flux\end{cases}\tag{2.9}$$

Another feature of FSW affecting heat flow is the welding parameters, particularly the ratio of rotation speed to translation speed, which governs the hot-to-cold classification of the weld:

$$\frac{n}{V}>4\Leftrightarrow \text{ Hot FSW Conditions}$$

$$2\le\frac{n}{V}\le4\Leftrightarrow \text{ Intermediate FSW Conditions}\tag{2.10}$$

$$\frac{n}{V}<2\Leftrightarrow \text{ Cold FSW Conditions}$$

$$\text{where }\begin{cases}[n]=rpm\\ [V]=mm/\min\end{cases}$$

The above values are derived from macrograph analysis and experience gained during temperature measurements [2.19]. For hot FSW conditions, the recrystallized material in the weld nugget develops in a form of 'onion rings'. The heat flow is approximately uniform around the tool. For cold FSW conditions, there is not such a well-defined centre for a recrystallized zone and higher temperatures exist at the retreating side surface. These conclusions were proved by experiment [2.22].

Hot and cold FSW conditions are incorporated into the analytical model by applying Equation 2.11 to the initial point power source.

$$q_{hot-cold} \equiv \begin{cases} q_0\left(1 + C_{hot-cold}\dfrac{1 - t\tanh\left[2\left(\dfrac{n}{V} - 3\right)\right]}{2}\right) \Leftrightarrow \text{Retreating Side} \\ q_0\left(1 - C_{hot-cold}\dfrac{1 - t\tanh\left[2\left(\dfrac{n}{V} - 3\right)\right]}{2}\right) \Leftrightarrow \text{Advanceing Side} \end{cases} \tag{2.11}$$

where $C_{hot-cold}$ is the constant to be calibrated for each material and thickness, indicating maximum asymmetric effect on the thermal field for cold conditions.

The function $\tanh(x) = \dfrac{e^{2x} - 1}{e^{2x} + 1}$ and the function for guidance control of the heat flow for cold and hot weld conditions are shown in Figure 2.8.

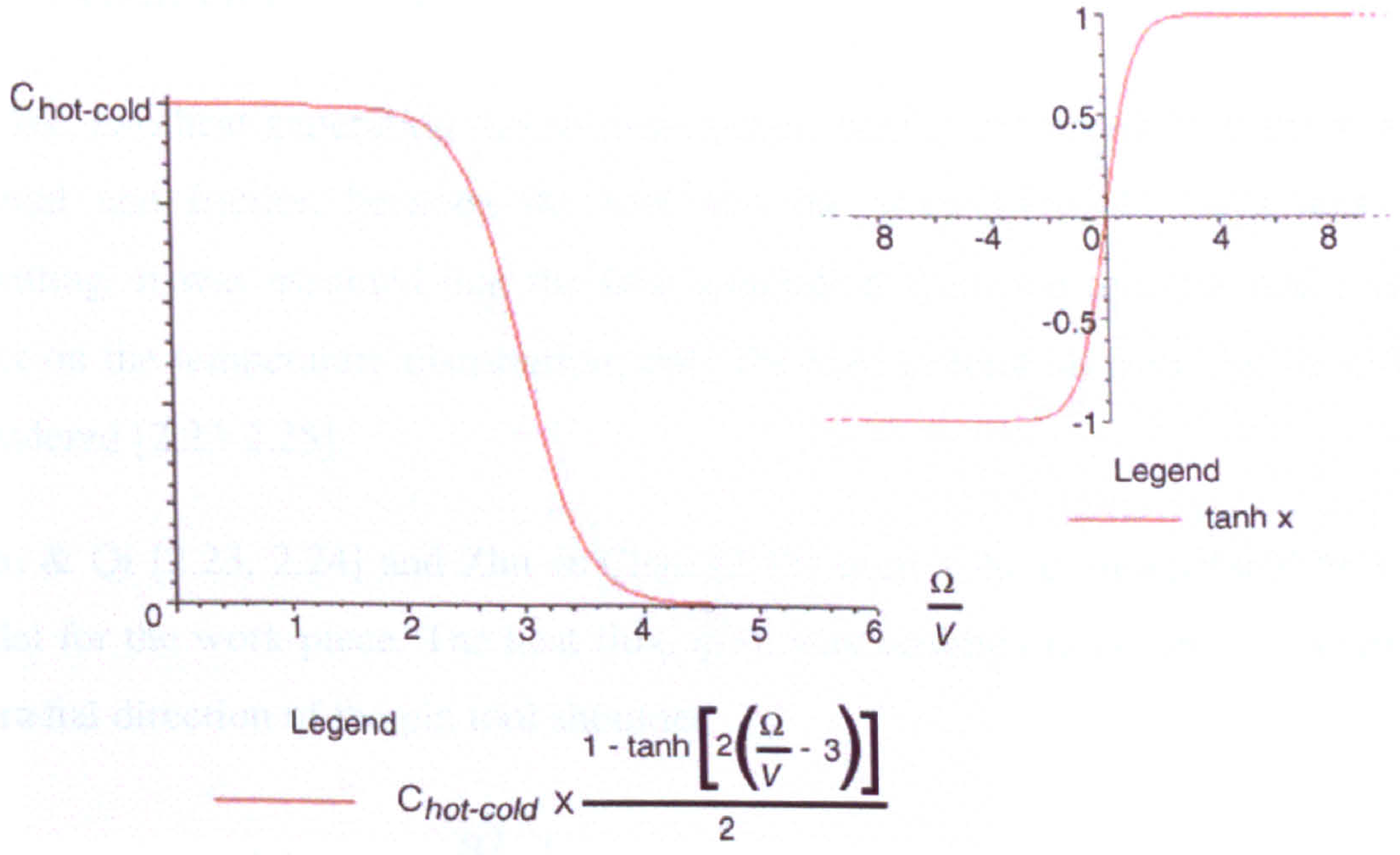

Figure 2.8 Plot of the function for guidance control of the heat flow [2.18].

All the above analytical thermal models are capable of predicting the thermal field and can provide relationships between welding parameters and temperature profiles. If employed in a "reverse engineering approach", the thermal field estimated by the analytical model could be adjusted to experimental measurements so as to attain the point power source and further to define the FSW efficiency.

However, all the analytical thermal models were based on the Rosenthal equation which describe the *quasi-steady state* temperature distribution for a moving *point* heat source of a constant velocity. The heat source was always assumed to be a line or point, on top of the surface or inside the workpiece. Hence this doesn't properly represent the heat transfer in the workpeice beneath the tool.

2.2.2 Numerical Thermal Modeling

After early analytical attempts at thermal simulation of FSW, numerical models, mainly based on the finite element method and computational fluid dynamics, have received increased attention due to the versatility of these models.

2.2.2.1 Heat Generation

In FSW, two heat generation mechanisms occur: plastic deformation of the work-piece material and friction between the tool and the work-piece. In early heat transfer modelling, it was assumed that the heat generation from the tool pin had little or no effect on the temperature distribution; only the heat generation from the shoulder were considered [2.23-2.25].

Chao & Qi [2.23, 2.24] and Zhu & Chao [2.25] used a three dimensional heat transfer model for the work-piece. The heat flux, *q(r)*, was assumed to be linearly distributed in the radial direction of the pin tool shoulder.

$$q(r)=\frac{3Q_{wp}r}{2\pi\left(R_{shoulder}^{3}-R_{pin}^{3}\right)} \quad for \quad R_{pin}\leq r\leq R_{shoulder} \tag{2.12}$$

where Q_{wp} is the total heat input energy to work-piece. In their analysis, an inverse analysis method was used to adjust the heat input until FEM calculated temperatures match the measured ones.

In recent models [2.26-2.32], the heat generation from the tool pin has been included. Chao *et al.* [2.26] lumped this heat into the friction heat at the interface of the tool and the work-piece. The heat input was assumed to be linearly proportional to the distance from the centre of the tool similar to Equation (2.12). Setting $R_{pin} = 0$, Equation (2.12) becomes

$$q(r) = \frac{3Q_{wp}r}{2\pi R_{shoulder}^3} \quad for \quad r \le R_{shoulder} \tag{2.13}$$

Frigaard et al. [2.27, 2.28] calculated the total heat input as the slide friction heat produced by rotating a circular shaft relative to the plate surface under an axial load. It was assumed that the local pressure applied to the work-piece, $p(r)$, was constant and equal to p. The total heat input was given by

$$Q_{wp} = \frac{2}{3}\pi \; p\mu\omega R_{shoulder}^3 \tag{2.14}$$

The heat source was divided into a fixed number of square grid points. The uniform heat flux at each grid point was obtained by dividing the total heat input by the number of square grid points.

Colegrove [2.29] provided an expression for calculating the heat from the pin which consists of three parts: heat generated by (1) shearing of the material; (2) friction on the threaded surface of the pin and (3) friction on the vertical surface of the pin.

$$Q_{pin} = 2\pi R_{pin} H_{wp} \bar{\tau}_{yield} \frac{V_m}{\sqrt{3}} + \frac{2\pi\mu k \bar{\tau}_{yield} R_{pin} H_{wp} V_{rp}}{\sqrt{3(1+\mu^2)}} + \frac{4F_p \mu V_m \cos\varphi}{\pi} \tag{2.15}$$

where $\varphi = 90^0 - \lambda - \tan^{-1}(\mu)$, $V_m = \dfrac{R_{pin}\omega \sin\lambda}{\sin(180^0 - \varphi - \lambda)}$ and $V_{rp} = \dfrac{R_{pin}\omega \sin\varphi}{\sin(180^0 - \varphi - \lambda)}$.

H_{wp} is the thickness of the workpiece, $\bar{\tau}_{yield}$ the average yield shear stress and λ the helix angle of the thread.

Based on this analytical estimation of the heat generation, Colegrove estimated that the amount of heat generated by the probe was as high as 20%. As a result, the analytical estimated pin heat generation contribution should not be neglected. The Equation 2.15 was also used in [2.30-2.32], where this pin generated heat was simplified to a uniform volumetric heat generation within a cylinder volume of the work-piece displaced by the tool pin.

Khandkar et al presented a novel 3-D heat input model in [2.33-2.35]. The heat input was correlated with the experimentally measured torque by introducing an averaged shear stress.

Torque at the shoulder-workpiece interface,

$$M_{shoulder} = \int_{R_{pin}}^{R_{shoulder}} 2\pi\bar{\tau}r^2 dr \tag{2.16}$$

Torque at the pin bottom surface,

$$M_{pinbottom} = \int_{0}^{R_{pin}} 2\pi\bar{\tau}r^2 dr \tag{2.17}$$

Torque at the vertical pin surface,

$$M_{pinVsurface} = 2\pi\bar{\tau}R_{pin}^2 H_{pin} \tag{2.18}$$

where $\bar{\tau}$ is the average shear stress.

The total torque, M_{tot}, is related to the power input by,

$$P_{av} = M_{tot}\omega \tag{2.19}$$

In their FE analysis, the heat flux applied to the contact surface was

$$q(r) = \omega\tau r \tag{2.20}$$

When calculating the frictional heat generation, all the models described above assumed the sliding contact condition at the interface between the tool and workpiece. Schmidt *et al.* [2.36, 2.37] presented an analytic heat generation model based on different contact condition assumptions: sliding, sticking and partial sliding/sticking.

Sliding. When the contact shear stress is lower than the workpiece material yield shear stress, the sliding condition applies.

Sticking. Under the sticking condition, the contact shear stress is equal to the matrix yield shear stress; i.e. the matrix at the interface is stationary relative to the rotating tool. The yield shear stress will increase at higher strain rates. If the contact shear stress still equals the yield shear stress at this high strain rate, a fully sticking condition will be established.

Partial Sliding/Sticking. The contact shear stress is less than the yield shear stress at high strain rates but higher than that at lower strain rates. The contact layer in workpiece then rotates with the tool at a lower speed.

A contact state variable was given to define three contact conditions,

$$\delta = \frac{V_{matrix}}{V_{tool}} = \begin{cases} 1 & \textit{Sticking} \\ (0,1) & \textit{Partial Sliding / Sticking} \\ 0 & \textit{Sliding} \end{cases} \tag{2.21}$$

The heat generation from the tool shoulder, pin vertical surface and pin bottom surface were presented as follows

$$Q_{shoulder} = \frac{2}{3}\pi\omega\left[\delta\tau_{yield} + (1-\delta)p\mu\right]\left(R^3_{shoulder} - R^3_{pin}\right)(1+\tan\alpha) \tag{2.22}$$

$$Q_{pinVsurface} = \pi\omega\left[\delta\tau_{yield} + (1-\delta)p\mu\right]\times 2R^2_{pin}H_{pin} \tag{2.23}$$

$$Q_{pinbottom} = \frac{2}{3}\pi\omega\left[\delta\tau_{yield} + (1-\delta)p\mu\right]\times R^3_{pin} \tag{2.24}$$

where α is conical shoulder angle. p is assumed constant over the contact surface. The total heat generation is

$$\begin{aligned} Q_{total} &= \frac{2}{3}\pi\omega\left[\delta\tau_{yield} + (1-\delta)p\mu\right] \\ &\times\left[\left(R^3_{shoulder} - R^3_{pin}\right)(1+\tan\alpha) + R^3_{pin} + 3R^2_{pin}H_{pin}\right] \end{aligned} \tag{2.25}$$

Only the friction heat generation mechanism was considered and the contact shear stress was calculated by Coulomb's law.

2.2.2.2 Other Modelling Problems

(a) Boundary conditions for workpiece

Tool shoulder/workpiece interface. All the models described above applied the shoulder surface heat flux to this interface.

Tool pin/workpiece interface. Part of the heat is generated at this interface. The heat transfer models in [2.33-2.35] neglect the heat generated here and the pin volume, thus no boundary condition was included. Models [2.30, 2.33-2.35] applied surface heat flux to the interface while a volumetric heat generation was used in [2.31].

Convection boundary conditions. All the surfaces of the workpiece exposed to air fall into this category. For the surface in contact with back-up plate, a large convective heat transfer was assumed to simplify the model [2.23-2.28, 2.30-2.32].

Including the backing plate in the modelling increases the complexity of the model and makes it much more computationally expensive. Heat transfer at the contact interface is complicated and uncertain. Different backing plates have a significant effect on the heat flow and temperature distribution. Models in [2.29, 2.34 and 2.35] included the backing plate in their simulations. Khandkar *et al.* [2.35] studied the effects of: (i) different backing plates and (ii) different contact gap conductance at the workpiece-backing plate interface on the thermal profiles. It was found that even for the same thermal contact conductance value, the lower conductivity of the backing plate considerably affected the overall thermal profile, particularly in the longitudinal direction. They also addressed the difficulty of fitting the uncertain thermal contact conductance, which depends on the roughness of the surfaces in contact and pressures involved.

(b) Thermal model for the tool

Thermal modelling research has mainly focused on the workpiece, as the weld quality is of primary concern. However a thermal model of the tool could help to calculate the heat losses into the tool, allowing the welding efficiency to be determined. The heat that flows into the tool dictates the life of the tool and the capability of the tool for the joining process [2.26].

Chao and Qi [2.26] performed an FE steady state heat transfer analysis. The model comprises of axisymmetric quadrilateral elements with temperature-dependent thermal material properties for the M2 tool steel. The boundary conditions of the model are shown schematically in Figure 2.9.

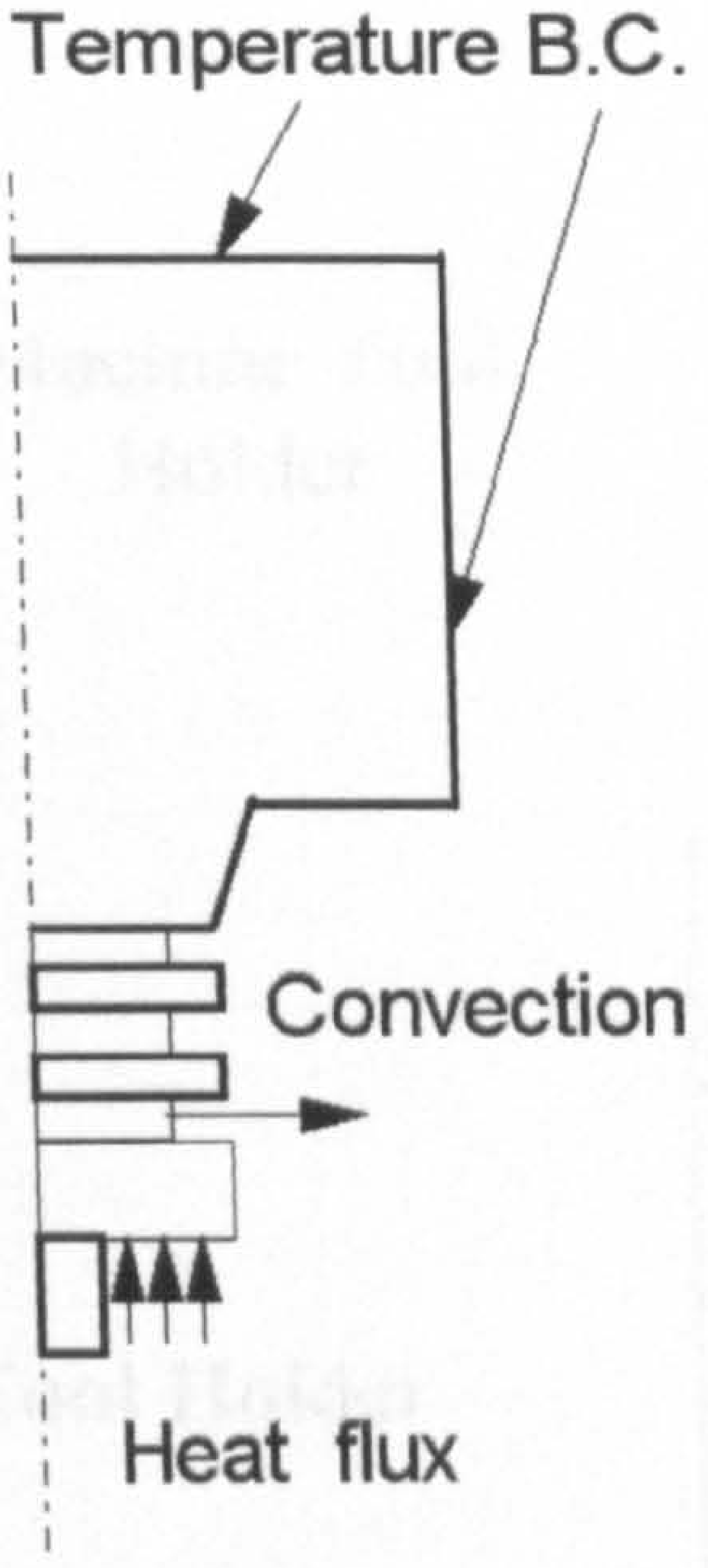

Figure 2.9 Boundary conditions for the tool [2.15].

Dickerson *et al.* [2.38] presented a transient heat transfer model with axisymmetric elements as shown in Figure 2.10. The boundary conditions are listed in Table 2.1.

Table 2.1 Boundary conditions applied to the FE model (2.38)

Description	Symbol
Fixed temperature at machine tool chuck	X
Contact conductivity between tool holders	O
Fixed Temperature at tool/weld interface	●
Heating (weld) time, including dwell	N/A
Convection (heat transfer coefficient)	Free Surfaces
Radiation (emissivity)	

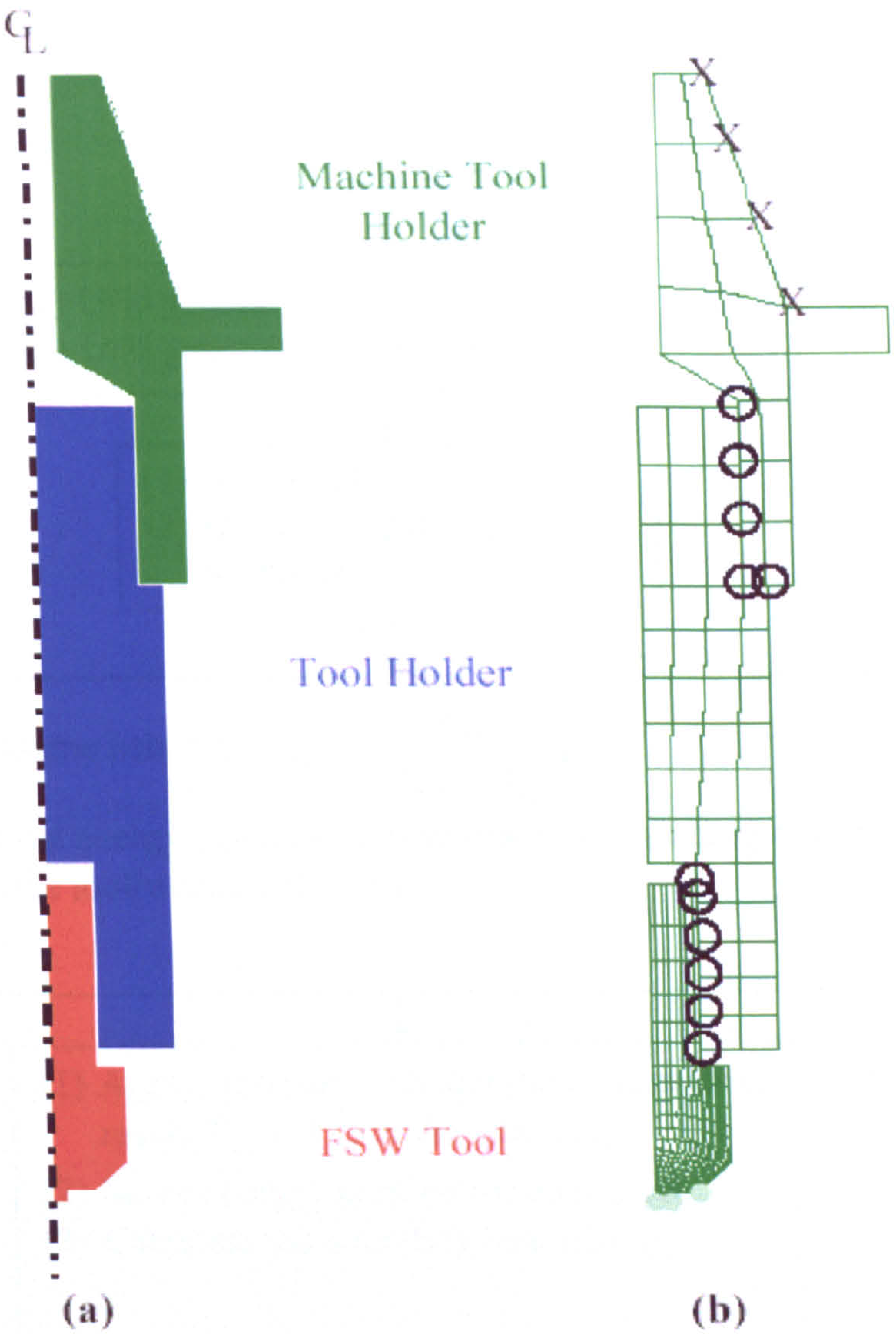

Figure 2.10 Axisymmetric finite element model and its holders [2.38].

(c) Coupled heat transfer model for both tool and workpiece

The heating is generated at the tool/workpiece interface and flows into the tool and the workpiece at same time. Song and Kovacevic [2.32] presented a coupled thermal model for both workpiece and tool in the FSW process. The two-dimensional axisymmetric tool and three-dimensional workpiece were created with a non-uniform grid to ensure enough nodes near the tool pin. The coupled calculation procedure at the interface is shown in Figure 2.11.

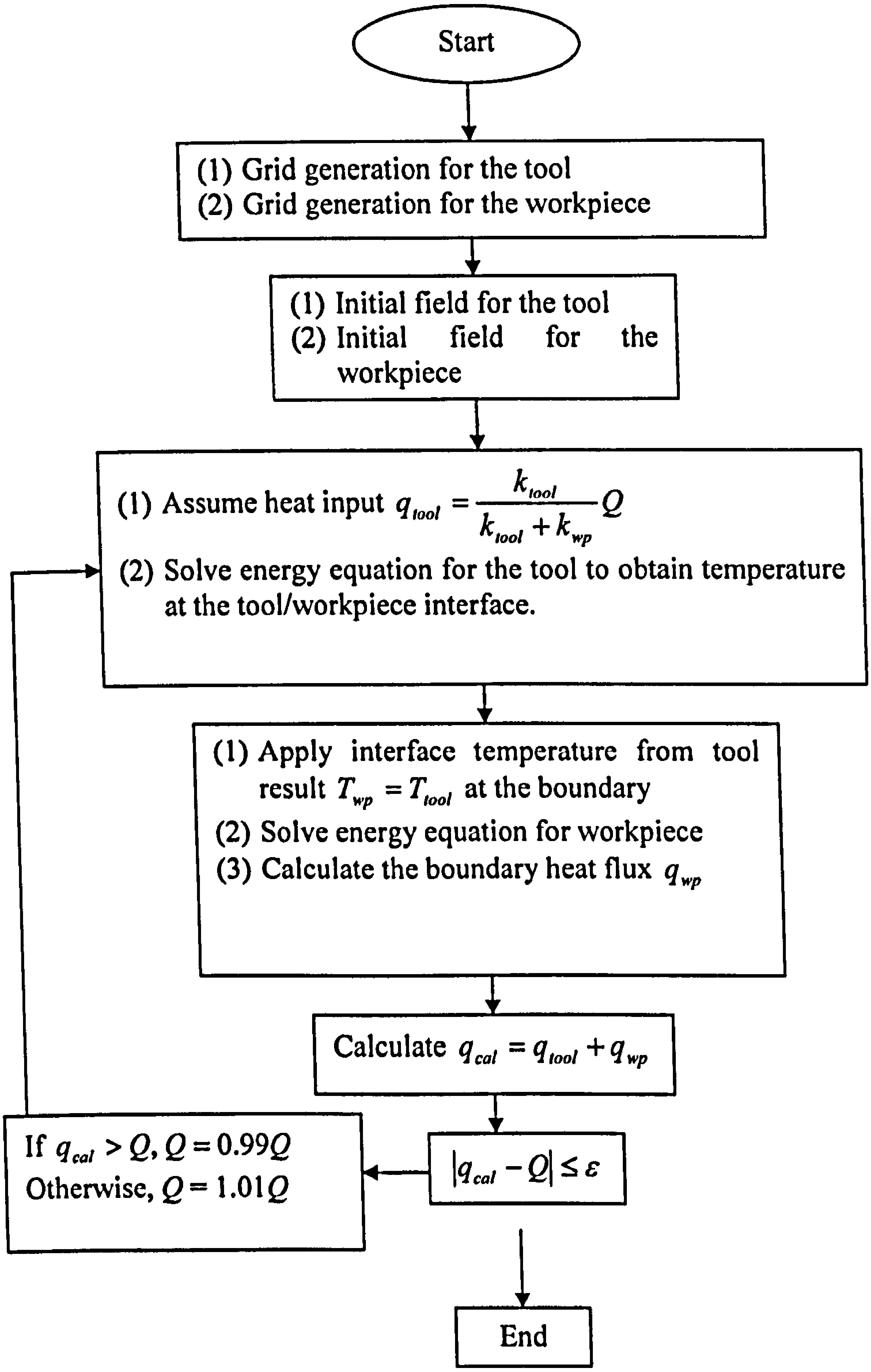

Figure 2.11 Flow chart of the calculation procedure of the coupled model [2.32].

where k_{tool} is thermal conductivity for tool material and k_{wp} for workpiece material. If the calculated temperature exceeds the melting temperature of the material, it is modified to the melting temperature in order to keep the FSW as a solid state process. They compared the calculated results with the microstructure morphology, infrared camera images and thermocouple results and concluded that their coupled heat transfer model can accurately describe the heat transfer process of both the tool and the workpiece in FSW.

2.3 Simplified Thermo-mechanical Models

Thermo-mechanical modelling of friction stir welding is intended to predict not only the transient temperature field, but also the residual stress and deformations in the workpiece. In the welding process, the movement of the tool generates the heat required to soften the material and cause the material to flow. It is desirable to include the mechanical reaction of the tool but this will induce various challenges in the thermo-mechanical models; such as complex contact behaviour, heat generation from friction and plastic deformation, heat transfer between the tool and plates, temperature and strain rate dependent material model etc. These challenges make the model computationally very expensive. In a simplified model, often referred to as non-mechanical heat source model, the tool is modelled as a moving heat source. This simplification removes the challenges mentioned above and significantly reduces the complexity of the model, at the expense of lower accuracy.

Simplified, non-mechanical heat source models are widely used, especially in the industrial field. For example, Engineers in the Hitachi Company used a simplified model to estimate the residual stress and structural deformation of a double-skinned train body component welded by FSW [2.39]. Common to those models is the prescribed non-mechanical heat input.

Zhu and Chao [2.40] presented a sequentially coupled thermo-mechanical model using WELDSIM, an FE code developed by the authors. An inverse analysis method was used for thermal analysis based on experimentally measured temperatures. Then the transient temperature profiles predicted by the thermal model were used to calculate thermal stress and displacement in the plates. In their FE model, only half of the plate was modelled due to the symmetry along the welding line. The temperature dependent thermal and yield stress material properties of 304L stainless steel with a constant plastic modulus were used. It was assumed that the heat flux was linearly distributed on the top surface of the plate and the heat generated at the tool pin was neglected. In subsequent mechanical analysis, the forces from the tool were not considered. The effect of fixture release when the weld cooled down to room temperature was studied. Comparison of numerical residual stress fields with the measured values by the neutron diffraction technique at several specific locations showed good agreement.

Chen and Kovacevic [2.41, 2.42] proposed a three-dimensional FE model to study the thermo-mechanical process in the butt-welding of aluminium alloy 6061-T6. The temperature-dependent properties of the alloy up to 371 °C were used, thereafter the properties were extrapolated. The heat generation caused by the friction was calculated using experimentally measured contact pressure and a constant value of the friction coefficient. The temperature datum at each time increment was used to evaluate the mechanical and thermal properties. The mechanical effect of the shoulder was considered assuming a Coulomb friction law for the interaction between the shoulder and the material. [2.41] mainly focused on predicting evolution of longitudinal, lateral and through-thickness stress in the plates. [2.42] not only studied the effect of process parameters such as tool traverse speed on residual stress but also computing the mechanical forces histories in the longitudinal, lateral and vertical directions.

Soundararajan et al [2.43] refined the FE model in [2.41] and [2.42] by applying an adaptive contact conductance at the interface of shoulder-workpiece. At the beginning of the FE thermo-mechanical analysis, a uniform contact conductance was used to predict the stress at the interface. This pressure distribution contours were applied to define the non-uniform pressure denpendent contact conductance in the thermal model, estimating the temperature profiles. The stress evolution was then calculated based on this temperature distribution. It was concluded that the model with adaptive contact conductance could provide more accurate thermal and residual stress results by comparing with experimental values.

All the above simplified model didn't include the contact pressure dependent heat transfer coefficient in their boundary condition definitions. Although Soundararajan et al [2.43] considered this, the calculated non-uniform contact conductance at the beginning of the analayis was kept constant and used throughout the whole welding process.

2.4 Coupled Thermo-mechanical Model

In a transient FSW process model, the heat generation by interfacial friction and material plastic deformation is calculated during the analysis, rather than through *a priori* thermal load input as in simplified models. As the mechanical action of the tool is included, the input parameters for the model are the same as those used in experiments, such as welding speed and tool rotating speed. The inclusion of these coupled physical phenomena makes the process models much more complex than the simplified ones. On the other hand, the model can be used to capture the weld formation and material flow, in addition to transient temperature and stress distributions.

Ulysse [2.44] provided a three dimensional visco-plastic model using the commercial software FIDAP [2.45] as shown in Figure 2.12.

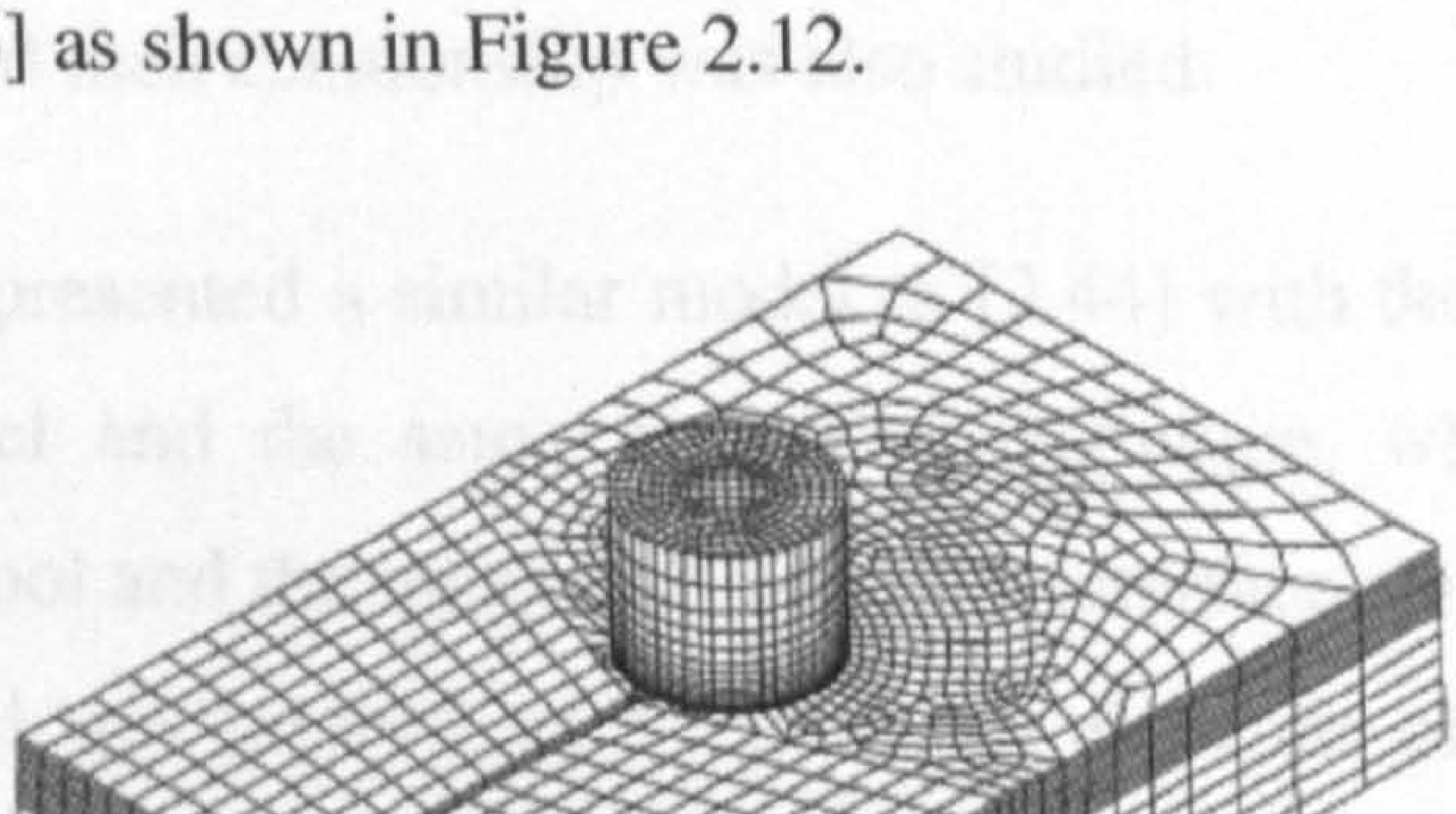

Figure 2.12 FE mesh of the welding model [2.44].

A rigid-viscoplastic temperature and strain-rate dependent material model was used in the model:

$$\sigma_e = \frac{1}{\alpha_m}\sinh^{-1}\left[\left(\frac{Z_m}{A_m}\right)^{1/n}\right], \quad Z_m = \dot{\varepsilon}\exp\left(\frac{Q_m}{RT}\right) \tag{2.26}$$

where α_m, Q_m, A_m and n are material constants, R the gas constant and T the absolute temperature. The heat generation was determined as the product of the effective stress and effective strain-rate.

In their model, the tool rotates and the plates are fed toward the tool. A constant tangential velocity on the tool surface was specified to simulate the rotation of the tool, assuming some velocity slip at the contact surface. The traverse movement of the workpiece is modelled by prescribing a velocity boundary condition on the incoming side of the workpiece. As only the heat from deformation energy dissipation was accounted for, a thermal contact conductance can be applied at the interface to study the heat transfer between the tool and workpiece. It was concluded that the measured temperatures were consistently over predicted by the model and the discrepancies probably resulted from an inadequate representation of the constitutive behaviour of the material used in FSW. Forces exerted on the tool were computed for various translating and rotating speeds and their relationship was also studied.

Santiago *et al* [2.46] presented a similar model to [2.44] with the same rigid and visco-plastic material model and the same modelling technique, where the plates moved towards the rotating tool and the material flow at the interface was specified as boundary condition. This model was meshed with tetrahedral elements of the Taylor-Hood type with quadratic interpolations for velocities and linear interpolations for stresses, as illustrated in Figure 2.13.

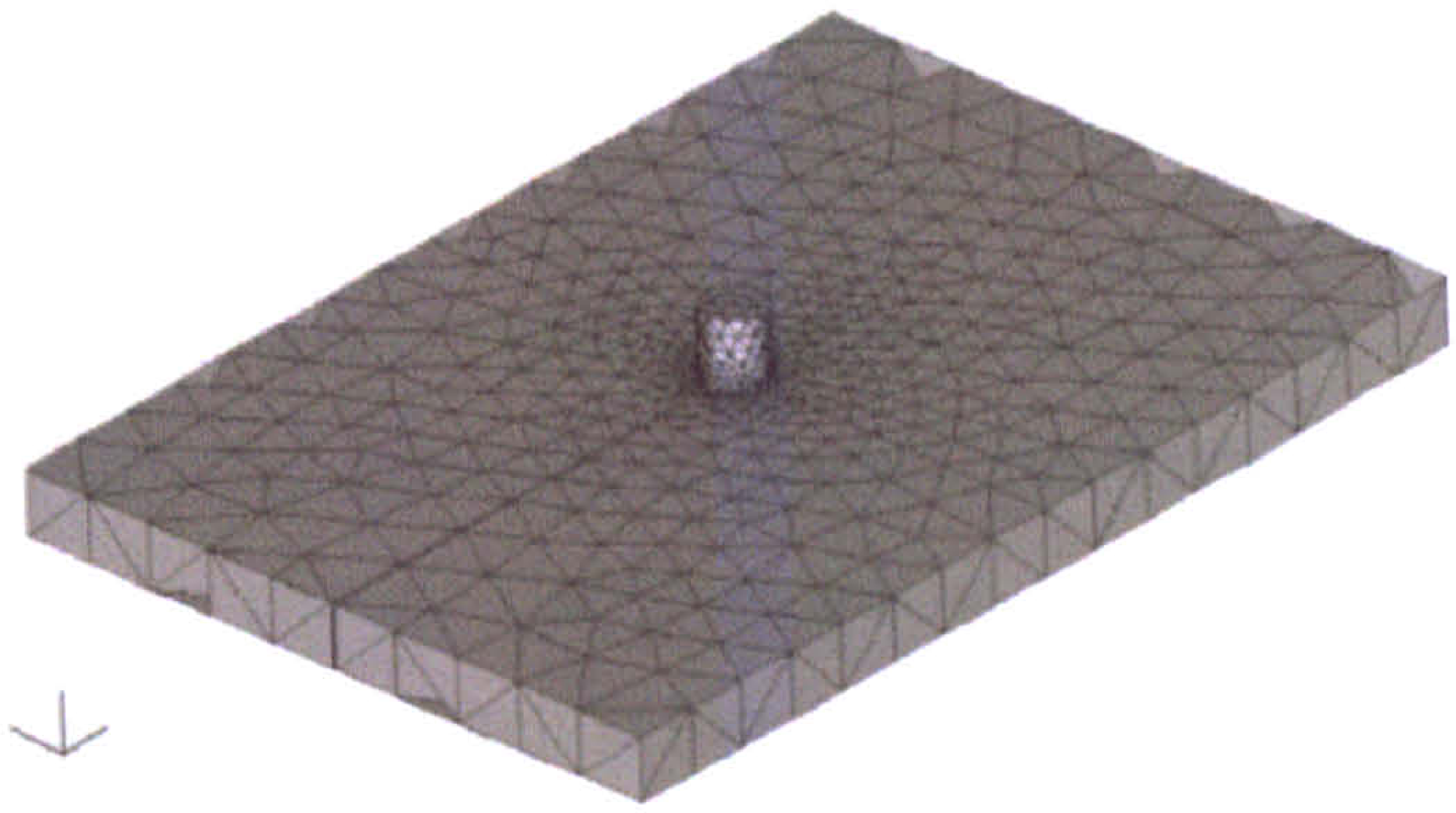

Figure 2.13 the tetrahedral finite element model [2.46].

A static analysis method was used for both models in [2.45] and [2.46], thus the results estimated from the model correspond to the steady state of the FSW process. Schmidt and Hattel [2.47] proposed a fully coupled thermo-mechanical dynamic analysis model, also aiming to achieve the steady welding state, using the arbitrary Lagrangian-Eulerian formulation in ABAQUS/Explicit [2.48]. The solid elastic-plastic Johnson-Cook material model was used:

$$\bar{\sigma} = \left[A + B\left(\bar{\varepsilon}^{pl}\right)^{n_{JC}}\right]\left(1-\hat{T}^{m_{JC}}\right)\left[1+C_{JC}\ln\left(\frac{\dot{\bar{\varepsilon}}^{pl}}{\dot{\varepsilon}_0}\right)\right] \tag{2.27}$$

where A_{JC}, B_{JC}, C_{JC}, m_{JC}, n_{JC} and $\hat{T}^{m_{JC}}$ are material constants, $\bar{\varepsilon}^{pl}$ the effective plastic strain, $\dot{\bar{\varepsilon}}^{pl}$ the effective plastic strain rate and $\dot{\varepsilon}_0$ the normalizing strain rate.

A disc-shaped plate was created for the convenience of meshing. Similar to the models in [2.45] and [2.46], velocity equal to the welding speed was assigned to the material on the incoming side of the plate. At the tool-workpiece interface, Coulomb's Law of friction was used to model the contact behavior with a constant friction coefficient of 0.3. The most notable improvement over the previous models is the ability to predict the suitable thermo-mechanical conditions under which the weld can form. The computing time to achieve the steady-state for their proposed model was 14 days on a 3 GHz Pentium PC.

Lasley [2.49] developed a fully coupled thermo-mechanical finite element model with the transient explicit analysis capability to predict temperature evolution and material flow during the plunge phase. The commercial software Forge3 [2.50], which specializes in modeling high deformation forming processes by an automatic Lagrangian remeshing scheme, was used in the analysis. The model was built up of tetrahedral elements of various sizes. Smaller tetrahedrons were found closer to the pin as illustrated in Figure 2.14.

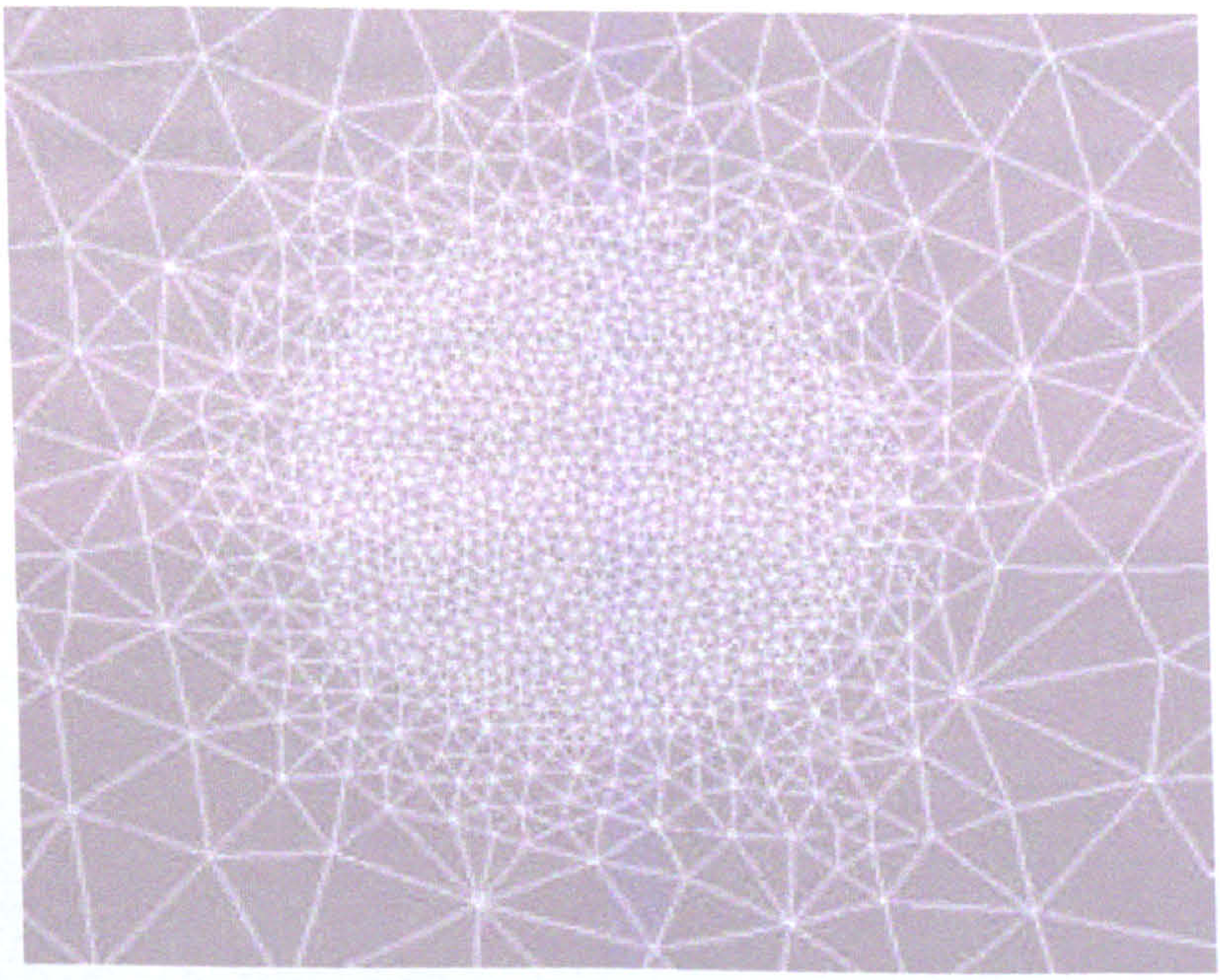

Figure 2.14 Meshing of the workpiece [2.49].

The temperature and strain rate dependent viscoplastic Norton-Hoff model with the Hansel and Spittel flow criteria was used in the model:

$$\sigma_f = Ae^{m_1 T} T^{m_9} \bar{\varepsilon}^{m_2} e^{m_4/\bar{\varepsilon}} \left(1+\bar{\varepsilon}\right)^{m_5 T} e^{m_7 \bar{\varepsilon}} \dot{\bar{\varepsilon}}^{m_3} \dot{\bar{\varepsilon}}^{m_8 T} \tag{2.28}$$

where σ_f is the flow stress, $\bar{\varepsilon}$ is the equivalent strain, $\dot{\bar{\varepsilon}}$ is the equivalent strain rate, T is temperature and A, m_1 to m_9 are material constants.

At the contact surface, the viscoplastic friction model was applied:

$$\boldsymbol{\tau} = -\mu \cdot K(T, \varepsilon) \cdot \dot{\gamma}^{p_s} \cdot \dot{\gamma} \tag{2.29}$$

here $\boldsymbol{\tau}$ is the frictional shear stress, p_s is the sensitivity to sliding and $\dot{\gamma}$ is the slip rate, velocity difference between the two surfaces. The model was validated by experimental temperature measurements with thermocouples at specific locations over the time.

The most recent model for friction stir welding process was proposed by Buffa *et al* [2.51] using the DEFORM-3D™ [2.52] Lagrangian implicit code. The FSW process was modelled from initial state (plunge stage) to steady state. A whole block continuum model was used; i.e. no interface between the two plates. A non-uniform mesh with adaptive remeshing was adopted, as shown in Figure 2.15.

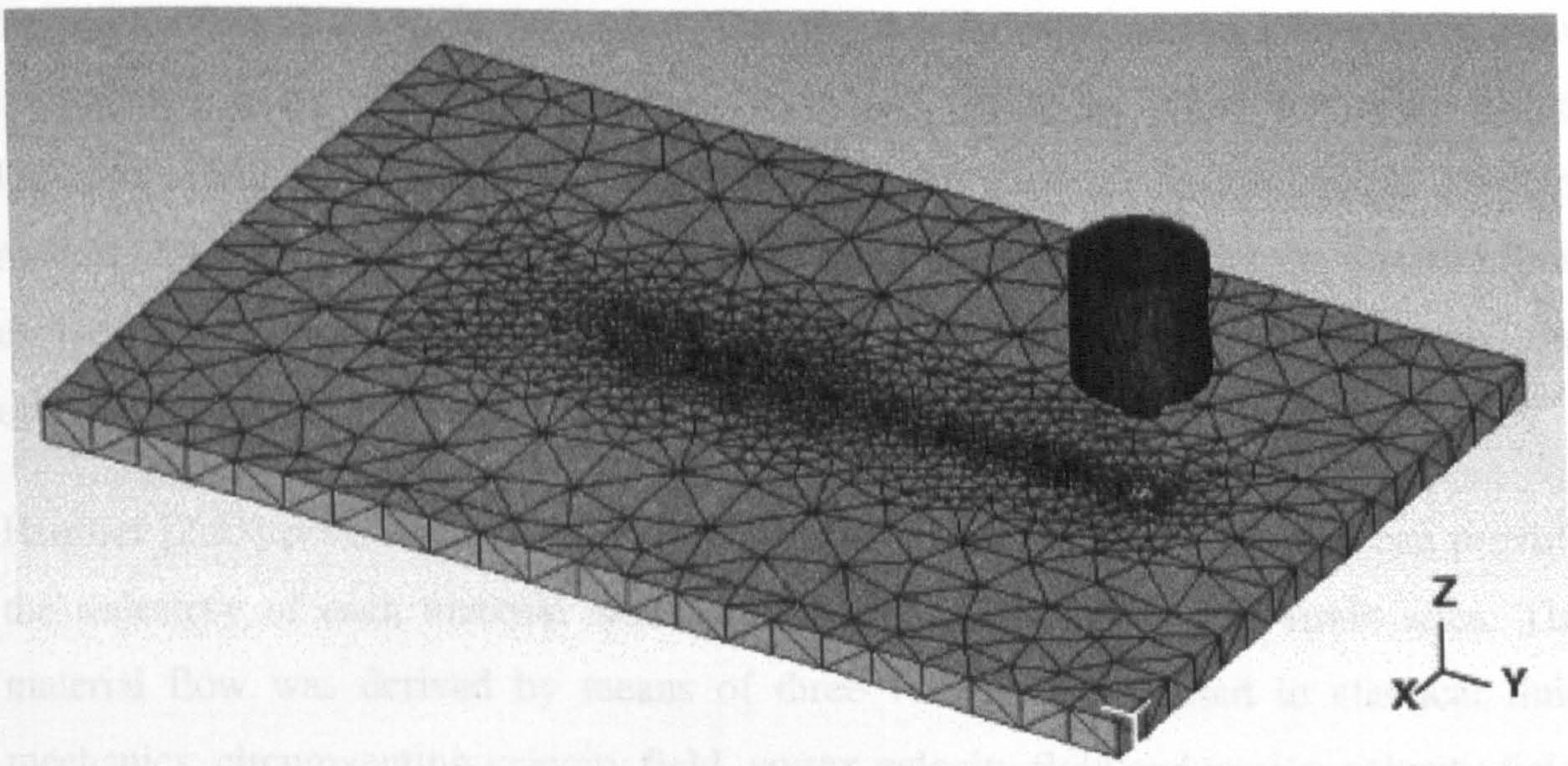

Figure 2.15 the FE model at the beginning of the simulation [2.51].

A rigid-viscoplastic material model was employed:

$$\sigma = KT^{A}\left(\dot{\bar{\varepsilon}}\right)^{B}\left(\bar{\varepsilon}\right)^{C} \tag{2.30}$$

where K, A, B and C are material constants determined by a numerical regression based on experimental data. It was assumed that the heat generation was due only to plastic and frictional conditions at the tool-workpiece interface. The model was able to predict the temperature, strain, strain rate as well as material flow and forces. A good agreement was obtained when comparing with experimental data.

All the above coupled models were not able to fully simulate the FSW. Models [2.44, 2.46 and 2.47] can only simulate the steady state of the traverse stage. Model [2.49] can only simulate the plunge stage. Although model [2.51] can simulate the whole process, but it used a visco-plastic, fluid-like material model, the stress results couldn't be predicted.

2.5 Material Flow Modeling for Friction Stir Welding

The complicated material flow process is the fundamental feature of FSW, as it explains the mechanism of the weld formation. The characteristics of material flow have been investigated using various modelling techniques, such as Finite Element, Finite Difference and Arbitrary Lagrangian Eulerian. All the thermo-mechanical process models [2.44, 2.46, 2.47, 2.49] in section 2.5 have the ability to predict the material flow characteristics, although some [2.44, 2.46, 2.47] are steady state flow patterns and the others are transient.

Heurtier [2.53] presented a semi-analytical three-dimensional model which can provide the trajectory of each material element of the weld, the strain and strain rates. The material flow was derived by means of three velocity fields used in classical fluid mechanics: circumventing velocity field, vortex velocity field and torsion velocity field, illustrated in Figure 2.16.

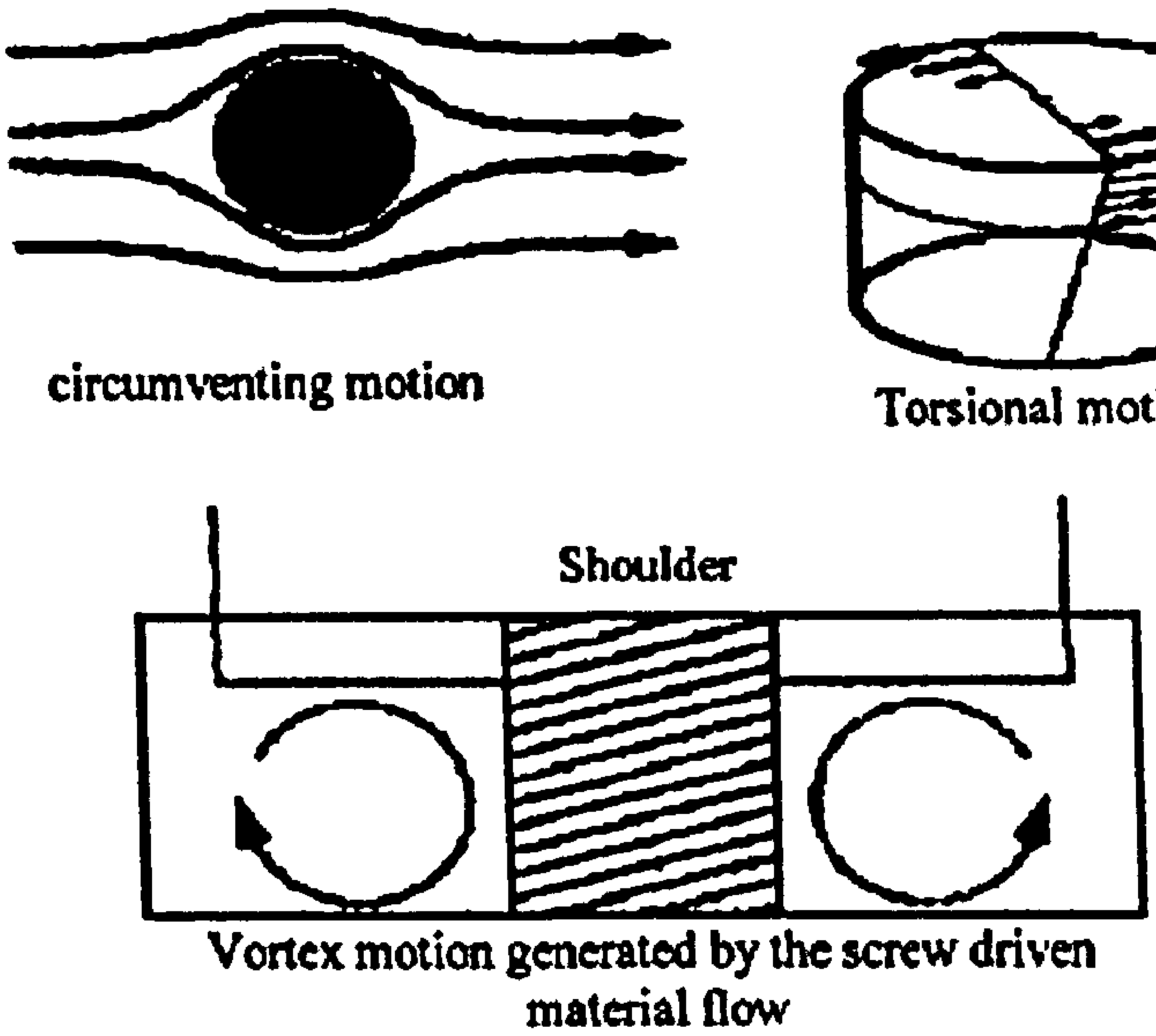

Figure 2.16 schematic representation of the three velocity fields [2.53].

The weld was divided in two zones, "flow army zone" and "nugget zone". The material velocity in each of the zones was described by the combination of three basic velocity fields. The calculated results were validated with experiment measurements of an AA2024-T35 alloy friction stir welded joint.

Xu et al [2.54] presented the first FE model to simulate the material flow pattern. A two dimensional steady state analysis was carried out to model the assumed plane strain state in the mid plane, predicting how material flows around the tool pin. At the tool-workpiece interface, two contact models were used: slipping and frictional contact. In the slipping interface model, the plate material at the interface rotates with a speed lower than that of the tool. In the latter model, the modified Coulomb friction law was prescribed. The temperatures around the pin were specified with measured data by thermocouples. AA6061-T6 was used in experiment and modelled as a rate independent and temperature dependent elastic plastic material. The model was built in ABAQUS with the Arbitrary Lagrangian Eulerian (ALE) finite element formulation and the predicted material flow compared well with experimental data. Subsequently, this 2-D model was adopted in [2.55-2.56] and extended to the three dimensional case [2.57].

The 3D material flow model used by Huang et al. [2.58] is very similar to those models [2.54-2.57] and they are not coupled thermo-mechanical analysis. It is not clear in [2.58] which solver in ABAQUS was used. The effect of variation of the welding parameters on the material flow in FSW was studied. The axial loads applied to the shoulder ranged from 10 to 100MPa in the simulation. The translational velocities applied to the boundaries of the welding plate ranged from 2 to 10 mm/s, and the angular velocities of the pin vary from 390 to 690 rpm. It was concluded that there was a quasi-linear relation between the change of the axial load on the shoulder and the variation of the equivalent plastic strain. The rotational and the translational speeds were both increased 1000 times in their analysis.

Cho et al. [2.59] used a 2D Eulerian formulation to model the steady state FSW of 304L stainless steel with a state variable constitutive model [2.60] that assumes isotropic strain hardening and separately characterizes the rate dependence of the flow strength and saturation limit of the state variable. The equations of conservation of mass, momentum and energy were solved using the finite element method to determine the velocity field and temperature distribution. They found that temperatures were higher on the advancing side than the retreating side by about 100K in both Eulerian modeling and experiments.

The CFD approach was also used to model the material flow around the tool [2.61-2.69]. Askari et al. [2.64] created a three dimensional flow model using the CTH hydro-code. It was assumed that the material at the interface had the same velocity as the tool. The temperature and strain rate dependent Johnson-Cook material model was used. They reported that very good agreement was obtained between the model output and marker experiments. Colegrove and Shercliff [2.65] applied the CFD code, FLUENT [2.70], to model the three-dimensional metal flow. The threaded tool profile and tool rake were considered. The model was solved as a steady-state problem so that the solution time was much less than a full transient analysis. In their isothermal model, a representative temperature was applied to the whole workpiece. The non-isothermal model calculated the heat generation from viscous dissipation. Two materials were used for the analysis:

aluminium alloys 5083 and 7075-T6. The flow stress for 5083 was obtained from Sellars and Tegart [2.66] constitutive law, whereas for 7075-T6, the flow stress came from interpolating experimental stress versus strain-rate data. The model captured some real material flow characteristics, but gave poor temperature predictions.

Nandan et al. [2.69] present a 3D model in a free CFD code, SIMPLE [2.71], to study the material flow and heat transfer during FSW of the hot rolled AISI 1018 steel. They found that significant plastic flow occurred near the interface and convective heat transfer was the main mechanism of heat transfer. The computed results showed slight asymmetry of the temperature distribution around the tool. The plastic flow streamlines revealed that material was transported mainly along the retreating side.

In material flow modelling, fluid dynamics models are widely used. Although these models are convenient to capture the flow behaviour around the tool, various assumptions have to be made at the contact interface. The heat generated by friction cannot be calculated by the CFD models. Further, it is not appropriate to use highly viscous fluid material models to represent the response of a solid material as the elastic-plastic behaviour of the material is not correctly captured. Thus it is not possible to obtain the stress evolution and residual stress information from fluid material models.

2.6 Summary

This chapter describes various models for the simulation of FSW, particular concentrating on thermal, thermomechanical and material flow models. The predictions from all the proposed heat transfer models show reasonable agreement with experimentally measured data. Boundary conditions play a critical role in the temperature profile, especially at the workpiece-backing plate interface. Including a non-uniform temperature and contact pressure dependent contact heat transfer coefficient has been found to provide more accurate temperature estimation. Determining these variables for different materials requires extensive tests and incorporating them in the model still needs a lot coding work.

In simplified thermomechanical models, the calculated mechanical variables, residual stresses and forces depend greatly on the temperature field, as the thermal stresses contribute a major part of the total stress. Increasing the accuracy of the thermal analysis will improve the subsequent mechanical analysis. To improve the thermal analysis, the contact pressure dependent heat transfer coefficient need to be used in the model.

The FSW process consists of several highly coupled physical processes. A fully coupled thermomechanical model with a solid, temperature and strain rate dependent material model would be the best model to describe the weld formation during the FSW process. However the computing cost, for a transient FSW process model, is a major barrier and progress relies greatly on the development of numerical modelling codes incorporating parallel solution and complex contact modelling abilities.

All of the proposed transient models based on finite element method proposed to date consider only smooth surface pins. More complex tool geometry makes the modelling very difficult and the material flow pattern around such tools is hard to achieve. This is due to the mesh distortion and convergence problems at the complex contact interface. Extremely fine elements are needed to capture the tool feature, resulting in unafordable eomputational cost.

2.7 References

[2.1] W.M. Thomas, E.D. Nicholas, S.D. Smith, in: S.K. Das, J.G. Kaufman, T.J. Lienert (Eds.), "Friction Stir Welding - Tool Developments", *Aluminum 2001—Proceedings of the TMS 2001 Aluminum Automotive and Joining Sessions*, New Orleans, LA, USA, pp. 213-224, 2001.

[2.2] W.M. Thomas, K.I. Johnson, C.S. Wiesner, "Friction Stir Welding - Recent Developments in Tool and Process Technologies", Advanced Engineering Materials, Volume 5, Issue 7, pp. 485-490, 2003

[2.3] W.M. Thomas, A.B.M. Braithwaite, R. John, "Skew Stir", *Proceedings of the Third International Symposium on Friction Stir Welding*, Kobe, Japan, September, 27–28, 2001.

[2.4] R.E. Dolby, W.M. Thomas, "Friction stir welding and related friction based technologies", *Proceedings of the Sixth International Conference on Trends in Welding Research*, Pine Mountain, GA, ASM International, pp. 203–211, 2003.

[2.5] R.S. Mishra and Z.Y. Ma, "Friction stir welding and processing", *Materials Science and Engineering: R: Reports*, Volume 50, Issues 1-2, pp. 1-78, 2005

[2.6] T.W. Nelson, "Friction Stir Welding-A Brief Review and Perspective for the Future" Friction Stir Welding and Processing III, 2005 TMS Annual Meeting, San Francisco, CA, ISBN 0-87339-584-0, pp.149-159, 2005

[2.7] A.J. Leonard, "Microstructure and aging behaviour of FSW in Al alloys 2014A-T651 and 7075-T651", *2nd International Symposium on FSW (CD ROM)*, 2000

[2.8] E.D. Nicholas, "Developments in the friction stir welding of metals", *ICAA-6: 6th International Conference on Aluminium Alloys*, 1998

[2.9] http://www.twi.co.uk/j32k/unprotected/band_1/fswproc.html, 2005

[2.10] http://www.twi.co.uk/j32k/unprotected/band_1/fswapp.html, 2007

[2.11] A., Murphy, M., Price, R., Curran, and P. Wang, "The Integration of strength and process modeling of friction-stir-welded fuselage panels", *AIAA Journal of Aerospace Computing, Information, and Communication*, vol. 3, pp. 159-176, April 2006

[2.12] A. Murphy, F. Lynch, M. Price and A. Gibson, "Modified stiffened panel analysis methods for laser beam and friction stir welded aircraft panels", *Proceedings of the Institution of Mechanical Engineers, Part G: Journal of Aerospace Engineering*, Volume 220(4), pp. 267–278, 2006

[2.13] R.S. Mishra, M.W. Mahoney, S.X. McFadden, N.A. Mara, A.K. Mukherjee, "High Strain Rate Superplasticity in a Friction Stir Processed 7075 Al Alloy", *Scripta Materialia*, Volume 42, Issue 2, pp. 163-168, 2000

[2.14] Z.Y. Ma, R.S. Mishra, M.W. Mahoney, "Superplastic Deformation Behaviour of Friction Stir Processed 7075Al Alloy", *Acta Materialia*, Volume 50, Issue 17, pp. 4419-4430, 2002

[2.15] M. Song, R. Kovacevic, 'Heat Transfer Modeling for both Workpiece and Tool in the Friction Stir Welding Process: A Coupled Model', *Proceedings of the Institute of Mechanical Engineers, Part B: J. Engineering Manufacture*, Vol. 217(B1), pp. 73-85, 2003

[2.16] J. Gould, 'Heat Flow Model for Friction Stir Welding of Aluminium Alloys', Journal of Materials Processing and Manufacturing Science, Vol.7, pp.185-194, 1998

[2.17] D., Rosenthal, R., Schemerber, "Thermal Study of Arc Welding", Welding Journal, 17(4):208s, 1938

[2.18] P. Vilaca, L. Quintino and J. Santos, "iSTIR-Analystical Thermal Model for Friction Stir Welding", *Journal of Materials Processing Technology*, Vol. pp. 2005

[2.19] D. Rosenthal, "The Theory of Moving Sources of Heat and Its Application to Metal Treatments", *Trans. ASME*, pp. 849–866, 1946

[2.20] R. Holm, "Calculation of the Temperature Development in a Contact heated in the contact surface, and application to the problem of the temperature rise in a sliding contact", *J. Appl. Phys.* Vol.10, pp. 361-366, 1948

[2.21] ASM International, *ASM Handbook, Friction Lubrication and Wear Technology*, Vol. 18, pp 41, 1992

[2.22] J.dos Santos, C. Shilling, S. Hheikhi, 'WAFS Consortium Restricted Draft on Temperature field of AA6056-T4 similar Friction Stir Weld', GJSS Forshungszentrum Germany, September 2001

[2.23] Y.J. Chao, X. Qi, 'Thermal and Thermo-mechanical Modelling of Friction Stir Welding of Aluminum Alloy 6061-T6 plates', *Journal of materials Processing and Manufacturing Science*, Vol. 7, pp. 215-233, 1998

[2.24] Y.J. Chao, X. Qi, 'Heat Transfer and Thermo-mechanical Modelling of Friction Stir Joining of AA6061-T6 Plates, *Proceedings of the First International Symposium on Friction Stir Welding*, Thousand Oaks, CA, USA, 1999.

[2.25] X.K. Zhu, X.J. Chao, 'Numerical Simulation of Transient Temperature and Residual Stress in Friction Stir Welding of 304L Stainless steel', *Journal of Materials processing Technology*, Vol. 146, pp. 263-272, 2004.

[2.26] Yuh J. Chao, X. Qi, W. Tang, 'Heat Transfer in Friction Stir Welding-Experimental and Numerical Studies', *Journal of Manufacturing Science and Engineering*, Vol. 125, pp. 138-145, 2003

[2.27] Φ., Frigaard, Φ., Grong and O.T. Midling, 'Modelling of the Heat Flow Phenomena in Friction Stir Welding of Aluminium Alloys, *Proceedings of the Seventh International Conference on Joints in Aluminium (INALCO '98)*, Cambridge, April 1998.

[2.28] Ф., Frigaard, Ф., Grong and O.T. Midling, 'A Process Model for Friction Stir Welding of Age Hardening Aluminium', *Metall. Mater. Trans. A*, 32A, May 2001

[2.29] P. Colegrove, '3-Dimentional Flow and Thermal Modelling of the Friction Stir Welding Process', *Proceedings of the 2nd International Symposium on Friction Stir Welding*, Sweden, August 2000.

[2.30] M. Song, R. Kovacevic, 'Thermal Modelling of Friction Stir Welding in a Moving Coordinate System and its Validation', International Journal of Machine Tools & Manufacture, Vol.43, pp. 605-615, 2003

[2.31] M. Song, R. Kovacevic, 'Numerical and Experimental Study of the Heat Transfer Process in Friction Stir Welding', Proc. *Instn Mech. Engrs., Part B: J. Engineering Manufacture*, Vol. 217, pp. 73-85, 2003.

[2.32] M. Song, R. Kovacevic, 'Heat Transfer Modelling for both Workpiece and Tool in the Friction Stir Welding Process: a Coupled Model', Instn Mech. Engrs., Part B: J. Engineering Manufacture, Vol. 218, pp. 17-33, 2004.

[2.33] M.Z.H. Khandkar, J.A. Khan, 'Experimental and Analytical Investigation of Friction Stir Welding', *Proceedings of BSME-ASME International Conference on Thermal Engineering*, Bangladesh Society of Mechanical Engineers, Dhaka, Bangladesh, pp. 725-732, 31 December 2001-2 January 2002.

[2.34] M.Z.H. Khandkar, J.A. Khan, A.P. Reynolds, 'Input Torque Based Thermal Model of Friction Stir Welding of AA-6061', *6th International Conference on Trends in Weldin Research*, Pine Mountain, Georgia, April, 2002.

[2.35] M.Z.H. Khandkar, J.A. Khan, A.P. Reynolds, 'A Thermal Model of the Friction Stir Welding Process', *Proceedings of IMECE2002*, ASME International Mechanical Engineering Congress & Exposition, New Orleans, Louisiana, November, 2002

[2.36] H.N.B. Schidt, J. Hattel, J. Wert, 'An Analytical Model for the Heat Generation in Friction Stir Welding', *Modelling and Simulation in Materials Science and Engineering*, Vol. 12, pp. 143-157, 2004

[2.37] H.N.B. Schmidt, J. Hattel, 'Heat Source Models in Simulation of Heat Flow in Friction Stir Welding', *International Journal of Offshore and Polar Engineering*, Vol. 14, No. 4, December 2004

[2.38] T. Dickerson, Q. Shi, H.R Shercliff, 'Heat Flow into Friction Stir Welding Tools', 4th International Symposium on Friction Stir Welding, Park City, Utah, USA, 14-16 May 2003.

[2.39] T. Kawasaki, T. Makino, K. Masai, H. Ohba, Y. Ina, M. Ezumi, 'Application of Friction Stir Welding to Construction of Railway Vehicles', *JSME International Journal,* Series A, Vol. 47, No. 3, 2004

[2.40] X.K. Zhu, Y.J. Chao, 'Numerical Simulation of Transient Temperature and Residual Stresses in Friction Stir Welding of 304L Stainless Steel', *Journal of Materials Processing Technology,* Vol. 146, pp. 263-272, 2004.

[2.41] C.M. Chen, R. Kovacevic, 'Finite Element Modelling of Friction Stir Welding-Thermal and Thermomechanical analysis', *International Journal of Machine Tols and Manufacture,* Vol. 43, pp. 1319-1326, 2003.

[2.42] C. Chen and R. Kovacevic, 'Thermomechanical Modelling and Force Analysis of Friction Stir Welding by the Finite Element Method', *Proceedings of the I MECH E Part C Journal of Mechanical Engineering Science,* Vol.218, pp. 509-519, 2004.

[2.43] Vijay Soundararajan, Srdja Zekovic and Radovan Kovacevic, 'Thermo-mechanical Model with Adaptive Boundary Conditions for Friction Stir Welding of Al 6061', *International Journal of Machine Tools and Manufacture,* Vol. 45, 14, pp. 1577-1587, 2005.

[2.44] P.Ulysse, 'Three-dimensional Modelling of the Friction Stir-welding Process', *International Journal of Machine Tools & Manufacture,* Vol. 42, pp. 1549-1557, 2002.

[2.45] FIDAP, Fluid Dynamic Analysis Package, version 7.6, Fluid Dynamics International, Evanston, IL

[2.46] Diego H. Santiago, F. Lombera, S. Urquiza, A. Cassanelli, L.A. V, 'Numerical Modeling of Welded Joints by the Friction Stir Welding Process', *Materials Research,* Vol. 7, No. 4, pp. 569-574, 2004

[2.47] H. Schmidt and J Hattel, 'A Local Model for the Thermo-mechanical Conditions in Friction Stir Welding', *Modelling and Simulation in Materials Science and Engineering,* Vol. 13, pp. 77-93, 2005

[2.48] ABAQUS Analysis Manual, Version 6.6-1, ABAQUS, Inc., Providence, USA, 2006

[2.49] Mark Jason Lasley, 'A Finite Element Simulation of Temperature and Material Flow in Friction Stir Welding', *Unpublished thesis,* Brigham Young University, Provo, UT, 2005

[2.50] Forge 3, Release 6.3. Transvalor S.A. 2004.

[2.51] G. Buffa, J. Hua, R. Shivpuri, L. Fratini, 'A Continuum Based Fem Model for Friction Stir Welding-Model Development', *Material Science and Engineering A*, Volume 419, Issues 1-2, pp. 389-396, 2006.

[2.52] DEFORM-3D, Scientific Forming Technologies Corporation (SFTC), Columbus, Ohio

[2.53] Heurtier, P., C. Desrayaud, & F. Montheillet, "A Thermomechanical Analysis of the Friction Stir Welding Process", *Materials Science Forum*, Volume 396, 4, pp. 1537-1542, 2002

[2.54] S. Xu, X. Deng, A.P. Reynolds and T.U. Seidel, 'Finite element simulation of material flow in friction stir welding', *Science and Technology of Welding and Joining,* Vol. 6, No. 3, pp.191-193, 2001.

[2.55] X. Deng, and S. Xu, "Solid mechanics simulation of friction stir welding process", *Transactions of NAMRI/SME, Vol. XXIX., Dearborn,* MI: Society of Manufacturing Engineers, pp. 631-638, 2001

[2.56] X. Deng, and S. Xu, "Two-Dimensional Finite Element Simulation of Material Flow in the Friction Stir Welding Process", *Journal of Manufacturing Processes*, Volume 6, No. 2, 2004

[2.57] S. Xu, X. Deng, 'A three-dimensional model for the friction-stir welding process', *Proc. of 21st Southeastern Conf. on Theoretical and Applied Mechanics (secTAM XXI)*, Orlando, FL, pp. 699-704, May 2002

[2.58] H.W. Zhang, Z. Zhang, and J.T. Chen, "3D Modeling of Material Flow in Friction Stir Welding under Different Process Parameters", *Journal of Materials Processing Technology*, Volume 183, pp. 62–70, 2007

[2.59] J.H. Cho, D.E. Boyce, P.R. Dawson, "Modeling Strain Hardening and Texture Evolution in Friction Stir Welding of Stainless Steel", *Materials Science and Engineering A*, Volume 398, pp. 146-163, 2005

[2.60] E.W Hart, "Constitutive Relations for the Non-elastic Deformation of Metals", *Journal of Engineering Materials and Technology*, Volume 98 pp.193-202, 1976

[2.61] G.J. Bendzsak, T.H. North and C.B. Smith, "An experimentally validated 3D model for friction stir welding", *Proceedings of the Second International Symposium on Friction Stir Welding,* TWI Ltd., Gothenburg, Sweden, 2000

[2.62] P. Colegrove, "Three Dimensional Flow and Thermal Modelling of the Friction Stir Welding Process", *Proceedings of the 2nd International Symposium on Friction Stir Welding*, Gothenburg, Sweden, 2000

[2.63] T.U. Seidel, A.P. Reynolds, "Two-dimensional Friction Stir welding Process Model Based on Fluid Mechanics", *Science and Technology of Welding & Joining*, Volume 8, Number 3, pp. 175-183, 2003

[2.64] Askari, A., S. Silling, B. London, and M. Mahoney, "Modeling and Analysis of Friction Stir Welding Processes", *the Minerals, Metals and Materials Society*, 2001

[2.65] Paul A. Colegrove and Hugh R. Shercliff, "3-Dimensional CFD modelling of flow round a threaded friction stir welding tool profile", *Journal of Materials Processing Technology*, Volume 169, Issue 2, pp. 320-327, 2005

[2.66] C.M. Sellars and W.J.Mc.G. Tegart, "Hot Workability", *International Metallurgical Review*, 17, pp. 1–24, 1972

[2.67] R. Nandan, G. G. Roy, T. DebRoy, "Numerical Simulation of Three-Dimensional Heat Transfer and Plastic Flow During Friction Stir Welding", *Metallurgical & Materials Transactions A*, volume 37, pp. 1247–1259, April 2006

[2.68] R. Nandan, G. G. Roy, T. J. Lienert, T. DebRoy, "Numerical Modelling of 3D Plastic Flow and Heat Transfer during Friction Stir Welding of Stainless Steel" *Science and Technology of Welding & Joining*, Volume 11, Number 5, pp. 526-537, 2006

[2.69] R. Nandan, G. G. Roy, T. J. Lienert, T. DebRoy, "Three-dimensional Heat and Material Flow during Friction Stir Welding of Mild steel", *Acta Materialia*, Volume 55, pp. 883-895, 2007

[2.70] FLUENT, Flow modeling software, Fluent Inc., U.S.A.

[2.71] S.V. Patankar, *Numerical heat transfer and fluid flow*, Hemisphere Publishing Corporation, New York, 1980

Chapter 3

Theoretical Background of Friction Stir Welding numerical modelling

3.1 Numerical Modelling Techniques

The physical phenomena accompanying the Friction Stir Welding (FSW) process are governed by the laws of physics and mechanics, expressed in terms of differential equations. These differential equations state the laws of conservation of mass, momentum and energy, and equilibrium of forces. For example the force equilibrium of the material particles in the workpiece is governed by the equation,

$$\rho \mathrm{a} = \rho \mathrm{g} + div(\sigma) \tag{3.1}$$

where σ is the stress tensor, g the body force per unit mass and a the acceleration. Common variables in these differential equations are time, position, velocity, acceleration, mass, density, momentum, energy, stress and force, among which time and position (x, y, z) are four independent variables whilst mass and density are known for specific materials.

To obtain information about the physical process being modeled, the governing equations must be solved for the unknown variables. In numerical methods, the basic solution approach is to approximate the derivatives or exact solution of a given differential equation to obtain a system of simpler equations with a finite number of unknowns, which may be solved using mathematical algorithms.

With the development of the computer, numerical modeling methods have been widely used to solve problems such as fluid motion, heat transfer, solid mechanics, chemical process and electrical/magnetism problems. In the following sections, the basic numerical modeling techniques relevant to FSW modeling are discussed.

3.1.1 Basics of Numerical Methods

The fundamental objective of numerical methods is to reduce a differential equation to an approximation in terms of algebraic equations. A continuous differential equation whose solution space is generally the whole defined domain is replaced with a set of algebraic equations whose solution space is a finite subdomain [3.1]. Four main numerical solution methods are used in engineering: the finite element method, spectral method, finite difference method and finite volume method (the finite volume method being a special case of the finite difference method). The primary differences between the approaches lie in the way in which the independent variables are approximated and the domain is discretizated [3.2].

Finite Element Method (FEM) The finite element method explicitly defines a simple piecewise *trial function* (e.g. linear or quadratic Lagrangian polynomials) for the unknown independent variables, to approximate the actual solution of the differential equation in a finite dimensional function space. In the Method of Weighted Residuals (MWR), the substitution of the approximate functions results in an error in the solution, defined as a residual. The error minimized by applying weight functions to the terms in the residual and integrating through the volume to obtain a system of algebraic equations. The three most common MWR routines are the subdomain method, the collocation method and the Galerkin method. The terminology *finite element method* is traditionally restricted to the Galerkin method, in which the trial and weight function are identical [3.1]. If they are different, the MWR methods are often named *Petro-Galerkin methods.* The finite element method was originally developed for structural stress analysis [3.2] using *energy methods.* These methods are based on functional minimization properties, such as minimum potential energy, and the resulting algebraic equations are identical to those derived by the Galerkin method, as there is always a Galerkin method which is equivalent to the energy method [3.3]. However, energy methods are not applicable to many physical systems and application mainly lies in solid mechanics problems.

Spectral Method Spectral method uses truncated Fourier series or series of Chebyshev polynomials as the approximation to the independent variables in the governing differential equations. The simple approximations are valid over the small finite domains in finite element methods. The algebraic equations for the coefficients of the Fourier or Chebyshev series are obtained by either applying a weighted residuals method or specifying the exact solution of the approximate function at grid points [3.2].

Finite Difference Method (FDM) The finite difference method proceeds by first defining a number of grid points in the domain of interest. Then truncated Taylor series are used to create finite difference approximations in terms of point values. For example, in one dimension, approximations for first and second derivatives of a continuous function *u(x)* at node point x_i may be obtained as follows,

$$\left.\frac{du}{dx}\right|_{x_i} = \frac{u_{i+1} - u_i}{\Delta x} \tag{3.2}$$

$$\left.\frac{d^2u}{dx^2}\right|_{x_i} = \frac{u_{i+1} - 2u_i + u_{i-1}}{(\Delta x)^2} \tag{3.3}$$

where Δx is the node space. These finite difference approximations are substituted into the governing equation to replace the derivatives, leading to a set of algebraic equations. The FDM has various applications such as weather/climate modelling, magnetism hydrodynamic modelling, heat transfer, wave and fluid dynamics modelling.

Finite Volume Method (FV) The Finite Volume method is a subset of the finite difference method. It uses approximations like Equation 3.2 to replace the derivatives in the governing equation. The next step, the key scheme of FV, is to integrate this equation over a control volume or finite size cell. This procedure produces a system of simple algebraic equations, solved by an iterative method. The FV method clearly expresses the underlying physical conservation principle (governing equation) for each control volume. It is widely used in Computational Fluid Dynamics (CFD) problems and is embedded in some popular commercial CFD codes such as PHOENICS, FLUENT and FLOW3D.

3.1.2 Lagrangian Formulation and Eulerian Formulation

Numerical methods provide approximate solutions to differential equations. For the FD, FE and FV methods, the differential equation is discretised by dividing the whole domain into subdomains with grids or elements. If the grids (or node points) are fixed in space, such method is called Eulerian formulation. If the grids move with the material, it is called a Lagrangian formulation.

Lagrangian formulation In this method [3.4-3.6], the motion description is based on a material reference system, in which the mesh follows the deformation of the material and no material flows between elements. The Lagrangian method is widely used in commercial FE codes. It is efficient and suitable for handling small and moderately large strain problems, where mesh distortion is not an important factor. Lagrangian formulation can provide very accurate results and can automatically capture the free surface of the material, which is the main advantage of this method. However, highly deformed surfaces with large plastic strains, complex friction and contact boundary conditions are not amenable to the Lagrangian formulation, due to mesh distortion and element entanglement. In addition, only one material can be modelled in each element.

Eulerian type formulation In the Eulerian method, the material flows through a fixed mesh. The deformation of the material is determined as a function of the current position and the time, rather than following the motion of material [3.7]. This method was initially designed for fluid dynamics but is also suitable for very large deformation problems. It is problematic in non-steady or dynamic analysis. The major disadvantage of this method is that a very fine mesh is required to capture the material response, particularly for problems with small strains [3.5].

3.1.3 Arbitrary Lagrangian and Eulerian Formulation (ALE)

In the Arbitrary Lagrangian and Eulerian (ALE) formulation, the node points need not follow the material nor be fixed in space but can be moved arbitrarily. Thus this formulation allows the mesh to move independently of the material, making it possible to maintain a high-quality mesh during an analysis. Combining the advantages of both Lagrangian and Eulerian methods, the ALE method is well suited to deal with large deformation problems, avoiding element distortion problems. The concept of ALE was first proposed for hydrodynamics problems, later introduced into the finite element method and is now widely used to solve finite strain deformation problem in solid mechanics [3.5]. This *adaptive meshing* technique has been incorporated in many commercial codes such as LS-DYNA and ABAQUS, where the ALE analysis is based on the computationally convenient *operator split* technique, in which a regular Lagrangian step is followed by an advection step [3.5] [3.7]. An overall flow of an ALE time step is as follows [3.8]:

1. Perform a Lagrangian time step
2. Perform an advection step.
   a. Decide which nodes to move
   b. Move the nodes
   c. Calculate the transport of the element-centred variables
   d. Calculate the momentum transport and update the velocity

At the end of the Lagrangian stage, if no further action is taken the code runs in a pure Lagrangian mode and proceeds to the next time step. If the nodes are placed back to their initial position at the beginning of the Lagrangian step, a pure Eulerian analysis is achieved. The user chooses a balance between minimising the number of advection steps and keeping the mesh undistorted, as the cost of an advection step is typically two to five times that of the Lagrangian step.

The new mesh is determined by basic smoothing methods: volume smoothing, Laplacian smoothing and equipotential smoothing. ABAQUS uses a combination of the three methods, the volume method is the default in ABAQUS/EXPLICIT, while the equipotential method is employed in LS-DYNA. The volume smoothing method repositions a node by calculating a volume-weighted average of the surrounding elements centres. Laplacian smoothing moves a node by calculating the average of the positions of adjacent nodes connected by an element edge. Equipotential smoothing method relocates a node by calculating a complex, higher-order weighted average of the positions of all the surrounding nodes. [3.9]

After the mesh has been updated, the solution variables are remapped from the old mesh to the new mesh. There are two remapping methods: a first-order method based on donor cell differencing and the second-order method based on the work of Van Leer [3.10]. The first-order method in one dimension is shown in Figure 3.1. The advection procedure for an element variable, ϕ, is given as follows:

1. Determine a constant value of ϕ for each old element.

2. The constant values are integrated over each new element.

3. Divide the value of each integral by the new element volume to get the new constant value of the variable ϕ^{new}

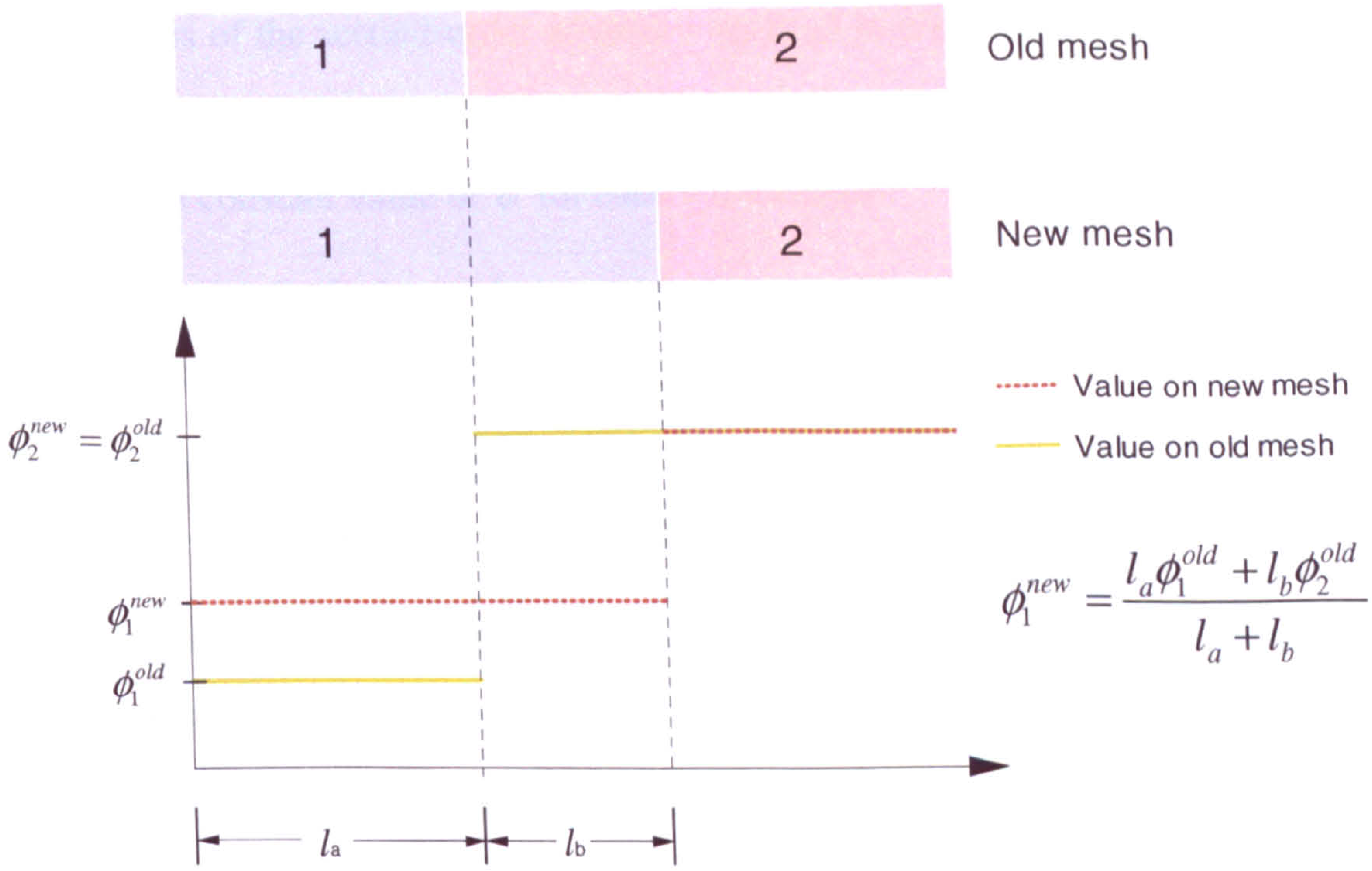

Figure 3.1 First-order Advection.

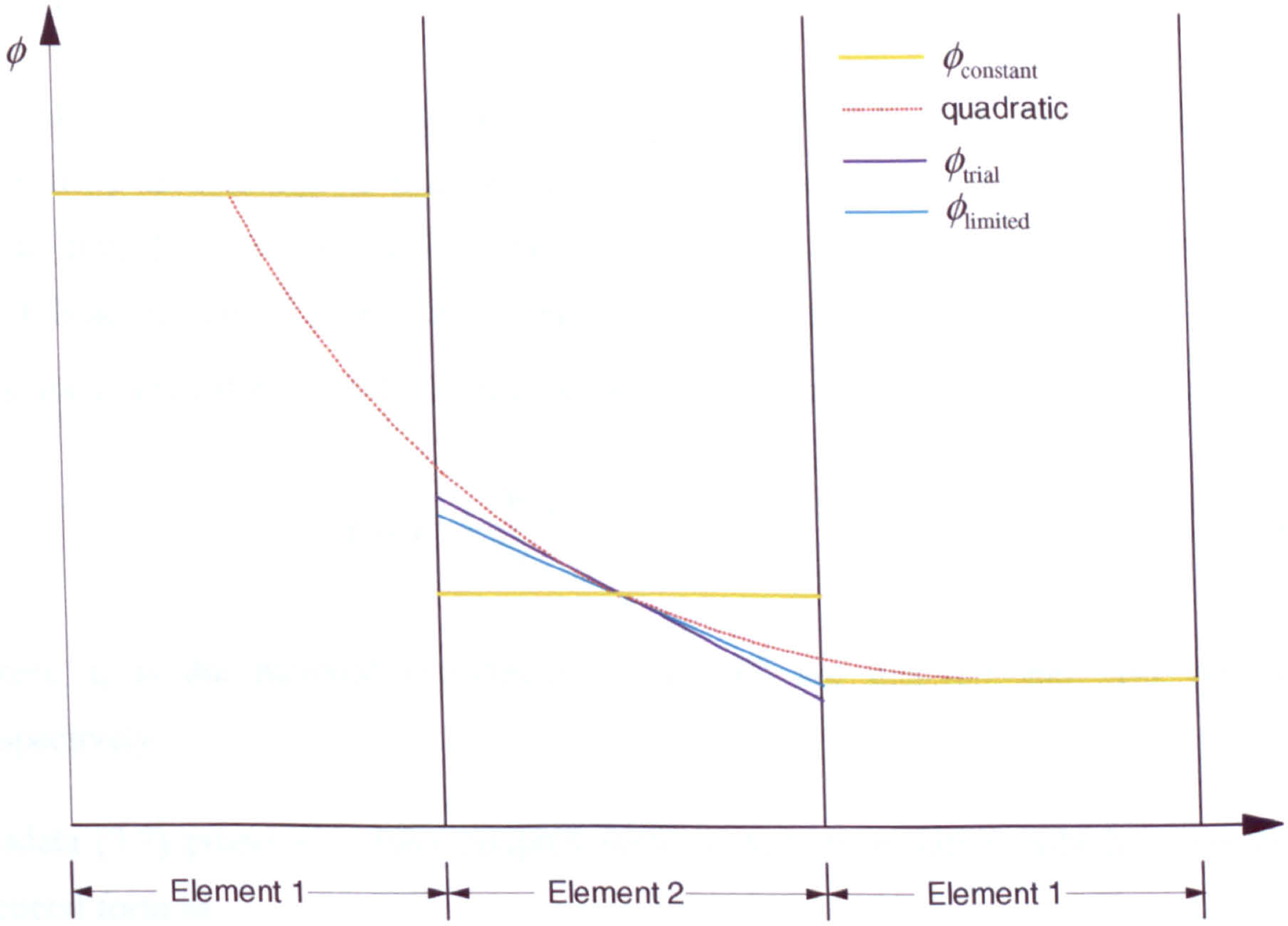

Figure 3.2 Second-order advection.

The procedures of the second-order advection method in one dimension are as shown in Figure 3.2:

1. Determine a constant value of ϕ for each old element.

2. Construct a quadratic interpolation with the constant values of ϕ at the integration points of the middle element and its neighbouring elements.

3. Differentiate the quadratic function to obtain the slope at the integration point of the middle element, and then construct a trial linear distribution ϕ_{trial}.

4. Limit the trial linear distribution within the range of the original constant values in the neighbouring elements by decreasing its slope.

5. Repeat step 3 and 4 to get the linear distribution for all elements, and then integrate them over each new element.

6. Divide the value of each integral by the new element volume to get the new constant value of the variable ϕ^{new}.

The ALE technique is a staggered method, while a coupled ALE formulation can be derived by substituting the relationship between the material time derivative and grid (node) time derivative into the governing equation. The transport of material through the mesh is accounted for in the ALE equation. The material time derivative of an arbitrary function f denoted by $\dot{f}$ and grid time derivative $\dot{f}^g$ posses the following relation:

$$\dot{f} = \dot{f}^g + \frac{\partial f}{\partial x_i}\left(v_i - v_i^g\right) \tag{3.4}$$

where x_i is the material coordinate, V_i and V_i^g are material and grid velocities respectively.

Gadala [3.7] proposed a fully coupled implicit ALE formulation, which is written in general form as

$$ {}^{t}\mathbf{K}\mathbf{u}^{(i)} - {}^{t}\mathbf{K}^{g}\mathbf{u}^{g(i)} = \mathbf{f}^{(i)} \tag{3.5} $$

where ${}^{t}\mathbf{K}$ and ${}^{t}\mathbf{K}^{g}$ are equivalent stiffness matrices corresponding to $\mathbf{u}^{(i)}$ and $\mathbf{u}^{g(i)}$, respectively, and $\mathbf{f}^{(i)}$ is the incremental load vector for iteration i. The grid displacement is related to the material displacement by

$$ \mathbf{u}^{g(i)} = \boldsymbol{\alpha}_{MeshM} + \mathbf{B}_{MeshM}\mathbf{u}^{(i)} \tag{3.6} $$

where $\boldsymbol{\alpha}_{MeshM}$ and $\mathbf{B}_{MeshM}$ are a vector and a matrix of mesh motion parameters, respectively, which can be obtained by the transfinite mapping method [3.11].

Substituting Equation 3.6 into 3.5 leads to

$$ \left({}^{t}\mathbf{K} - {}^{t}\mathbf{K}^{g}\mathbf{B}_{MeshM}\right)\mathbf{u}^{(i)} = \mathbf{f}^{(i)} + {}^{t}\mathbf{K}^{g}\boldsymbol{\alpha}_{MeshM} \tag{3.7} $$

When setting $\boldsymbol{\alpha}_{MeshM} = \mathbf{0}$ and $\mathbf{B}_{MeshM} = \mathbf{I}$, the ALE Equation 3.7 reduces to pure Lagrangian formulation, while $\boldsymbol{\alpha}_{MeshM} = \mathbf{0}$ and $\mathbf{B}_{MeshM} = \mathbf{0}$, it becomes pure Eulerian formulation.

The heat transfer equation in an ALE analysis includes a velocity convection term due to the node and material velocity difference.

$$ \nabla \cdot (\mathbf{K}_k \nabla T) + q_{hg} = \rho c\left(\frac{\partial T}{\partial t} + \left(\mathbf{\upsilon} - \mathbf{\upsilon}^{g}\right) \cdot \nabla T\right) \tag{3.8} $$

3.2 Heat transfer Fundamentals

The fist law of thermodynamics is the application of the conservation of energy principle to heat and thermodynamics processes [3.12] [2.13], Equation 3.9, with the assumption of incompressible medium.

$$ \dot{Q}_A = \frac{dE_I}{dt} \tag{3.9} $$

where $\dot{Q}_A$ is the rate of heat added to the control volume and dE_I the change in internal energy.

$$\dot{Q}_A = \int_s \mathbf{q}_{hf} \mathbf{n} dS + \int_v q_{hg} dV \tag{3.10}$$

$$\frac{dE_I}{dt} = \int_v \left(\rho c \frac{\partial T}{\partial t} \right) dV \tag{3.11}$$

where

S	Surface of control volume
$T=T(x, y, z, t)$	Temperature (^{o}K)
V	Volume of control volume
$\mathbf{q}_{hf}$	Heat flux vector (W/m^2)
q_{hg}	Heat generation rate per unit volume (J/m^3)
$\mathbf{n}$	Unit outward vector

Applying Gauss's theorem and combining Equations 3.10 and 3.11, a new equation is obtained:

$$-\nabla \cdot \mathbf{q}_{hf} + q_{hg} = \rho c \frac{\partial T}{\partial t} \tag{3.12}$$

Fourier's law describes the relationship between the heat flux vector and the temperature gradient, implying that the heat flow results from temperature non-uniformities.

$$\mathbf{q}_{hf} = -\mathbf{K} \nabla T \tag{3.13}$$

where ∇ represents the *grad* operator and $\nabla \cdot$ represents the *divergence* operator, $\mathbf{K}_k$ is the conduction matrix. It is assumed the material has *orthotropic* properties, i.e., the conductivities are given along their principal directions.

$$\mathbf{K}_k = \begin{bmatrix} k_{xx} & 0 & 0 \\ 0 & k_{yy} & 0 \\ 0 & 0 & k_{zz} \end{bmatrix}$$

where k_{xx}, k_{yy}, k_{zz} are conductivities in the element x, y, and z directions, respectively.

The final expression of the governing equation can be obtained by substituting equation 3.13 into 3.12:

$$\nabla \cdot (\mathbf{K}_k \nabla T) + q_{hg} = \rho c \frac{\partial T}{\partial t} \tag{3.14}$$

$$\rho c \frac{\partial T}{\partial t} = \frac{\partial}{\partial x}\left(k_{xx}\frac{\partial T}{\partial x}\right) + \frac{\partial}{\partial y}\left(k_{yy}\frac{\partial T}{\partial y}\right) + \frac{\partial}{\partial z}\left(k_{zz}\frac{\partial T}{\partial z}\right) + q_{hg} \tag{3.15}$$

Apart from the governing differential equations, appropriate boundary is required to complete the formulation of a problem. Figure 2.3 shows a most common type of boundary conditions, where Ω is the domain of definition and S the domain surface.

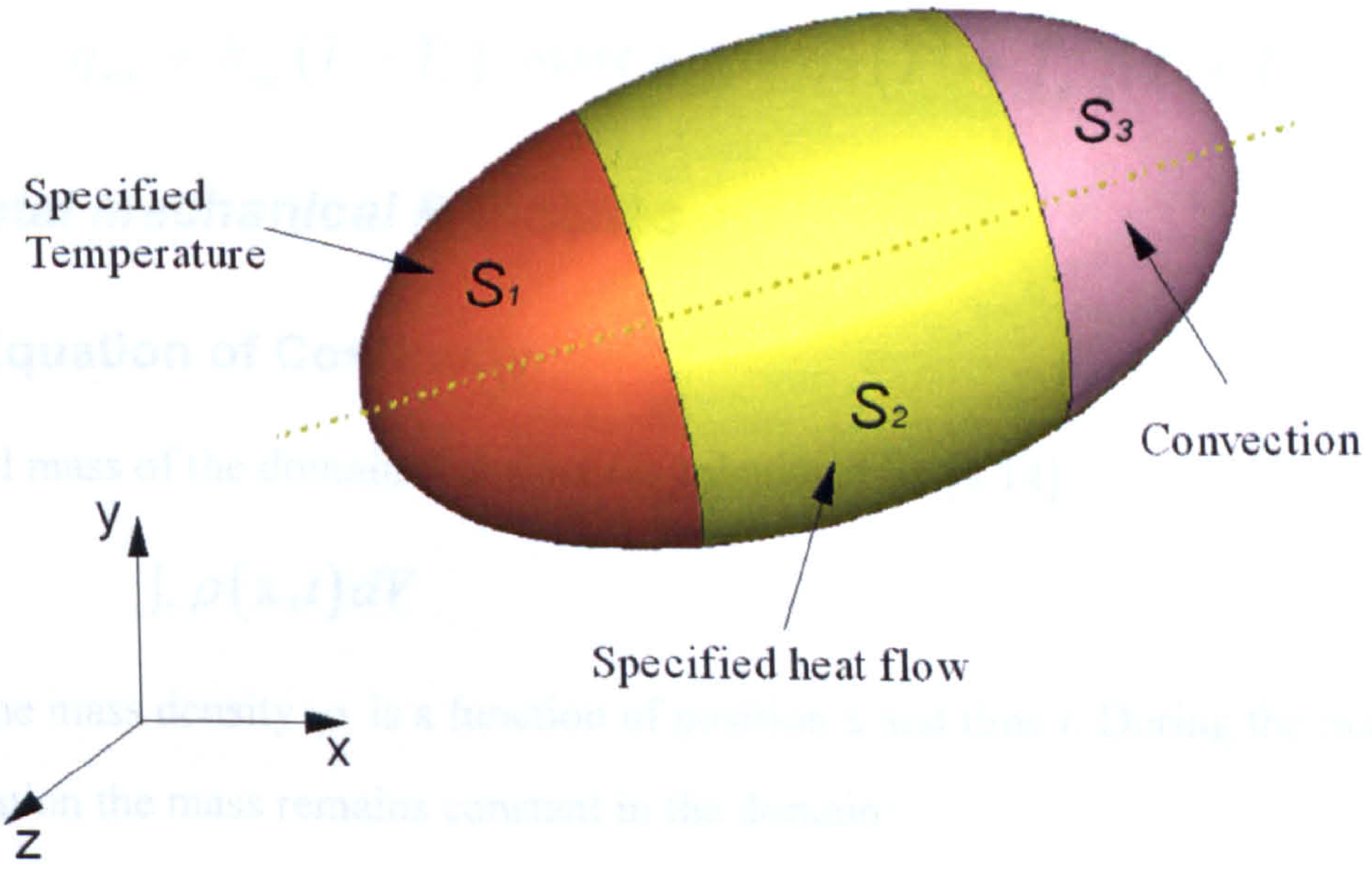

Figure 3.3 Typical boundary conditions for heat transfer problems.

Three main boundary conditions are applied over the surface of the domain:

1. Temperature prescribed on surface S_1, such that $T|_{S_1} = T^*$, where T^* is the prescribed temperature.

2. Heat flow specified on surface S_2, such that $k\frac{\partial T}{\partial \mathbf{n}}|_{S_2} + q^* = 0$, where q* is the specified heat flow (W/m^2).

3. Convection condition on surface S_3, such that $k\frac{\partial T}{\partial \mathbf{n}}|_{S_3} + h_f(T - T_S) = 0$, where h_f is the film coefficient and T_S the surrounding medium temperature. The film coefficient h_f has two categories, convection h_{fc} and radiation h_{fr} film coefficients.

In a particular case, $k\frac{\partial T}{\partial \mathbf{n}} = 0$ represents the adiabatic boundary condition.

In some cases, radiation should be considered, the radiation heat flux will follow the well known Stefan-Boltzman law, h_{rad} is the radiation coefficient.

$$q_{rad} = h_{rad}(T - T_s), \text{ where } h_{rad} = \sigma\varepsilon(T^2 + T_s^2)(T + T_s)$$

3.3 Metal Mechanical Principles

3.3.1 Equation of Continuity

The total mass of the domain V at time t is calculated by [3.14]

$$\int_V \rho(\mathbf{x},t)\,dV \tag{3.16}$$

where the mass density ρ is a function of position $\mathbf{x}$ and time t. During the material deformation the mass remains constant in the domain:

$$\frac{d}{dt}\int_V \rho(\mathbf{x},t)\,dV = 0 \tag{3.17}$$

Taking the derivative of the integral, this becomes

$$\int_V \left(\frac{d\rho}{dt} + \rho div(\upsilon) \right) dV = 0 \tag{3.18}$$

Any subdomain in V satisfies Equation 3.18, so the integrand must be zero:

$$\frac{d\rho}{dt} + \rho div(\upsilon) = 0 \tag{3.19}$$

For incompressible material, the density is constant and the above equation can be written

$$div(\upsilon) = 0 \tag{3.20}$$

3.3.2 Equation of Motion

The law of linear Momentum Conservation states that the rate change of linear momentum is equal to the resultant applied force [3.15]. In a fixed domain, the resultant force includes the resultant body force per unit mass and the sum of the surface tractions.

$$\frac{d}{dt}\int_V \rho\upsilon dV = \int_V \rho g dV + \int_s \boldsymbol{\sigma} \cdot \mathbf{n} dS \tag{3.21}$$

where $\boldsymbol{\sigma}$ is the stress tensor and $\mathbf{n}$ the outward normal to the surface.

The left-hand side of Equation 3.21 is the derivative of the integral and can be expressed as:

$$\frac{d}{dt}\int_V \rho\upsilon dV = \int_V \left(\frac{d(\rho\upsilon)}{dt} + \rho\upsilon div(\upsilon) \right) dV \tag{3.22}$$

$$\frac{d(\rho\upsilon)}{dt} = \frac{d\rho}{dt}\upsilon + \rho\frac{d\upsilon}{dt} \tag{3.23}$$

Combining Equations 3.22, 3.23 and 3.19 gives

$$\frac{d}{dt}\int_V \rho\upsilon dV = \int_V \rho\frac{d\upsilon}{dt} dV \tag{3.24}$$

According to the divergence theorem the surface integral on the right-hand side of Equation 3.21 can be expressed as

$$\int_s \boldsymbol{\sigma} \cdot \mathbf{n} dS = \int_v div(\boldsymbol{\sigma}) dV \tag{3.25}$$

Substitution of Equations 3.24 and 3.25 into Equation 3.21 yields

$$\int_v \rho \frac{d\upsilon}{dt} dV = \int_v \rho \mathbf{g} dV + \int_v div(\boldsymbol{\sigma}) dV \tag{3.26}$$

which is true for any domain in a body, and the acceleration $\mathbf{a} = d\upsilon/dt$. Hence

$$\rho \mathbf{a} = \rho \mathbf{g} + div(\boldsymbol{\sigma}) \tag{3.27}$$

3.3.3 The Virtual Work Principle

The principal of virtual work is not a law of conservation but a "weak form" of the equilibrium equations and provides the basic equilibrium statement for finite element formulation. A virtual displacement field $\delta\mathbf{u}$ or virtual velocity can be defined in the domain. Multiplying Equation 3.27 by $\delta\mathbf{u}$ on both sides and integrating over the whole domain give

$$\int_v \rho \mathbf{a} \cdot \delta\mathbf{u} dV = \int_v \rho \mathbf{g} \cdot \delta\mathbf{u} dV + \int_v div(\boldsymbol{\sigma}) \cdot \delta\mathbf{u} dV \tag{3.28}$$

Writing the last integral in Equation 3.28 in component format and applying Green theorem for each component lead to

$$\int_v \sum_{ij} \frac{\partial \sigma_{ij}}{\partial x_j} \delta u_i dV = \int_s \sum_{ij} \sigma_{ij} n_j \delta u_i dS - \int_v \sum_{ij} \sigma_{ij} \delta \varepsilon_{ij} dV \tag{3.29}$$

which can be rewritten in matrix format

$$\int_v div(\boldsymbol{\sigma}) \cdot \delta\mathbf{u} dV = \int_s \boldsymbol{\sigma}\mathbf{n} \cdot \delta\mathbf{u} dS - \int_v \boldsymbol{\sigma} \cdot \delta\boldsymbol{\varepsilon} dV \tag{3.30}$$

Substituting into Equation 3.28, the general virtual work principle is obtained

$$\int_v \rho \mathbf{a} \cdot \delta\mathbf{u} dV + \int_v \boldsymbol{\sigma} \cdot \delta\boldsymbol{\varepsilon} dV = \int_v \rho \mathbf{g} \cdot \delta\mathbf{u} dV + \int_v \boldsymbol{\sigma}\mathbf{n} \cdot \delta\mathbf{u} dS \tag{3.31}$$

For a static equilibrium or quasi-static problem the acceleration is considered as zero, the above equation reduces to

$$\int_v \sigma \cdot \delta \varepsilon dV = \int_v \rho \mathbf{g} \cdot \delta \mathbf{u} dV + \int_s \sigma \mathbf{n} \cdot \delta \mathbf{u} dS \quad (3.32)$$

The virtual work principle has the physical interpretation that the work done by the external forces subjected to the virtual displacements is equal to the virtual work of the internal forces.

3.4 Thermo-mechanical Principles

3.4.1 Energy Conservation

The conservation of energy principle is one of the basic principles of all science disciplines. The first law of thermodynamics is the application of the conservation of energy principle in thermodynamic systems [3.16]. It states that the time rate change of kinetic energy and internal energy for a fixed body of material is equal to the sum of the rate change of heat input and the rate of work done by the surface and body forces [3.17].

$$\frac{dE_I}{dt} + \frac{dE_K}{dt} = \frac{dE_W}{dt} + \frac{dQ}{dt} \quad (3.33)$$

where E_I is the internal energy, E_K is the kinetic energy, E_W is the work of external and body forces and Q is the heat input.

$$\frac{dE_I}{dt} = \frac{d}{dt}\int_v \rho e_I dV = \int_v \rho \frac{de_I}{dt} dV \quad (3.34)$$

where e_I is defined as the internal energy density.

$$\frac{dE_K}{dt} = \frac{d}{dt}\int_v \frac{1}{2}\rho \upsilon^2 dV = \int_v \rho \upsilon \cdot \mathbf{a} dV \quad (3.35)$$

$$\frac{dE_W}{dt} = \int_v \rho \mathbf{g} \cdot \upsilon dV + \int_s \sigma \cdot \mathbf{n} \cdot \mathbf{v} dS \quad (3.36)$$

$$= \int_v \rho \upsilon \cdot \mathbf{a} dV + \int_v \sigma : \dot{\varepsilon} dV$$

$$\frac{dQ}{dt} = -\int_s \mathbf{q} \cdot \mathbf{n} dS = -\int_v div(\mathbf{q}) dV \quad (3.37)$$

The substitution of Equations 3.34-3.37 into Equation 3.33 leads to

$$\int_V \rho \frac{de_I}{dt} dV = \int_V \sigma : \dot{\varepsilon} dV - \int_V div(\mathrm{q}) dV \tag{3.38}$$

The above equation must hold for any subdomain in the body, hence

$$\rho \frac{de_I}{dt} = \sigma : \dot{\varepsilon} - div(\mathrm{q}) \tag{3.39}$$

For convenience, the dissipated parts of the internal energy are split off [3.18]:

$$\begin{aligned} E_D &= \int_0^t \left(\int_V \sigma : \dot{\varepsilon} dV \right) dt \\ &= \underbrace{\int_0^t \left(\int_V \sigma^c : \dot{\varepsilon} dV \right) dt}_{E_C} + \underbrace{\int_0^t \left(\int_V \sigma^v : \dot{\varepsilon} dV \right) dt}_{E_V} \\ &= \underbrace{\int_0^t \left(\int_V \sigma^c : \dot{\varepsilon}^{el} dV \right) dt}_{E_S} + \underbrace{\int_0^t \left(\int_V \sigma^c : \dot{\varepsilon}^{pl} dV \right) dt}_{E_P} + \underbrace{\int_0^t \left(\int_V \sigma^c : \dot{\varepsilon}^{cr} dV \right) dt}_{E_T} + \underbrace{\int_0^t \left(\int_V \sigma^v : \dot{\varepsilon} dV \right) dt}_{E_V} \end{aligned} \tag{3.40}$$

where σ^c is the stress derived from the user-specified constitutive equation, without viscous dissipation effects, σ^v is the viscous stress (defined for bulk viscosity, material damping, and dashpots), the strain rate $\dot{\varepsilon} = \dot{\varepsilon}^{el} + \dot{\varepsilon}^{pl} + \dot{\varepsilon}^{cr}$ (where $\dot{\varepsilon}^{el}$, $\dot{\varepsilon}^{pl}$, and $\dot{\varepsilon}^{cr}$ are elastic, plastic, and creep strain rates, respectively), E_V is the energy dissipated by viscous effects, E_C is the energy dissipated without viscous effects, E_S is the elastic strain energy E_P is the energy dissipated by plasticity, and E_T is the energy dissipated by time-dependent deformation.

3.4.2 The Second Law of Thermodynamics

The second law of thermodynamics states that *the entropy of an isolated system not in equilibrium will tend to increase over time, approaching a maximum value at equilibrium* [3.19]. The mathematical expression for this theorem is as follows

$$\frac{dS_{en}}{dt} \geq \frac{1}{T} \frac{dQ}{dt} \tag{3.41}$$

where S_{en} is the entropy of the system, if s_{en} is defined as the density of entropy, the total entropy for a domain Ω is expressed as

$$S_{en} = \int_{\Omega} \rho s_{en} dV \tag{3.42}$$

After several arrangements of Equation 3.41, the Clausius-Duhem inequality can be obtained [3.17]:

$$\rho \frac{ds_{en}}{dt} + \frac{div(q)}{T} - \frac{q \cdot \nabla T}{T^2} \geq 0 \tag{3.43}$$

Substituting Equation 3.39 into Equation 3.43 gives

$$\rho\left(T\frac{ds_{en}}{dt} - \frac{de_I}{dt}\right) + \sigma : \dot{\varepsilon} - \frac{q \cdot \nabla T}{T} \geq 0 \tag{3.44}$$

The free energy Ψ is defined as

$$\Psi = e_I - Ts_{en} \tag{3.45}$$

$$\frac{d\Psi}{dt} = \frac{de_I}{dt} - \frac{dT}{dt}s_{en} - T\frac{ds_{en}}{dt} \tag{3.46}$$

Combining Equation 3.46 and 3.44 leads to the second form of the Clausius-Duhem inequality:

$$-\rho\left(\frac{d\Psi}{dt} + s_{en}\frac{dT}{dt}\right) + \sigma : \dot{\varepsilon} - \frac{q \cdot \nabla T}{T} \geq 0 \tag{3.47}$$

3.4.3 Heat Equation for Plastic or Viscoplastic Materials

The internal energy, entropy and free energy defined above are state functions which follow the evolution of the system. They are independent of the state path and characterized by the state variables and the internal variables. The internal state variables describe changes in physical phenomena, such as the phase change proportion, the dislocation density, the material microstructure and the equivalent plastic strains [3.17].

If the definition of the free energy function Ψ, Equation 3.46, is used in conjunction with the first thermodynamic principle, Equation 3.39, a new equation can be derived:

$$\rho\left(\frac{d\Psi}{dt}+\frac{dT}{dt}s_{en}+T\frac{ds_{en}}{dt}\right)-\boldsymbol{\sigma}:\dot{\boldsymbol{\varepsilon}}+div(\mathbf{q})=0 \tag{3.48}$$

For elastoviscoplasticity and elastoplasticity the free energy function is assumed to be a function of elastic strain, internal variables $\boldsymbol{\alpha}$ and temperature only. Hence

$$\frac{d\Psi}{dt}=\frac{\partial\Psi}{\partial\boldsymbol{\varepsilon}^{el}}:\dot{\boldsymbol{\varepsilon}}^{el}+\frac{\partial\Psi}{\partial\boldsymbol{\alpha}}:\dot{\boldsymbol{\alpha}}+\frac{\partial\Psi}{\partial T}\dot{T} \tag{3.49}$$

The thermodynamic forces $\mathbf{A}_\alpha$ corresponding to $\boldsymbol{\alpha}$ can be expressed by

$$\mathbf{A}_\alpha=\rho\frac{\partial\Psi}{\partial\boldsymbol{\alpha}} \tag{3.50}$$

Substituting Equation 3.49 into Equation 3.47, the Clausius-Duhem inequality becomes

$$\left(\boldsymbol{\sigma}-\rho\frac{\partial\Psi}{\partial\boldsymbol{\varepsilon}^{el}}\right):\dot{\boldsymbol{\varepsilon}}^{el}+\boldsymbol{\sigma}:\dot{\boldsymbol{\varepsilon}}^{pl}-\mathbf{A}_\alpha:\dot{\boldsymbol{\alpha}}-\rho\left(\frac{\partial\Psi}{\partial T}+s_{en}\right)\frac{dT}{dt}-\frac{\mathbf{q}\cdot\nabla T}{T}\geq 0 \tag{3.51}$$

and

$$\boldsymbol{\sigma}-\rho\frac{\partial\Psi}{\partial\boldsymbol{\varepsilon}^{el}}=0 \tag{3.52}$$

$$\frac{\partial\Psi}{\partial T}+s_{en}=0 \tag{3.53}$$

With the help of Equations 3.49, 3.52 and 3.53 the Equation 3.48 becomes

$$\rho T\frac{ds_{en}}{dt}+\boldsymbol{\sigma}:\dot{\boldsymbol{\varepsilon}}^{pl}-\mathbf{A}_\alpha:\dot{\boldsymbol{\alpha}}+div(\mathbf{q})=0 \tag{3.54}$$

$$\begin{aligned}\frac{ds_{en}}{dt}&=\frac{\partial s_{en}}{\partial\boldsymbol{\varepsilon}^{el}}:\dot{\boldsymbol{\varepsilon}}^{el}+\frac{\partial s_{en}}{\partial\boldsymbol{\alpha}}:\dot{\boldsymbol{\alpha}}+\frac{\partial s_{en}}{\partial T}\dot{T}\\&=-\frac{1}{\rho}\frac{\partial\boldsymbol{\sigma}}{\partial T}:\dot{\boldsymbol{\varepsilon}}^{el}-\frac{1}{\rho}\frac{\partial\mathbf{A}_\alpha}{\partial T}:\dot{\boldsymbol{\alpha}}+\frac{\partial s_{en}}{\partial T}\dot{T}\end{aligned} \tag{3.55}$$

The specific heat is defined as

$$c = T\frac{\partial s_{en}}{\partial T} \tag{3.56}$$

The new heat equation is obtained by putting Equation 3.55 into Equation 3.54:

$$\rho c\frac{dT}{dt} = \boldsymbol{\sigma} : \dot{\boldsymbol{\varepsilon}}^{pl} - \mathbf{A}_{\alpha} : \dot{\boldsymbol{\alpha}} + div(\mathbf{K}_k \nabla T) + T\left(\frac{\partial \boldsymbol{\sigma}}{\partial T} : \dot{\boldsymbol{\varepsilon}}^{el} + \frac{\partial \mathbf{A}_{\alpha}}{\partial T} : \dot{\boldsymbol{\alpha}}\right) \tag{3.57}$$

For the sake of convenience, the effect of internal state variables is considered as a fraction 0-0.1 of *plastic dissipation energy*. The last term on the right-hand side of Equation 3.57 is often neglected, giving the simpler form of the heat equation when plastic or viscoplastic deformation occurs:

$$\rho c\frac{dT}{dt} = \boldsymbol{\sigma} : \dot{\boldsymbol{\varepsilon}}^{pl} + div(\mathbf{K}_k \nabla T) \tag{3.58}$$

3.5 Finite Element Formulation of the Fully Coupled Thermal and Mechanical Analysis

For the material mechanical response the general virtual work principle, Equation 3.31 can be used to construct the FE formulations. The Matrix form of the equation is expressed as

$$\int_{\Omega} \rho \mathbf{N}'\mathbf{N} \cdot \ddot{\mathbf{d}}\, dV - \int_{\Omega} \rho \mathbf{g} \cdot \mathbf{N}\, dV + \int_{\Omega} \boldsymbol{\sigma} \cdot \mathbf{B}\, dV - \int_{\Gamma} \boldsymbol{\Phi} \cdot \mathbf{N}\, dS = 0 \tag{3.59}$$

It can be written in a more compact form

$$\mathbf{M}\ddot{\mathbf{d}} = \mathbf{F}_{ext} - \mathbf{F}_{in} \tag{3.60}$$

where

$\mathbf{u} = \mathbf{N} \cdot \mathbf{d}$, $\ddot{\mathbf{u}} = \mathbf{N} \cdot \ddot{\mathbf{d}}$, $\dot{\mathbf{u}} = \mathbf{N} \cdot \dot{\mathbf{d}}$, $\boldsymbol{\varepsilon} = \mathbf{B} \cdot \mathbf{d}$

$\mathbf{u}$, $\dot{\mathbf{u}}$ and $\ddot{\mathbf{u}}$ are respectively the position vector, the velocity and the acceleration

$\mathbf{d}$, $\dot{\mathbf{d}}$ and $\ddot{\mathbf{d}}$ are respectively the nodal position, the nodal velocity and the nodal acceleration

N is the shape function and Φ is the surface tractions

M, $\mathbf{F}_{in}$ and $\mathbf{F}_{ext}$ are assembled mass, internal force and external force matrices, respectively

The corresponding element matrices are:

$$\mathbf{m} = \int_V \rho \mathbf{N}^T \mathbf{N} dV$$

$$\mathbf{f}_{in} = \int_V \boldsymbol{\sigma} \cdot \mathbf{B} dV$$

$$\mathbf{f}_{ext} = \int_V \rho \mathbf{g} \cdot \mathbf{N} dV + \int_S \boldsymbol{\Phi} \cdot \mathbf{N} dS$$

Using the standard Galerkin approach the discretized heat equation 3.14 is expressed in matrix form as

$$\mathbf{C}\dot{\mathbf{T}} + \mathbf{K}_T \mathbf{T} = \mathbf{S}_T \tag{3.61}$$

where the upper case letters denotes assembled matrix:

$\mathbf{K}_T = \mathbf{K}_k + \mathbf{H}_c$	conductivity and boundary convection matrices
$\mathbf{S}_T = \mathbf{S}_B + \mathbf{S}_h + \mathbf{S}_Q$	heat source vector including all thermal sources

The corresponding lower case letters represent element matrices:

$\mathbf{c} = \int_V \mathbf{N}^T \mathbf{N} \rho c dV$	heat capacity matrix
$\mathbf{k}_k = \int_V \mathbf{B}^T \mathbf{K} \mathbf{B} dV$	conductivity matrix
$\mathbf{h}_c = \int_S \mathbf{N}^T \mathbf{N} h_{fc} dS$	boundary convection matrix, h_{fc} is the convective film coefficient
$\mathbf{s}_B = \int_S \mathbf{N} q_B dS$	boundary heat flux vector, q_B is boundary heat flux
$\mathbf{s}_h = \int_S \mathbf{N}^T h_f T_e dS$	boundary convection vector
$\mathbf{s}_Q = \int_V \mathbf{N}^T \boldsymbol{\sigma} : \dot{\boldsymbol{\varepsilon}}^p dV$	heat generation vector

At this point, the discretized FE formulations of the heat equation and the mechanical governing equation have been obtained. Numerical solution methods fall into two schemes, namely explicit and implicit. When the dependent variables are directly calculated in terms of already known quantities, the computation procedure is referred to as explicit analysis. In an implicit analysis, the dependent variables are determined by a set of equations and a matrix or iterative technique is required to obtain the solution.

3.5.1 Implicit Analysis

In pure dynamic analysis, a set of linear equations is solved by a direct solution method such as Newton's method. Newton's method aims to satisfy dynamic equilibrium at the end of the increment $t+\Delta t$ and to calculate displacements and other variables simultaneously. In a nonlinear problem, each time increment usually requires several iterations to achieve a solution within the prescribed convergence tolerances. Each Newton iteration solves for a correction, $\mathbf{c}_j$, to the incremental displacements, $\Delta\mathbf{u}_j$.

$$\hat{\mathbf{K}}_j\mathbf{c}_j=\mathbf{F}_{ext_j}-\mathbf{F}_{in_j}-\mathbf{M}_j\ddot{\mathbf{d}}_j \tag{3.62}$$

The effective stiffness matrix, $\hat{\mathbf{K}}_j$, is a linear combination of the tangent stiffness matrix.

For coupled thermal-stress analysis, the thermal and mechanical solutions must be obtained simultaneously rather than sequentially. The nonlinear coupled system can be solved by Newton's method.

$$\begin{bmatrix} \dfrac{\partial \mathbf{P}_M}{\partial \mathbf{u}} & \dfrac{\partial \mathbf{P}_M}{\partial \mathbf{T}} \\ \dfrac{\partial \mathbf{P}_H}{\partial \mathbf{u}} & \dfrac{\partial \mathbf{P}_H}{\partial \mathbf{T}} \end{bmatrix} \begin{bmatrix} \mathbf{c}_M \\ \mathbf{c}_H \end{bmatrix} = \begin{bmatrix} \mathbf{R}_M \\ \mathbf{R}_H \end{bmatrix} \tag{3.63}$$

In ABAQUS/Standard the fully coupled thermal-stress analysis neglects initial effect, the left-hand side of Equation 3.60 is zero, the right-hand side is represented by $\mathbf{P}_M$. The

Equation 3.61 is written symbolically as $\mathbf{P}_H(\mathbf{u},\mathbf{T}) = 0$. $\mathbf{c}_M$ and $\mathbf{c}_H$ are the respective corrections to the incremental displacements and temperature.

$\mathbf{R}_M$ and $\mathbf{R}_H$ are the mechanical and thermal residual vectors, respectively.

$\frac{\partial \mathbf{P}_M}{\partial \mathbf{T}}$ is the mechanical coupling on the temperature distribution

$\frac{\partial \mathbf{P}_H}{\partial \mathbf{T}}$ is the thermal coupling in the mechanical equation

The time increment in an implicit procedure is relatively larger than that in an explicit procedure; however the computational cost of solving this set of equations in each increment is high in comparison with the relatively low cost of the nodal calculations in the explicit method.

3.5.2 Explicit Analysis

In an explicit method, the heat transfer and mechanical solutions are obtained simultaneously by the explicit time integration approaches. As a result, no iterations or tangent stiffness matrices need be calculated. The following shows the flow chart of the code, beginning with the domain at time *t*, the $(i+1)^{\text{th}}$ time increment Δt^{i+1} and temperature $\mathbf{T}^t$:

A. Determine the displacement field $\mathbf{d}^{t+\Delta t}$.

B. Update the domain at $t + \Delta t^{i+1}$.

C. Calculate the temperature $\mathbf{T}^{t+\Delta t}$ using the plastic work dissipation computed with the variables at *t*.

A typical solution procedure for Step A and Step B as below is used.

1. Nodal variable calculation

   a. Accelerations at the beginning of the current increment *t*

$$\ddot{\mathbf{d}}^t = \mathbf{M}^{-1}\left(\mathbf{F}_{ext}^t - \mathbf{F}_{in}^t\right) \tag{3.64}$$

b. Integrate with the central difference rule to calculate velocities

$$\dot{\mathbf{d}}^{t+\frac{\Delta t}{2}} = \dot{\mathbf{d}}^{t-\frac{\Delta t}{2}} + \frac{\left(\Delta t^{t+1} + \Delta t^{t}\right)}{2}\ddot{\mathbf{d}}^{t} \tag{3.65}$$

c. Integrate through time to calculate displacements

$$\mathbf{d}^{t+\Delta t} = \mathbf{d}^{t} + \Delta t^{t+1}\dot{\mathbf{d}}^{t+\frac{\Delta t}{2}} \tag{3.66}$$

2. Element calculation

   a. Compute element strain increments, $d\varepsilon$ from the strain rate, $\dot{\varepsilon}$.

   b. Compute stresses σ from constitutive equations

$$\sigma^{t+\Delta t} = f\left(\sigma^{t}, d\varepsilon\right) \tag{3.67}$$

   c. Compute $\mathbf{F}_{in}^{t+\Delta t}$ by assembling nodal internal forces.

3. Set $t + \Delta t^{t+1}$ to t and Repeat step 1 and 2.

The heat transfer equation 3.61 is integrated using the explicit forward-difference time integration rule.

$$\mathbf{T}^{t+\Delta t} = \mathbf{T}^{t} + \Delta t^{t+1}\dot{\mathbf{T}}^{t} \tag{3.68}$$

The nodal temperature rate at t is obtained by

$$\dot{\mathbf{T}}^{t} = \mathbf{C}^{-1}\left(\mathbf{S}_T - \mathbf{K}_T\mathbf{T}^{t}\right) \tag{3.69}$$

A large number of small time increments are usually needed in an explicit procedure. The time increment is restricted by the central-difference and forward-difference operators, which are conditionally stable. The stability limit for both operators is given by

$$\Delta t \le \min\left(\frac{2}{\omega_{\max}}, \frac{2}{\lambda_{\max}}\right) \tag{3.70}$$

where $\omega_{\max}$ is the highest frequency in the system of equations of the mechanical solution response and $\lambda_{\max}$ is the largest eigenvalue in the system of equations of the thermal solution response.

The stability limit for the forward-difference operator in the thermal solution response is approximated by

$$\Delta t = \frac{L_{\min}^2}{2\varsigma} \tag{3.71}$$

where $L_{\min}$ is the smallest element dimension in the mesh and $\varsigma = k/\rho c$ is the thermal diffusivity of the material.

The mechanical solution response the stability limit is often estimated as the smallest transit time of a dilatational wave across any of the elements in the mesh

$$\Delta t = \frac{L_{\min}}{c_d} \tag{3.72}$$

where c_d is the dilatational wave speed determined by effective Lamé's constants $\hat{\lambda}$ and $\hat{\mu}$.

In an isotropic, elastic material the dilatational wave speed can be defined in terms of Young's modulus, E, and Poisson's ratio, ν, by

$$c_d = \sqrt{\frac{E\nu/(1+\nu)(1-2\nu)+E/(1+\nu)}{\rho}} \tag{3.73}$$

3.6 Metal Plasticity

In classical plasticity theory, if the stress within the material is less than the yield point, the corresponding strain will be elastic and the material will return to its original shape when the load is removed. Elastic behaviour may be linear or non-linear. If the stress exceeds the yield stress, the material exhibits plastic behavior: after loading and subsequent unloading, the material is found to have permanently deformed. Plasticity theory was developed to describe this inelastic behavior. Different materials exhibit different inelastic behavior under different loading conditions, in practice, stress-strain curves are generally obtained by being fitted to experimental measurements.

3.6.1 Yield Criteria

Yield of ductile material is assumed to be independent of the equivalent pressure stress (also known as hydrostatic pressure). This has been validated experimentally for most metals (except voided metals) under positive pressure stress. Thus the yield criterion is dependent only on the *deviatoric* stress tensor.

$$\mathbf{S} = \boldsymbol{\sigma} + p\mathbf{I} \tag{3.74}$$

$$p = -\frac{1}{3} trace(\boldsymbol{\sigma}) \tag{3.75}$$

where S is the deviatoric stress and p is the hydrostatic pressure. If the metal is isotropic, the material has the same properties in all directions and yielding is related to the magnitudes of the principal stresses, that is, only dependent on the ***invariants*** of the deviatoric stress tensor, J_1, J_2, J_3.

$$\begin{aligned} J_1 &= 0 \\ J_2 &= -(S_1S_2 + S_2S_3 + S_3S_1) \\ J_3 &= S_1S_2S_3 \end{aligned} \tag{3.76}$$

Therefore, the yield surface can be reduced from $f(\sigma_1, \sigma_2, \sigma_3) = 0$ to a function of two variables J_2, J_3. Apart from its isotropy and pressure-independence, the metal is often observed to have similar plastic response in initial tension or compression loading [3.15], [3.20]. With this assumption the yield function becomes $f(J_2) = constant$. If J_2 is expressed in terms of stress, the well-known **von Mises yield function** can be derived:

$$(\sigma_1 - \sigma_2)^2 + (\sigma_2 - \sigma_3)^2 + (\sigma_3 - \sigma_1)^2 = constant \tag{3.77}$$

The *constant* in above equation is called the equivalent stress $\bar{\sigma}$. Its value is equal to the yield stress σ_y of the material when yield occurs. Rearranging (3.77) gives:

$$\bar{\sigma} = \sqrt{\frac{(\sigma_1 - \sigma_2)^2 + (\sigma_2 - \sigma_3)^2 + (\sigma_3 - \sigma_1)^2}{2}} \tag{3.78}$$

Figure 3.4a shows the 3D yield surface corresponding to Equation (3.78), which is an infinite cylinder with the axis $\sigma_1 = \sigma_2 = \sigma_3$. The yield surface in 2D is an ellipse with major axis along $\sigma_1 = \sigma_2$.

Tresca yield criterion is based upon maximum shear stress, and states that yielding occurs when the largest shear stress within the system equals the shear yield stress in a tensile specimen, $\bar{\sigma}/2$, i.e.

$$\max\{|\sigma_1 - \sigma|, |\sigma_2 - \sigma_3|, |\sigma_3 - \sigma_1|\} = \bar{\sigma} \tag{3.79}$$

The Tresca yield surface is a hexagonal surface as illustrated in Figure 3.4b. The Tresca yield criterion is simple and conservative, but not smooth. Most commercial finite element analysis programs use the von Mises criterion for isotropic materials. In the case of anisotropic plastic behaviour (stress-strain curves are different in different directions) **Hill's quadratic yield criterion** is widely used.

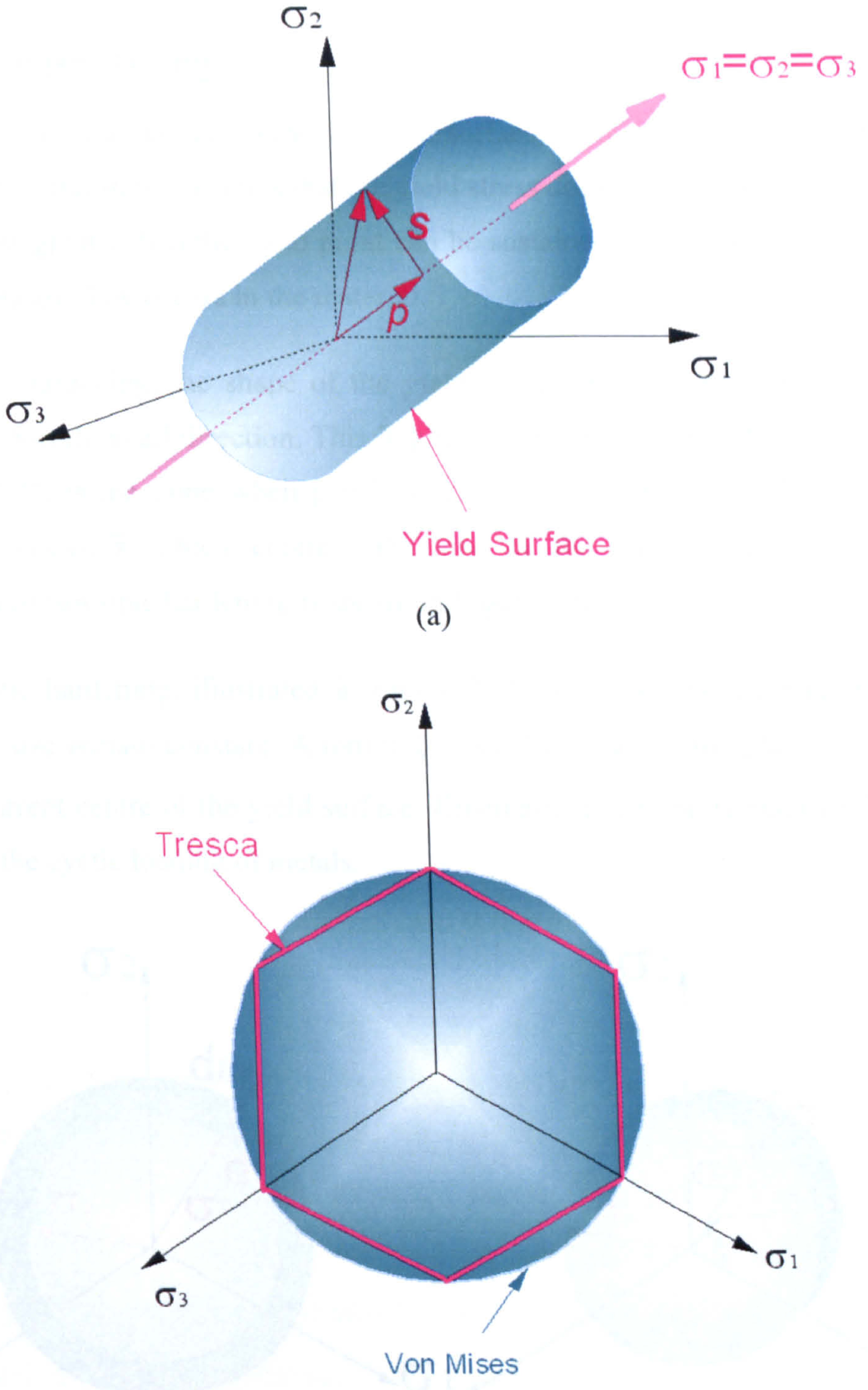

(a)

(b)

Figure 3.4 Von Mises and Tresca yield surfaces (a) in 3D and (b) 2D representation, looking down the axis of the cylinder.

3.6.2 Strain Hardening

Strain hardening laws governs how the yield surface evolves with strain when yielding occurs. Perfect plasticity assumes that the yield stress does not change with plastic strain and no stress greater than the yield point can be sustained. On reaching the yield point, unlimited plastic flow occurs in the material.

In isotropic hardening, the shape of the yield surface remains the same and the size changes uniformly in all direction. This implies that the basic form of the yield function, Equation 3.78, is the same when plastic straining occurs except for the magnitude of equivalent stress, $\overline{\sigma}$ which controls the size of the yield surface. A conceptual illustration of isotropic hardening is shown in Figure 3.5a.

In kinematic hardening, illustrated in Figure 3.5b, the yield surface translates but the shape and size remain constant. A tensor ξ is used to describe the plastic strain history and the current centre of the yield surface. Kinematic hardening is mainly of interest in modeling the cyclic loading of metals.

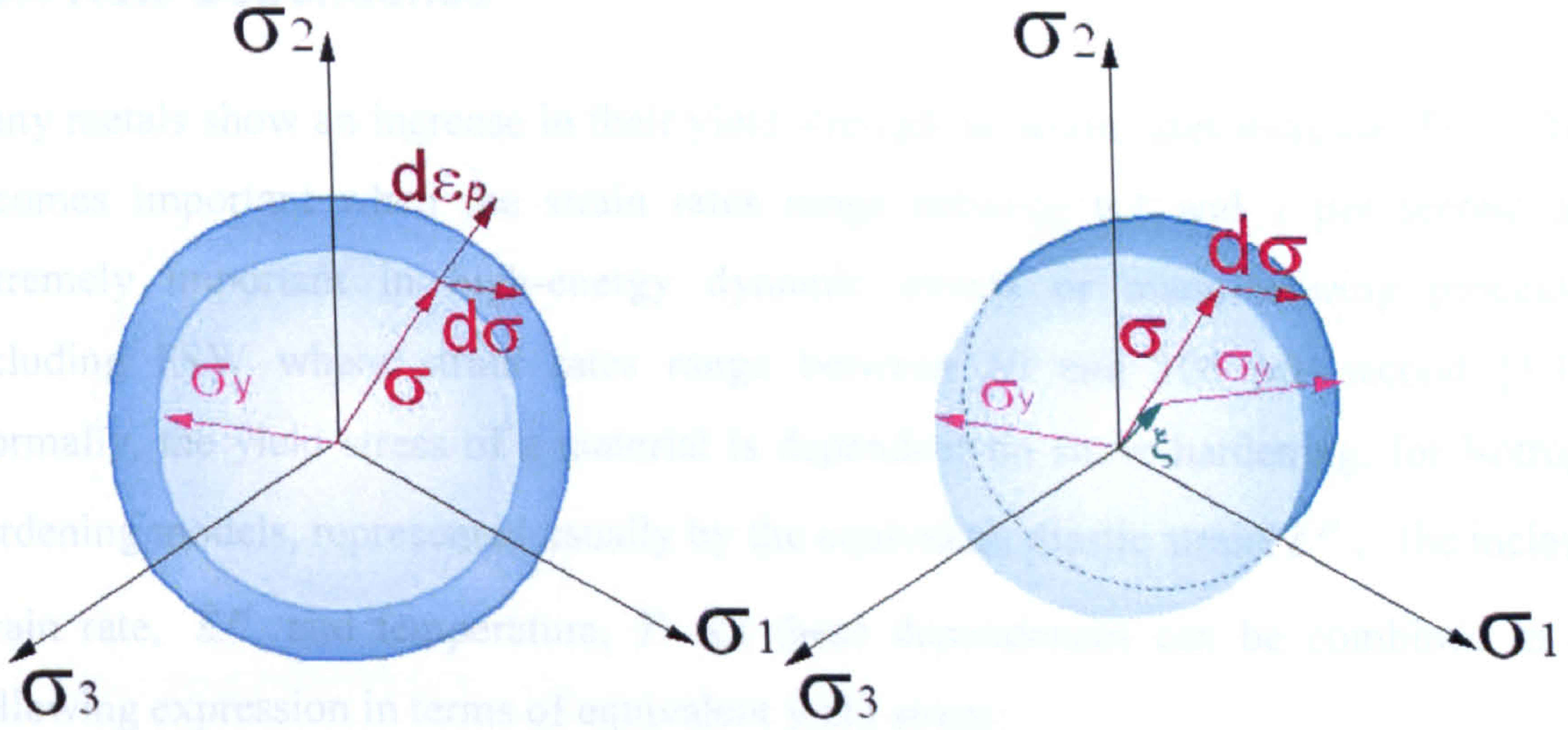

(a) (b)

Figure 3.5 Evolution of yield surface: (a) isotropic hardening and (b) kinematic hardening.

3.6.3 Flow Rule

The normality condition (or the associated flow rule) states that as the material yields, the inelastic strain increment is in the direction of the normal to the yield surface, written mathematically as

$$d\varepsilon^{pl} = d\bar{\varepsilon}^{pl} \frac{\partial f(\sigma)}{\sigma} \tag{3.80}$$

where $d\bar{\varepsilon}^{pl} = \sqrt{\frac{2}{3} d\varepsilon^{pl} \cdot d\varepsilon^{pl}}$. If the deviatoric stress tensor S and von Mises yield function are used, the equivalent expression of Equation 3.80 can be obtained:

$$d\varepsilon^{pl} = \frac{3\mathrm{S}}{2\bar{\sigma}} d\bar{\varepsilon}^{pl} \tag{3.81}$$

This equation shows that the plastic strain rate has the same direction as the deviatoric stress tensor. A simple graphical interpretation is shown in Figure 3.5a.

3.6.4 Rate Dependence

Many metals show an increase in their yield strength as strain rates increase. This effect becomes important when the strain rates range between 0.1 and 1 per second and extremely important in high-energy dynamic events or manufacturing processes, including FSW where strain rates range between 10 and 100 per second [3.18]. Normally, the yield stress of a material is dependent on strain hardening, for isotropic hardening models, represented usually by the equivalent plastic strain, $\bar{\varepsilon}^{pl}$, the inelastic strain rate, $\dot{\bar{\varepsilon}}^{pl}$ and temperature, *T*. All these dependences can be combined in the following expression in terms of equivalent yield stress:

$$\bar{\sigma} = \bar{\sigma}\left(\bar{\varepsilon}^{pl}, \dot{\bar{\varepsilon}}^{pl}, T\right) \tag{3.82}$$

3.7 Surface Interaction

3.7.1 Mechanical Contact

Velocity expression of the contact problem A function $g(\mathbf{x},t)=0$ of space coordination $\mathbf{x}$ and time t can be defined to represent the surface of the tool or a master surface in contact with other bodies [3.17]. Any point inside the master contact body satisfies $g(\mathbf{x},t)<0$. The direction vector of the outward normal to the master surface is defined by

$$\mathbf{n}=\frac{1}{\left|\partial g/\partial \mathbf{x}\right|}\frac{\partial g}{\partial \mathbf{x}} \tag{3.83}$$

At a given time and space coordination, the material velocities are $\boldsymbol{\upsilon}_{master}$ and $\boldsymbol{\upsilon}_{slave}$ for material points on the master surface and slave surface, respectively. Therefore, the contact condition can be written as

$$\left(\boldsymbol{\upsilon}_{master}-\boldsymbol{\upsilon}_{slave}\right)\cdot\mathbf{n}=\Delta\boldsymbol{\upsilon}\cdot\mathbf{n}=0 \tag{3.84}$$

Hard contact The contact pressure, $p_{contact}$ between two surfaces at a point is related to the "overclosure," $d_{contact}$ of the surfaces. In "hard" contact, their relationship is expressed as

$$\begin{aligned} p_{contact}&=0 \quad \text{for } d_{contact}<0 \quad \text{(open)}\\ d_{contact}&=0 \quad \text{for } p_{contact}>0 \quad \text{(closed)} \end{aligned} \tag{3.85}$$

No contact pressure exists unless the slave surface and the master surface are in contact. As the penetration is not allowed between surfaces, there is no limit to the magnitude of contact pressure that can be transmitted.

Softened contact In a "softened" contact relationship the contact pressure is a function of the clearance between two surfaces. In an exponential function relationship the surfaces begin to transmit contact pressure once the clearance reduces to c_0, as shown in Figure 3.6. As the clearance decreases further the contact pressure increases exponentially.

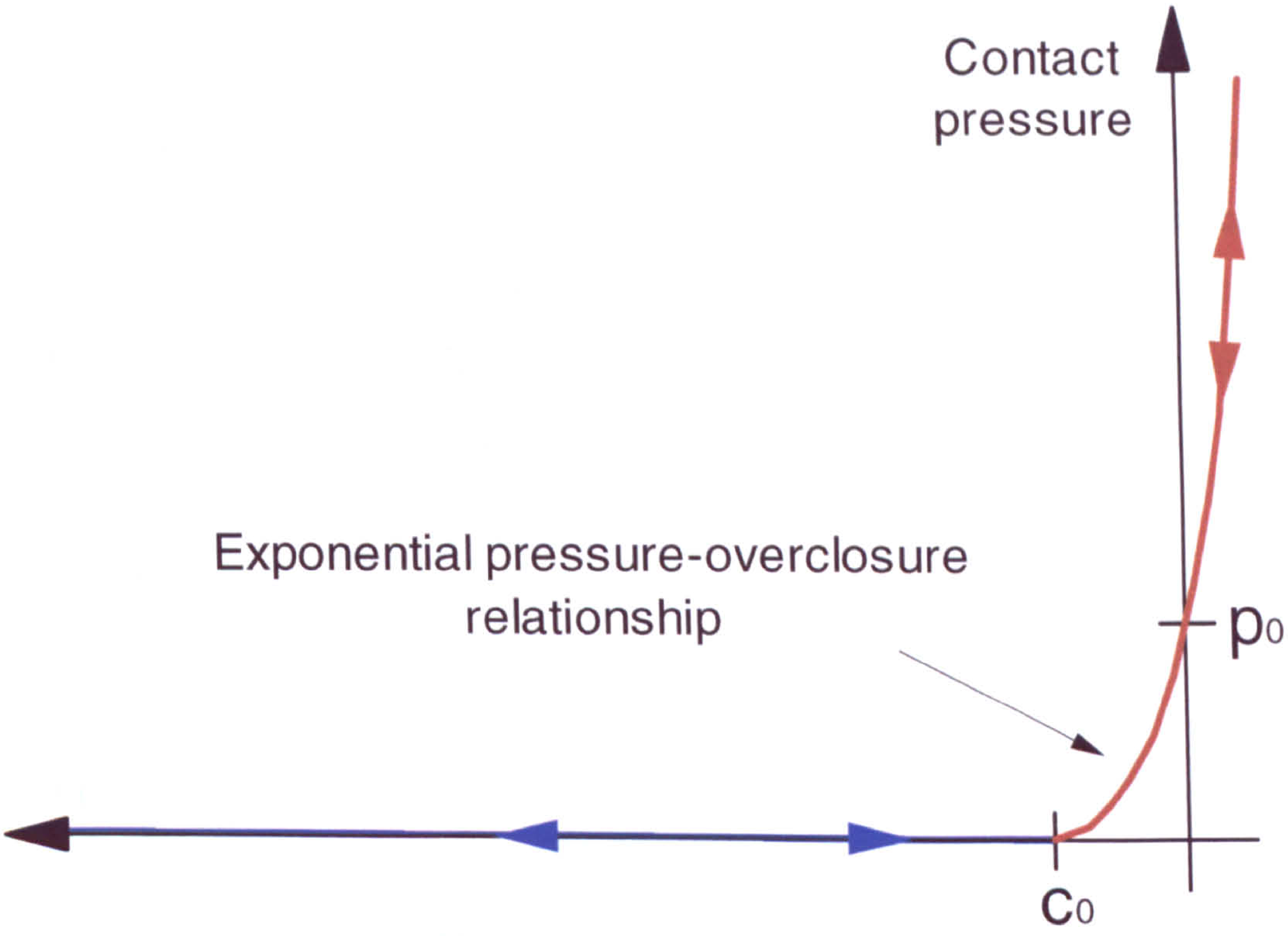

Figure 3.6 Exponential “softened” pressure-overclosure relationship.

3.7.2 Friction

Generally, the friction shear stress is in the form

$$\boldsymbol{\tau} = -f\left(\Delta\boldsymbol{\upsilon}, \sigma_n\right)\frac{\Delta\boldsymbol{\upsilon}}{|\Delta\boldsymbol{\upsilon}|} \tag{3.86}$$

where $\Delta\boldsymbol{\upsilon}$ is the tangential velocity difference between two surfaces and f is a function of $\Delta\boldsymbol{\upsilon}$ and the normal stress σ_n.

The Coulomb friction model states that there is no relative motion if the friction shear stress is less than the critical stress, $\tau_{crit} = \mu_s p_{contact}$, where μ_s is the static friction coefficient, which depends on the contact pressure, the slip rate and the surface temperature at the contact point. The friction stress cannot exceed the shear yield strength of the material. Thus the maximum shear stress is $\bar{\sigma}/2$ for a Tresca material and $\bar{\sigma}/\sqrt{3}$ for a von Mises material (Refer to Equations 3.78 and 3.79 for the meaning of $\bar{\sigma}$).

The friction coefficient at the initiation of slipping from a sticking condition, called the "static" friction coefficient, is different from the "kinetic" friction coefficient in an established slipping condition. A smooth transition zone between a static friction coefficient, μ_s, and a kinetic friction coefficient, μ_k, can be approximated by an exponential curve, as illustrated in Figure 3.7.

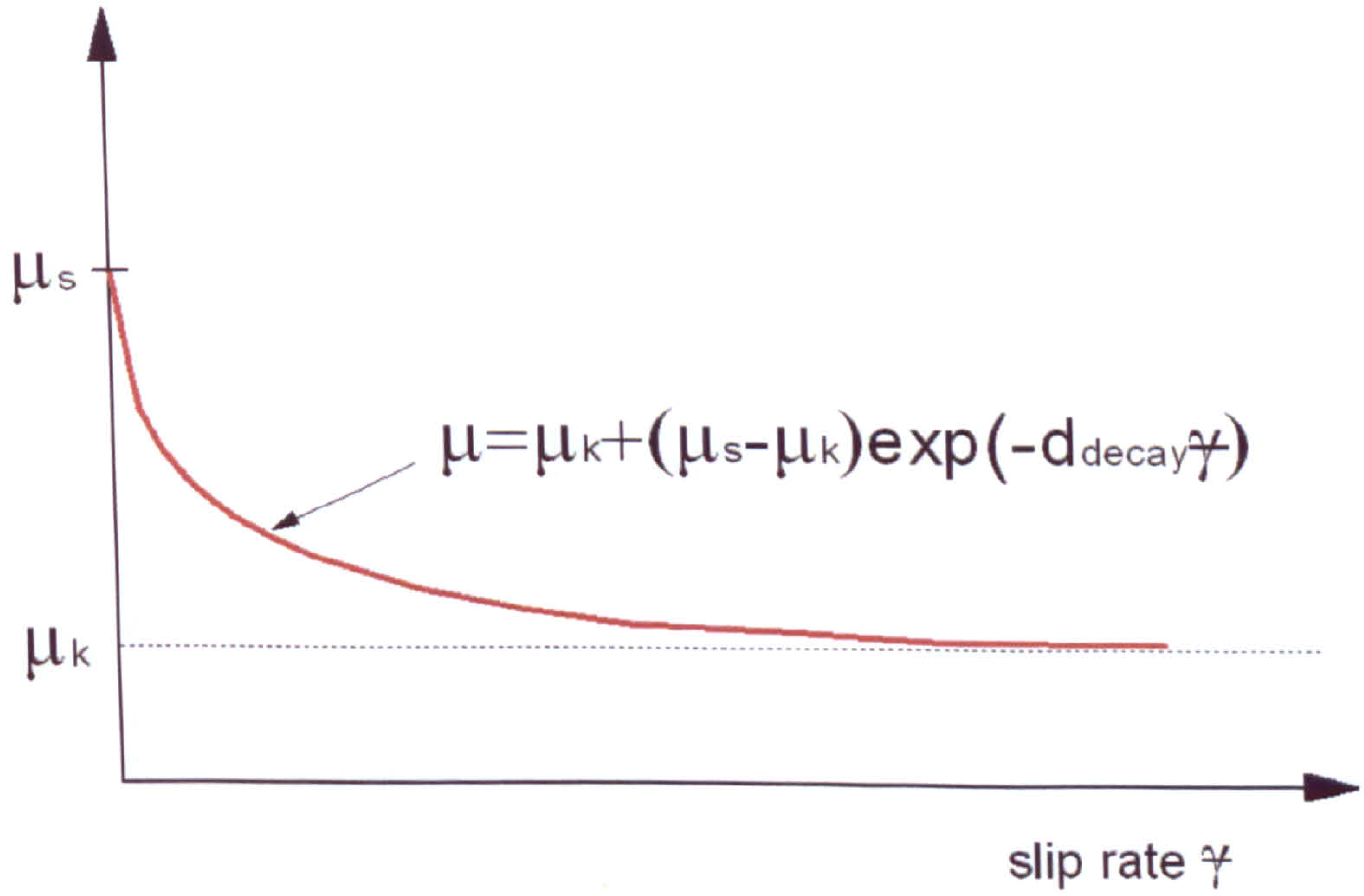

Figure 3.7 Exponential decay friction model.

3.7.3 Thermal Contact

When two surfaces come in contact, heat flows from the hotter body to the colder body. Heat conduction between the contact surfaces is governed by

$$q_{gap} = k_{gap}(T_1 - T_2) \tag{3.87}$$

coefficient, which depends on the contact pressure, the slip rate and the surface temperature at the contact point. The friction stress cannot exceed the shear yield strength of the material. Thus the maximum shear stress is $\bar{\sigma}/2$ for a Tresca material and $\bar{\sigma}/\sqrt{3}$ for a von Mises material (Refer to Equations 3.78 and 3.79 for the meaning of $\bar{\sigma}$).

The friction coefficient at the initiation of slipping from a sticking condition, called the "static" friction coefficient, is different from the "kinetic" friction coefficient in an established slipping condition. A smooth transition zone between a static friction coefficient, μ_s , and a kinetic friction coefficient, μ_k , can be approximated by an exponential curve, as illustrated in Figure 3.7.

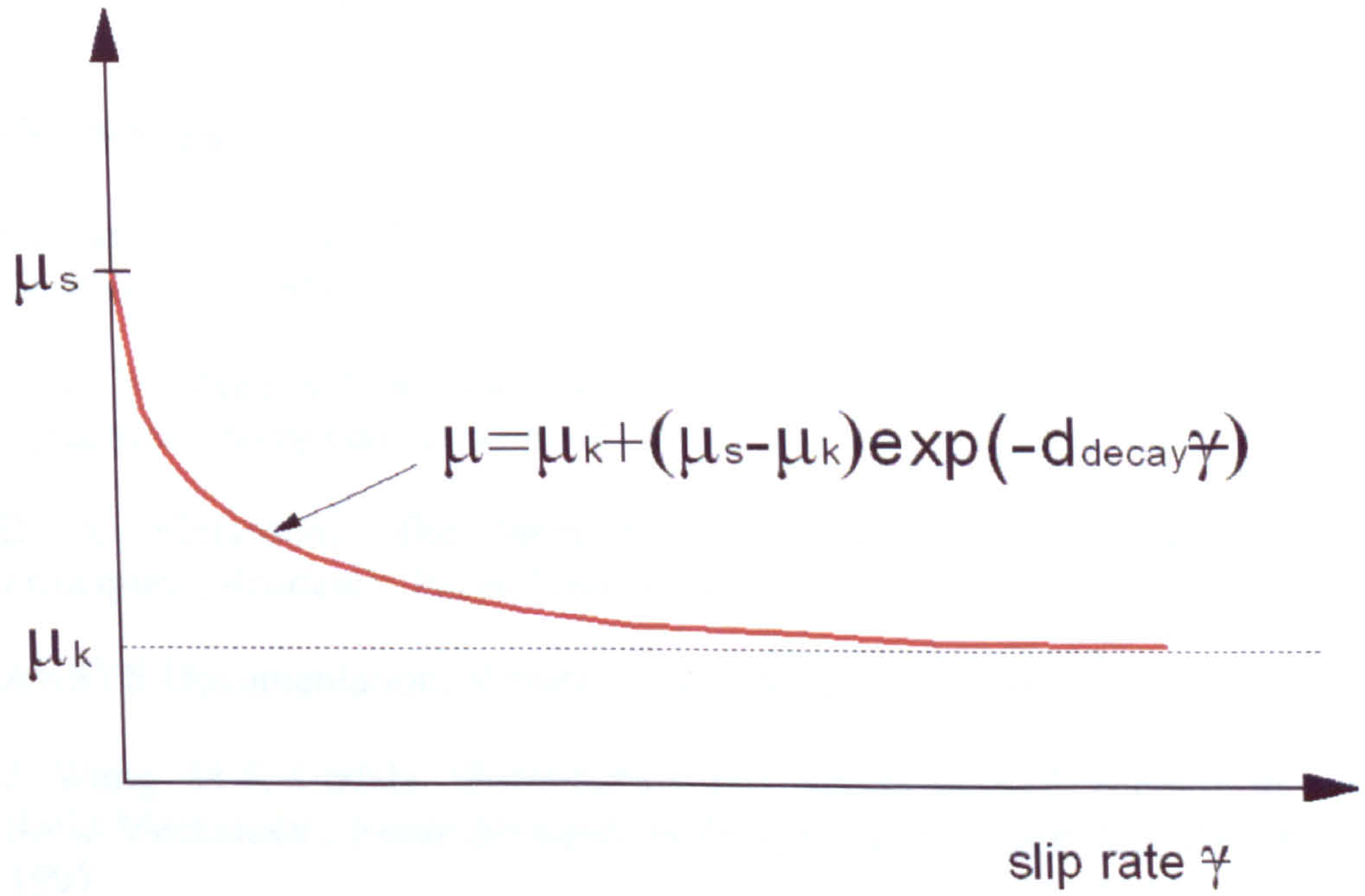

Figure 3.7 Exponential decay friction model.

3.7.3 Thermal Contact

When two surfaces come in contact, heat flows from the hotter body to the colder body. Heat conduction between the contact surfaces is governed by

$$q_{gap} = k_{gap}(T_1 - T_2) \tag{3.87}$$

where q_{gap} is the heat flux per unit area across the interface, T_1 and T_2 are the temperatures of the points on the surfaces, and k_{gap} is the gap conductance which is defined as

$$k_{gap} = k(\bar{T}, d_{clear}, p_{contact}) \tag{3.88}$$

where

$\bar{T} = \frac{1}{2}(T_1 + T_2)$ is the average of the surface temperatures

d_{clear} is the clearance between surfaces

$p_{contact}$ is the contact pressure across the interface

3.8 References

[3.1] Michael A. Celia, William G. Gray, 'Numerical Methods for Differential Equations', *Prentice Hall,* New Jersey, 1992.

[3.2] H. K. Versteeg and W. Malalasekera, 'An Introduction to Computational Fluid Dynamics', *Longman Scientific & technical,* Essex, England, 1995.

[3.3] B. A. Finlayson, 'The Method of Weighted Residuals and Variationals Principles', *Academic Press,* New York, 1972

[3.4] ANSYS Documentation, Version 10.0, ANSYS Inc., 2005

[3.5] J. Wang, M.S. Gadala, 'Formulation and Survey of ALE Method in Nonlinear Solid Mechanics', *Finite Elements in Analysis and Design,* Vol. 24, pp 253- 269, 1997

[3.6] M.S. Gadala, G.AE. Oravas and M.A. Dokainish, 'A Consistent Eulerian Formulation of large Deformation Problems in Static and Dynamics', *International journal of Non-linear Mechanics,* Vol. 18, pp 21-35, 1983

[3.7] M.S. Gadala, 'Recent Trends in ALE Formulation and Its Applications in Solid Mechanics', Computer methods in applied mechanics and Engineering, Vol. 193, pp 4247-4275, 004

[3.8] LS-DYNA Theoretical Manual, Livermore Software Technology Corporation, Livermore, California, May, 1998

[3.9] ABAQUS Theoretical Manual, Version 6.6-1, ABAQUS, Inc., Providence, USA, 2006

[2.10] B. Van Leer, 'Towards the Ultimate Conservative Difference Scheme IV. A New Approach to Numerical Convection', *Journal of Computational Physics*, Vol. 23, pp 276-299, 1977

[3.11] R. Haber, M.S. Shepard, J.F. Abel, R.H. Gallagher, D.P. Greenberg, 'A general two-dimensional, graphical finite element pre-processor utilizing discrete transfinite mappings', *International Journal for Numerical Methods in Engineering*, Vol. 17, pp 1015-1044, 1981

[3.12] Gianni Comini, Stefano Del Giudice, Carlo Nonino, 'Finite Element Analysis in Heat Transfer', *Taylor & Francis*, Washington, DC, 1994

[3.13] ANSYS 10.0 Documentation, ANSYS Inc., Theory Reference, Heat Flow, 2005

[3.14] A. J. M. Spencer, *Continuum Mechanics*, Dover publications, New York, 2003

[3.15] R.H.Wagoner and J.-L. Chenot, *Fundamentals of Metal Forming*, Wiley, New York,1997.

[3.16] http://hyperphysics.phy-astr.gsu.edu/hbase/conser.html#engfun

[3.17] R.H.Wagoner and J.-L. Chenot, *Metal Forming Analysis*, Cambridge University Press, 2001.

[3.18] ABAQUS Analysis Manual, Version 6.6-1, ABAQUS, Inc., Providence, USA, 2006

[3.19] Clausius, Rudolf , "On the Application of the Theorem of the Equivalence of Transformations to Interior Work." Communicated to the Naturforschende Gesellschaft of Zurich, Jan. 27th, 1862; published in the Vierteljahrschrift of this Society, vol. vii. P. 48; in Poggendorff's Annalen, May 1862, vol. cxvi. p. 73; in the Philosophical Magazine, S. 4. vol. xxiv. pp. 81, 201; and in the Journal des Mathematiques of Paris, S. 2. vol. vii. pp 209.

[3.20] T.Z. Blazynski, *Plasticity and modern metal-forming technology*, Elsevier Applied Science, 1989

Chapter 4

Simplified Thermo-mechanical Modelling of Friction Stir Welding

4.1 Introduction

The simplified thermo-mechanical Friction Stir Welding (FSW) models aim to predict the transient temperature and stress evolution in the welding process, particularly the residual stress. Common to the simplified FSW models is the use of an estimated non-mechanical heat source; for example, surface heat flux and volume heat generation. These heat sources are applied as external loads to the model. In a conventional FSW process, the heat is produced by interactions between the tool and workpiece and there is no other direct external heat input into the plates, except in some special purpose welding processes such as laser assisted FSW. Therefore, the simplified models are not coupled-field models and consequently are not used to investigate the fundamental mechanisms related to the welding formation process. The temperature distribution affects the mechanical deformation of the structure but the mechanical results have no effect on the thermal analysis. In reality, part of the heat generated in FSW comes from plastic dissipation energy in the plates and the temperature field is strongly coupled with the stress field.

Two methods can be used to solve the thermo-mechanical problem, the *direct method* and *sequential method.* The *direct method* usually requires only one analysis by using a coupled-field element type which contains the necessary degrees of freedom, temperature and displacement. This is advantageous to use when the analysis exhibits a high degree of nonlinear interaction, but there may be a large number of iterations between the different physical fields until the specified level of convergence is achieved. The *sequential method* involves at least two sequential analyses, each of which deals with a different field. As the different field analyses are independent of each other this method is more efficient and hence used in present study.

4.2 Model Description

All simplified models were created in ANSYS Version 10.0 [4.1]. In a sequential thermal-stress analysis, a nonlinear transient thermal analysis is performed first, and then the nodal temperatures from any load step or time point in the thermal analysis are read in and applied as loads for the subsequent stress analysis.

4.2.1 Heat Transfer Model

In FSW, the amount of heat input and output to the system is not yet well understood. A substantial effort is usually needed to determine how much heat flows into the tool and how much to the plates. This is highly dependent on the changing friction coefficient, downward force, temperature and the tribology conditions of the contacting surfaces [4.2]. For simplified models, it is essential to know this and to apply the corresponding heat input to the FE model. The inverse method determines heat input conditions by varying estimated values. The best match with measured temperatures is used in the model. Here the torque approach is implemented in the model. The heat input is correlated with experimental torque results measured from the rotating spindle, eliminating part of the matching process.

The total weld power is the product of toque and angular velocity:

$$P_{av} = M_{toq}\omega \tag{4.1}$$

The process efficiency is defined as the percentage of the average power input into the workpiece in the total weld power,

$$P_w = \eta_{FSW} P_{av} \tag{4.2}$$

It is assumed that a uniform contact pressure exists at the interface between the shoulder and the workpiece and all the heat generated comes from friction. Hence heat flux is linearly distributed in the radial direction and in proportion to the distance from the tool.

$$q_s(r) = \frac{3P_{ws}r}{2\pi\left(R_{shoulder}^3 - R_{pin}^3\right)} \quad for \quad R_{pin} \le r \le R_{shoulder} \tag{4.3}$$

The heat generated by tool pin is applied to the FE model in the format of nodal volumetric heat generation rate. The whole FSW process including plunge, dwell, traverse, pull out and cooling stages are modeled. The ratio of the heat generated from shoulder and tool pin at the steady state welding condition is estimated using Equations 2.23-2.25 in Chapter 2, regardless of the contact condition.

$$f_{shoulder/pin} = \frac{\left(R_{shoulder}^3 - R_{pin}^3\right)\left(1 + \tan\alpha_s\right)}{R_{pin}^2\left(R_{pin} + 3H_{pin}\right)} \tag{4.4}$$

In the plunge period, no heat flux is applied to the shoulder-workpiece surface until the end of this stage. The nodal volumetric heat generate rate is calculated by dividing the tool pin's heat contribution by its volume, mathematically expressed as

$$q_{pin} = \frac{P_w}{\pi R_{pin}^2 H_{pin}\left(1 + f_{shoulder/pin}\right)} \tag{4.5}$$

The number of nodes generating heat increases proportionally with plunge speed. During the dwell stage, both the surface heat flux and nodal volumetric heat generation are applied to the model. After a specified time the heat source then moves along the joint line. When the tool comes to the end of the traverse stage, the surface heat load is deleted and the number of nodes generating heat starts to decrease. As there is no force applied at the interface and no heat will be generated during the pull out period, all heat sources become zero. A flow chart of applied heat source is shown in Figure 4.1 for the entire welding process. An algorithm was created using the ANSYS APDL Macro language to incorporate this flow chart into the model input file.

The heat transfer model uses the 3-D solid element SOLID70, which has eight nodes each with a single temperature degree of freedom, as shown in Figure 4.2.

The boundary conditions for thermal analysis are illustrated in Figure 4.3. Convection boundary conditions with film coefficient h_l are specified for workpiece surfaces which are exposed to the air. The radiation heat transfer of the surfaces is lumped into the convection, as it is reportedly small [4.2]. The conduction heat exchange between the bottom surface of the workpiece and the backing plate is simplified by using a larger convective coefficient. This is due to the lack of gap conductivity data and the difficulty to obtain an accurate value. The gap conductance is highly dependent on the welding conditions, such as material, contact pressure and temperature. Thus the complexity of gap conductance is circumvented by assigning a convection boundary condition.

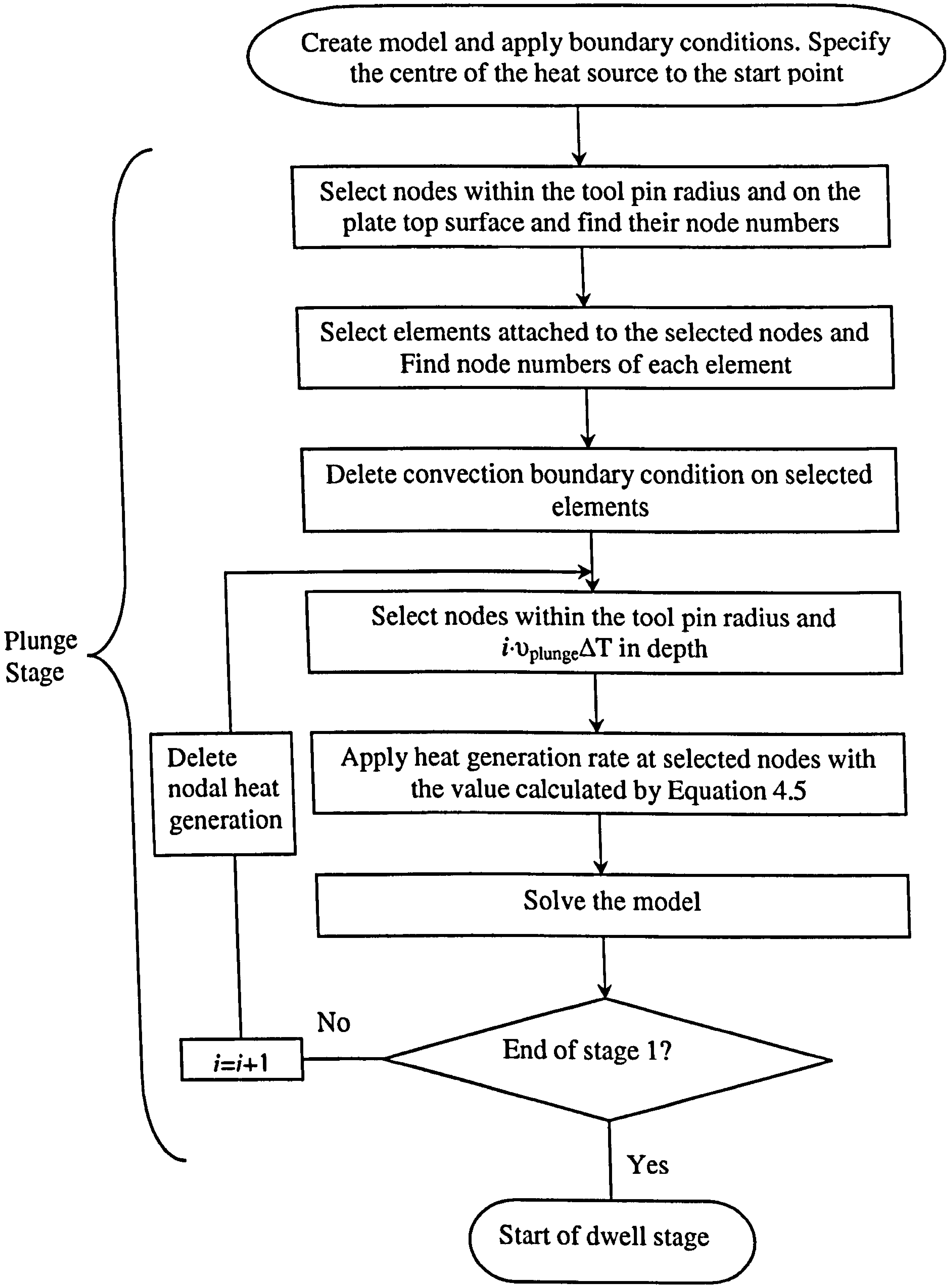

Figure 4.1 (a) the FE model flow chart of the plunge stage.

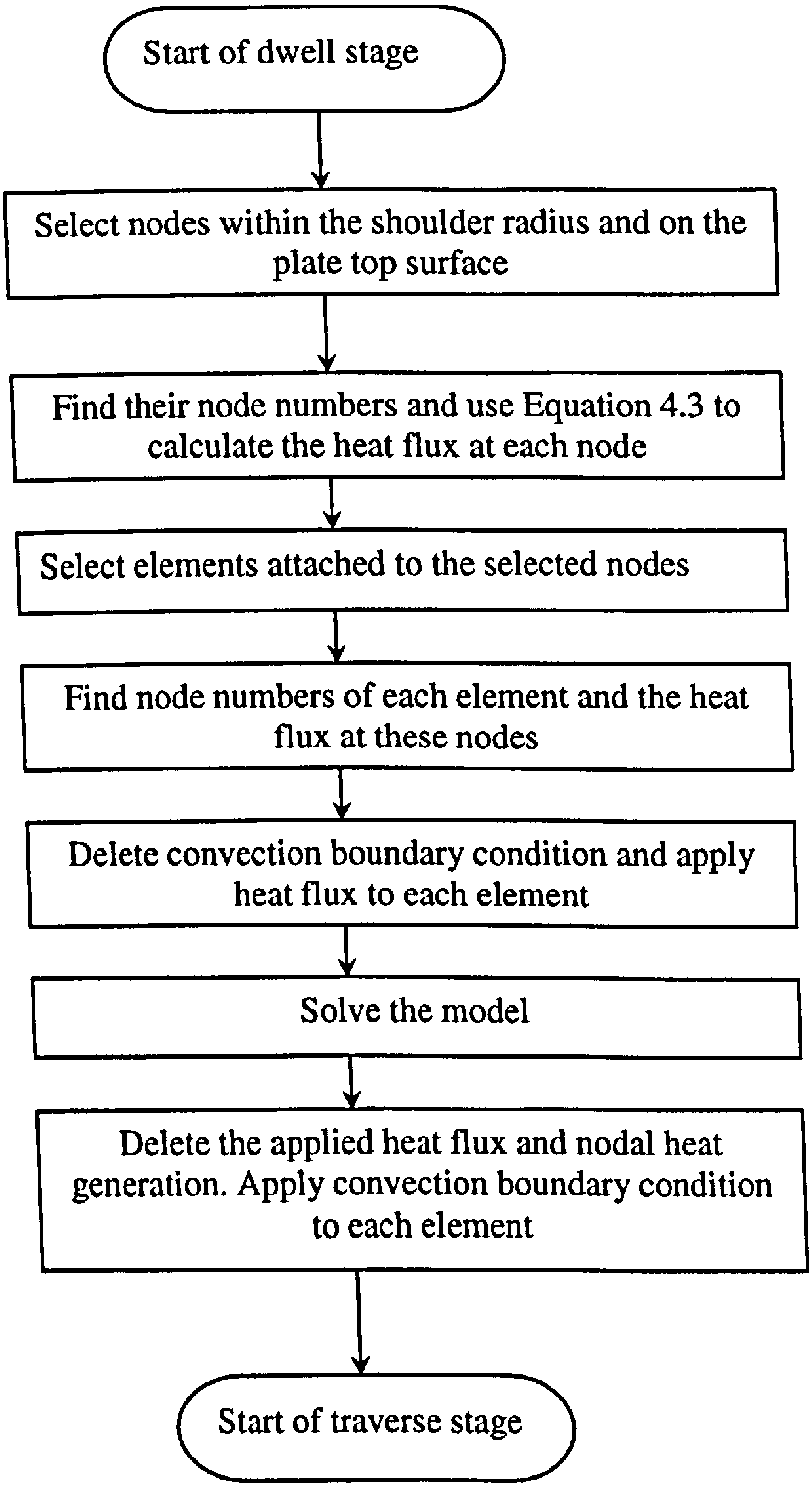

Figure 4.1 (b) the FE model flow chart of the dwell stage.

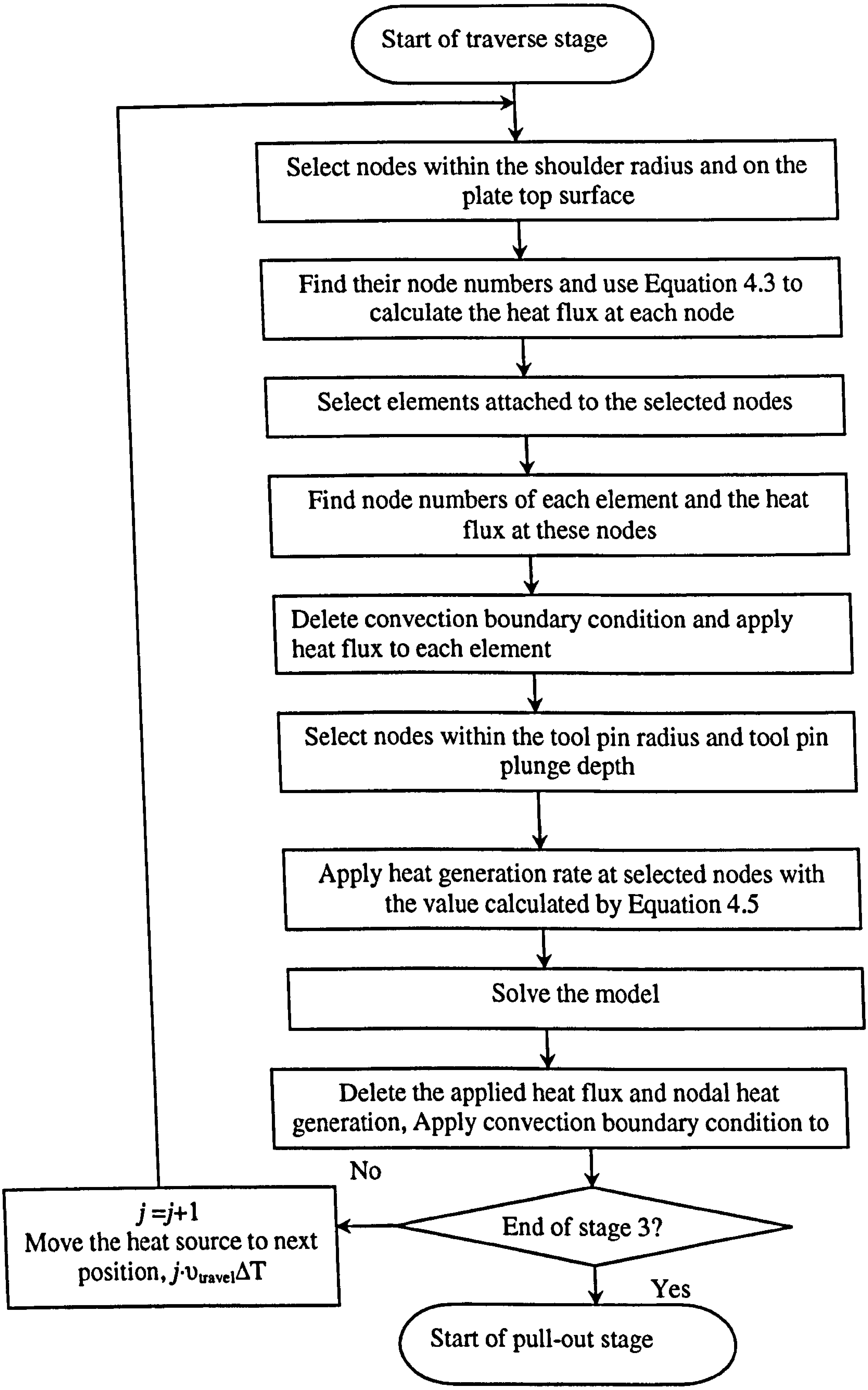

Figure 4.1 (c) the FE model flow chart of the traverse stage.

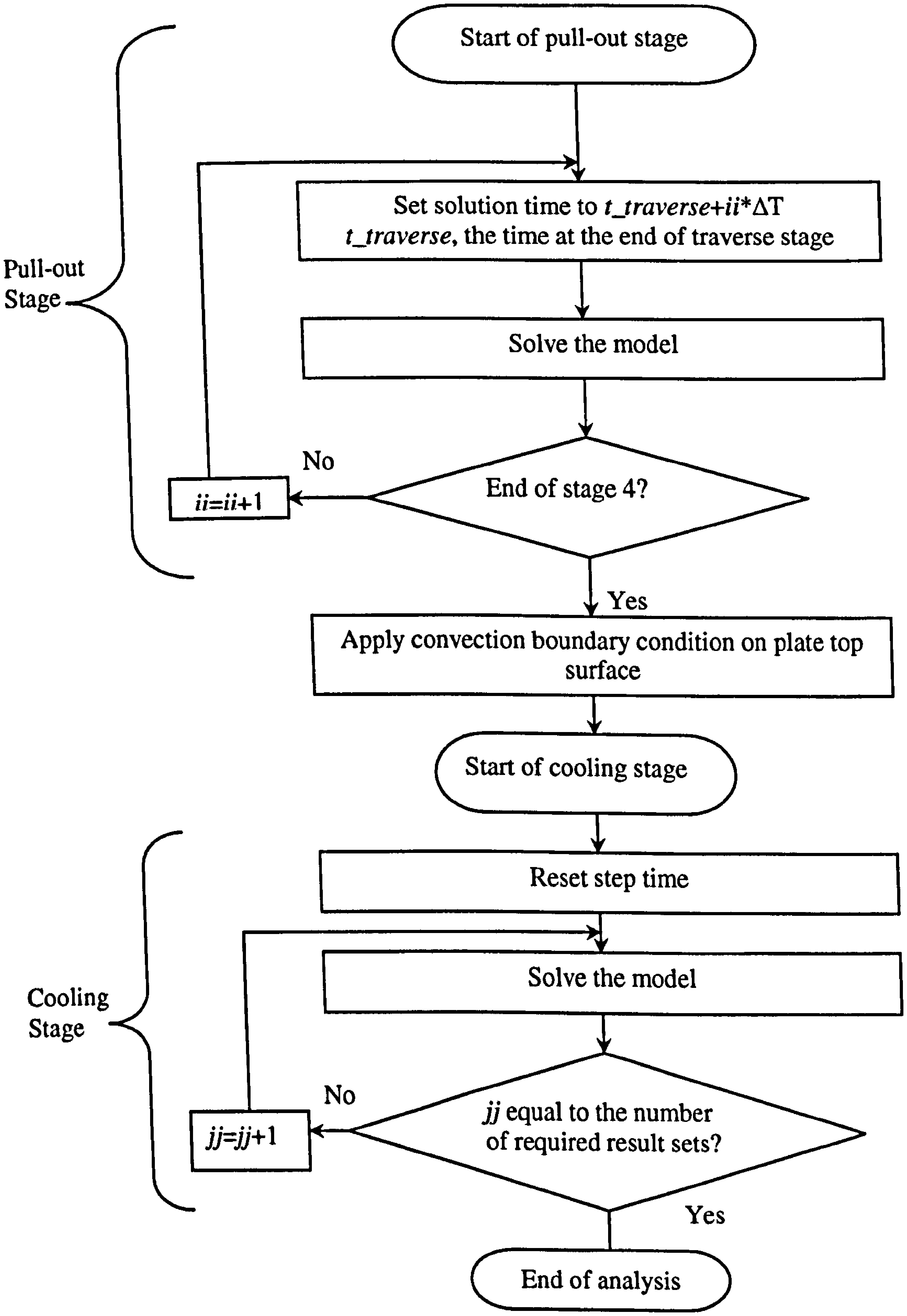

Figure 4.1 (d) the FE model flow chart of the pull-out and cooling stages.

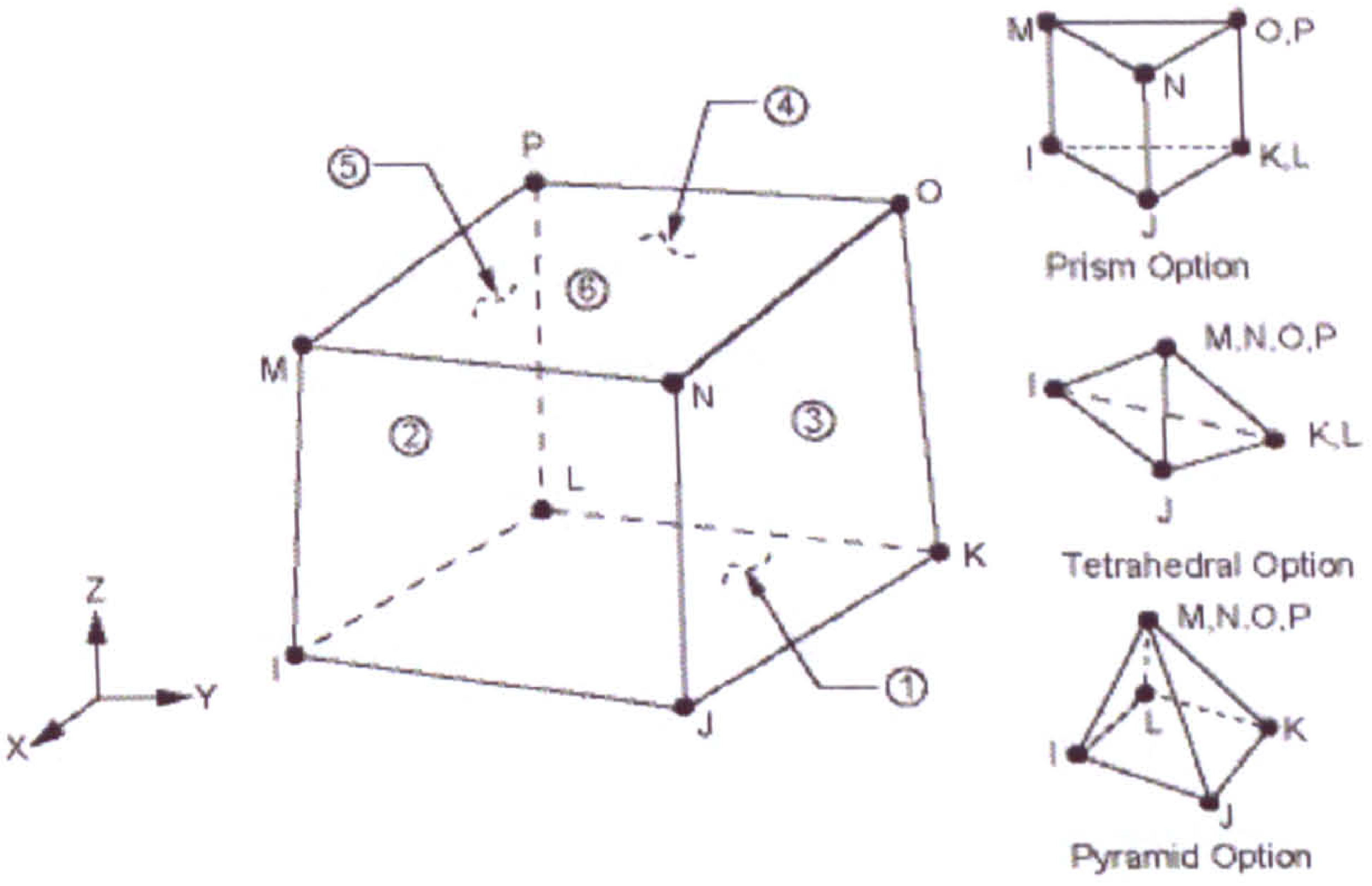

Figure 4.2 Solid70 element geometry and its deteriorated formats [4.1].

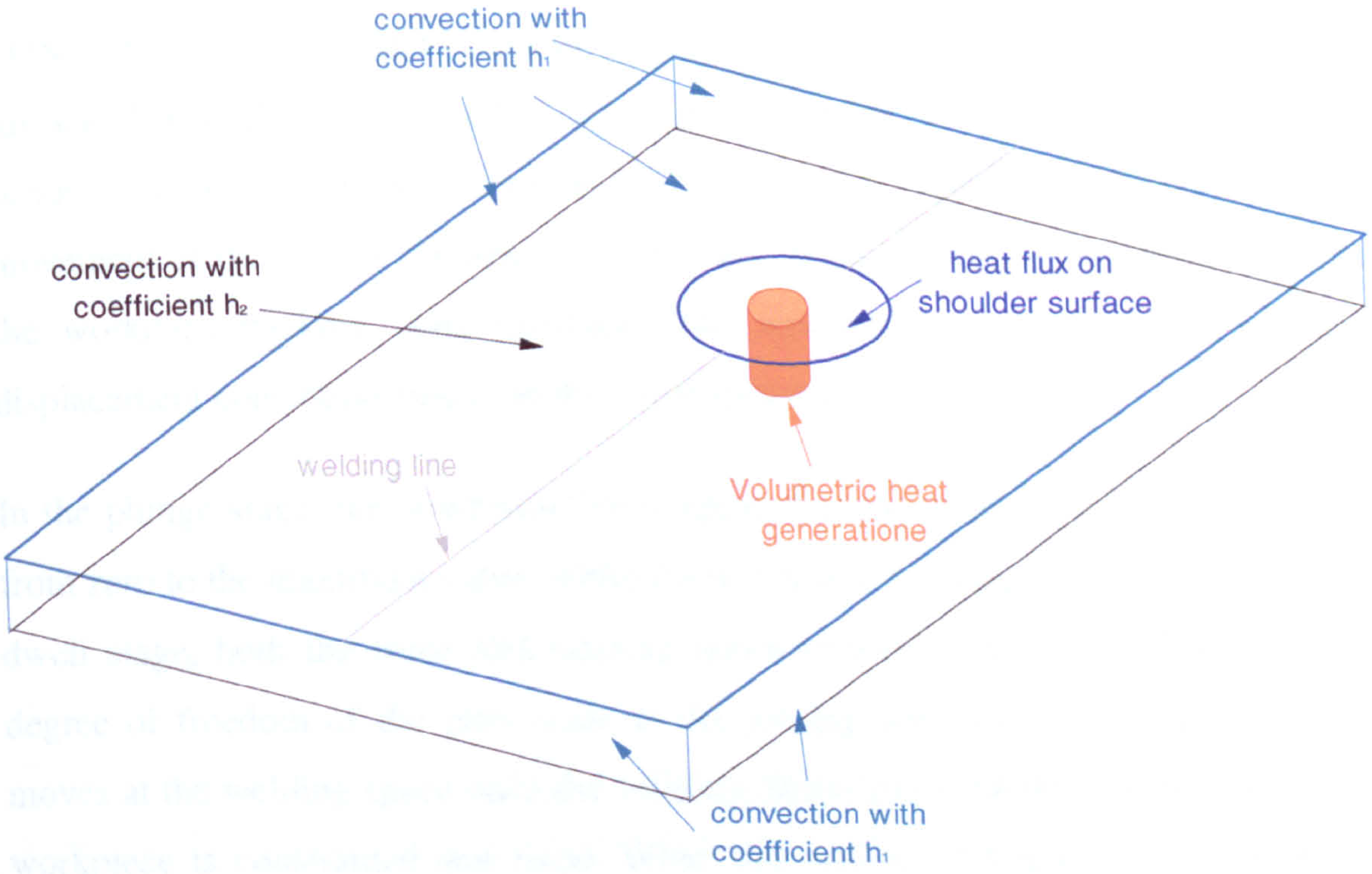

Figure 4.3 Thermal boundary conditions for the simplified FSW Models.

4.2.2 Mechanical Model

The thermal model is converted to a mechanical model for subsequently thermo-mechanical analysis by changing the element type to SOLID45 while maintaining the same mesh and load step size. After the completion of thermal analysis, the temperature results are imported to the mechanical model. Thus the thermal strain and thermal stress are produced in the workpiece, causing deformation and distortion of the plates.

The elastic-perfect plastic material model was adopted to characterise the stress-strain relationship. The material plastic deformation is assumed to obey the von Mises yield criterion and associated flow rule. Like the temperature dependent conductivity and specific heat used in thermal model, the temperature dependence of the material yield strength is incorporated in the mechanical model.

To simulate the mechanical action of the tool on the workpiece, including friction and downward force, a contact pair is established, with the contact-target elements CONTA173 and TARGET170 used on the workpiece top surface and tool bottom surface. The tool was assumed to be cylindrical without the pin and the tool bottom surface circular, with the radius $R_{shoulder}$. A pilot node is created to control the movement of the Target Elements, i.e. the tool. Similar contact pairs are constructed at the workpiece-backing plate interface. The workpiece is clamped by applying the displacement constraints based on the experimental setup.

In the plunge stage, the downward force applied to the pilot node of the tool increases from zero to the maximum value, while the tool keeps rotating at a constant speed. In the dwell stage, both the force and rotating speed remains unchanged. The displacement degree of freedom of the pilot node in the joining direction is activated and the tool moves at the welding speed once the welding phase starts. During the whole process the workpiece is constrained and fixed. When the tool has covered the specified welding distance, the contact pair at the tool-workpiece interface separates as the tool is lifted and pulled out from the workpiece. The rotation of the tool then has no effect on the workpiece, so the rotating speed can be set to zero at the start of the pull out phase. It should be noted that the same step size as in the thermal model mush be used in the mechanical model.

4.3 AISI 1018 Steel

4.3.1 Material Properties

The welding behaviour of plates of AISI 1018 steel is considered in this section. The tool material is a molybdenum and tungsten based alloy. AISI 1018 is a low-carbon mild steel which can easily welded by most welding processes. The chemical composition of AISI 1018 is given in Table 4.1. The temperature varying thermal and mechanical material properties are presented in Table 4.2. The rest of material properties used in the model are tabulated in Table 4.3. Temperature dependent Young's modulus, E, will have a great impact on the results, but limited to weld zone with high temperature. In current model a constant E is used for the whole workpiece.

Table 4.1 Composition of AISI 1018 steel [4.3].

% C	% Mn	% P	% S	% Si
0.18	0.82	0.011	0.006	< 0.01

As the FSW is a solid state welding technique, no melting occurs during the process (as shown by the numerical results presented below), therefore no enthalpy values are required in the model.

4.3.2 Model Specifications

The FE model employs the welding parameters and welding conditions used in the experimental work of [4.3], which allows the comparison of numerical results and measured temperature data. Each plate to be butt welded has a length of 20.3 cm, a width of 10.1 cm and a thickness of 6.35 mm. The tool shoulder radius is 9.5 mm, the pin radius is 3.95 mm and the height of the pin is 6.22 mm. the tool plunge speed can be calculated by dividing the pin height by 178 second, the total time of the first stage. The tool rotating and travelling velocities are set to 450 rpm and 0.42 mm/s, respectively.

Table 4.2 The temperature dependent material properties of AISI 1018 steel [4.4] [4.5].

Temperature (°C)	Thermal conductivity (Watt/m°K)	Specific heat (J/Kg°K)	Yield stress (MPa)
25	52	480	386
100	51.5	490	
150	50.5	500	
200	49.5	515	300
250	48	530	
300	47	550	270
400	42	600	250
500	38	670	200
600	34	750	110
700	31	800	50
750	29	840	
800	26.5	900	30
850	26	970	
900	26.5	1050	15

Table 4.3 The temperature independent material properties of AISI 1018 steel [4.6].

Young's Modulus (GPa)	Poisson's Ratio	Thermal Expansion coefficient (10^{-6}/K)	Density (Kg/m^3)
200	0.29	12.2	7870

The friction coefficient between the tungsten and the 1018 steel is considered to be temperature dependent but limited data is available in the literature. Based on the previous work of friction welding of steel bars [4.7] [4.8], the friction coefficient was calculated using the relative velocity which increases linearly from zero at the axis of the tool to the maximum at the periphery of the shoulder. A form of μ is suggested by [4.7] [4.9] as follows:

$$\mu = \mu_0 \exp(-\lambda_\mu \delta \omega r) \tag{4.6}$$

where δ is the percentage sticking and r is the radial distance from the tool axis. In Nandan's work [4.5], a value of 0.4 was used for μ_0 and 1 s/m for λ_μ. Plots of friction coefficient and fractional slip variations with r are shown in Figure 4.4. In practice however, it was found very difficult to apply the varying friction coefficient. Hence a constant value of 0.4 was used. This assumption is believed to be reasonable for simplified models, as the heat is not directly generated by the friction. Actually the frictional force has significant *indirect* effect on the global deformation of the workpiece; it affects heat generation, temperature, thermal stress and consequently deformation.

The total heat input was calculated by torque method. The experimentally measured torque data is given in Figure 4.5. The total time of stage one is 178 seconds and at the 175th second the tool shoulder contacted the top surface of the workpiece. After 175 seconds there is a sharp increase in both force and torque curves, then decreases to a relatively steady average value. During the welding period, the average axial force and average torque are 18.7 kN and 55 Nm, respectively. The torque and force history data used in FE model is idealized and illustrated in Figure 4.6.

To determine the heat input to the workpiece in the FE model, i.e. the process efficiency, an analytical expression of the ratio of the heat flowing into workpiece to that into the tool [4.10] is given as,

$$\frac{P_w}{P_T}=\sqrt{\frac{k_w\rho_w C_w}{k_T\rho_T C_T}} \tag{4.7}$$

where the subscripts w and T represent the workpiece and the tool, respectively.

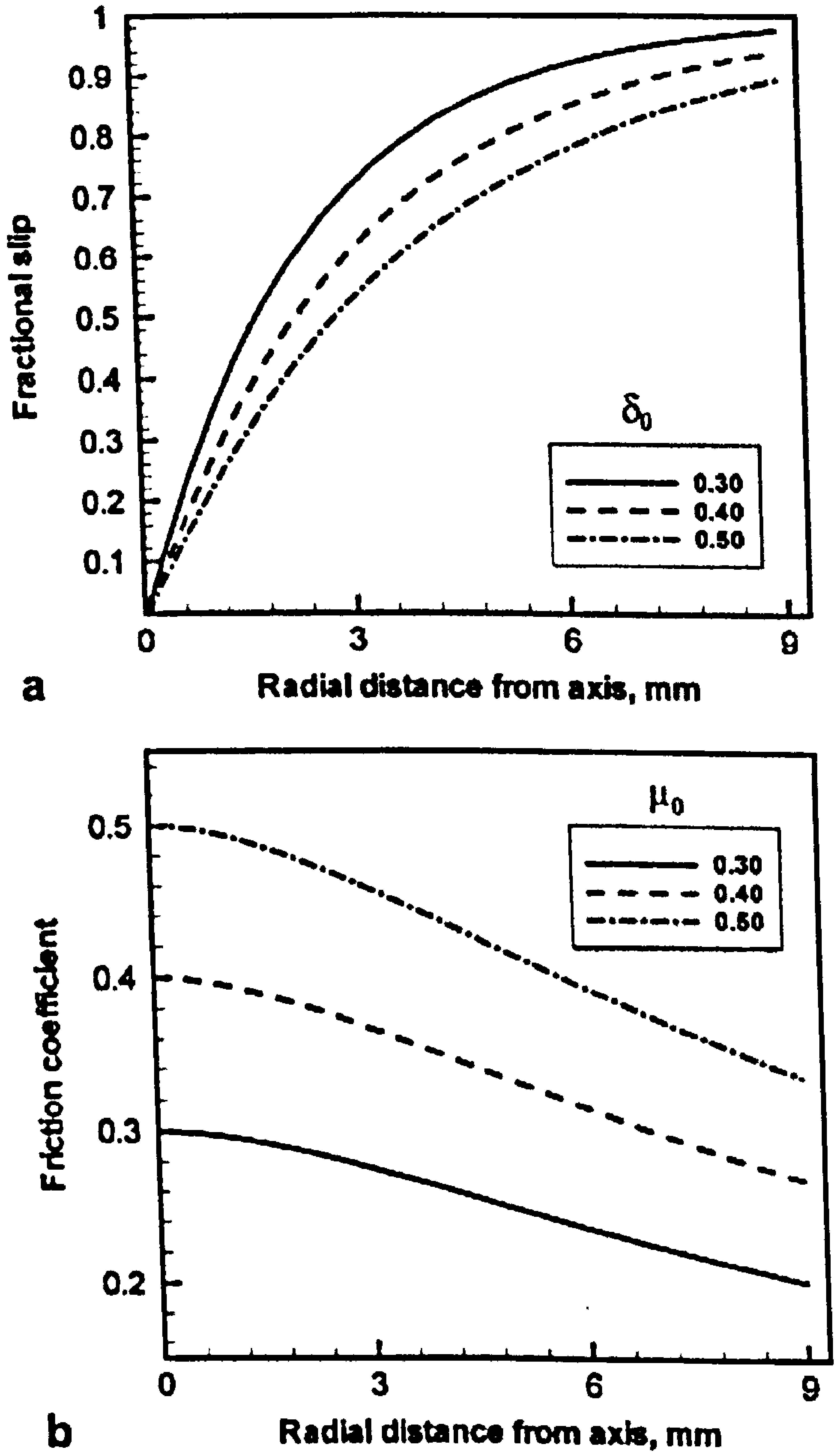

Figure 4.4 Variations of (a) fractional slip (δ) and (b) friction coefficient (μ) with radial distance from the tool axis for different scaling constants. For (b), δ_0 was fixed at 0.40. Rotational speed was 450 rpm. [4.5].

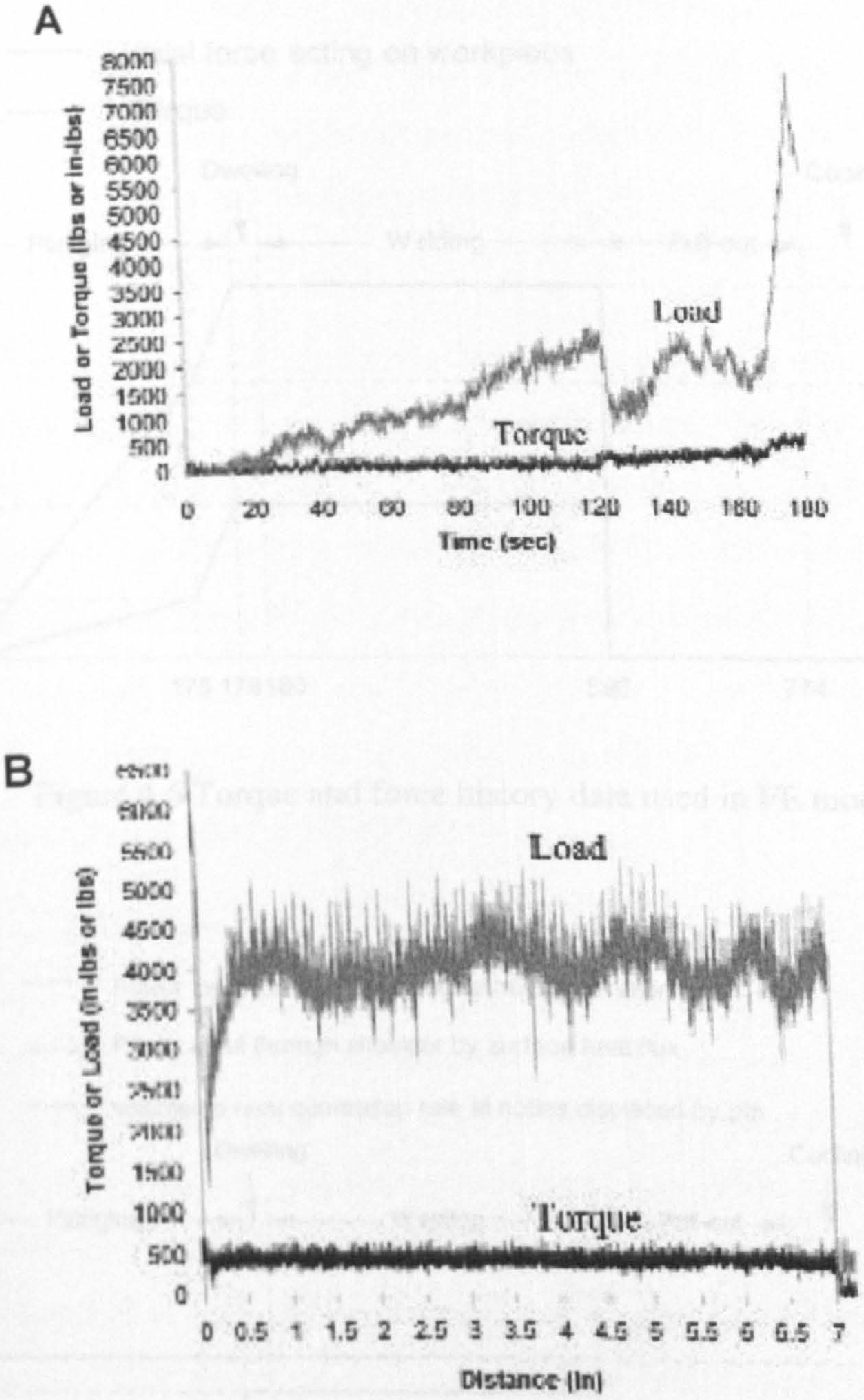

Figure 4.5 experimentally measured axial load and torque cures during (A) plunging stage and (B) welding stage [4.3].

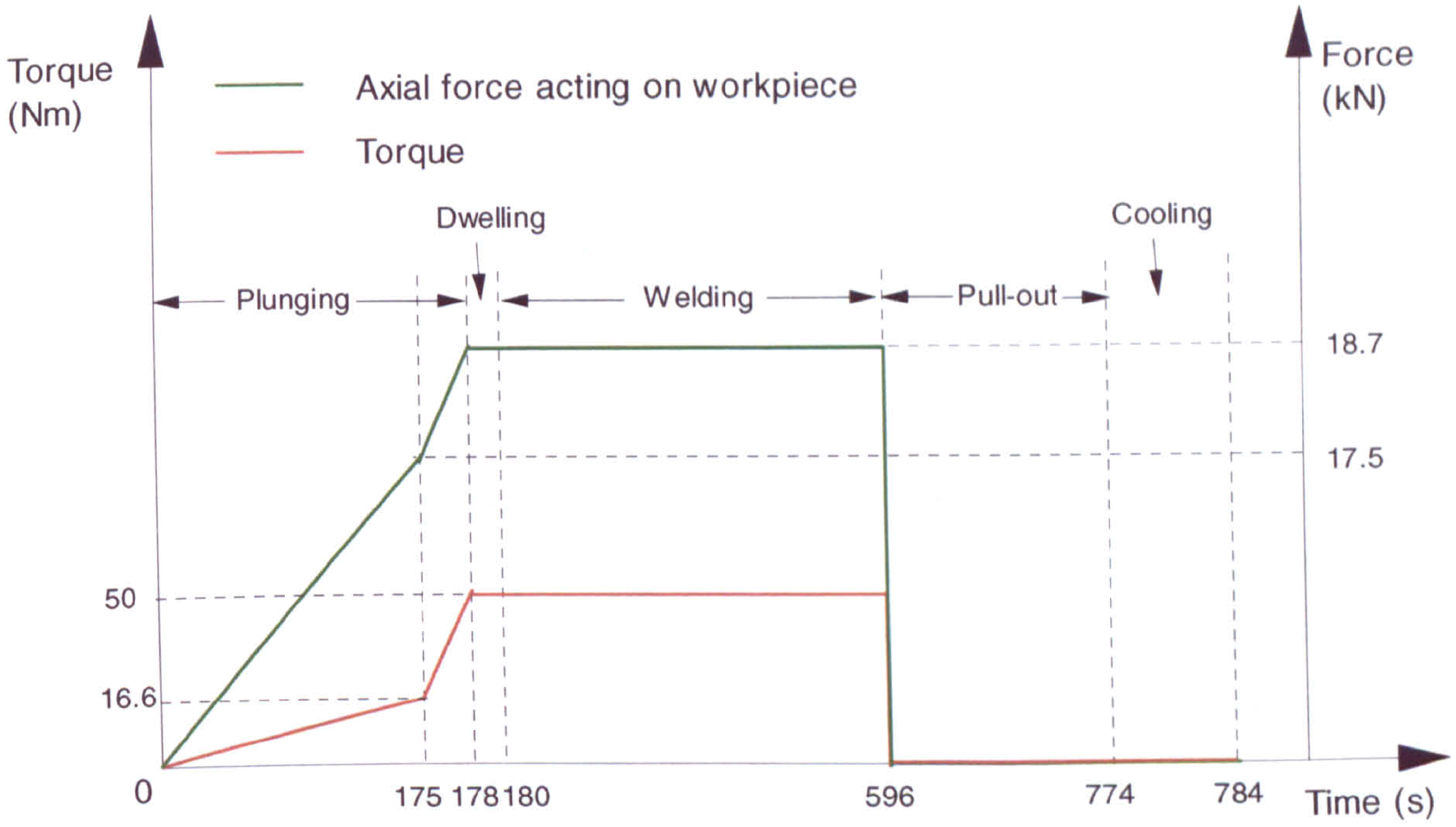

Figure 4.6 Torque and force history data used in FE model.

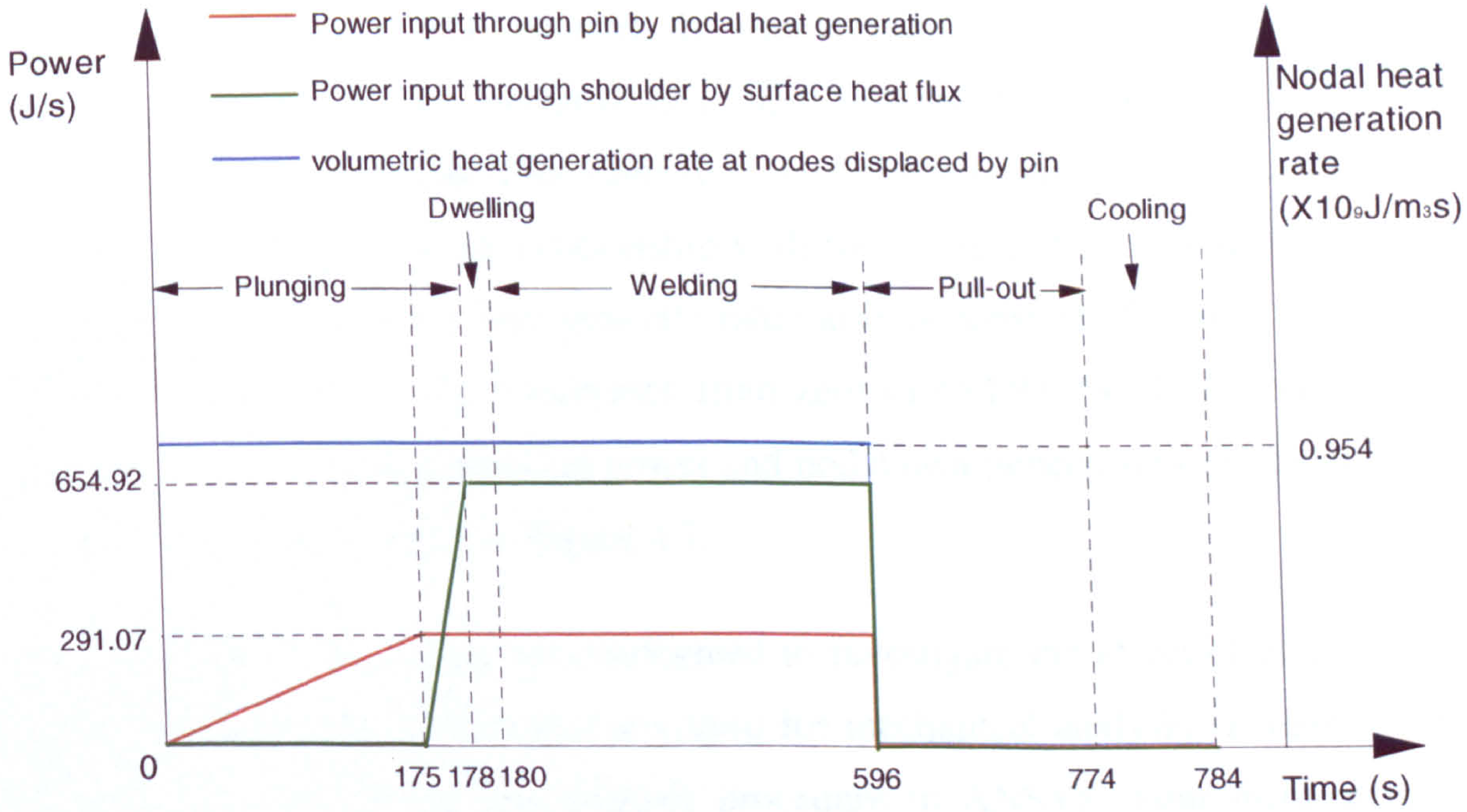

Figure 4.7 Power input model and nodal heat generation rate applied to the FE model.

The conductivity of the tool is about four times higher than AISI 1018. The tool density is 19400 kg/m^3, around two and a half times greater. The ratio is about 0.75 using the specific heat at 750 °C. Thus, 36.5% of the total heat flows into workpiece. In Zhu's work [4.11], about 44% of the total mechanical energy output from the machine was transformed to heat the workpiece.

Based on the current tool geometry, using the Equation 4.4 the ratio of heat partition between the tool shoulder and the tool pin is 2.25 during the dwelling and welding stages. With the rotation speed, 450 rpm and the measured average toque, 55 Nm, the total power generated is 2591.8 *J*/s, of which 946 *J*/s flows into workpiece: 654.92 *J*/s through the shoulder and 291.07 *J*/s through the pin. Substituting q_{ws}=654.92 *J*/s into Equation 4.3 leads to the heat flux value at the nodes on the shoulder-workpiece interface and substituting q_w =946 *J*/s into Equation 4.5 gives rise to the nodal volumetric heat generate rate 0.954E+09 *J*/m^{3}s.

In the first part of the plunge, 0 - 125 s, and pull out stages, no surface heat flux was applied as there is no contact between the shoulder and the workpiece. The volumetric heat generation is the only format of heat input into the workpiece. The total power is proportional to the time and at the same time the volume (number of nodes) displaced by the tool pin also has a linear relationship with time, due to the constant plunge speed. Thus the nodal volumetric heat generate rate value is constant. The heat input into the shoulder during 125 – 128 s increases from zero to 654.92 *J*/s. The surface heat flux power, volumetric heat generation power and nodal heat generation rate are summarized for the whole FSW process in Figure 4.7.

A mesh study of the model was performed to investigate the effect of element size on the thermal analysis. Same mesh was used for mechanical analysis, as required by the sequential thermo-mechanical analysis procedure in ANSYS. Four different sizes of element in the region close to the tool (nugget and thermo-mechanical affected zone) were considered: 1mm, 1.5 mm, 2 mm and 3mm. Variation of peak temperatures at two points (one on top surface and the other on the middle plane) with the element size is plotted in Figure 4.8. When the size reduces from 3 mm to 1 mm the peak temperature tends to approach a steady state. It was also found that the number of elements across the plate thickness did not affect the results for the case where the element size was fixed to 2 mm in the working plane and in the thickness direction the element number increased from three to six. It was therefore decided to use the model with the element size of 1.5 mm in the region close to the tool and a coarser mesh in the region remote from the tool. The model is shown in Figure 4.9.

In the thermal analysis, a total of 32010 nodes and 17688 8-noded brick thermal elements were used in the model, replaced by 8-noded brick mechanical elements in subsequent mechanical analysis. 8182 CONTA173 elements and 1396 TARGET170 elements were used to simulate the contact behavior among tool shoulder, workpiece and backing plate.

All the surfaces exposed to the air were subjected to the same convective boundary conditions. The ambient temperature for the welding system was set at 25 °C. A normal heat transfer convection coefficient of a mild steel, $h = 30$ W/m^2 °C to ambient air was employed in the model [4.12]. As it was not clear what kind of material was used for backing plate and what kind of contact condition existed at the interface, the exact heat conductance value was uncertain. Here a constant convective heat transfer coefficient of 250 W/m^2 °C was adopted using inverse engineering analysis method.

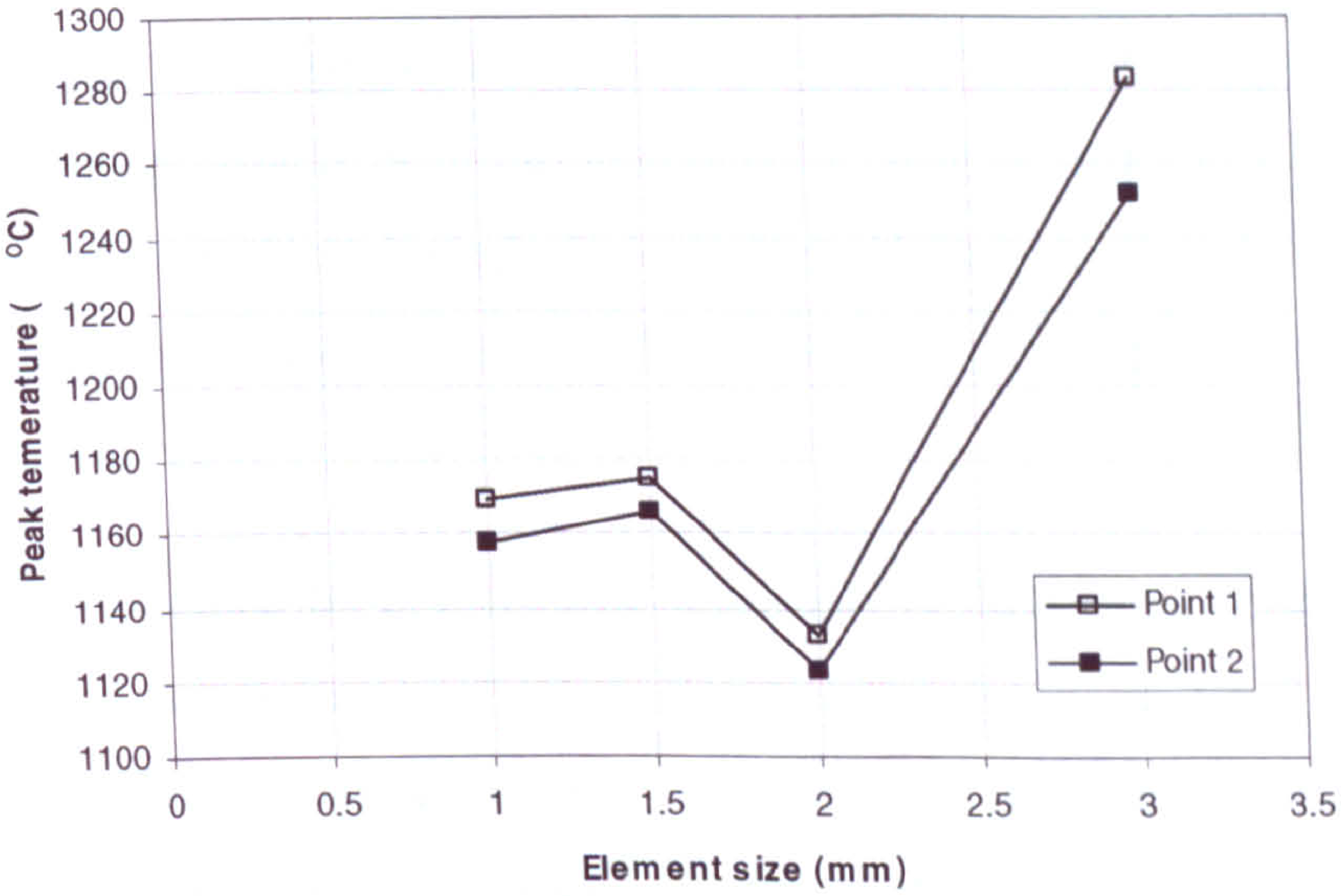

Figure 4.8 Mesh size study of the model for AISI 1018 Steel.

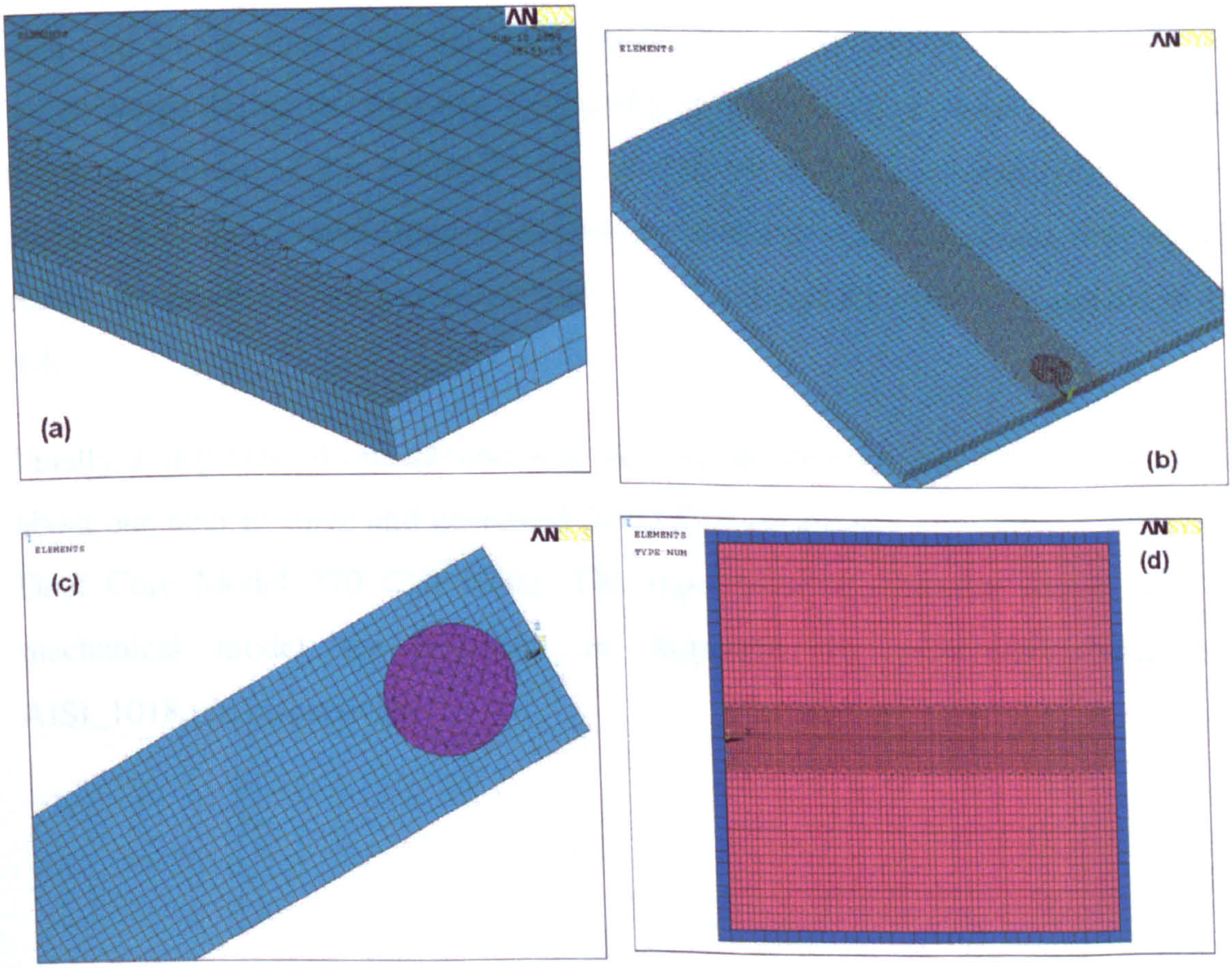

Figure 4.9 Simplified AISI1018 model (a) a half plate mesh view, (b) whole FE model, (c) workpiece-tool contact pair, (d) backing plate-workpiece contact pair.

The color contour plots of the thermal loads applied to the FE model at four characteristic time points are shown in Figure 4.10 (a-d). Each of the figures represents a time point in the plunge, dwell, welding and pull-out stages. In Figure 4.10 (b) and (c), both heat flux and volumetric heat generation are applied to the model: the left part of the contour legend corresponds to surface flux value and the right-hand side stands for nodal heat generation rate.

Time step size was decided by considering the total welding time, model convergence, size of database and computing cost (CPU time). A long process time, 784s, has to be simulated in the model. As there are two contact pairs involved in the analysis, it is required that the step time should be small enough (normally less than 0.1s) to make the solution converge. If a time step of 0.5s used, the estimation of results file size is about 196 GB and CPU time around 40 days, although only the basic results at the last set of each step was written to the database. There is also a possibility that the solution may not converge during the analysis. This problem is discussed in detail in Section 4.4. As the main purpose of this example is to validate the heat source model used in thermal analysis and as measured stress values are not available for comparison, only the thermal results are presented and discussed here. The mechanical model is evaluated in Section 4.4.

Finally a step size of one second was used in the thermal analysis. The analysis took about one hour to solve and generated 8.5 G files on a computer with 2 x AMD Operton Dual Core Model 270 (2.0 GHz). The input files for thermal model and thermo-mechanical model are provided in Appendix A, AISI_1018_thermal.txt and AISI_1018.txt, respectively.

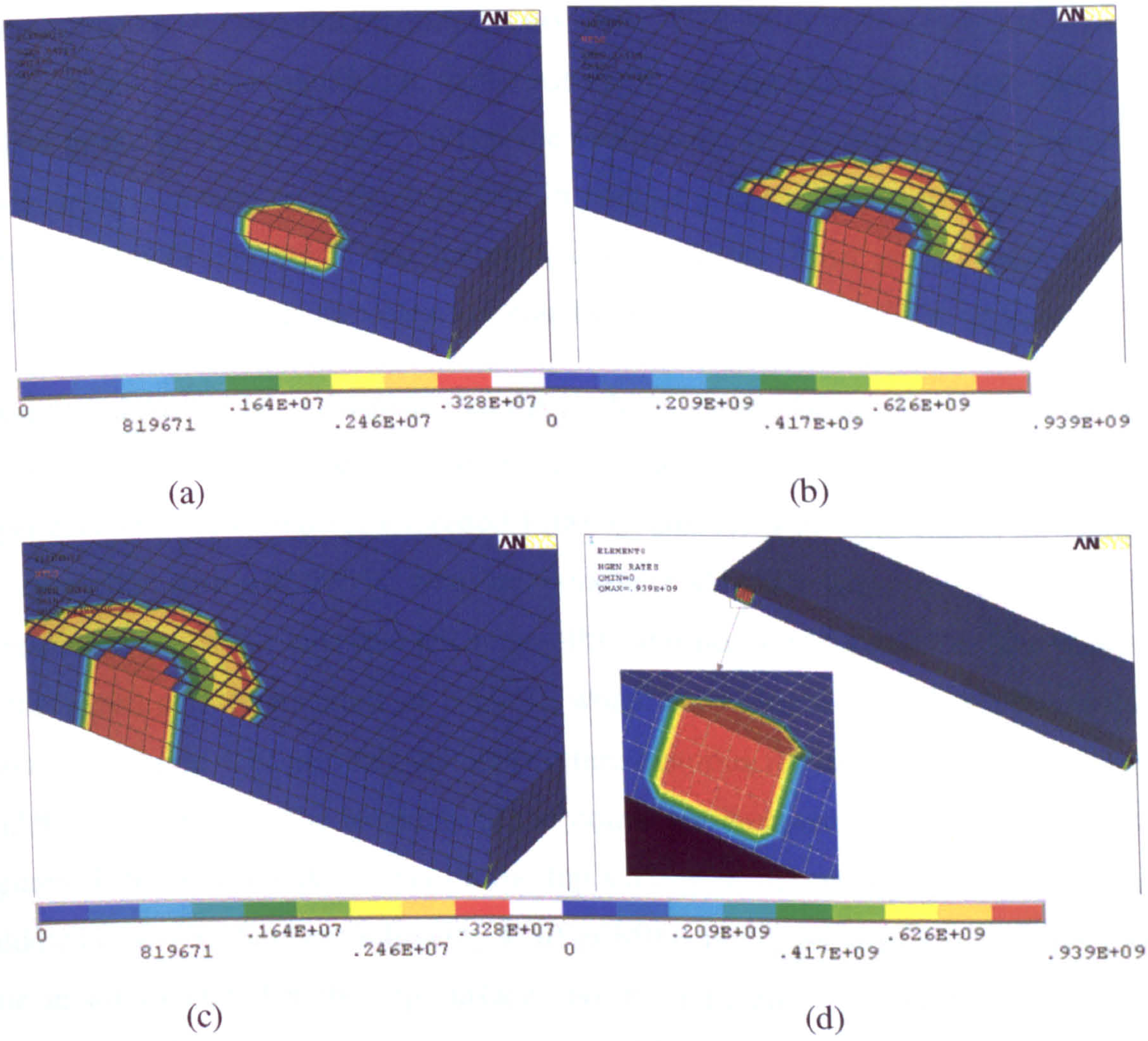

(a) (b) (c) (d)

Figure 4.10 Thermal loads at four characteristic time points (a) 80 s, (b) 180 s, (c) 220 s, (d) 600 s.

4.3.3 Thermal Results and Comparison with Experimental Work

The calculated temperature profile on top surface is compared with experimental results in Figure 4.11. The experimental data was measured by thermocouples located at 12.7 mm from the welding line on both retreating and advancing sides. It was recorded that peak temperatures were between 590 °C and 650 °C and it was observed that the temperature distribution was relatively symmetric about the peak temperature point [4.3]. A good match between the calculated and the measured curves was found, indicating that the current FE model is able to predict the evolution of thermal results in the welding process. A large discrepancy occurs after 300 s, with the cooling rate higher in the FE model. This is mainly due to the assumed constant heat convection coefficient applied in the numerical model. When the tool passes the thermocouples, the contact conductance decreases with the reduction in contact pressure at the workpiece-backing interface immediately below the thermocouple positions. Thus greater heat loss was predicted, with an unchanged contact conductance, than in the true FSW process.

It was found during the experiment that the flashing around the perimeter of the shoulder glowed with a reddish-orange color. This indicates that the peak temperature experienced by the workpiece exceeded 1100 °C. But the peak temperature measured by the infrared system was 990 °C near the workpiece-shoulder interface. Measurement of temperature inside the interface not impossible and hence not available. The numerical results give a peak temperature of 1060 °C, which is reasonable but slightly lower than it should be. Figure 4.12 presents the temperature histories for eight selected points on the middle-length plane. The locations of the points are demonstrated in the legend of the figures. TOP indicates the points on the top surface of the workpiece and MID on the middle layer. The numbers following TOP or MID signify the distance from the joining line in mini-meter. On the top surface shown in Figure 4.12 (a), there was no big difference in the peak temperature, around 1000 °C, for points whose distances from the welding line are within 6 mm (pin's radius, 3.95mm). For other locations the peak temperature gradually decreased with the increase in distance from the welding line as illustrated in Figure 4.12 (b).

The evolution of the temperature during the entire process for the whole model was also extracted from the results database. The video clips were saved in the file AISI_1018_temp.avi, Appendix A in the CD attached to this thesis. Here colored contour plots at ten characteristic time points are given in Figure 4.13. For clarity, only one plate is shown. The time point for each contour plot can be found in the annotation at the left-top corner of the picture. It should be noted that the maximum value of the legend in each plot is different.

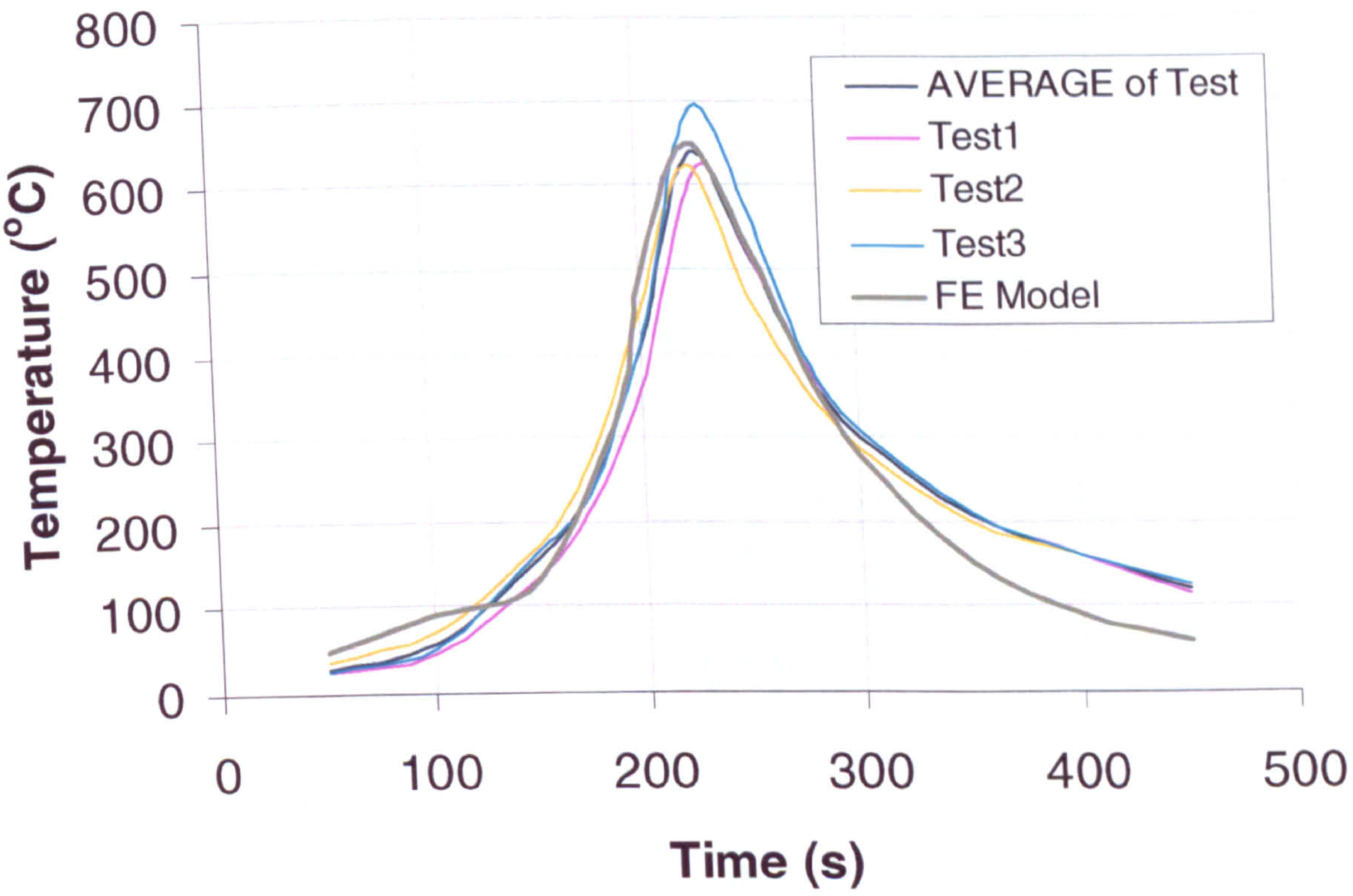

Figure 4.11 Comparison of the numerical and the measured temperature histories at a point 12.7 mm from the joining line, 450 rpm, 25.2 mm/min, AISI 1018 Model.

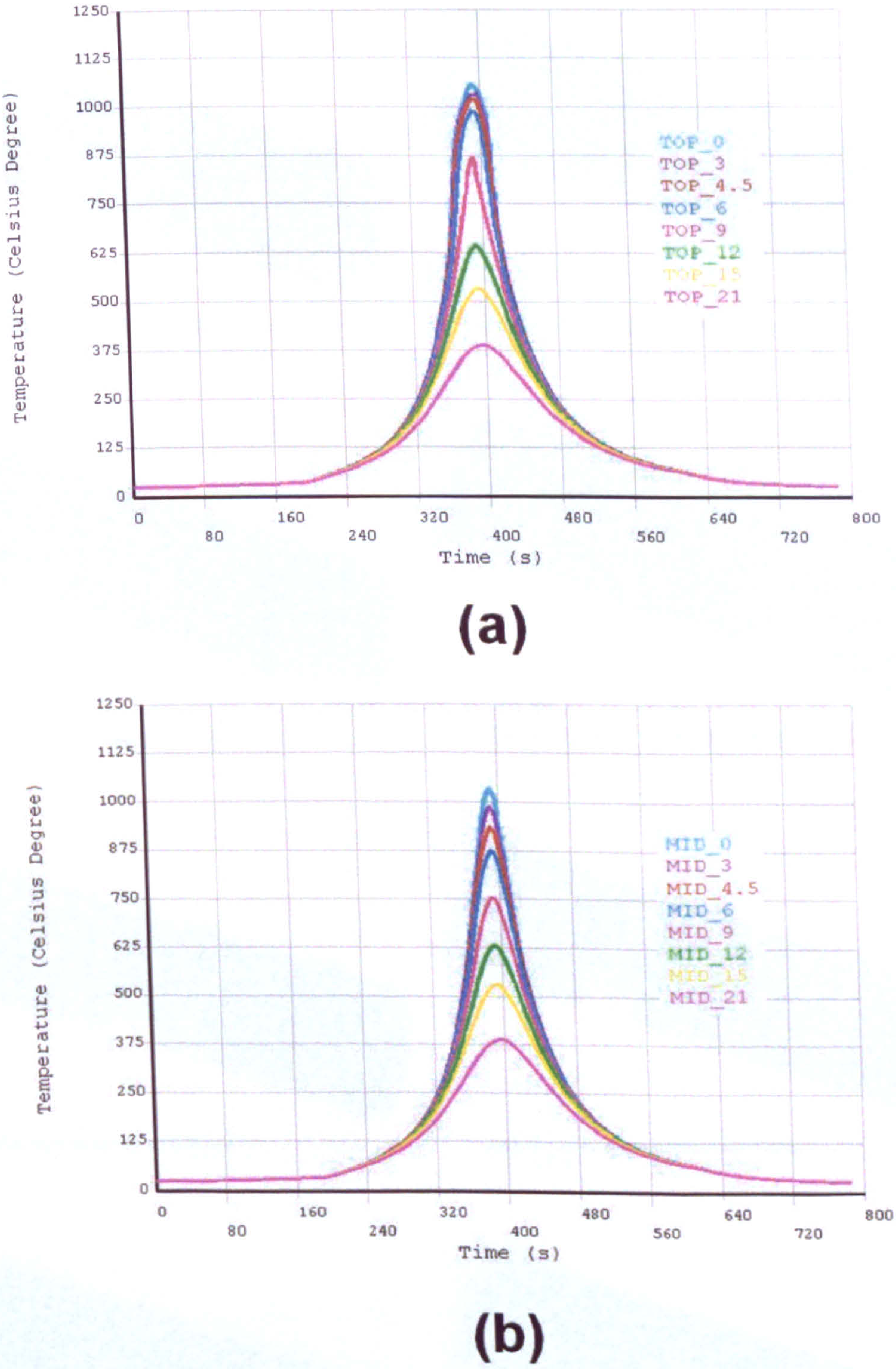

Figure 4.12 Temperature profiles of the points at middle-length plane (a) on top surface, (b) on middle layer of the plates, AISI 1018 Model.

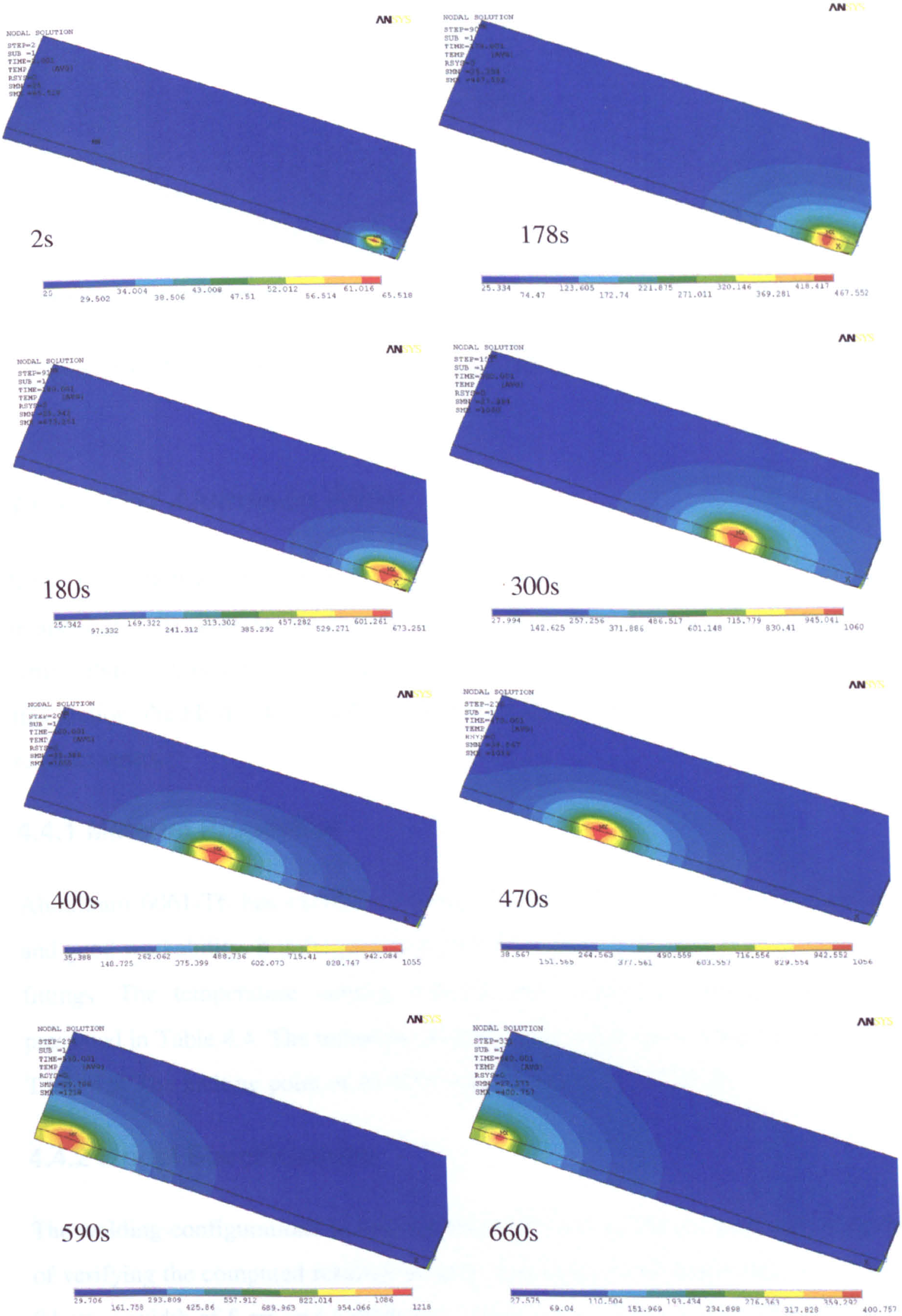
2s
25
29.502
34.004
38.506
43.008
47.51
52.012
56.514
61.016
65.518
178s
25.334
74.47
123.605
172.74
221.875
271.011
320.146
369.281
418.417
467.552
180s
25.342
97.332
169.322
241.312
313.302
385.292
457.282
529.271
601.261
673.251
300s
27.994
142.625
257.256
371.886
486.517
601.148
715.779
830.41
945.041
1060
400s
35.388
148.725
262.062
375.399
488.736
602.073
715.41
828.747
942.084
1055
470s
38.567
151.565
264.563
377.561
490.559
603.557
716.554
829.554
942.552
1056
590s
29.706
161.758
293.809
425.86
557.912
689.963
822.014
954.066
1086
1218
660s
27.575
69.04
110.504
151.969
193.434
234.898
276.363
317.828
359.292
400.757

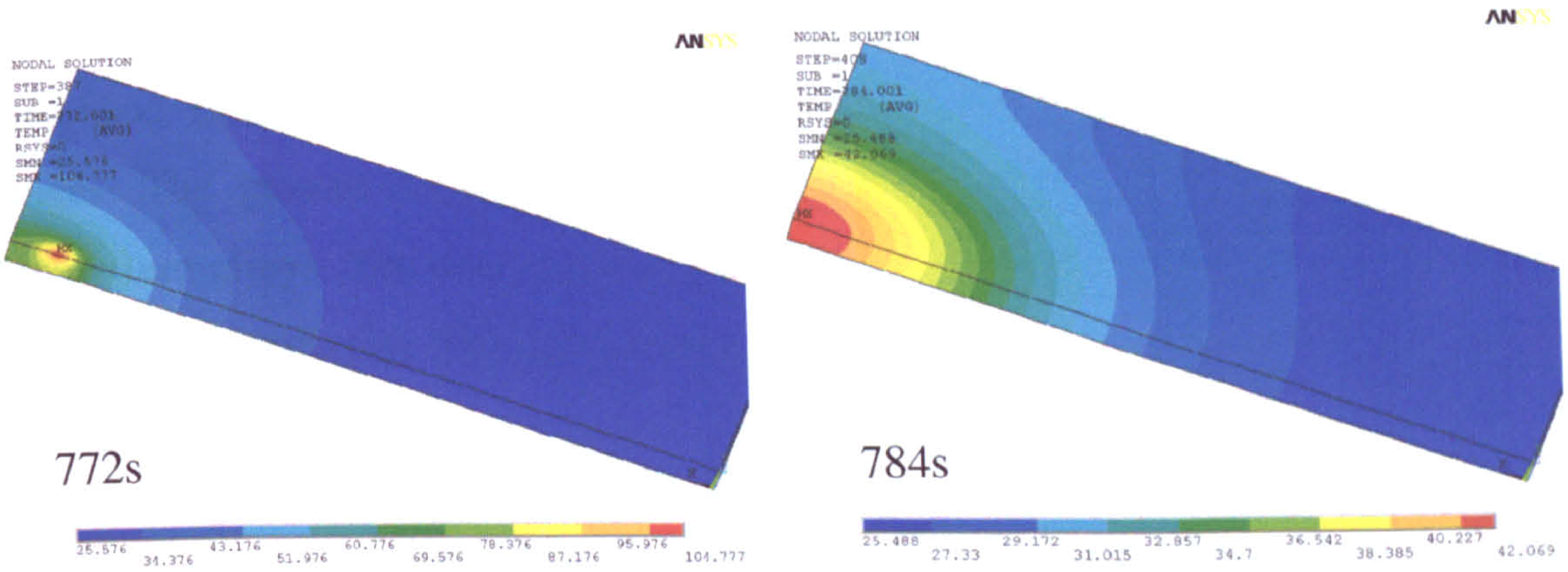

Figure 4.13 Temperature contour plots at ten characteristic time points, AISI 1018 Model.

4.4 Al 6061 Aluminum Alloy

It has been shown in section 4.3 that the proposed FE model was able to predict the temperature distribution developed during the welding process. The calculated temperature results have a good agreement with the experimentally measured values. In this section, the FE model is further assessed by comparing the calculated and measured residual stress.

4.4.1 Material Properties

Aluminum 6061-T6 has excellent joining characteristics with relatively high strength and good workability. It is frequently used in aerospace industry, particularly for aircraft fittings. The temperature varying thermal and mechanical material properties are presented in Table 4.4. The remaining material properties used in the model are given in Table 4.5. The melting point of Al 6061 is in the range 582–652 °C.

4.4.2 Model Specifications

The welding configurations in the experimental work [4.20] are used here with the aim of verifying the computed residual stresses. Each plate to be butt welded has a length of 24 cm, a width of 5 cm and a thickness of 6mm. The tool shoulder radius is 12 mm and the pin radius is 3 mm. The height of the pin was not given in the paper; a value of 6 mm was used. Chen et al. [4.20] did not provide any information on the plunge and dwell stages. The present model assumes a plunge speed of 0.2 mm/s, usually used for aluminium alloys. The tool rotating and travelling velocities are set to 500 rpm and 140 mm/min, respectively. The same element types and element size as the AISI 1918 Steel model were used.

Table 4.4

The temperature dependent material properties of 6061-T6.

Temperature (°C)	Specific heat (J/Kg°K) [17]	Yield stress (MPa) [18]
0	910	280
40	950	275
125	1000	270
225	1050	220
325	1100	70
425	1150	20
575	1270	0
645	1310	0

Table 4.5

The temperature independent material properties of Al 6061 [4.19].

Young's Modulus (GPa)	Poisson's Ratio	Thermal Expansion coefficient (10^{-6}/K)	Thermal conductivity (Watt/m°K)	Density (Kg/m^3)
68.9	0.33	25	167	2700

As the power input (measured torque data) to the welding system, required by the proposed model in section 4.2.1, is unknown, it was decided to adopt an inverse engineering approach to determine heat input quantities. The estimated heat flux value was adjusted to match with the measured temperature curves. The best fit was then employed in the model. This expedient method is believed to be reasonable, given that the main purpose is to compare the predicted residual stresses with experimental ones.

Based on current tool geometry, using Equation 4.4, the ratio of heat partition between the tool shoulder and the tool pin is 8.7 during the dwelling and welding stages. After several trials, a total heat input of 2134 J into the workpiece was chosen. 220 J was applied through nodal volumetric heat generation and 1914 J through surface heat flux. Figure 4.14 shows both predicted and measured temperature histories at the location 10 mm to the weld centerline and 1.6 mm below the top surface of the plate. An excellent match between the two curves was obtained. The stress analysis was then carried out with the temperature results from the thermal analysis.

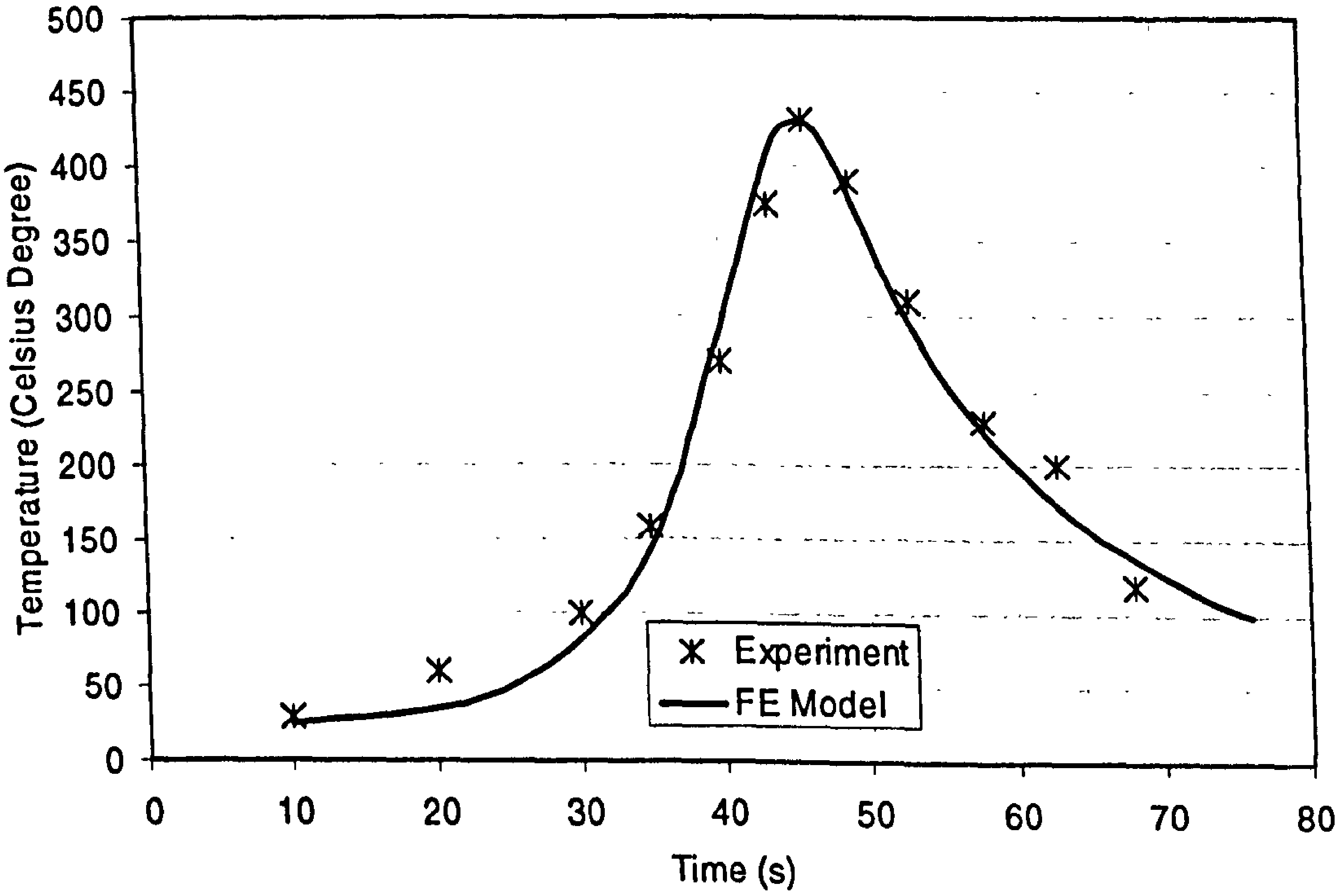

Figure 4.14 Comparison of the numerical and the measured temperature histories at a point 10 mm from the joining line and 1.6mm below the top surface, Al 6061.

4.4.3 Stress Analysis

As stated in section 4.3, there is a possibility that the solution may not converge during the analysis as a result of the incorporated two contact pairs. This problem was encountered here, especially in dwell and traverse states. Figure 4.15 (b, c) shows the deformed mesh and corresponding stress distribution at a time in the plunge stage. A displacement scale factor of 200 was used to amplify the deformed plate shape, but it had no effect on the rigid tool and backing plate. The greatest deformation occurred at the plate where the heat flux and nodal volumetric heat generation were applied. This was caused by the high temperature and temperature gradient at this region, as thermal strain is directly linked to the temperature changes. The reason that the solution was not converged mainly came from the large local deformation and abrupt separation of contacting elements. One of the typical errors was "`Contact element 10053 (real ID 3) status changes abruptly from no-contact -> contact (with target element 9374)`".

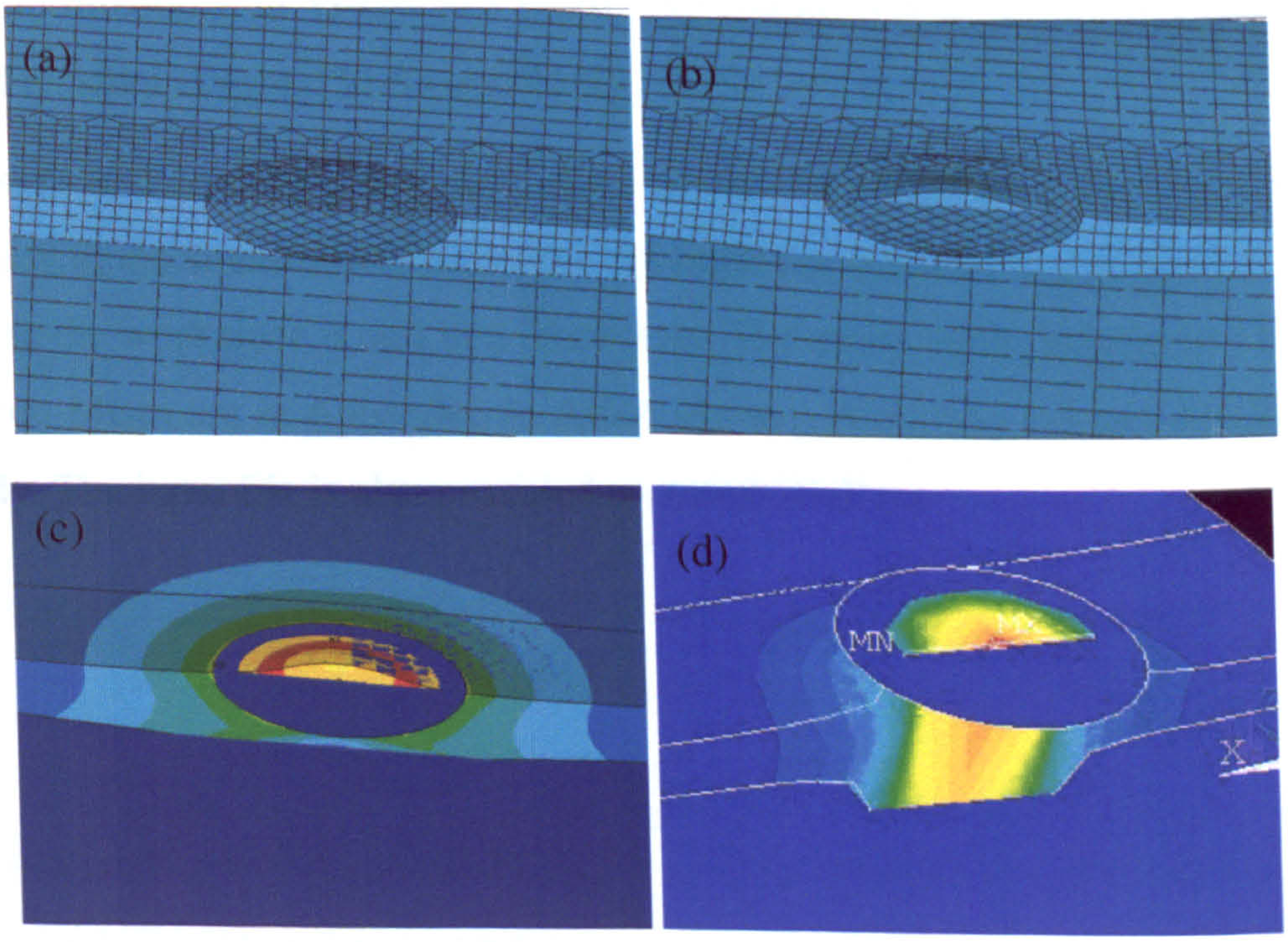

Figure 4.15 Mesh and stress plot for simplified Al 6061 model (a) undeformed mesh, (b) deformed mesh, (c) a stress plot during plunging stage and (d) a temperature plot at the dwell stage.

The lack of convergence could be further explained in picture (d) in Figure 4.15, an exaggerated temperature distribution on a deformed plate shape during the dwell stage. The high temperature is concentrated in the workpiece under the tool, causing significant high thermal expansion and deformation. When the applied heat source moves forward along the welding line, the material ahead of the tool will also experience a large deformation and complex residual stress field forms in the material behind the tool. Under such circumstances an error "Sudden change in contact status of an element" is issued. This makes the convergence difficult and finally terminates the analysis.

To avoid this convergence problem, the contact pairs were suppressed in the stress analysis, as the thermal stress accounts for the major part of the total stress built up during the FSW process [4.13]. The same method was also used in [4.11] [4.14]. Moreover, this simplification does not impair the characteristics of the heat input source model used in the thermo-mechanical analysis. However another convergence problem turned up when the fixture was released. The predicted stresses in X (longitudinal) and Z (transverse) directions at 117.2s just before the fixture release were compared with the measured residual stresses, M-Sx and M-Sy, shown in Figure 4.16.

The stresses in Z direction are very close to the measured ones but there is a large discrepancy in the stresses in X direction, although the overall trend is similar. This may be because the workpiece is still in a fixed state. The stress evolutions up to 117.2 for Sx, Sy and von Mises are in Appendix A, Al6061Sx.avi, Al6061Sy.avi and Al6061VM.avi, separately. The input file is also provided as Al6061INP.txt.

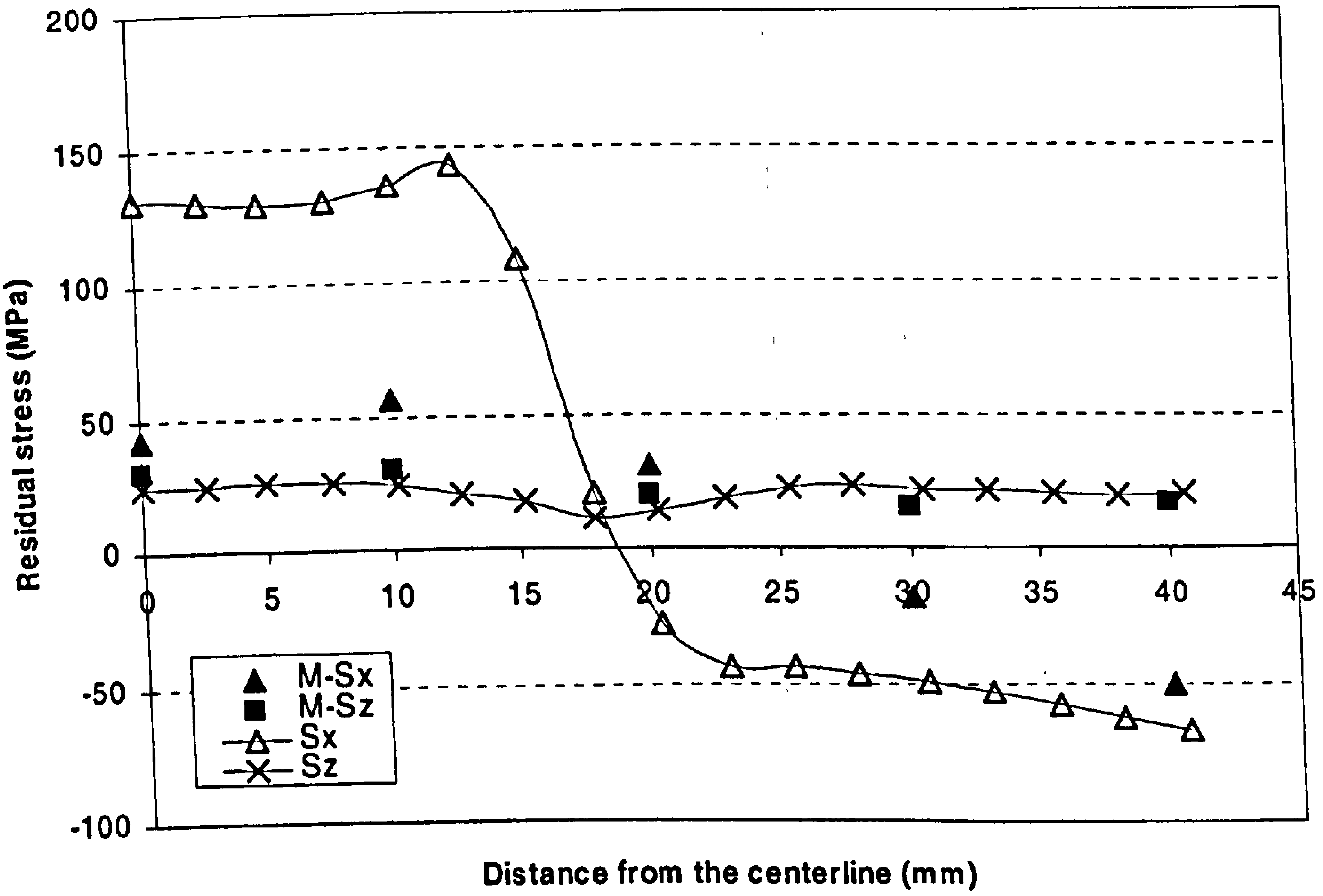

Figure 4.16 Stresses on the top surface and at the mid-plane of the Al6061 workpiece.

4.5 An Adaptive Convective Boundary Condition Algorithm

In the FSW process, a backing plate is required to support the workpiece. A considerable amount of heat is lost through this contact interface. Backing plates with different conductivities can influence the temperature evolution across the workpiece and finally the quality of the weld. A faulty weld may be produced if too much heat is lost to the backing plate [4.15]. Hence it is necessary to consider the heat transfer at the workpiece-backing plate interface.

The predominant mode of heat transfer at the contact interface is contact conduction. Thermal contact conductance is defined as the ratio of heat flux across the joint to the additional temperature drop as a result of the imperfect contact at the interface [4.16]. It is affected by many factors such as contact pressure, interstitial materials, surface roughness and flatness. During FSW, the contact region immediately below the tool has the highest contact pressure, causing the highest contact conductance. In some other parts of the contact surface, a small gap may be created due to lack of clamping, leading to a much smaller contact conductance (also called a gas gap conductance). Therefore, to make the model more robust, the variant non-uniform contact conductance should be taken into account.

In all the previous numerical FSW models in the literature, the conductive heat loss through the backing plate is simulated by applying a large average convective heat transfer coefficient to the bottom surface of the workpiece. Furthermore, most of the models assumed a constant convective coefficient on the whole surface. Only one recently work by Soundararajan et al. [4.13] used a contact pressure dependent heat transfer coefficient. An initial thermo-mechanical analysis with a uniform contact conductance value was performed to determine the stress at the workpiece-backing plate. According to the stress distribution contours, the bottom surface of the workpiece was divided into eight parts, each of which was assigned a constant convective heat transfer coefficient. This thermal boundary condition was then used to predict the thermal history in the workpiece. It should be noted that the determined convective coefficient pattern at the beginning of the analysis was used and kept unchanged through out the subsequent thermal analysis. Due to the different contact conditions at different stages of the process, the unchanged thermal boundary condition is not appropriate.

A new adaptive non-uniform convective boundary condition is proposed here, in which the contact conductance matches the stress distribution and evolves with the development of the contact pressure. At the beginning of the analysis a constant convective value is used to obtain the contact pressure at the contact interface. Then the convective film which is obtained according to the contact pressure at each element is applied to the element surfaces facing the backing plate for the thermo-mechanical analysis at next time increment. At the end of each analysis (time step) the contact pressure is extracted until the end of the welding process. This procedure is simply illustrated in Figure 4.17. The input file, adap.txt, is included in Appendix A.

An example contour plot of convection coefficient applied at the bottom surface of the workpiece is presented in Figure 4.18 (ignore the blue element edge). Figure 4.18 (a) shows the thermal boundary condition at the beginning of traverse stage and (b) when the tool moves to about half length of the plate. The contact conductance data, i.e. the relationship between the contact pressure /contact gap and heat transfer coefficient, was recruited from Rohsenow et al. [4.21]. A significant discrepancy in convection coefficient was predicted. Contact gap existed in the blue-colored region and a much lower convection coefficient value was applied to it.

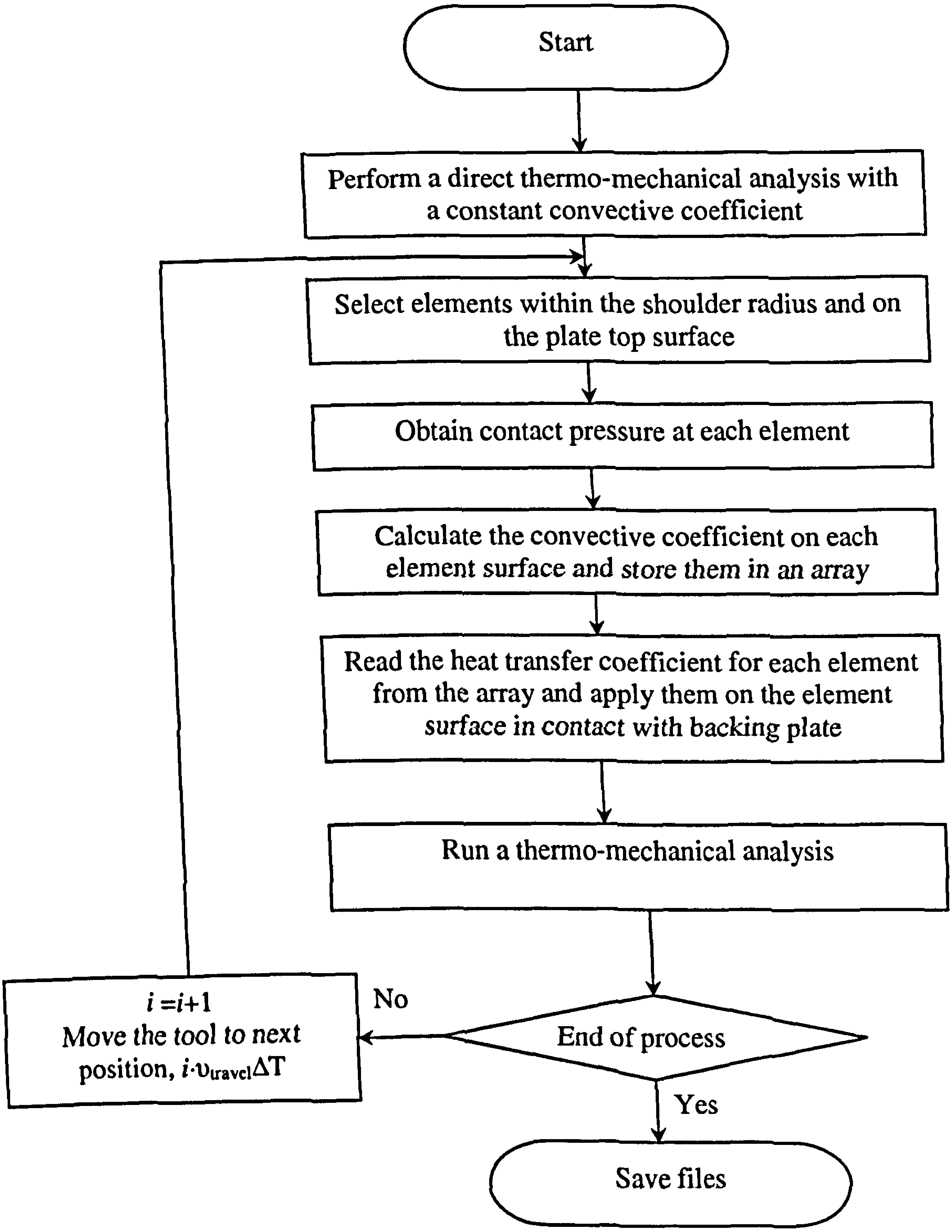

Figure 4.17 an adaptive convective boundary condition algorithm for bottom surface of the workpiece.

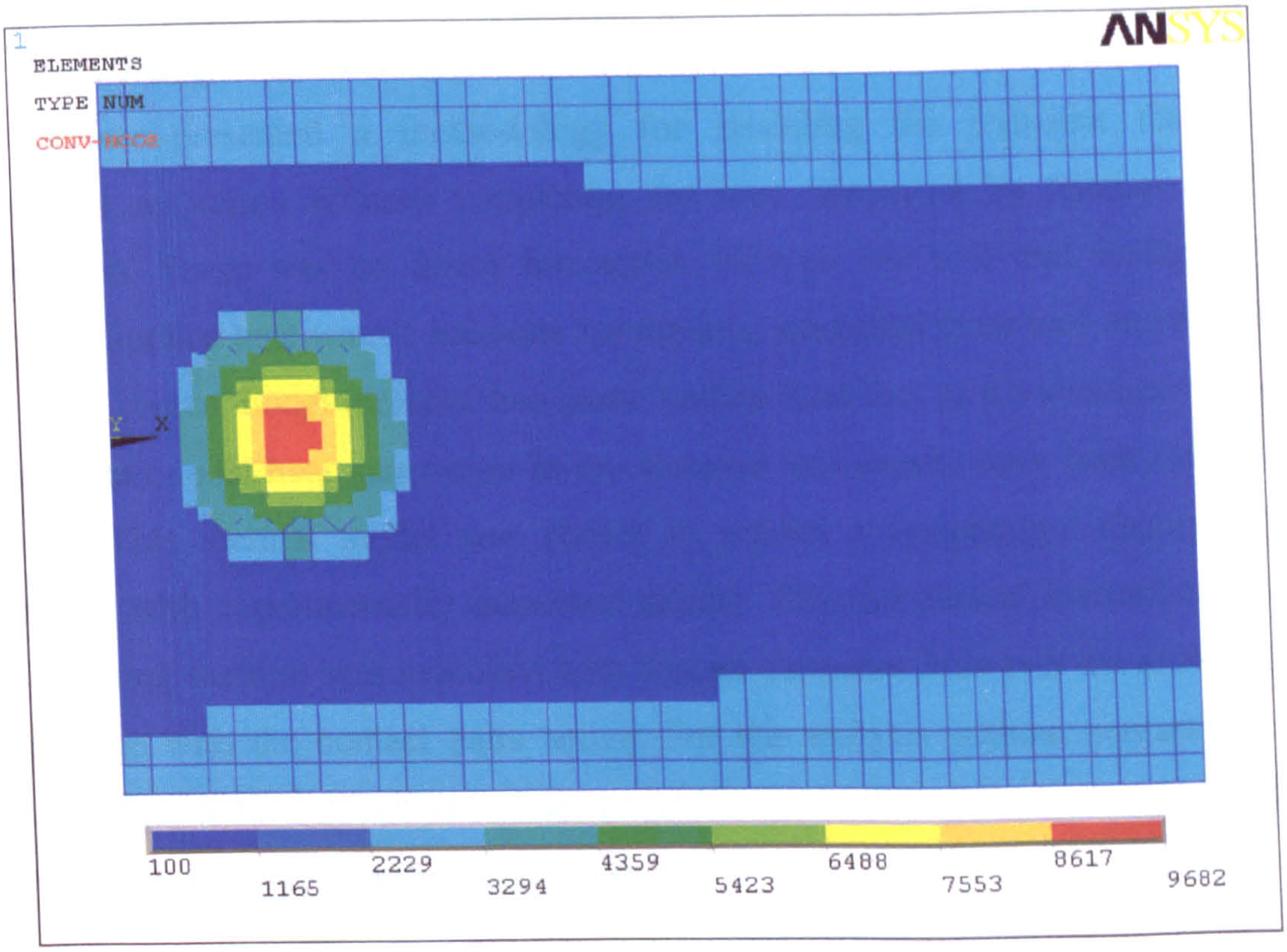

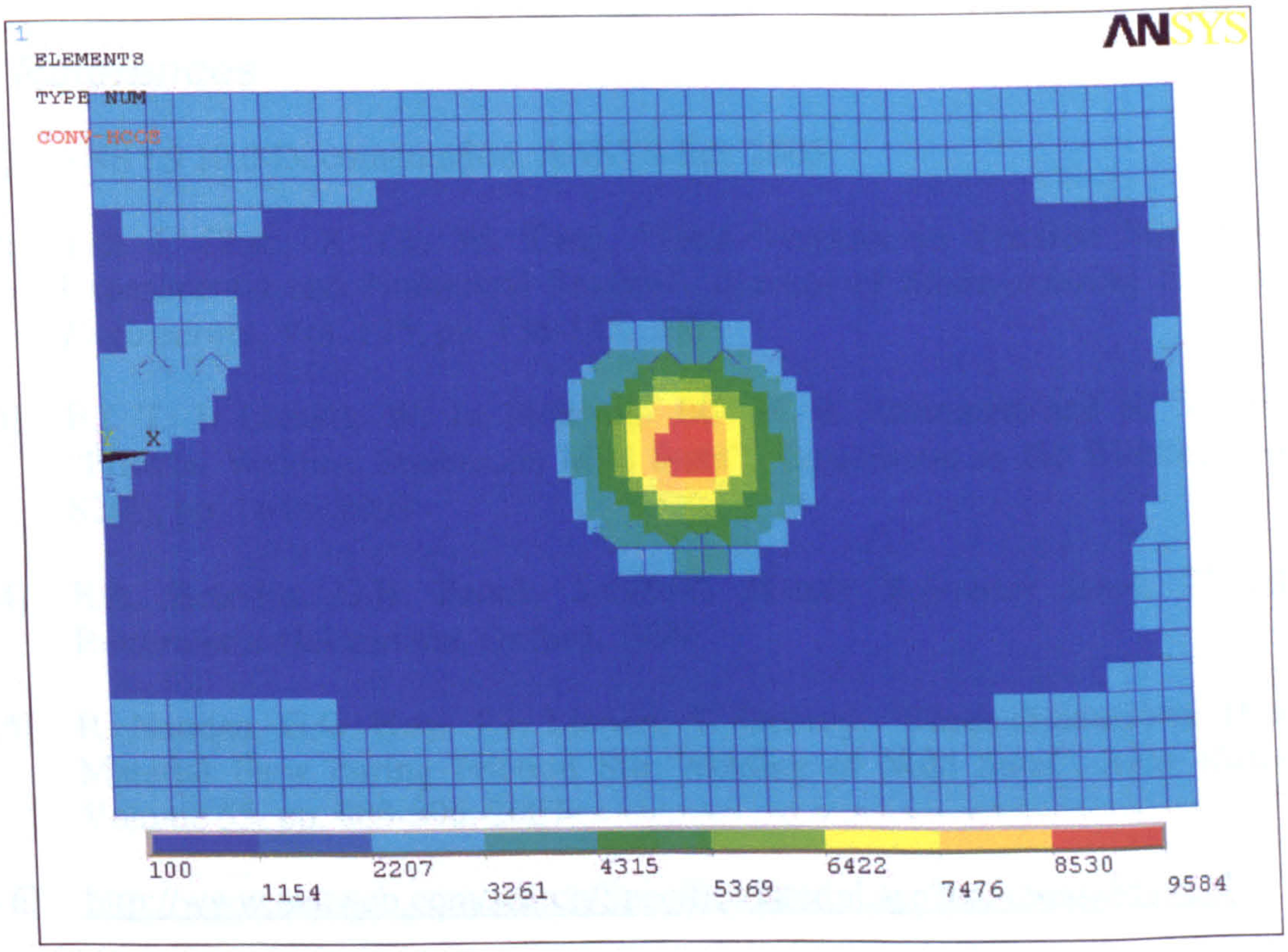

Figure 4.18 Examples of adaptive convective boundary conditions.

4.6 Summary

This chapter presented a methodology for modeling the transient thermal and mechanical responses without computing the heat generated by friction or plastic deformation. There was no direct interaction between the tool and workpiece. The externally applied heat source accounts for the heat generated from tool movement. The novel heat source model includes two parts: surface heat flux at the shoulder-workpiece interface and nodal heat generation in the material that should have been displaced by the tool. This thermal model was shown to predict a temperature history in good agreement with experimentally measured results. The mechanical interaction between the contacting surfaces was modelled with contact elements. However the analysis failed to converge with the contact pairs active. For the analysis without contact pairs, the predicted longitudinal direction stresses matched well with experiment but the transverse direction stresses were significantly different.

4.7 References

[4.1] ANSYS 10.0 Documentation, ANSYS Inc. 2005

[4.2] Yuh J. Chao, X. Qi, W. Tang, "Heat Transfer in Friction Stir Welding-Experimental and Numerical Studies", *Journal of Manufacturing Science and Engineering*, Vol. 125, pp. 138-145, 2003

[4.3] BY T. J. Lienert, W. L. Stellwag, JR., B. B. Grimmett and R. W. Warke, "Friction Welding Studies on Mild Steel", *Supplement to the Welding Journal*, 82(1), pp. 1s-9s, 2003

[4.4] E.A. Brandes, G.B. Brook, *Smithells Metals Reference Book*, 7th edition, Butterworth-Heinemann, Oxford, 1999

[4.5] R. Nandan, G.G. Roy, T.J. Lienert, T. Debroy, "Three-dimensional Heat and Material Flow during Friction Stir Welding of Mild Steel", *Acta Materialia*, Volume 55, pp. 883-895, 2007

[4.6] http://www.matweb.com/search/SpecificMaterial.asp?bassnum=M1018I

[4.7] H.S Kong, M.F. Ashby, "Friction-Heating Maps and Their Applications", *MRS Bulletin*, Volume 16, No. 10, 1991

[4.8] V.I. Vill, *Friction Welding of Metals*, New York American Welding Society, pp. 42-51, 1962

[4.9] Z. Deng, M.R. Lovell, K.A. Tagavi, "Influence of Material Properties and Forming Velocity on the Interfacial Slip Characteristics of Cross Wedge Rolling", *Journal of Manufacturing Science and Engineering*, Volume 123, Issue 4, pp. 647-653, 2001

[4.10] A. Bastier, M.H. Maitournam, K. Dang Van, F. Roger, "Steady State Thermomechanical Modelling of Friction Stir Welding", *Science and Technology of Welding & Joining*, Volume 11, Number 3, pp. 278-288, 2006

[4.11] X.K. Zhu, Y.J. Chao, "Numerical Simulation of Transient Temperature and Residual Stresses in Friction Stir Welding of 304L Stainless Steel", *Journal of Materials Processing Technology*, Volume 146, pp. 263-272, 2004

[4.12] W. Jiang, K. Yahiaoui, F.R. Hall, T. Laoui, "Finite Element Simulation of Multipass Welding: Full Three-Dimensional Versus Generalized Plane Strain or Axisymmetric Models", *The Journal of Strain Analysis for Engineering Design*,Volume 40, Number 6, 2005

[4.13] V. Soundararajan, S. Zekovic, R. Kovacevic, "Thermo-mechanical Model with Adaptive Boundary Conditions for Friction Stir Welding of Al 6061", International Journal of Machine Tools & Manufacture, Volume 45, pp. 1577-1587, 2005

[4.14] M.Z.H. Khandkar, J.A. Khan, A.P. Reynolds, M.A. Sutton, "Predicting Residual Thermal Stresses in Friction Stir Welded Metals", *Journal of Materials Processing Technology*, Volume, 174, pp. 195-203, 2006

[4.15] C. Conner, Feasibility Study and Initial Design of a Friction Stir Welding Rig, Unpublished Undergraduate Thesis, University of Strathclyde, 2006

[4.16] Syed M.S. Wahid, C.V. Madhusudana, "Gap Conductance in Contact Heat Transfer", *International Journal of Heat and Mass Transfer*, Volume 43, pp. 4483-4487, 2000

[4.17] M. Song, Numerical Simulation of Heat Transfer in Friction Stir Welding, PhD Thesis, Southern Methodist University, 2003

[4.18] Y. Cao, X. Qi, "Thermal and Thermo-mechanical Modeling of Friction Stir Welding of Aluminum Alloy 6061-T6", Journal of Materials Processing and Manufacturing Science, Volume 7, Number 10, pp. 215-233, 1998

[4.19] http://asm.matweb.com/search/SpecificMaterial.asp?bassnum=MA6061T6

[4.20] C.M. Chen, R. Kovacevic, "Finite Element Modeling of Friction Stir Welding-Thermal and Thermomechanical Analysis", *International Journal of Machine Tools & Manufacture*, Volume 43, pp. 1319-1326, 2003

[4.21] W. M. Rohsenow, J.P. Hartnett, E.N. Ganic, Handbook of Heat Transfer Fundamentals, second edition, McGraw-Hill, pp. 4-19, 1985

Chapter 5

Coupled Thermo-mechanical Friction Stir Welding Models

5.1 Selection of Simulation Methods

The choice of finite element method appropriate for fully coupled simulation of the Friction Stir Welding (FSW) process is determined by a number of factors, including available models of physical phenomena, meshing capabilities, solver technology and computing requirements.

The materials in contact with the rotating tool experience very large plastic deformations and strains, and may move at a velocity close to that of the tool; however the material flow behaviour is still well understood. In continuum solid mechanics finite element analysis, there are two commonly used methods to tackle large strain/deformation problems: Arbitrary Lagrangian-Eulerian (ALE) and complete remeshing formulations. ALE combines the advantages of both Lagrangian and Eulerian methods and allows the mesh to move independently of the material, making it possible to maintain a high-quality mesh during an analysis. The mesh topology does not change in the model, which means that the number of elements and their connectivity remains the same. However, this means that new (damaged) surfaces cannot be created in the ALE method and application is limited to geometries where the material flow is relatively predictable. In the FSW process, the tool travels a long distance along the plate, the ALE approach may fail when mesh distortion reaches unacceptable levels. To improve the simulation it would be necessary to use an FE technique which allowed remeshing of the domain, however, the computational cost of such an approach is greater than ALE and not all the

FE codes incorporate a remeshing feature, (especially when using explicit solvers). For ABAQUS, remeshing is only available in the implicit solver ABAQUS/STANDARD.

Friction stir welding is a high-speed dynamic process that can be extremely costly to analyze using implicit solvers. However, explicit solvers are well-suited for analyzing transient dynamic response and in addition allow better representation of complex contact interactions when the contact surface is not known a priori. The process itself is a coupled thermo-mechanical process, heat generated by mechanical friction and tool stirring will affect the temperature dependent material properties and consequently the plastic deformation of plate material; hence a coupled analysis using an element with both temperature and displacement degrees of freedom should be used.

Taking the above factors into account, it was decided to base the simulation on ABAQUS/EXPLICIT analysis using the ALE formulation and a temperature and rate dependent isotropic hardening plasticity material model to perform a fully coupled explicit solution of the plunge and dwell stages of the FSW process.

5.2 Constitutive Equations

The success of a FE simulation of FSW process is highly dependent upon the accuracy with which the constitutive equations characterize the behaviour of the deforming material. In FSW the plates are joined together under the constant stirring of the tool, as the temperature rises the material softens and flows around the tool. The maximum deformation rates may be on the same order as the tool rotating speed. Temperature could increase up to near melting temperature of the material and bonding happens in the solid state by diffusion and grain changes across the boundary. Thus, the chosen material model should be temperature, strain and strain rate dependent. A few such models with varying degrees of accuracy have been developed, such as Johnson-Cook [5.1-5.3], Zerilli-Armstrong [5.4-5.6], Steinberg-Guinan [5.7] and Follansbee-Kocks (mechanical threshold stress model) [5.8].

For rigid-viscoplasticity the elasticity is neglected. It has restricted application without modification as the stresses inside the yield function are indeterminate with regard to strain increments space. If the material is assumed to be viscoplastic, elements with mixed formulation in terms of virtual velocity and pressure fields are preferred. However, a viscoplastic model cannot return residual stress as a result of the analysis. A temperature and strain rate dependent material model incorporating the effect of elastic deformation is required to fully determine the flow, temperature, stress (residual) and strain of the workpiece material near the tool. In the fully coupled models the Johnson-Cook material law is used.

5.2.1 Johnson-Cook Material Model

The empirically based Johnson-Cook (JC) material model represents the flow stress with analytical forms of the hardening law and rate dependence. JC hardening is a special kind of isotropic hardening where the static yield stress is expressed in the following form [5.9]:

$$\sigma^0 = \left[A_{JC} + B_{JC}\left(\bar{\varepsilon}^{pl}\right)^{n_{JC}}\right]\left(1 - \hat{T}^{m_{JC}}\right) \qquad (5.1)$$

where σ^0 is the static yield stress, $\bar{\varepsilon}^{pl}$ is the equivalent plastic strain, n_{JC} is the work hardening exponent, A_{JC}, B_{JC}, and m_{JC} are material constants. $\hat{T}^{m_{JC}}$ is the nondimensional temperature defined as

$$\hat{T}^{m_{JC}} = \frac{T - T_{transition}}{T_{melt} - T_{transition}} \qquad (5.2)$$

where T is the current temperature, T_{melt} is the melting temperature and is typically taken as the solidus temperature for an alloy, $T_{transition}$ is the one at or below which the yield stress is not dependent on the temperature. If $T \geq T_{melt}$, the material will behave like a fluid $\sigma^0 = 0$ and $\hat{T}^{m_{JC}} = 1$. If $T \leq T_{melt}$, $\hat{T}^{m_{JC}} = 0$.

JC strain rate dependence is assumed to be of the form

$\dot{\bar{\varepsilon}}^{pl} = \dot{\varepsilon}_0 e^{\left[\frac{1}{C_{JC}}(R_{JC}-1)\right]}$ (5.3) and $\bar{\sigma} = \sigma^0\left(\bar{\varepsilon}^{pl}, T\right) R_{JC}\left(\dot{\bar{\varepsilon}}^{pl}\right)$ (5.4)

where $\bar{\sigma}$ is the yield stress at nonzero strain rate, $\dot{\bar{\varepsilon}}^{pl}$ is the equivalent plastic strain rate, $\dot{\varepsilon}_0$ is the normalizing strain rate (typically 1.0 s^{-1}), C_{JC} is the material constant, and $R_{JC}\left(\dot{\bar{\varepsilon}}^{pl}\right)$ is the ratio of the yield stress $\bar{\sigma}$ to the static yield stress.

The complete form of JC model is expressed as

$$\bar{\sigma} = \left[A + B\left(\bar{\varepsilon}^{pl}\right)^{n_{JC}}\right]\left(1 - \hat{T}^{m_{JC}}\right)\left[1 + C_{JC} \ln\left(\frac{\dot{\bar{\varepsilon}}^{pl}}{\dot{\varepsilon}_0}\right)\right] \tag{5.5}$$

The material model parameters, A_{JC}, B_{JC}, C_{JC}, m_{JC} and n_{JC} are calculated through an empirical fit of flow stress data to Equation 5.5.

5.2.2 Integration Procedure

The isotropic hardening plasticity and the von Mises yield surface with associated flow rule are used in the JC material model. Elastoplastic behaviour is described by decomposing the strain rate or strain increment into elastic and plastic parts.

$$\dot{\varepsilon} = \dot{\varepsilon}^{el} + \dot{\varepsilon}^{pl} \tag{5.6}$$

Jaumann stress rate is employed to define the material behaviour, that is, the stress rate is purely due to the elastic part of the strain rate and shown in terms of Hook's law by

$$\dot{\sigma} = \lambda trace\left(\dot{\varepsilon}^{el}\right)I + 2\mu\dot{\varepsilon}^{el} \tag{5.7}$$

where $trace\left(\dot{\varepsilon}^{el}\right) = \dot{\varepsilon}^{el}_{ii} = \sum_{i=1}^{n} \dot{\varepsilon}^{el}_{ii}$, λ and μ are elastic constants.

Integrating in a corotational framework,

$$\Delta\sigma = \lambda trace\left(\Delta\varepsilon^{el}\right)I + 2\mu\Delta\varepsilon^{el} \tag{5.8}$$

Mises yield function,

$$\sqrt{\frac{3}{2}\mathbf{S}:\mathbf{S}} - \sigma_y = 0 \tag{5.9}$$

where $\mathbf{S}:\mathbf{S} = S_{ij}S_{ij}$, σ_y is uniaxial yield stress, is defined as a function of equivalent plastic strain, strain rate and temperature. S is the deviatoric stress and p the hydrostatic pressure.

$$\mathbf{S} = \boldsymbol{\sigma} + p\mathbf{I} \tag{5.10}$$

$$p = -\frac{1}{3}trace(\boldsymbol{\sigma}) \tag{5.11}$$

First the predicted deviatoric stress $\boldsymbol{\sigma}^{pr}$ is calculated based on Equations 5.8-5.10,

$$\boldsymbol{\sigma}^{pr} = \boldsymbol{\sigma}^{old} + \lambda trace(\Delta\boldsymbol{\varepsilon}^{el})\mathbf{I} + 2\mu\Delta\boldsymbol{\varepsilon}^{el} \tag{5.12}$$

$$\mathbf{S}^{pr} = \boldsymbol{\sigma}^{pr} - \frac{1}{3}trace(\boldsymbol{\sigma}^{pr}) \tag{5.13}$$

where the superscript *old* means the stress at the beginning of the time increment in Equation 5.12.

Then the predicted von Mises stress,

$$\bar{\sigma}^{pr} = \sqrt{\frac{3}{2}\mathbf{S}^{pr}:\mathbf{S}^{pr}} \tag{5.13}$$

If this predicted von Mises stress exceeds current yield stress, plastic flow occurs.

The new stress is then calculated as,

$$\boldsymbol{\sigma}^{new} = \boldsymbol{\sigma}^{pr} - 2\mu\Delta\boldsymbol{\varepsilon}^{pl} \tag{5.14}$$

$$\mathbf{S}^{new} = \mathbf{S}^{pr} - 2\mu\Delta\boldsymbol{\varepsilon}^{pl} \tag{5.15}$$

where the superscript "new" means , the stress at the end of the increment.

Plastic flow law,

$$\dot{\varepsilon}^{pl} = \frac{3}{2}\frac{\mathbf{S}}{\sigma_y}\dot{\bar{\varepsilon}}^{pl} \tag{5.16}$$

The backward Euler approach is used to integrate the flow rule Equation 5.16,

$$\Delta\varepsilon^{pl} = \frac{3}{2}\frac{\mathbf{S}^{pr}}{\bar{\sigma}^{pr}}\Delta\bar{\varepsilon}^{pl} \tag{5.17}$$

Substitute Equations 5.15 and 5.17 into yield function Equation 5.9,

$$\bar{\sigma}^{pr} - 3\mu\Delta\bar{\varepsilon}^{pl} = \sigma_y^{new} \tag{5.18}$$

The uniaxial stress strain relationship of JC model can be expressed by the flow rate definition,

$$\dot{\bar{\varepsilon}}^{pl} = f(\sigma_y, \bar{\varepsilon}^{pl}, T) \tag{5.19}$$

Using the backward Euler method to integrate this equation gives

$$\Delta\bar{\varepsilon}^{pl} = \Delta t\, f(\sigma_y^{new}, \bar{\varepsilon}^{pl}, T) \tag{5.20}$$

To obtain σ_y as a function of $\Delta\bar{\varepsilon}^{pl}$ the above equation can be inverted, combining Equations 5.18 and 5.20 give a nonlinear equation for $\Delta\bar{\varepsilon}^{pl}$ solved by Newton's method [5.9],

$$c^{pl} = \frac{\bar{\sigma}^{pr} - 3\mu\Delta\bar{\varepsilon}^{pl} - \sigma_y^{new}}{3\mu + H} \tag{5.21}$$

where $H = \dfrac{d\sigma_y}{d\bar{\varepsilon}^{pl}}$

$$\Delta\bar{\varepsilon}^{pl} = \Delta\bar{\varepsilon}^{pl} + c^{pl} \tag{5.22}$$

Equations 5.21 and 5.22 are iterated until convergence is achieved.

Once $\Delta\bar{\varepsilon}^{pl}$ is given, the solution is thoroughly defined. Substituting $\Delta\bar{\varepsilon}^{pl}$ into Equation 5.14 leads to the yield stress at the end of the time increment.

5.2.3 Material Property Data

The JC model is widely used and incorporated in most commercial FE code. One of the problems facing users is the implementation of the model and particularly the choice of the model parameters. Identification of the JC model constants requires high-rate testing and data obtained at high strain rates and large strains. However this is considered to be beyond the scope of present study. All the model constants were collected in published literature and tabulated in Table 5.1. The material properties of AA2024-T3 are used in the FE models presented in this chapter. The Young's modulus is 73.1 GPa and the Poison's ratio is 0.33.

Table 5.1 Material constants for Johnson-Cook model.

Material	Reference	T_{melt} (°C)	A_{JC}(MPa)	B_{JC} (MPa)	C_{JC}	n_{JC}	m_{JC}
OFHC copper	[5.3]	1356	440	150	0.025	0.31	1.09
AA2024-T3	[5.10]	502	369	684	0.0083	0.73	1.7
Ti6Al4V	[5.10]	1630	1098	1092	0.014	0.93	1.1
Al 6082-T6	[5.11]	582	428.5	327.7	0.00747	1.008	1.31
AISI 1045	[5.11]	1460	553.1	600.8	0.0134	0.234	1
1080 steel	[5.12]	2800	514	2830	0.031	0.612	0.890
Vascomax 300 steel	[5.12]	1413	2070	1980	0.006	0.416	1.425
XC48 steel	[5.13]	------	497.6	2060	0.0198	0.6088	------

5.3 Geometry of the Initial Model

The dimensions of the initial model are shown below in Figure 5.1. Two separate plates to be welded are modelled as one to allow material movement in a continuous body and avoid mesh tangling at the plate-plate interface. The plate is 3 mm in thickness, 80 mm in width and 100 mm in length. The backing plate is modelled as a rigid surface which has a dimension of 100 mm X 120 mm. A smooth tool pin with cylindrical surface was adopted to reduce complexity of the FE model although the threaded pin surface has a better welding performance. The tool pin has a height of 2 mm and a radius of 2.5 mm. At the intersection of vertical and bottom surfaces of the tool pin a fillet radius of 0.2 mm was used to avoid surface definition problems. The shoulder diameter is 14 mm and the fillet radius at the pin-shoulder corner is 0.5 mm.

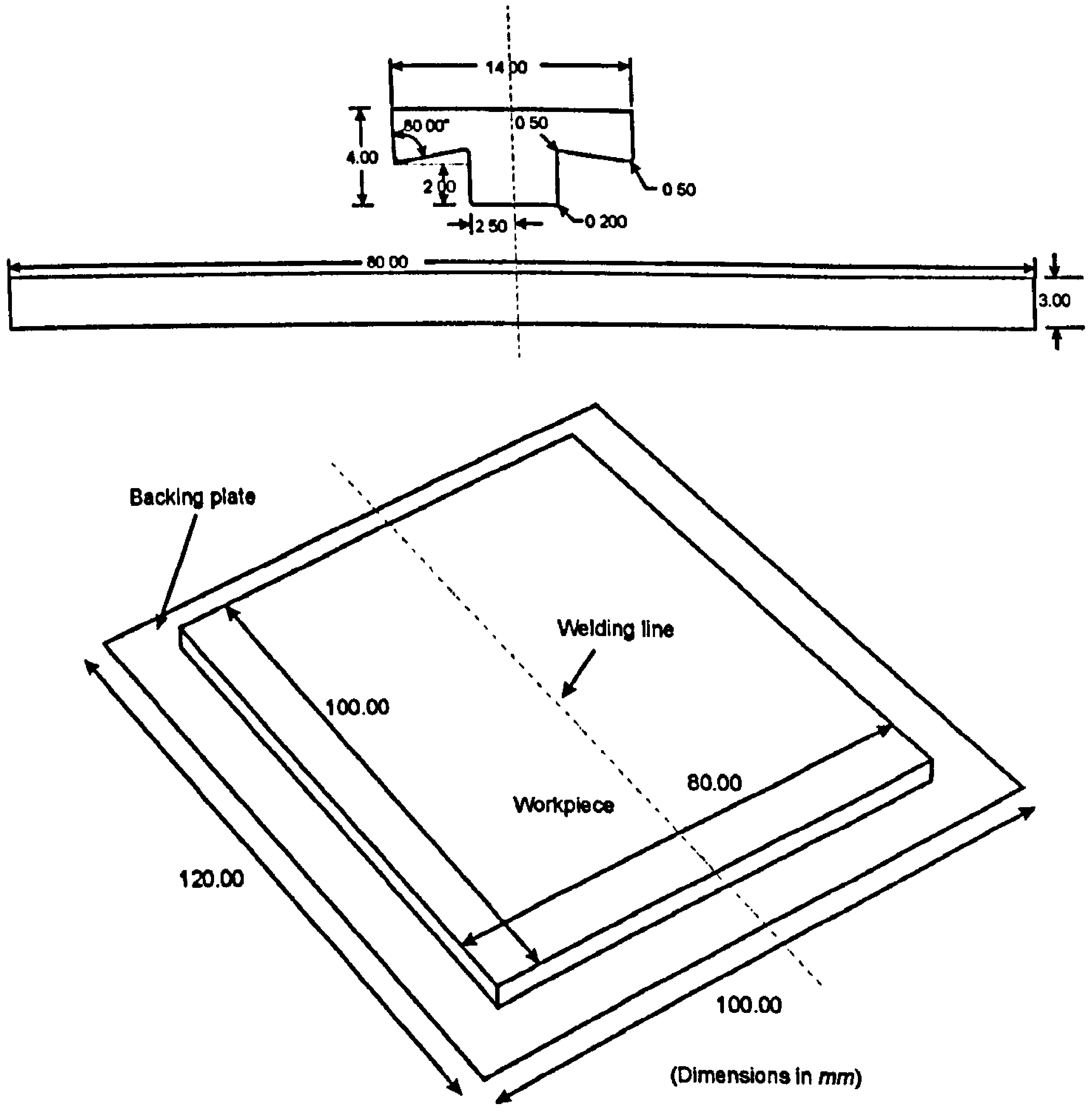

Figure 5.1 FSW model geometry.

5.4 Meshing

5.4.1 Element Type

For the workpiece, the ABAQUS/EXPLICIT element library offers 3D linear and quadratic coupled temperature-displacement elements. Only hexahedral (brick-shaped) elements use a reduced-integration scheme, while all wedge and tetrahedral solid elements use full integration. Reduced integration uses one fewer integration point in each direction to form the element stiffness. The mass matrix and distributed loadings use full integration. For a linear reduced-integration brick element just one single integration point is used at the element's centroid. One point integration element is advantageous owing to savings on computational cost and robustness in cases where large deformations occur. Reference [5.14] also recommends a fine mesh of linear, reduced-integration elements for large-strain analysis which involves very large mesh distortions. In three dimensions brick elements should be used wherever possible as the best results can be achieved for the minimum cost.

Although the linear tetrahedral C3D4T and wedge C3D6T elements are considered poor elements in terms of accuracy, due to its flexibility and convenience to model complex geometries the tetrahedral C3D4T was tried to examine its feasibility. It was found that using tetrahedral elements in the ABAQUS FE model could cause ALE domain definition problems in that every surface node that is connected to more than 15 elements is made non-adaptive. Each node highlighted in red in Figure 5.2, has more than 15 elements locally connected to that node.

The reduced-integration, first-order interpolation brick element C3D8RT is appropriate and adopted in the FE model. This element has both displacements and temperatures nodal variables at its 8 nodes. The geometry, node and integration point locations, and the coordinate system for this element are shown in Figure 5.3.

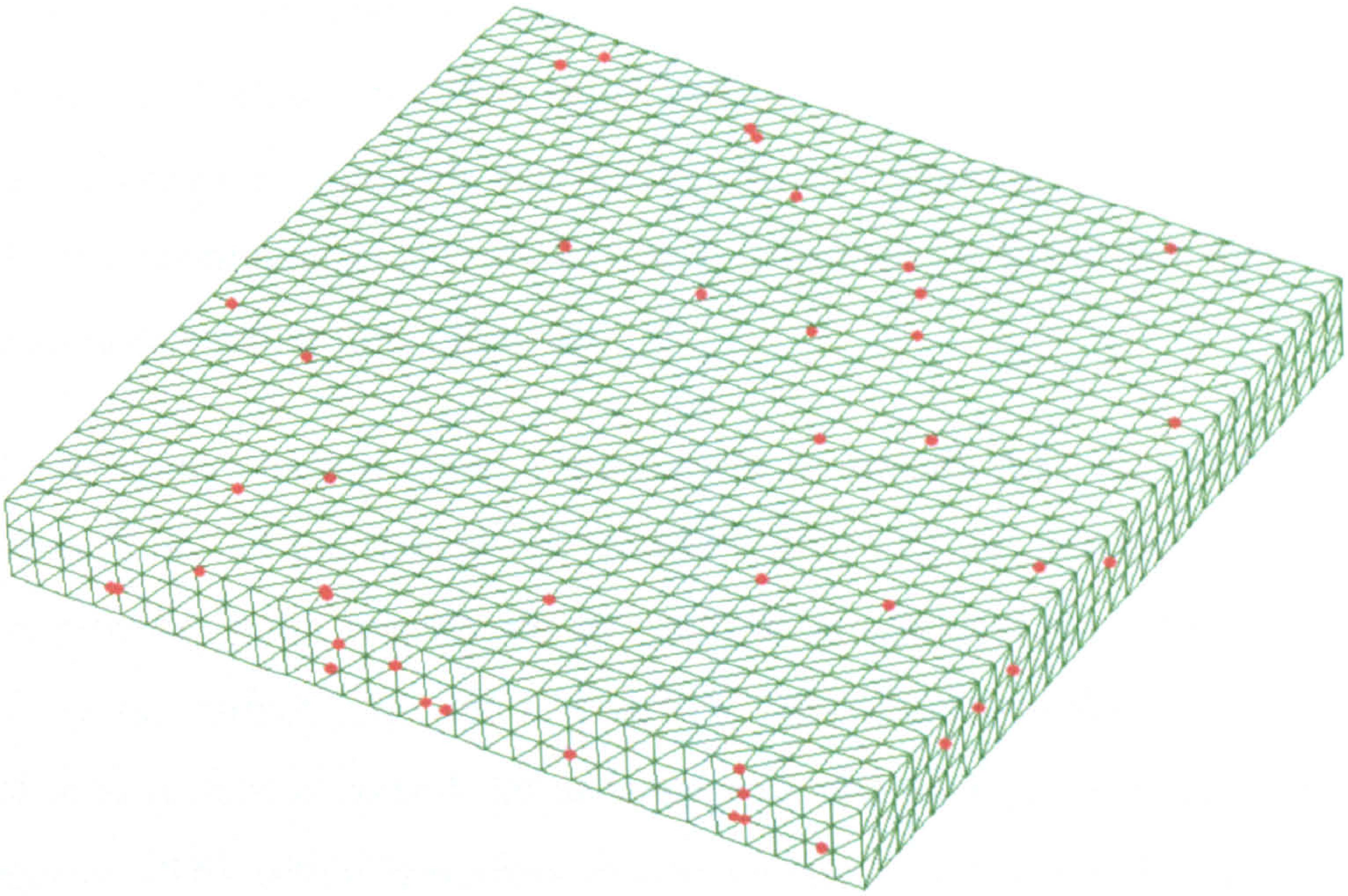

Figure 5.2 Non-adaptive nodes in an ALE domain meshed with tetrahedral elements.

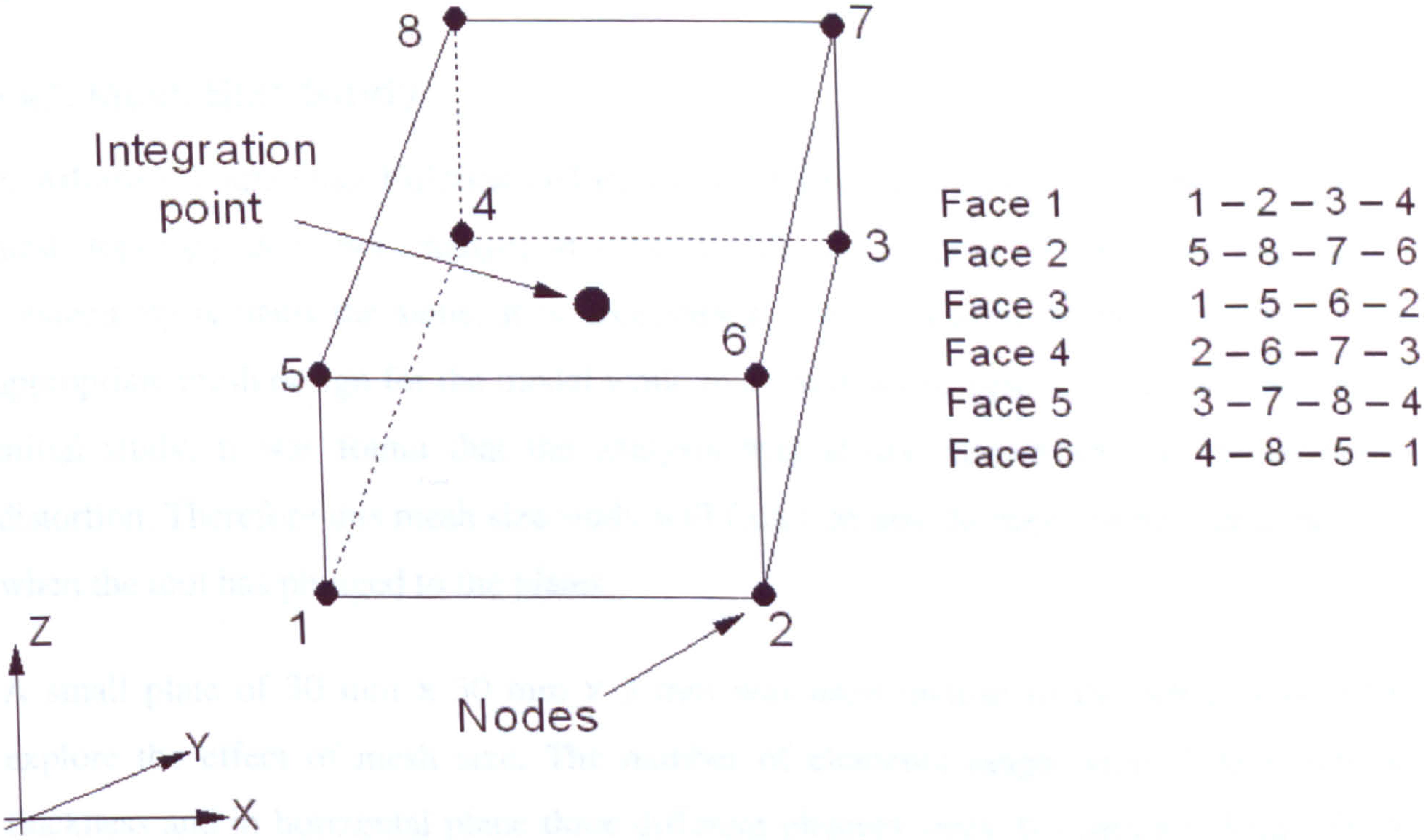

Face 1	1 – 2 – 3 – 4
Face 2	5 – 8 – 7 – 6
Face 3	1 – 5 – 6 – 2
Face 4	2 – 6 – 7 – 3
Face 5	3 – 7 – 8 – 4
Face 6	4 – 8 – 5 – 1

Figure 5.3 C3D8RT element features.

For the backing plate a 4-node 3D rigid quadrilateral element, R3D4 is used. As the geometry of the tool is relatively complex, the analytical rigid surface is employed instead of the rigid elements. This rigid surface has the ability to parameterize the surface with curved line segments and thus results in a smoother surface description. A great decrease in computational cost can also be obtained for the reason that it is actually a geometric surface rather than elements.

Due to the dynamic analysis type, a mass must be specified for the tool rigid surface. This is because not all the degrees of freedom (DOF) of the tool are fully constrained. ABAQUS provides point masses which could be attached to the reference node of the analytical rigid surface. In fully coupled temperature-displacement analysis the analytical rigid surface is considered as isothermal and the rigid body reference node has a temperature DOF which describes the temperature of the whole rigid body. If the temperature DOF is not specified, ABAQUS/EXPLICT requires the isothermal bodies to have a non-zero heat capacitance. This requirement can be fulfilled by connecting a capacitance element to the rigid body reference node.

5.4.2 Mesh Size Study

In Arbitrary Lagrangian-Eulerian (ALE) formulations, unlike complete remeshing, the mesh topology does not change; in other words the number of elements and their connectivity remains the same. It is necessary to carry out a mesh study to choose an appropriate mesh design for the model while maintaining the quality of the results. From initial study, it was found that the analysis was always terminated due to element distortion. Therefore this mesh size study will focus on how to improve the mesh pattern when the tool has plunged to the plates.

A small plate of 30 mm x 30 mm x 3 mm was used instead of the whole model to explore the effect of mesh size. The number of elements ranges from 3 to 6 across thickness and in horizontal plane three different element sizes, 0.5 mm x 0.5 mm, 0.75 mm x 0.75 mm and 1 mm x 1 mm were studied. The cross-section views of the meshes at the beginning of analysis and when the tool is inserted into the plate are shown in

Figure 5.4 (*a–d)* for element size 0.5 mm, Figure 5.5 (a-c) for element size 0.75 mm and Figure 5.6 (a-b) for element size 1 mm.

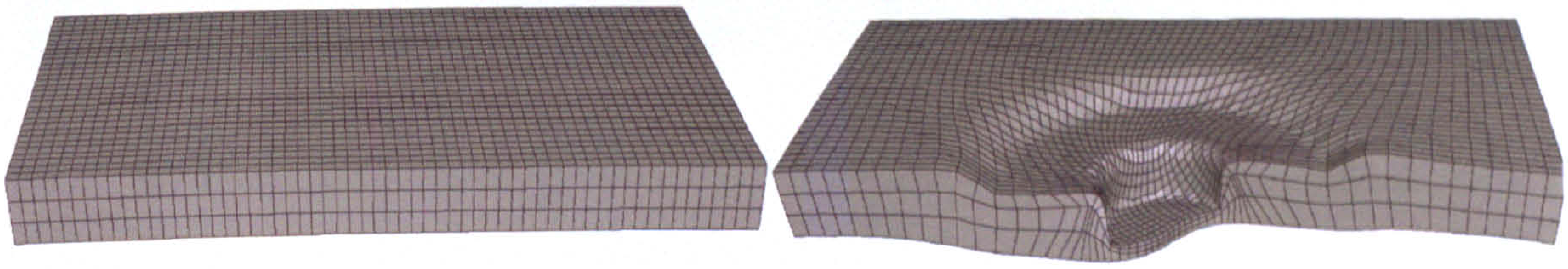

(*a*) Three elements in thickness and 0.5 mm x 0.5 mm in horizontal plane

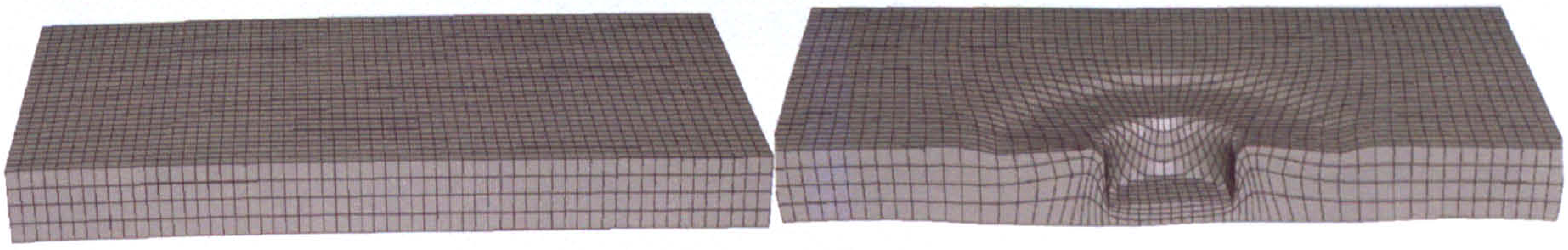

(*b*) Four elements in thickness and 0.5 mm x 0.5 mm in horizontal plane

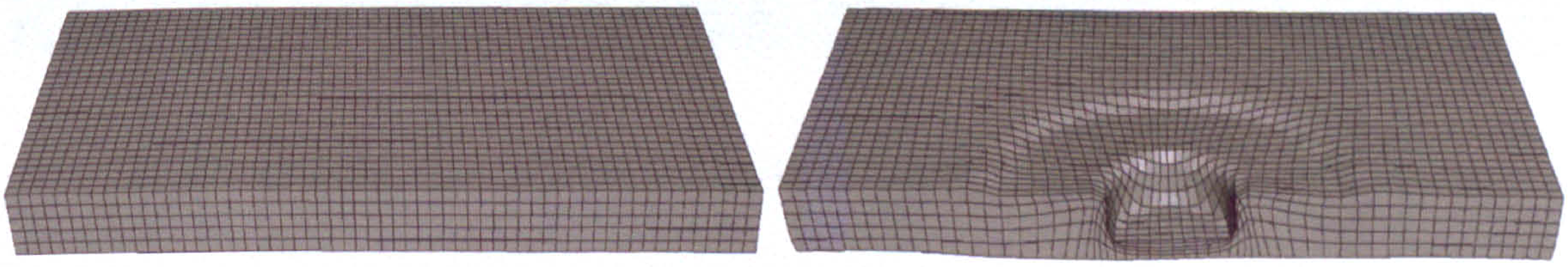

(*c*) Five elements in thickness and 0.5 mm x 0.5 mm in horizontal plane

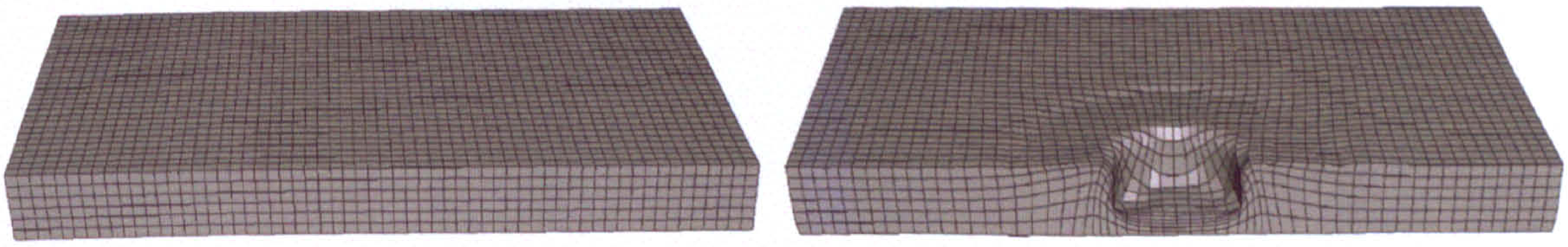

(*d*) Six elements in thickness and 0.5 mm x 0.5 mm in horizontal plane

Figure 5.4 (*a-d*) Cross-section views of the plate for element size 0.5 mm.

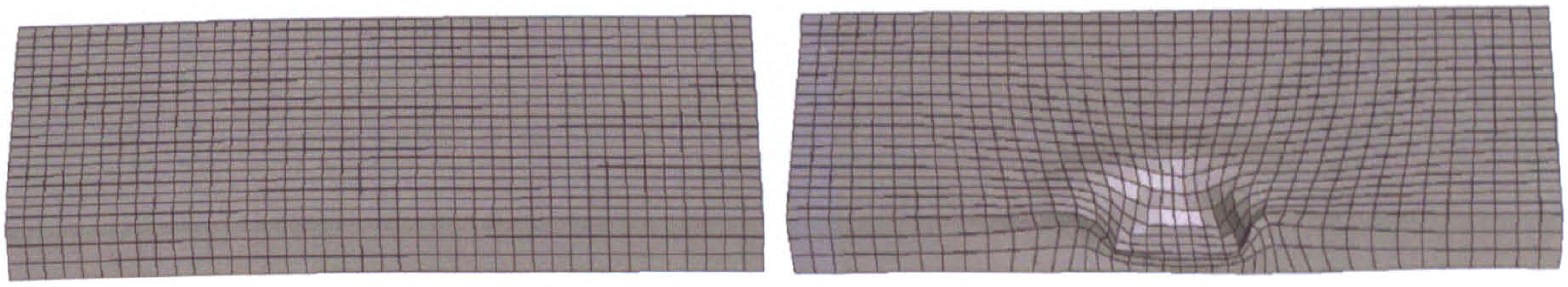

(*a*) Three elements in thickness and 0.75 mm x 0.75 mm in horizontal plane

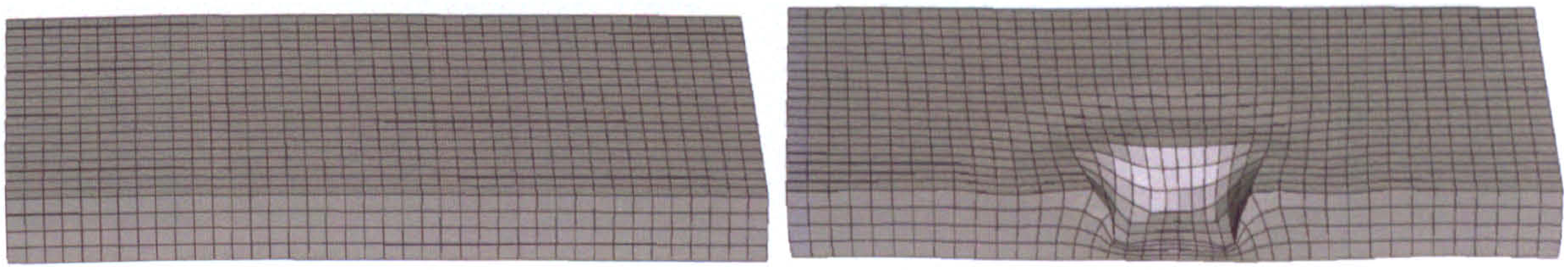

(*b*) Four elements in thickness and 0.75 mm x 0.75 mm in horizontal plane

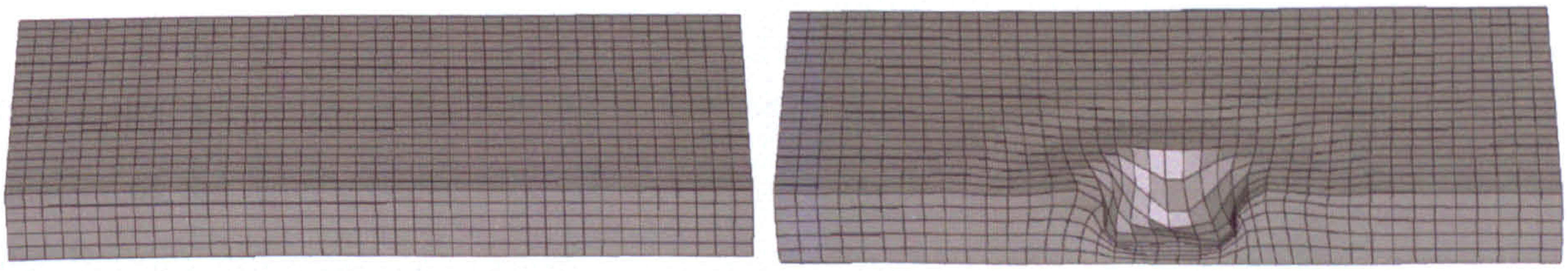

(*c*) Five elements in thickness and 0.75 mm x 0.75 mm in horizontal plane

Figure 5.5 (*a-c*) Cross-section views of the plate for element size 0.75 mm.

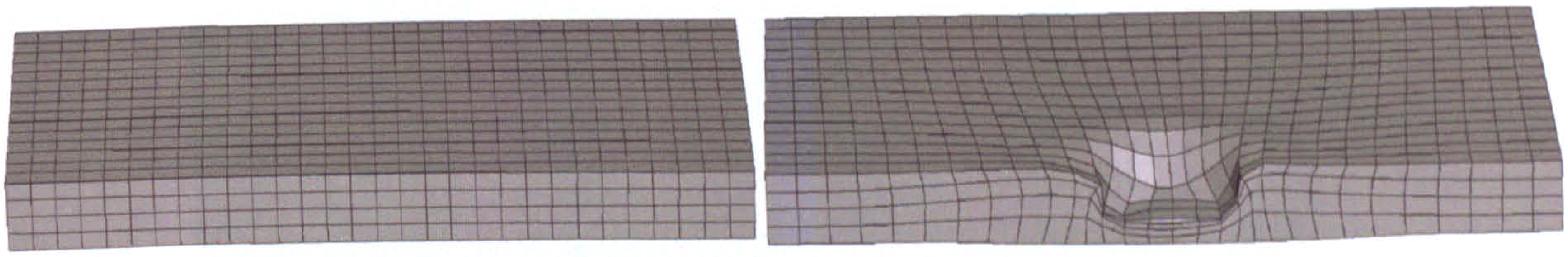

(*a*) Four elements in thickness and 1 mm x 1 mm in horizontal plane

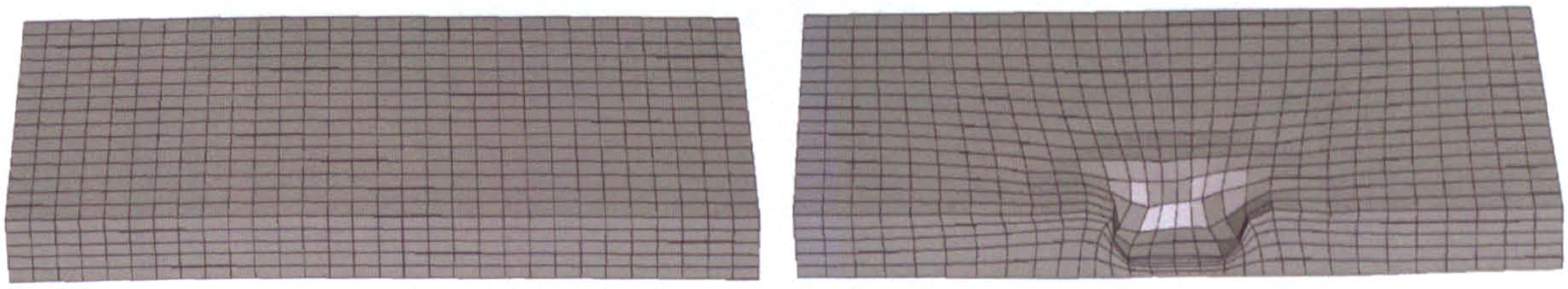

(*b*) Five elements in thickness and 1 mm x 1 mm in horizontal plane

Figure 5.6 (*a-b*) Cross-section views of the plate for element size 1mm.

It is found that increasing the mesh density through the thickness will not improve the quality of the mesh, especially when more than five elements are used. The elements at the bottom pin edge are prone to be squashed into thin sheet and their aspect ratio deteriorates as the tool is inserted into the plate. In Figure 5.7 (a) the enlarged view of Figure 5.4 (c) illustrates this problem with improperly deformed meshes which may result in the early termination of the simulation. The number of elements along the tool pin, when plunged in the workpiece, is determined by the element size in the horizontal plane. Figure 5.5 and Figure 5.6 show mesh patterns that don't have enough mesh around the tool. An enlarged picture of Figure 5.6 (a) is given in Figure 5.7 (b) where the coarse elements will not be sufficient to accurately capture the material state. The radius of fillet at the pin-shoulder is 0.5 mm; hence larger elements will not be able to accurately represent the curve of tool, giving rise to poor contact behaviour between the tool and plates. The required element size in the horizontal plane is suggested to be smaller than 0.5mmX0.5mm and the number of elements in thickness should be either three or four.

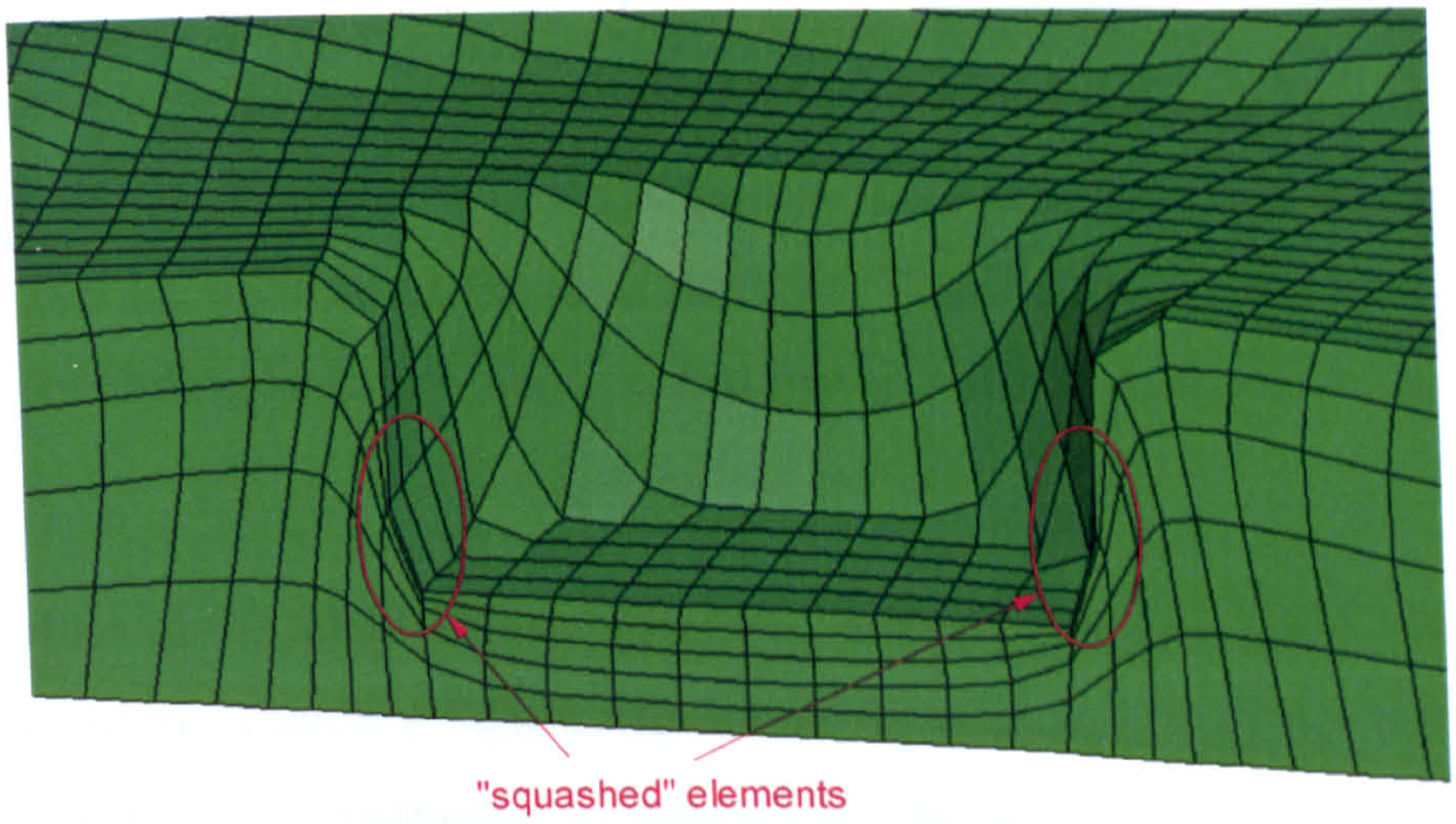

(a)

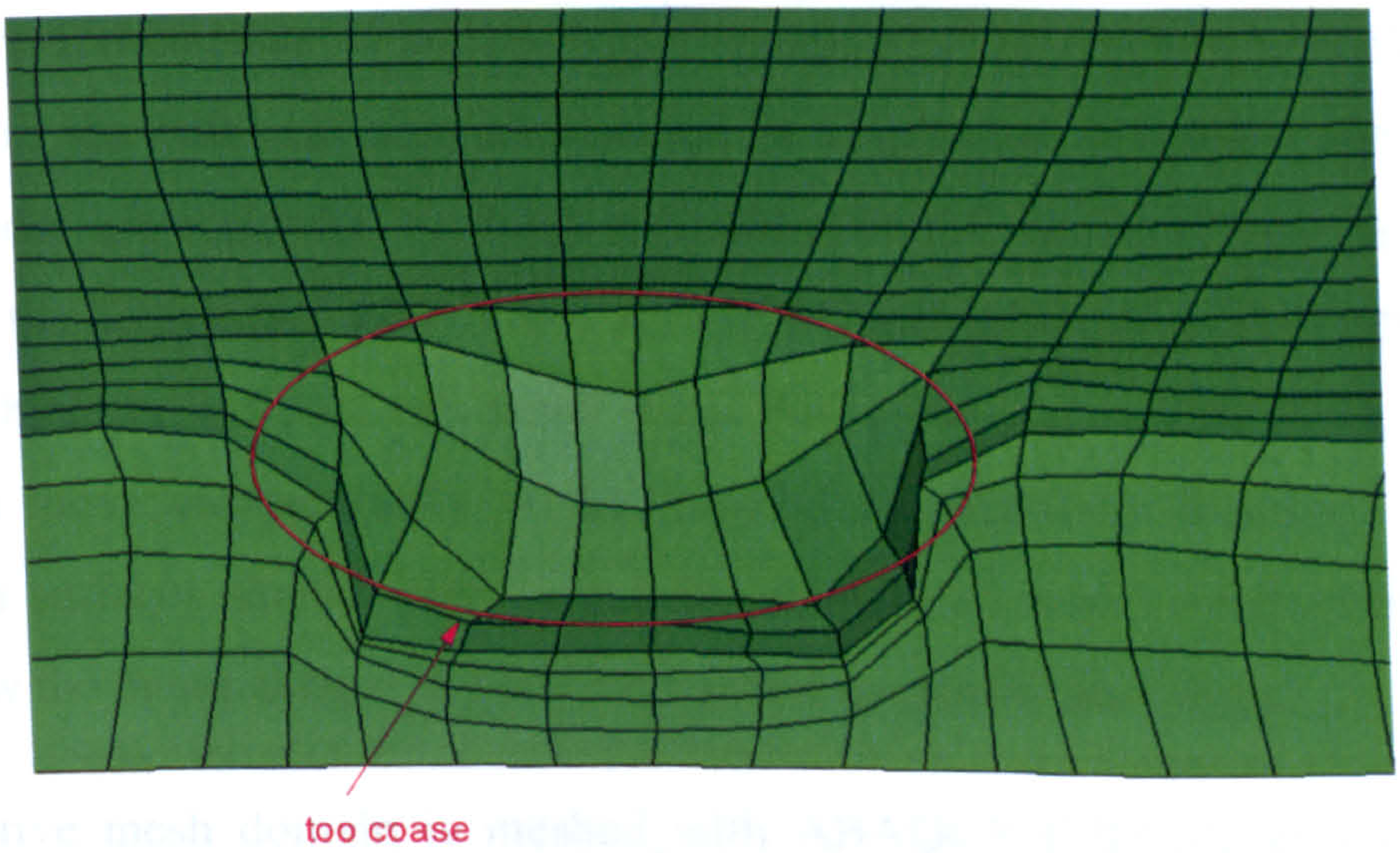

(b)

Figure 5.7 Improper deformed meshes (a) five elements in thickness and 0.5mm X 0.5mm in horizontal plane (b) four in thickness and 1mm X 1mm in horizontal plane.

5.4.3 Use of ALE in the Initial FE Model

In the initial mesh, it is not intended to move the tool across the whole length of the plates. Hence only a rectangular strip along the joint line, 1/6 of the plate, is defined as the adaptive mesh domain, with the remainder as lagrangian domain. The adaptive mesh domain has six boundary regions (surfaces) as highlighted by red lines in Figure 5.8.

Adaptive mesh boundary regions are separated by edges and can be either Lagrangian, sliding, or Eulerian. Eulerian boundary regions allow material flow across the boundary in a sense like an inlet or outlet of a domain. This behavior makes it different from Lagrangian or sliding boundary regions and hence Eulerian boundary regions will not be used here.

The top surface of the adaptive mesh domain, ADAP_TOP highlighted in green color is assigned as sliding boundary region which will be in contact with the tool. The nodes on this sliding surface is constrained to move with the material in the normal direction to the surface, but completely free to move in the tangential directions. The sliding boundary region consists of sliding edges which are free to slide over the underlying material. All the other surfaces are defined as Lagrangian boundary region where the surface nodes are restricted to move with the material in the normal direction to the surface of the boundary region. The Lagrangian boundary region has Lagrangian edges through which the material can never pass. For a free Lagrangian surface, the surface nodes can move independently of the material in tangential direction. While for the lagrangian surfaces shared with Lagrangian domain all nodes on the boundary region will follow the material flow in both normal and tangential directions.

The adaptive mesh domain is meshed with ABAQUS C3D8RT elements with three elements in plate thickness direction. The mesh is denser at the starting end of the plate and coarser at the other end along the welding joint line with the element size about 0.5mmX0.5mm at the initial tool position. The element sizes in other parts of the plate increase gradually to reduce the total number of elements in the mesh. One rigid element R3D4 is used to mesh the backing plate. The meshed FE model including plates, tool and backing plates is shown in Figure 5.9 (*a, b*).

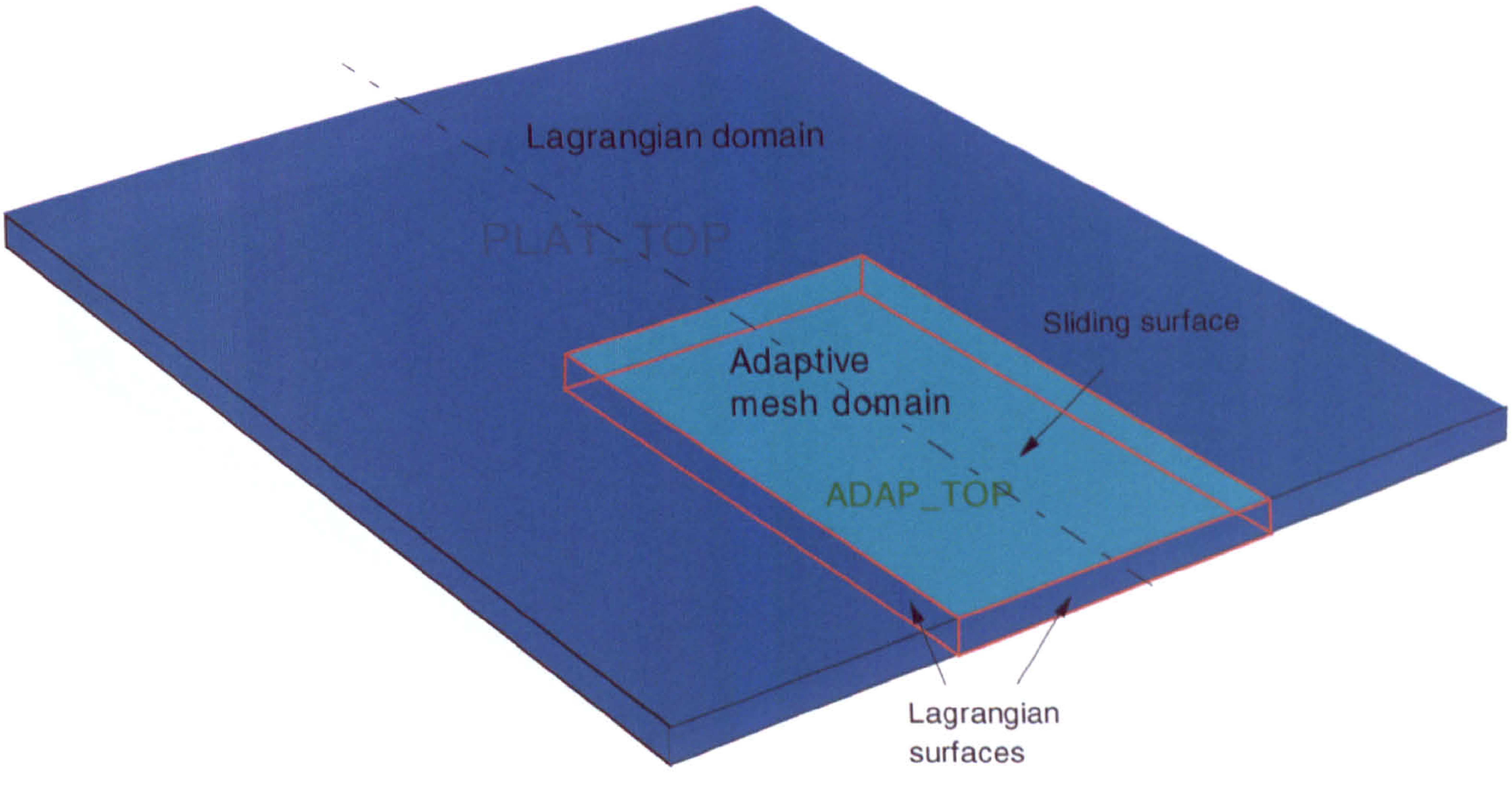

Figure 5.8 Illustration of the use of ALE in the FSW model.

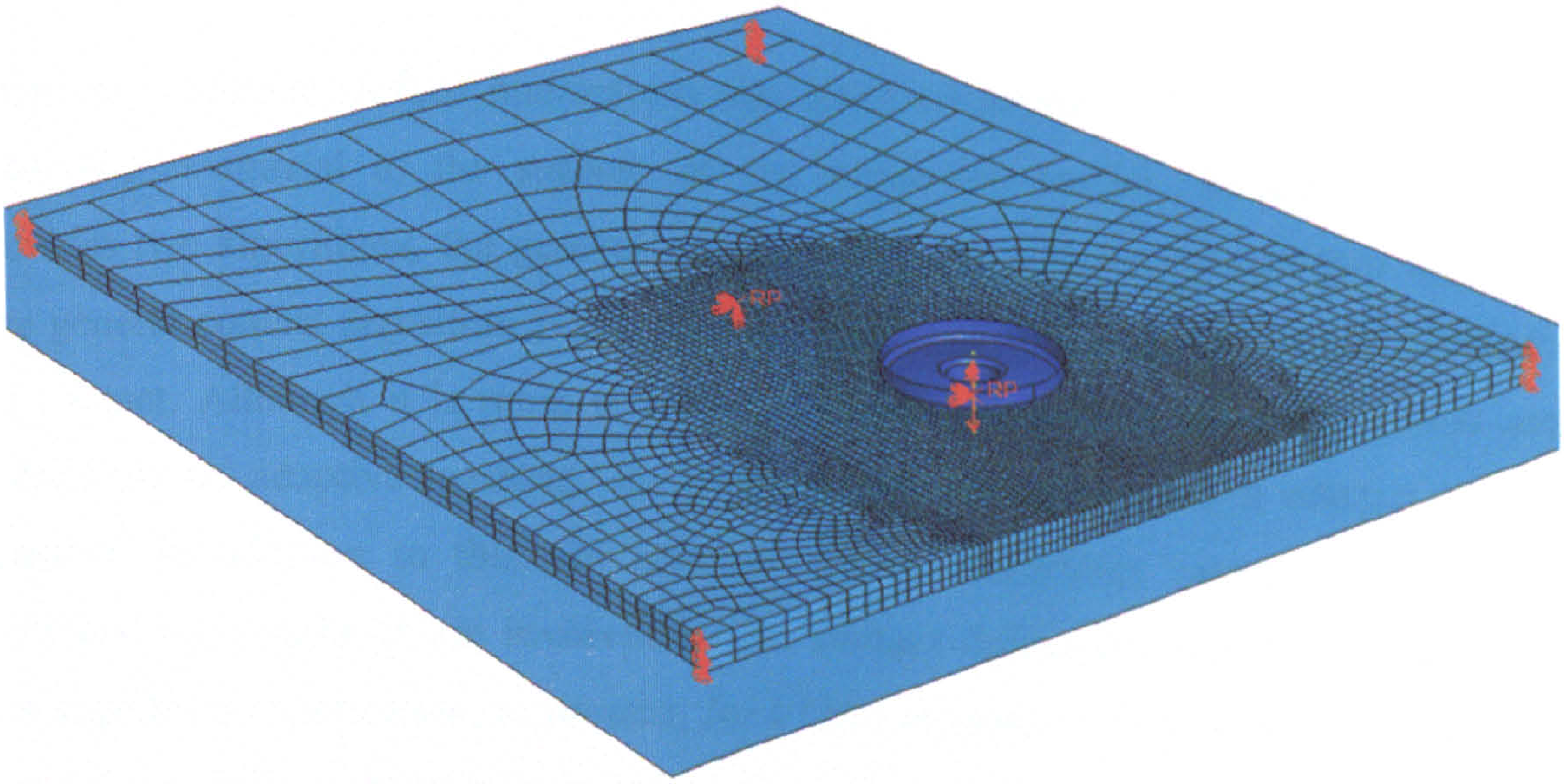

(a)

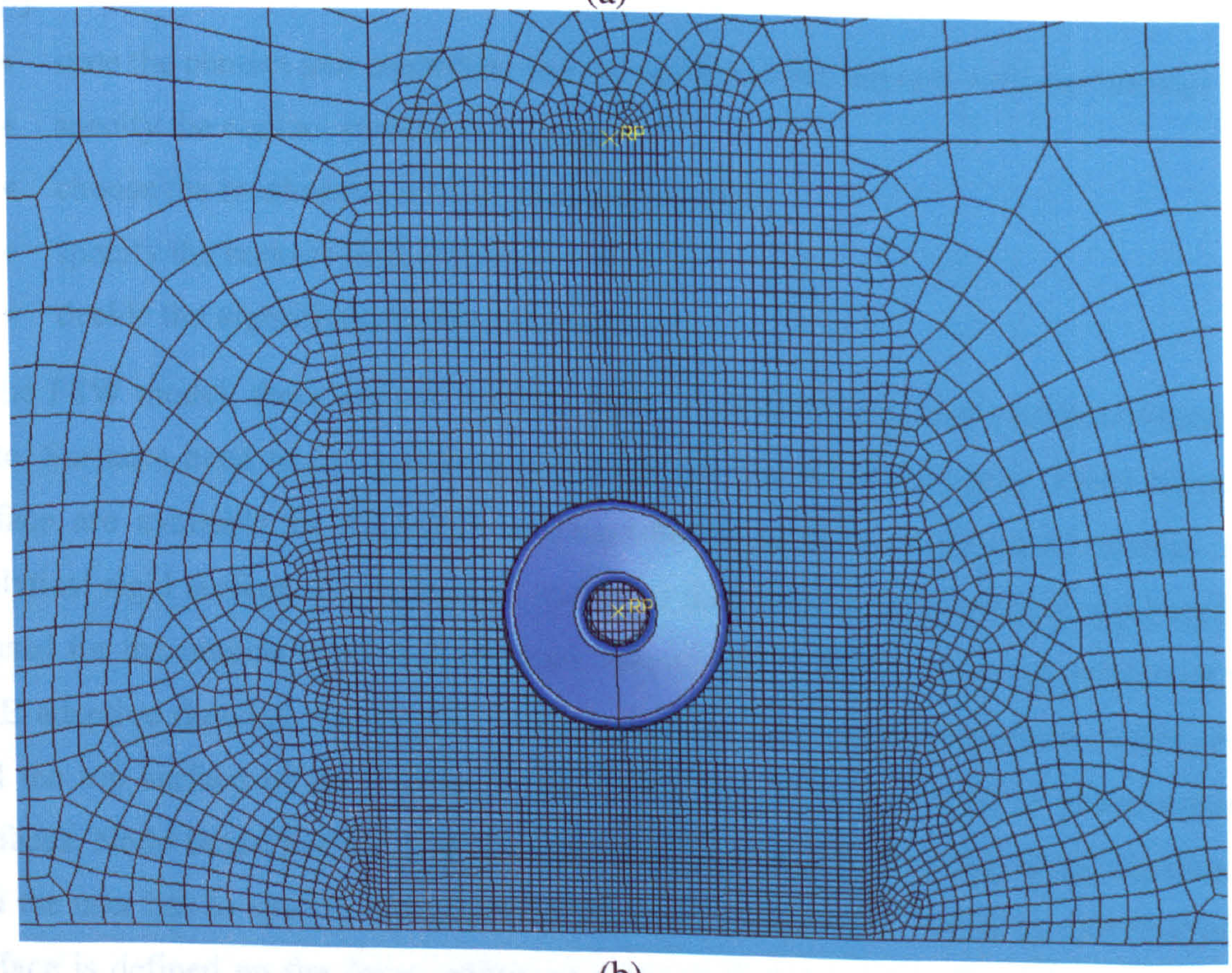

(b)

Figure 5.9 The initial FE model of the FSW process.

5.5 Contact Modeling

Relatively complex surface interactions are involved in the FSW process and contact modelling is crucial to the success of the numerical model. ABAQUS/EXPLICIT provides two algorithms, the general contact algorithm and the contact pair algorithm. The general contact algorithm is almost automatic and allows a very easy definition of the contact. Although it is more powerful, the general contact algorithm places more restrictions on adaptive meshing, for example, all nodes in general contact are non-adaptive. In addition to this, the general contact algorithm cannot be used when analytical rigid surfaces are involved in the contact definition. Due to this restriction, this impedes its application, at present, for FSW simulation. The contact pair algorithm meets the modelling requirements and was therefore chosen in this study.

The procedure of defining a contact pair interaction consists of the following steps [5.14]:

- state the contact pair algorithm and the surfaces that interact with one another
- specify the contact surface properties
- choose the mechanical contact property models
- specify the contact formulation
- decide the algorithmic contact controls

In the FSW model, there are two contact pairs: tool-workpiece and workpiece-backing plate. Surfaces need to be specifically defined for use in contact pair. Three types of surface are available in ABAQUS: element-based surfaces, node-based surface and analytical rigid surface. As mentioned earlier in this chapter the analytical rigid surface is used for the outside surface of the tool, named CON_TOOL. The top surface of the ALE adaptive domain, ADAP_TOP, the bottom surface of the workpiece, CON_BOT and the top surface of the backing plate, CON_BACK, are defined as element-based surfaces. Node-based surface was not used since it is based on nodes, is not continuous and the user has to specify the area associated with each node. While an element-based surface is defined on the faces, edges, or ends of elements and ABAQUS can relate a surface area to each node and calculate accurate contact stresses acting on the surface.

Surfaces CON_TOOL and CON_BOT are designated as the master surface and surfaces CON_TOP and CON_BOT are the slave surface in the two contact pair. By default contact constraints are enforced by means of a kinematic contact formulation for all contact pairs. In each increment of the explicit analysis, the kinematic state of the model precedes into a predicted configuration without taking into account the contact conditions. The depth of each slave node's penetration is then determined, together with the mass associated with it and the time increment; the force needed to resist penetration can then be calculated. These resisting forces of all the slave nodes are exerted as generalized forces on the related rigid body. The generalized forces and masses, including the added mass from each contacting slave node, are used to calculate an acceleration correction for the master surface nodes. Acceleration corrections for the slave nodes are then calculated from the acceleration of the master surface. Finally, a corrected configuration where the contact constraints are enforced can be obtained. In the current model, all the DOF of the two master surfaces are constrained at their reference node. As a result of this the kinematic contact formulation is not appropriate and the alternative penalty contact formulation was chosen. The penalty contact algorithm determines slave node penetrations in the current configuration. The equal and opposite contact forces are a function of penetration distance and penalty stiffness and are applied to the slave nodes to counter the penetration.

In the tangential direction, the workpiece-backing plate contact pair is assumed to be frictionless. For the tool-workpiece contact interfaces, the Coulomb friction model is used to describe the relationship between the frictional stress across an interface and the contact pressure. The two shear stress components are combined into an equivalent shear stress, $\bar{\tau} = \sqrt{\tau_1^2 + \tau_2^2}$. An optional equivalent shear stress limit, $\bar{\tau}_{\max}$ can be specified so that if the equivalent shear stress reaches this value sliding will occur irrespective of the magnitude of the contact pressure stress. A reasonable upper bound estimate for $\bar{\tau}_{\max}$ is $\sigma_y/\sqrt{3}$ [5.9], where σ_y is the Mises yield stress of the material in contact. Both the friction coefficient and $\bar{\tau}_{\max}$ are assumed constant with the values, 0.3 and 200MPa, respectively.

5.6 Boundary Conditions

The mechanical boundary conditions are also included in Figure 5.9. The backing plate is fully fixed at its reference node. Three translational degrees of freedom of the nodes on four corner edges are constrained to clamp the plate. The movement of the tool is controlled by velocity BC constraints. In the plunge stage, the downward and axial rotation speeds are set to 0.25 mm/s and 50 rad/s, respectively. All the other four velocities are equal to zero. In the dwell stage, the tool stops from further plunging and the downward speed is reset to zero. During the final traverse stage, the translational DOF in the welding direction is activated and a translational speed of 2 mm/s is used.

It is assumed that no direct heat transfer occurs across the plate and backing plate. In other words, the thermal contact conductivity between them was not modeled directly but taken into account in the form of convection. This is because the thermal contact conductivity is a function of contact pressure and temperature, which are not known before the analysis. A heat transfer coefficient, $1000\,{}^{W}\!/_{m^2K}$ is applied to the workpiece bottom surface and $10\,{}^{W}\!/_{m^2K}$ to the rest surfaces of the plate [5.28].

5.7 Heat Generation

The heat source consists of plastic energy dissipation and frictional energy dissipation. The plastic heat fraction was chosen as $\eta = 0.9$ for current study (refer to page 66), hence the heat flux per unit volume generated by plastic straining is calculated by:

$$q^{pl} = \eta\sigma\dot{\varepsilon}^{pl} \tag{5.23}$$

where η is a user-defined factor, σ is the stress, and $\dot{\varepsilon}^{pl}$ is the rate of plastic straining.

The rate of frictional energy dissipation is given by:

$$q^{fr} = \tau \cdot \dot{\gamma} \tag{2.24}$$

where τ is the frictional stress and $\dot{\gamma}$ is the slip rate.

The plastic energy dissipation is taken into account by solving the thermal energy balance governing equation as discussed in Chapter 3. While the frictional energy dissipation is put into the model by means of a heat flux boundary condition. It is assumed that 80% heat generated by the friction is released on ADAP_TOP surface (plates) and 20% on CON_TOOL (tool). This assumption is reasionable and will not affect the process modelling in the workpiece, as the weld can be produced by tools with different types of material, and different tools have different heat transfer properties.

5.8 Special Purpose Techniques

5.8.1 Hourglass Control

In section 5.4.1, the reduced-integration, first-order interpolation hexahedral element C3D8RT was chosen as it is robust for large deformations and results in the saving extensive amounts of computing time. However the biggest drawback in its use is the occurrence of zero-energy modes, also called hourglassing modes which typically have no stiffness and give a zigzag appearance to a mesh known as hourglass deformations. Since there is only one integration point in an 8-node element, a number of deformation modes could lead to zero strain increment, for example, when diagonally opposite nodes, within one element, have identical velocities. Undesirable hourglass modes are oscillatory in nature and tend to have periods that are much shorter than those the structural response, i.e. physically impossible mathematical states. Once these modes are excited no stresses can occur to resist the deformation and therefore this leads to severe mesh distortion.

Hourglass control is used to minimize this problem without bringing in unnecessary constraints on the element's physical response. This is usually done by adding stiffness to the element which resists hourglass modes and damping velocities in the direction of hourglass modes. In ABAQUS/Explicit three methods are available to suppress the hourglass modes: the Integral Viscoelastic approach, the Kelvin-type viscoelastic approach and the Enhanced Hourglass Control approach [5.14].

For the case where sudden dynamic loading is more probable, the Integral Viscoelastic approach produces more resistance to hourglass forces in the analysis. This approach is the most computationally intensive hourglass control method and can be used for all reduced-integration elements except for those with hyperelastic and hyperfoam materials.

For solid elements, the integral viscoelastic approach is defined as

$$F_{hg} = \int_0^t s^s k_{hg} \left(t - t'\right) \frac{df_{hg}}{dt} dt' \tag{5.25}$$

where f_{hg} is an hourglass mode magnitude, F_{hg} is the force (or moment) conjugate to f_{hg}, k_{hg} is the hourglass stiffness selected by ABAQUS/Explicit and s^s is the scale factor for the hourglass stiffness which is dimensionless and relates to specific displacement degrees of freedom.

The Kelvin-type viscoelastic approach is expressed as

$$F_{hg} = s^s \left[\left(1 - \alpha_{hg}\right) k_{hg} + \alpha_{hg} C_{hg} \frac{df_{hg}}{dt} \right] \tag{5.26}$$

where C_{hg} is the linear viscous coefficient. The stiffness term works to maintain a nominal resistance to hourglassing and the viscous term provides additional resistance to hourglassing under dynamic loading conditions. α_{hg} is a scale factor. When it equals zero, the general form reduces to pure stiffness which is recommended for both quasi-static and transient dynamic simulations; if it is one, the general form becomes a pure viscous hourglass control which is the most computationally efficient method and especially suitable for high-rate dynamic simulations but not for low frequency dynamic or quasi-static problems. In FSW process, there are a few elements which are close to but not in contact with the tool experiencing large deformation. Therefore the Kelvin-type viscoelastic approach is not suitable for controlling hourglass for these elements.

The enhanced hourglass control approach can be seen as a refined pure stiffness method in which the enhanced assumed strain method is used to calculate the stiffness coefficients. It generates increased resistance to hourglassing for nonlinear materials. This method was chosen and used for current study through the command, *SECTION CONTROLS, HOURGLASS=ENHANCED.

5.8.2 Bulk Viscosity

To improve stability of the high-speed dynamic analysis, damping related to volumetric straining need to be introduced via bulk viscosity. ABAQUS/Explicit uses two forms of bulk viscosity: linear and quadratic.

Linear bulk viscosity creates a bulk viscosity pressure that is proportional to the volumetric strain rate

$$p_{bv1} = b_1 \rho c_d L_e \dot{\varepsilon}_{vol} \tag{5.27}$$

where b_1 is the first damping coefficient, ρ is the current material density, c_d is the current dilatational wave speed, L_e is an element characteristic length, and $\dot{\varepsilon}_{vol}$ is the volumetric strain rate. This bulk viscosity pressure provides a truncation frequency damping to suppress "ringing" in the highest element frequency.

The second form of bulk viscosity pressure is in a quadratic relationship with the volumetric strain rate

$$p_{bv2} = \rho\left(b_2 L_e \dot{\varepsilon}_{vol}\right)^2 \tag{5.28}$$

where b_2 is the second damping coefficient. Quadratic bulk viscosity is applied only when the volumetric strain rate is compressive. The quadratic bulk viscosity pressure will absorb a shock front across several elements and prevent elements from collapsing under very high velocity gradients.

When calculating the material point stresses the bulk viscosity pressure is not accounted for as it is used as a numerical effect only and in other words, it will not affect the material's constitutive response. With the first and second damping coefficients, the fraction of critical damping of each element is expressed by

$$\xi = b_1 - b_2^2 \frac{Le}{c_d} \min(0, \dot{\varepsilon}_{vol}) \tag{5.29}$$

With damping, the stable time increment for the mechanical response is different from the one used in Chapter 3 (first term inside the bracket in Equation 3.70) and adjusted as

$$\Delta t \leq \frac{2}{\omega_{\max}} \left(\sqrt{1 + \xi_{\max}^2} - \xi_{\max} \right) \tag{5.30}$$

where $\xi_{\max}$ is the fraction of critical damping in the mode with the highest frequency. It is clear from the above equation that introducing damping to the solution reduces the stable time increment.

In ABAQUS/Explicit a small amount of damping is brought in through bulk viscosity to control high frequency oscillations. The default values, b_1=0.06 and b_2=1.2, are specified in the model by *BULK VISCOSITY.

5.8.3 Tracer Particles

In adaptive mesh domains, the mesh moves independently of the underlying material. The variables such as displacement and temperature histories at those nodes do not represent any physical meanings. Therefore, in order to track field and history information at specific material points tracer particles should be used. Tracer particles are defined with node sets whose current locations are coincident with the material points of interest. The number of birth stages can be specified so that tracer particles are released from their parent nodes periodically at evenly spaced intervals during the step and follow the material motion throughout an analysis regardless of the mesh motion. Two types of output results can be requested from tracer particle: field output and history output. Displacement is the only valid field request, while in history output the valid requests are displacement, velocity, acceleration and coordinates, additionally any available element integration point variable can be obtained. Figure 5.10 shows the tracer particles used in the initial model.

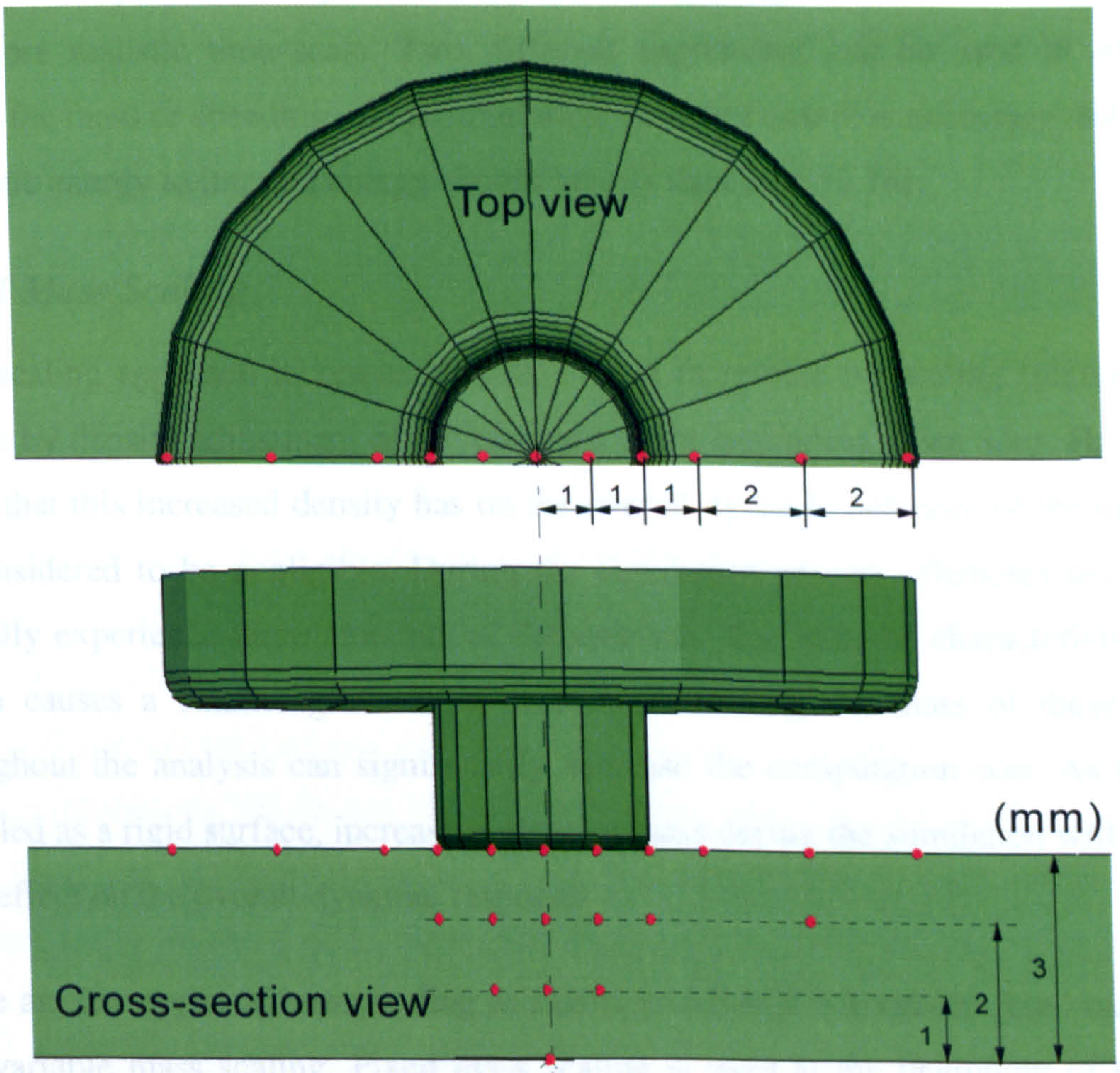

Figure 5.10 Locations of defined tracer particles for the initial model at the beginning of analysis.

5.8.4 Reducing Computational Cost

In dynamic analysis in order to capture the real transient response, it is desirable to use the natural time scale and an accurate representation of the physical mass and inertia in the model. The CPU time required to run a simulation analysis using explicit integration formulation with a given mesh is proportional to the time period of the event. For the initial FSW model used, the plunge stage takes about 9 seconds while the stable time increment is 5e-08 seconds meaning that 1.6e+08 increments and about 125 days are needed to complete the analysis. Therefore, it is necessary to reduce the computing time to a more realistic time scale. Two different approaches can be used in ABAQUS: scaling the mass or speeding up the simulation. In either case it is necessary that the ratio of kinetic energy to internal energy should be less than 10% [5.14].

5.8.4.1 Mass Scaling

Mass scaling approach increases the stable time increment by scaling (increasing) the masses by density adjustment of the elements at the beginning of the step. However the effect that this increased density has on the overall dynamic behavior of the model may be considered to be negligible. During the simulation process, elements near the tool typically experience large amounts of deformation. The reduced characteristic element length causes a smaller global time increment. Scaling the mass of these elements throughout the analysis can significantly decrease the computation cost. As the tool is modeled as a rigid surface, increasing element mass during the simulation will have very little effect on the overall dynamic response.

There are two types of mass scaling available in ABAQUS/Explicit: fixed mass scaling and variable mass scaling. Fixed mass scaling is used at the beginning of the step to scale the originally defined element masses that are assembled into the global nodal mass matrix. The resulting scaled mass matrix is then used, for the rest of the analysis, unless variable mass scaling is also used. Variable mass scaling is performed at the beginning and throughout the analysis to scale the mass of elements in addition to any fixed mass scaling factor that is already set. Only a minimum stable time increment needs to be specified and the corresponding scaling factor will be computed automatically.

In the preliminary study, three factors of the fixed mass scaling factors, 25, 100, 10000 and three minimum stable time increments of the variable mass scaling, 1E-05, 5E-06, 1E-06, were investigated. For the variable mass scaling, a frequency of five was used, i.e. the mass scaling will occur at every five increments. The CPU time required to insert the tool to a depth of 1 mm is summarized in Table 5.2.

Table 5.2 Effect of mass scaling on CPU time.

	Fixed mass scaling factor			Variable mass scaling increment		
	25	100	10000	1E-06	5E-06	1E-5
CPU time (hours)	192	93	11.2	46.4	9	4.5

In the cases of mass scale factors 25, 100 and the variable mass scale increment 1E-06, the large amount of CPU time required impedes their use in the model. As expected, a nearly linear relationship exists in the variable mass scaling case. However due to excess element distortion the analysis was terminated before the completion of plunge stage for the time increments, 5E-06 and 1E-5. The reduced element length during analysis causes a decreasing global time increment. While the variable mass scaling method tends to keep the analysis at a constant time increment, as a result extremely high mass scaling at some critical elements leads to the simulation termination. Finally the fixed mass factor, 10000 is chosen for the coupled FSW model.

5.8.4.2 Speeding up Simulation

Speeding up simulation is the other way to reduce the total number of increments required. The tool rotation, plunge and traverse speeds were increased up to 100 times of their normal value while keeping the speed ratio between them unchanged. As a result the time period of the event is artificially reduced to 1% of the time in the actual process. Due to the rate dependence of the material model, the increased inertial forces will significantly affect the computed results, thus this material behavior has to be suppressed. It was found that, in the test model, the temperature calculated was well above melting point reaching 2000 Celsius degree. The problem is directly linked to the increased tool speeds. In order to get a reasonable temperature plot, the material properties and thermal boundary conditions should be adjusted accordingly. With a time-consuming trial and error approach, reasonable results were given by a combination of changed parameters: thermal conductivity, 24200 W/mK, top surface convection coefficient, 1000 W/m^2K, and bottom surface convection coefficient 20000 W/m^2K, compared with 121 W/mK, 10 W/m^2K and 1000 W/m^2K before adjustment.

5.8.5 Parallel Processing

ABAQUS 6.6 has the capability of parallel execution which can be implemented with two different schemes: threads and message passing. Message passing implementation is chosen on all platforms whenever it is supported. Thread-based parallelization mode is available on all platforms but only for shared memory parallel (SMP). Threads are lightweight processes carrying out different tasks simultaneously within the same application. They communicate relatively easily by sharing the same memory pool. Message Passing Interface (MPI)-based parallelization mode uses multiple analysis processes that communicate with each other via the MPI. It is available for both SMP and DMP (Distributed Memory Parallel). However, it is not supported on Windows/x86-32 or x86-64, other platforms like Linux, HP-UX/Itanium, AIX/Power have to be used.

Two parallelization implementation methods exist in ABAQUS/Explicit: domain level and loop level. The domain-level method divides the model into a number of topological domains referred to as parallel domains to distinguish them from other domains associated with the analysis. The domains are assigned evenly to the available processors. Then the computing in each domain is performed independently. As the domains share common boundaries, information must be passed between the domains in each increment. This can be done by both MPI and thread-based parallelization modes.

One of the limitations of domain level parallelization is that adaptive mesh domains cannot be split into parallel domains. Adaptive nodes on the surface of the adaptive mesh domain can only belong to one parallel domain. When parallel domains are selected, all nodes shared by adjacent adaptive mesh domains will be made nonadaptive and the analysis results may show significant discrepancy from that of a solution without parallel domains. The other limitation is that a contact pair can not span parallel domains. All of the nodes associated with a contact pair, using the kinematic contact algorithm, should be within a single parallel domain. For a contact pair with the penalty contact algorithm, the associated nodes can be part of a single parallel domain and may also be part of other parallel domains.

If domain level mode is used in the model, the defined adaptive domain ADAPDOMAIN can be assigned to a processor as a separate parallel domain, while the remaining non-adaptive part of the model is treated as the other parallel domain. Unfortunately similar crumpling problems occurred at the top surface of the plate as reported by Oliphant [5.15] and Lasley [5.16] when running simulations over a parallel processing node or network. During the phase that the tool penetrated into the plate, the contacting surface in the adaptive mesh domain displayed a very bumpy and jagged appearance as shown in Figure 5.11. Several domain-level parallel processed models were attempted, each of which ended abruptly during the analysis with the same error, excessively distorted elements.

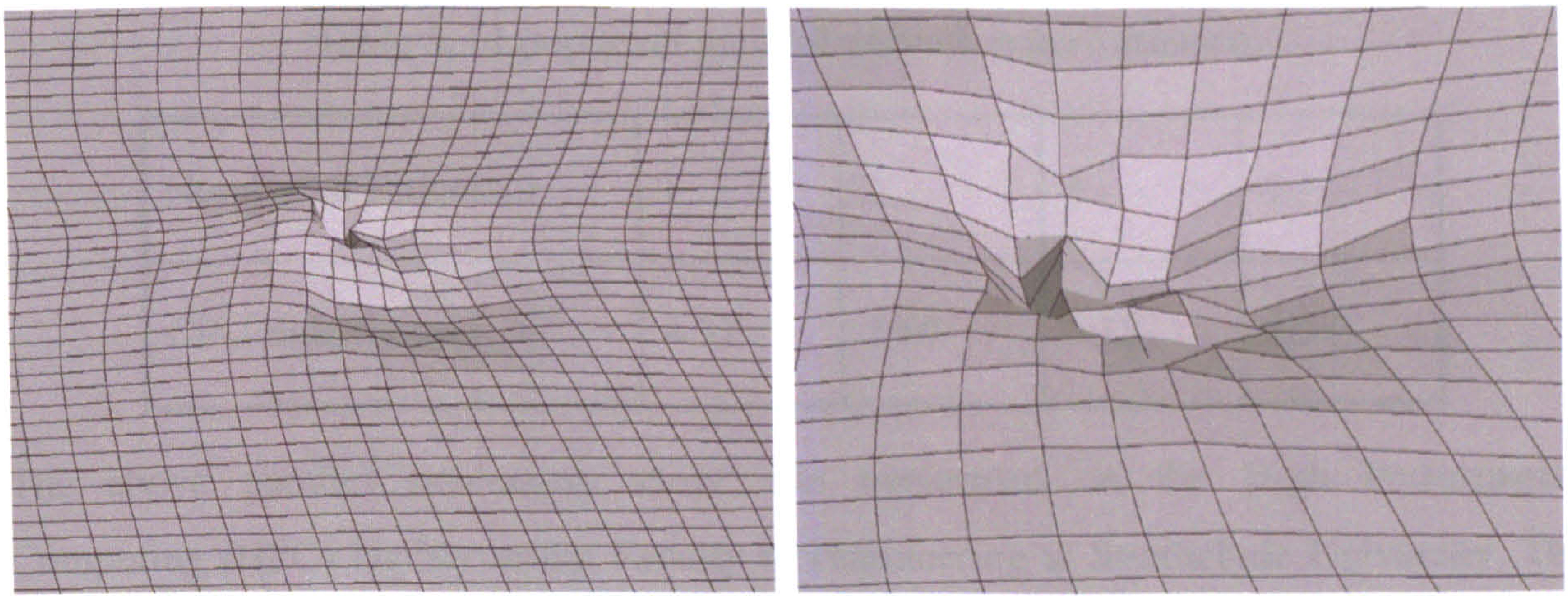

Figure 5.11 Dimples and crumpling on top plate surface in Domain-Level parallel mode.

The loop-level method parallelizes low-level loops in the code that are responsible for most of the computational cost. Some features like the general contact algorithm and kinematic constraints don't allow the use of parallel loops. The speedup factor may be significantly less than that with domain-level parallelization [5.14]. If the loop method is used with multiple parallel domains, this may cause a degraded parallel performance. The loop-level method may also scale poorly for more than four processors for some analysis.

An assessment of the parallel performance was made by comparing CPU time consumed when the tool is inserted to the plates 0.1mm in the initial model. The results are summarized in Table 5.3.

It is apparent from the table that increasing the processor number does not lead to improvement in computational cost saving in this particular application. Thus a decision was made to use single processor in the ongoing analysis.

Table 5.3 Loop level parallel execution performance.

Number of Processor	1	2	3	4
CPU time (hours)	4.37	5.10	6.15	8.31

The above parallel processing study was performed on the High Performance Computing (HPC) facility in the Faculty of Engineering at Strathclyde University. The HPC has 50 AMD Opteron Dual Core processors (2.0 Ghz), 224Gb memory and 6950 Gb disk size.

5.9 Other Analysis Options

5.9.1 Precision Level

ABAQUS/Explicit can be run in single-precision or double precision level, by default the double-precision level is used on machines with 64-bit word lengths and the single-precision level on 32-bit machines. The single-precision execution typically results in a CPU savings of 20% to 30% in comparison with the double-precision execution, and it provides accurate results for most cases. However the current analysis involving FSW requires greater than approximately 300,000 increments, and single precision tends to be inadequate. The analysis has to run with double precision for both element matrices and solver. If the double precision execution for output is used, floating point data is written to the ABAQUS/Explicit results file in double precision.

5.9.2 Stable Increment Estimator

There are two stable increment estimators available in ABAQUS/Explicit to determine the stability limit: element-by-element for both the thermal and mechanical solution responses and global for the mechanical solution response. The global estimator will not be used when adaptive meshing is included in the model, so the element-by-element is left to be the only choice. This element-by-element estimate is determined using the smallest time increment size based on the thermal and mechanical solution responses in each element. It is conservative and will give a smaller stable time increment than the true stability limit because the true stability limit is related to the maximum natural frequency of the entire model and considers the effect of boundary conditions and other constraints (Refer to section 3.5.2).

5.9.3 ALE Options

The mesh quality and the computational efficiency of adaptive meshing depend on the frequency of remeshing, advection sweeps performed, and the size of the adaptive mesh domains. Mesh sweep is the process of relocating the nodes and creating new mesh. While in an advection sweep solution variables from an old mesh is mapped to a new mesh (Refer to section 3.1.3). The number of advection sweeps is automatically determined according to the adaptive meshing frequency, mesh sweep frequency and the nodal movement in each mesh sweep. Normally, the cost of one advection sweep is several times greater than the cost of one mesh sweep. If adaptive meshing is performed too infrequently and/or a high number of mesh sweeps is specified multiple advection sweeps will be activated. For transient analysis without Eulerian boundaries or adaptive mesh constraints, the default frequency for adaptive meshing is 10 (i.e. every 10 solution increments), and the default number of mesh sweeps is 1. The default values are usually suitable for low- to moderate-rate dynamic problems undergoing moderate deformation. A typical adaptive mesh application will require adaptive meshing every 5–100 increments [5.14]. Thus a study was carried out to investigate the effect adaptive meshing frequency has on the coupled FSW model. The adaptive meshing at every 5, 10, 20, 50 and 100 increments were chosen in the study. The CPU time consumed when the tool is inserted to the plates 0.1mm are compared in Table 5.4.

Table 5.4

The CPU time consumed when the tool is inserted to the depth of 0.1mm (hours).

Mesh Sweeps	Adaptive Meshing Frequency				
	5	10	20	50	100
1	0.93	0.86	0.86	0.83	0.85
2	0.95	0.87	0.87	0.88	0.86

Table 5.4 demonstrates that, in this study, the adaptive meshing frequency has no significant effect on CPU time. However in the case that adaptive meshing is too infrequent and a small number of mesh sweeps is used, solution variables are not accurately mapped to the new mesh, which will cause excessive element distortion and termination of the analysis. Hence an adaptive meshing frequency of 10 was chosen in the on-going analysis. The accuracy was maintained in ABAQUS/EXPLICIT by automatically ajusting the advectiong frequency in each increment.

5.10 Assessment of the Initial Model

As mentioned before, there are four distinct phases in the FSW process, namely plunge, dwell, traverse and pull-out. With the parameters and options defined in previous sections, the initial model can successfully simulate the first two stages and the results data such as temperature, energy, strain, stress, and displacement can be obtained. However when this initial model is used to simulate the traverse phase, the analysis run terminates when the tool has moved a very small distance. Excessive distorted elements and zero or negative mass (a result from serious mesh deformation) were reported from ABAQUS as the cause of the early termination the analysis.

A diagnostics study of the elements at the end of step one (t=8.3s-) and the beginning of step two (t=8.3s+) was carried out. The discrepancy in the element size is noticeably demonstrated in Figure 5.12. The elements around the tool were smoothed and enlarged immediately after the completion of step one. This is due to the only operation between these two steps, adaptive meshing, which aims to minimize distortion and optimize element aspect ratios. If the mesh is initially highly distorted, the meshing algorithms in ABAQUS/Explicit will automatically smooth the mesh before the step starts so that the best possible mesh is utilized throughout the step. But this intervention is not welcomed in current application. By default two and five mesh sweeps are performed at the beginning of the second step for a uniform smoothing objective and a graded smoothing objective, respectively. To maintain the mesh pattern at the end of the plunge, an analysis without these initial mesh sweeps should be executed.

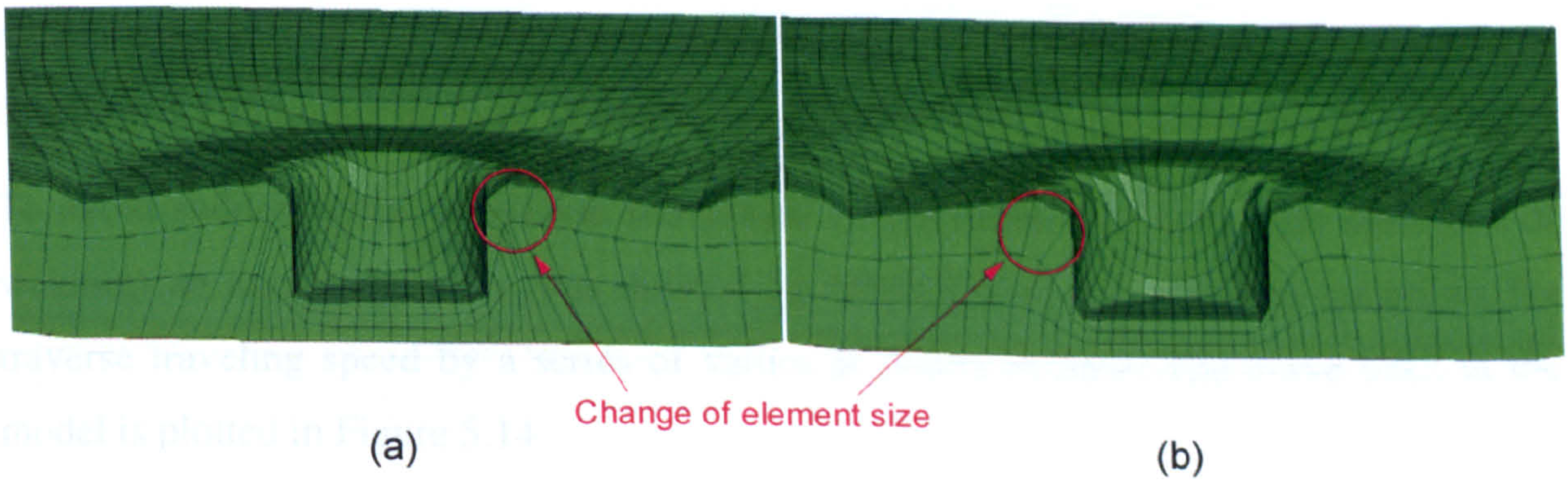

Figure 5.12 Deformed mesh of the initial model at (a) the end of step 1 and (b) beginning of step 2.

It was also found that the non-adaptive mesh domains surrounding the adaptive domain affected and restrained the adaptive remeshing process for the reason that the nodes on a boundary region between an adaptive mesh domain and a non-adaptive domain are always non-adaptive. If the transverse movement of the tool is included in the simulation, it is desirable to define the whole plate as the adaptive domain. For the plate configurations used here, however, remeshing the whole plate will significantly increase the computational costs. Thus a smaller plate model is needed for the purpose of the complete FSW process simulation which considers the trade off between model solution time and model size. Such a model is proposed and discussed in the following Section 5.11. Although others [5.15-5.17] have tried to simulate the whole process, they didn't succeed and only plunge stage was modeled in their models.

5.11 Improved Model and Results

In the improved model, the plate is much smaller than the initial model with a length of 60 mm and a width of 30 mm. It was meshed uniformly with element size 0.5mm X 0.5mm in the X-Y plane and 1 mm in the Z direction. The FE model (top view and cross-section view) is shown in Figure 5.13. The ALE adaptive meshing algorithm was applied to the entire model except the rigid surface TOOL and BACKING PLATE regions. The rest of the model configurations including thermal boundary conditions, contact pairs and other analysis options were kept the same as the initial model.

To avoid sudden initial transverse movement (i.e. infinite acceleration at the onset of welding) an amplitude curve was defined in ABAQUS to specify time variations for traverse traveling speed by a series of values at points in time. The curve used in the model is plotted in Figure 5.14.

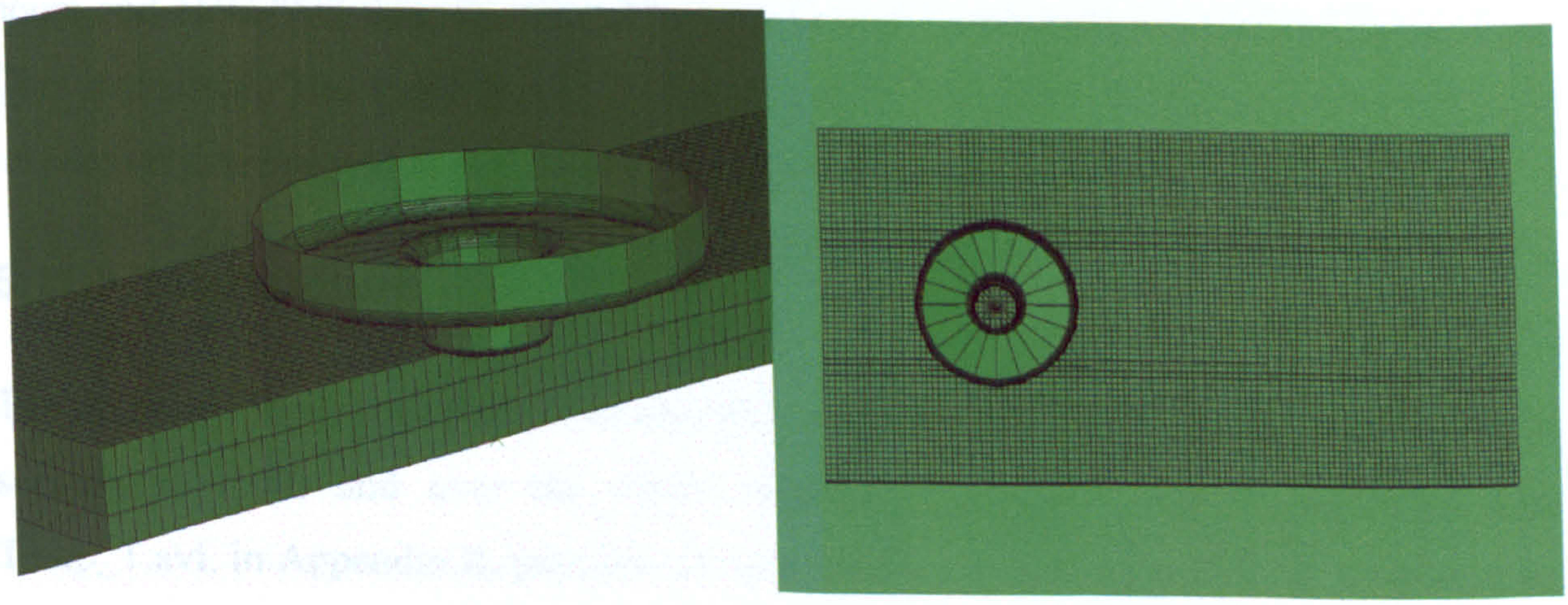

Figure 5.13 Improved FE model for FSW process - Cross-section view and top view.

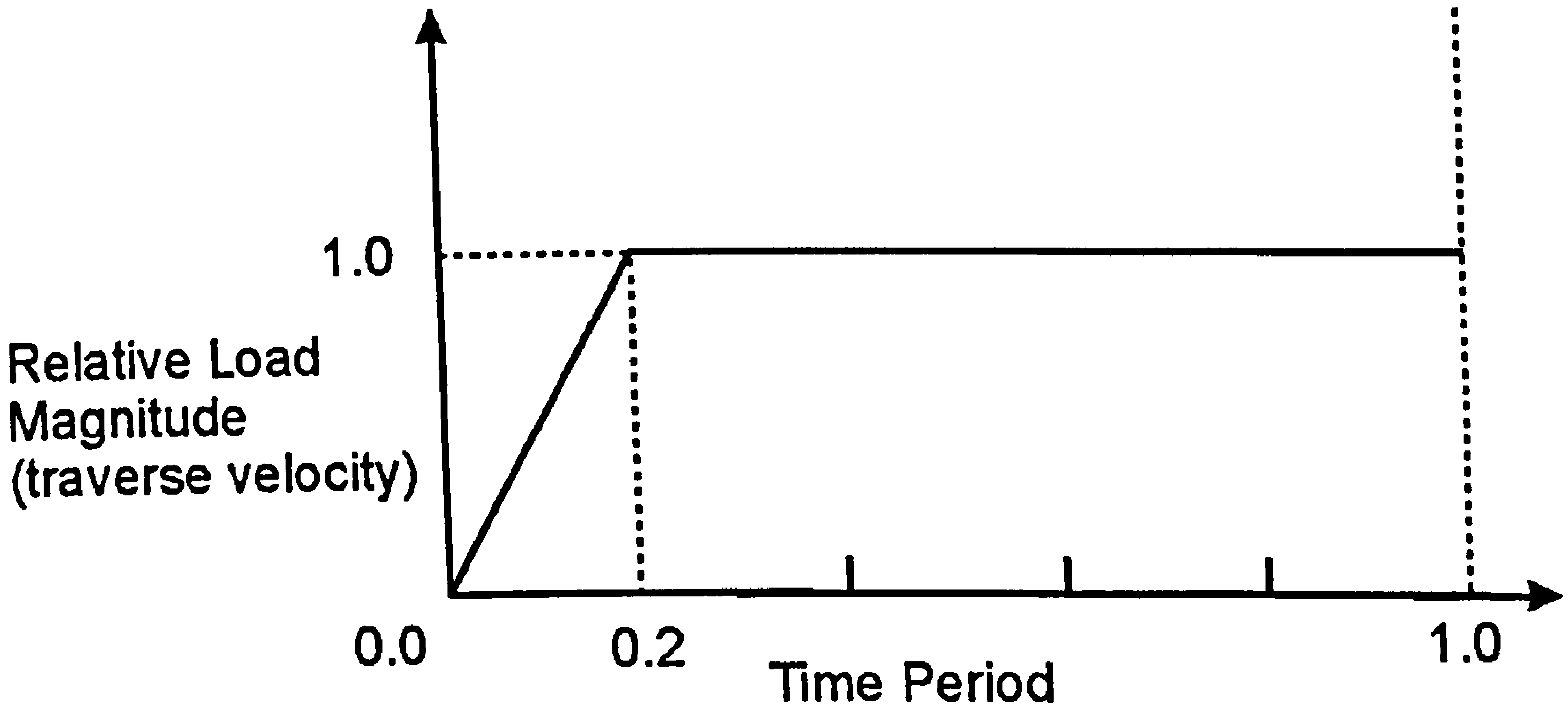

Figure 5.14 Amplitude curve for welding traverse velocity in the traverse stage.

The tool has a penetration speed of 0.25 mm/s and a plunging time of 8.3 seconds which equate to a sinking depth of 0.075 mm. Following the plunge stage is the 0.1 second dwell phase. This was found to be appropriate to generate a suitable temperature field and to keep the welding material in a well-plasticized state so that a sound weld can be produced [5.18]. The welding speed and welding time during the final traverse stage were set to 2 mm/s and 14 seconds, respectively. The whole process took 21 days and 6 hours and 15927977 time increments to run on a PC with 2.0 Ghz AMD Opteron Dual Core processor. The input file and solution status file named input.inp and status.sta, respectively, are provided in folder Appendix B of the appendix CD.

5.11.1 Temperature

The improved model can predict temperature evolution through the whole process (22.4 seconds in total) and over the whole volume. The video files Temp_X.avi and Temp_T.avi, in Appendix B, presents the animation, over 22.4 seconds, of cross-section view and top view of the temperature contour plot, respectively. The temperature distributions at six representative time points 6.8s, 8.3s, 8.4s, 10.4s, 15.4s and 22.4s are shown in Figure 5.15. The top row pictures give the cross-section views along the welding joint line while the bottom row pictures provide the views from the top.

When only the pin was in contact with the workpiece, the maximum temperature in the workpiece occurred somewhere adjacent to the edge of the pin bottom surface. Thereafter, the maximum temperature moved towards the corner between pin and shoulder surfaces. At 6.8s the shoulder surface started to contact the workpiece, where upon the maximum temperature was around the shoulder-workpiece interface. At 8.3s the full contact condition was established between tool surface and top surface of the workpiece. A high temperature gradient with a "basin" or “V” shape appeared in the workpiece beneath the tool demonstrating high heat flux between the interface layer and workpiece's material outside the shoulder radius. After the 0.1s dwelling, the temperature was distributed more even between the leading side and trailing side of the tool. Then the tool started to traverse to join the plates together. The welding process quickly reached steady state and the temperature distribution pattern around the tool exhibited little variation as displayed at 10.4s, 15.4s and 22.4s in Figure 5.15.

The temperature contour looks almost symmetric along the joint line on both the retreating and advancing sides. It means the rotating direction will not affect the temperature distribution.

The maximum temperature was found to be greater than melting point, the reason for this maybe due to the boundary condition between the tool and workpiece. The tool was assumed to be rigid isothermal and has no temperature DOF, there is no direct heat transfer between the tool and workpiece. Only a concentrated heat capacity was specified and 20% of the total frictional energy was set to flow into the tool. The remaining 80% of the frictional energy together with the plastic dissipation energy could possibly account for the temperature in an element being greater than the melting point. In reality, the fraction of frictional energy into the workpiece depends on the temperature and heat conductivities in the tool and workpiece. The total frictional energy was calculated with a constant friction coefficient, which is a function temperature and contact pressure. However the most plausible reason is thought to do with mass scaling; the significantly increased material density had changed the original physical problem as the density is involved in both the mechanical and thermal governing equations.

5.11.2 Stress Distribution

One of the most important features of the proposed model is the ability to predict the stress distributions (active stress and residual stress) over the whole FSW process. The evolution of von Mises stress field is presented in video format in the Appendix B files, Stress_X.avi and Stress_T.avi as well as in picture format in Figure 5.16 Figure 5.16 shows the von Mises stress plots at nine characteristic time points, 0.2s, 1.0s, 3.0s, 6.6s, 7.1s, 8.3s, 10.4s, 15.4s and 22.4s from the start of the process. At the commencement of plunging, an axial force was exerted on the material beneath the tool pin where distinct high stress existed. With the growth of the heat at the pin-workpiece interface, the material was softening. At 3.0s the stress in the plates under the tool pin nearly approached zero ascribed to the extremely high temperature in this area. The reduction of stress is a result of an increase in temperature as signified from the constitutive equations. The maximum stress migrated to somewhere remote from the pin-workpiece interface. But there was still a cylindrical layer of material surrounding the tool pin that had fairly high stress as shown in the von Mises stress plot at 6.6s.

After the tool shoulder touched the workpiece, the cylindrical high stress layer gradually disappeared since the material was heated up by the heat generated at the shoulder-pin interface. At 8.3s most of the material under the tool was softened and in a state that it could be easily stirred. During the welding stage no obvious variation in the stress field around the tool was found. From the observation of the stress field evolution, in Figure 5.16 in pages 161-162, it can easily be concluded that the temperature variation imposes a significant effect on the stress and consequently on the formation of the weld.

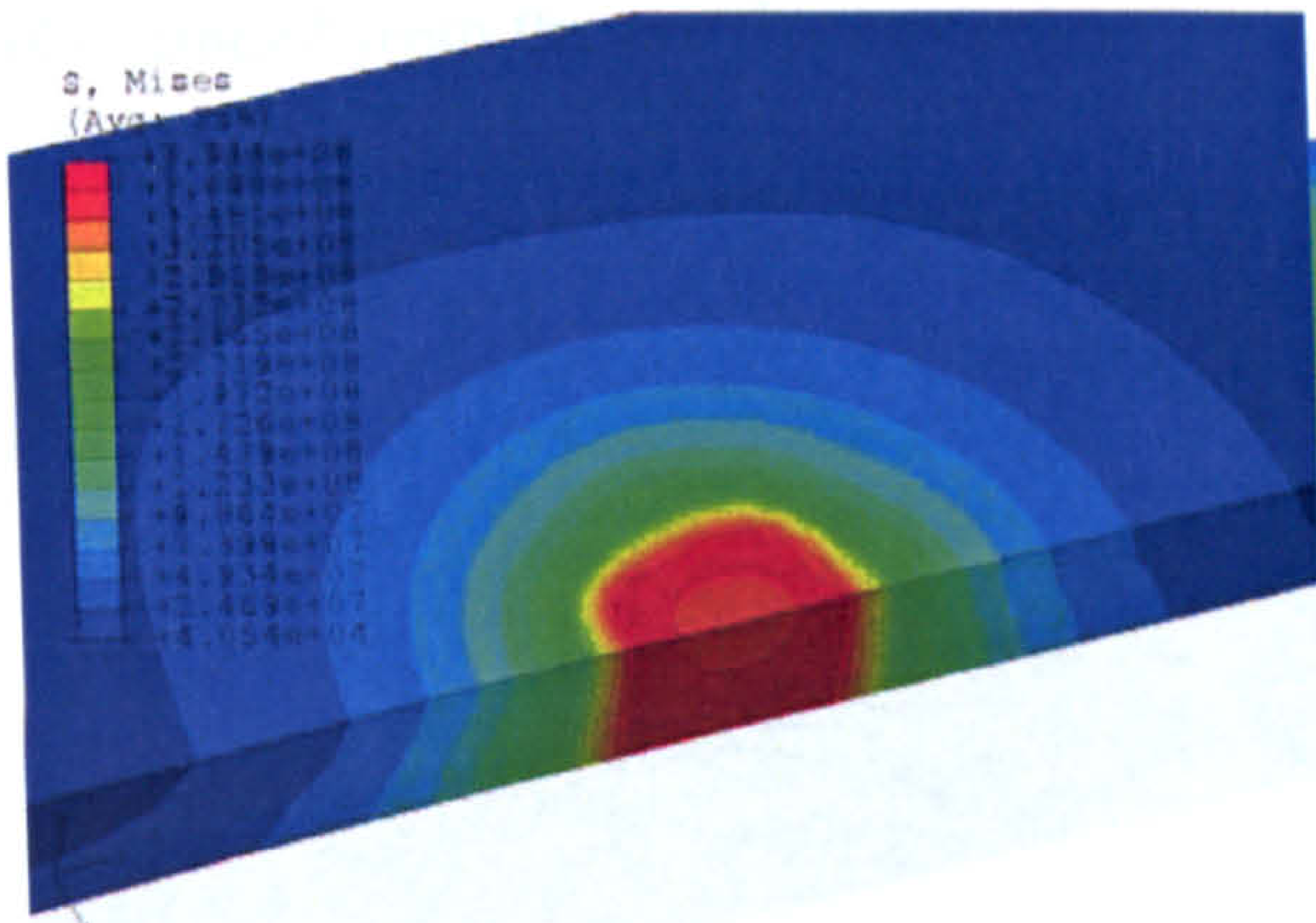

0.2s

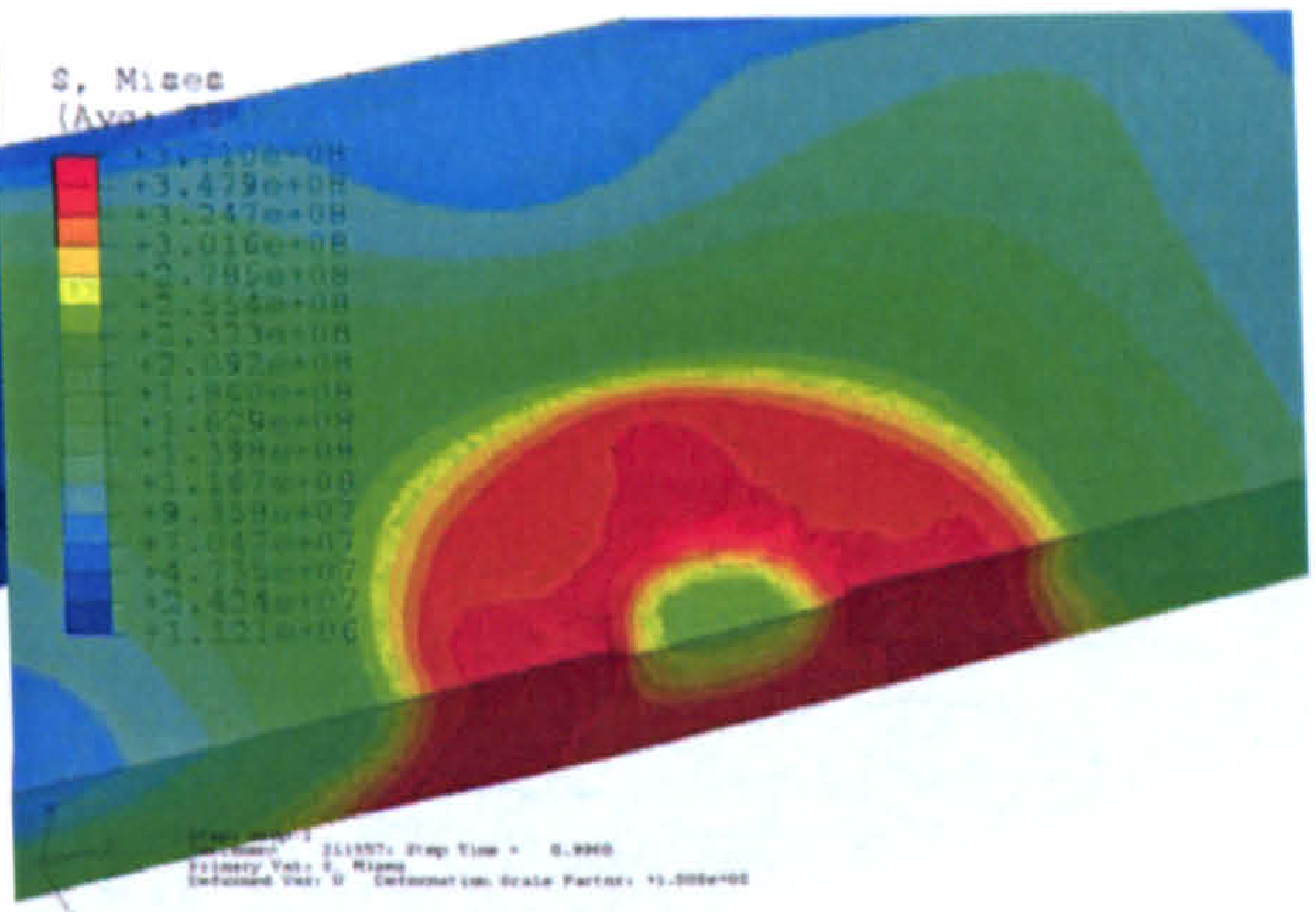

1.0s

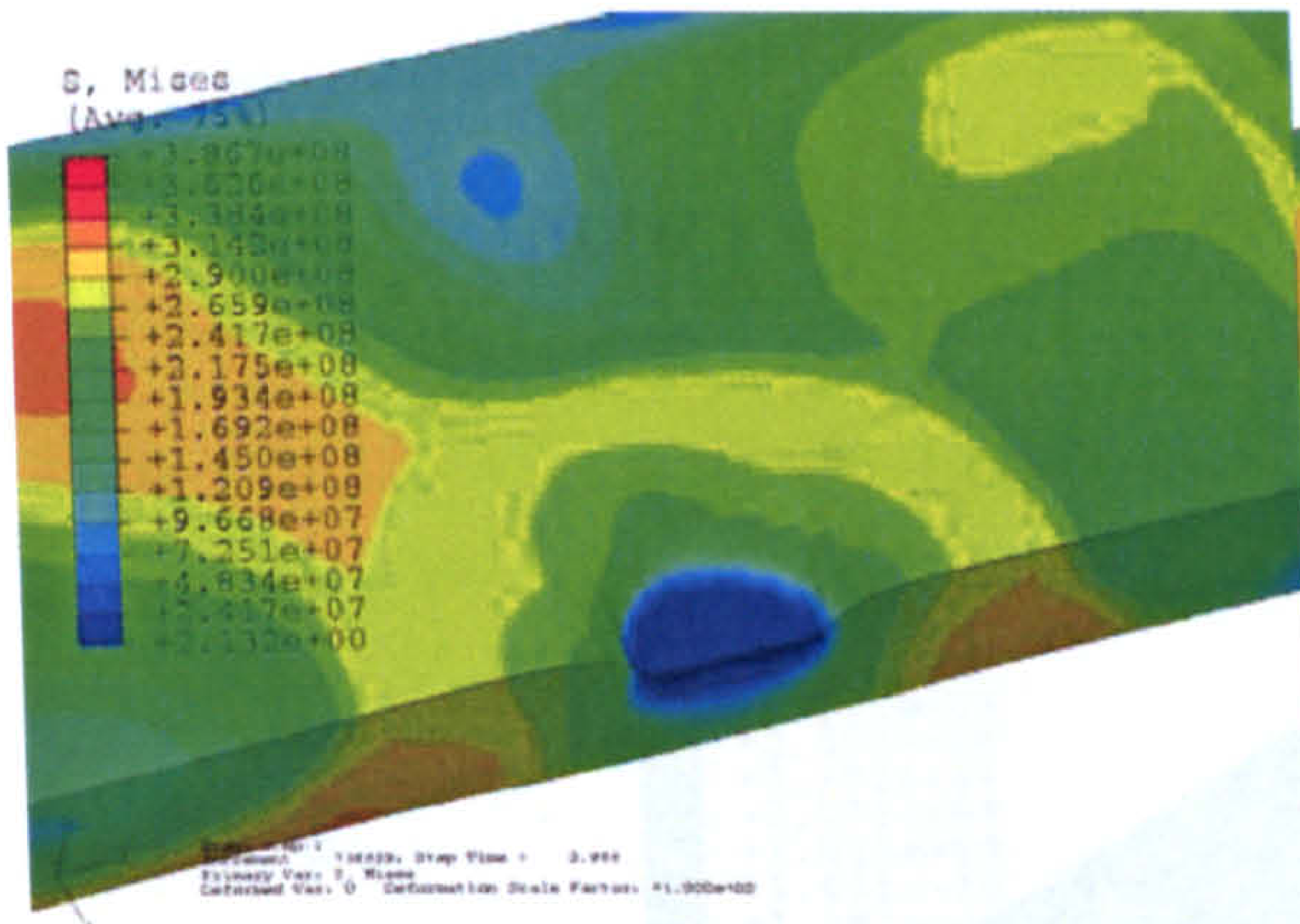

3.0s

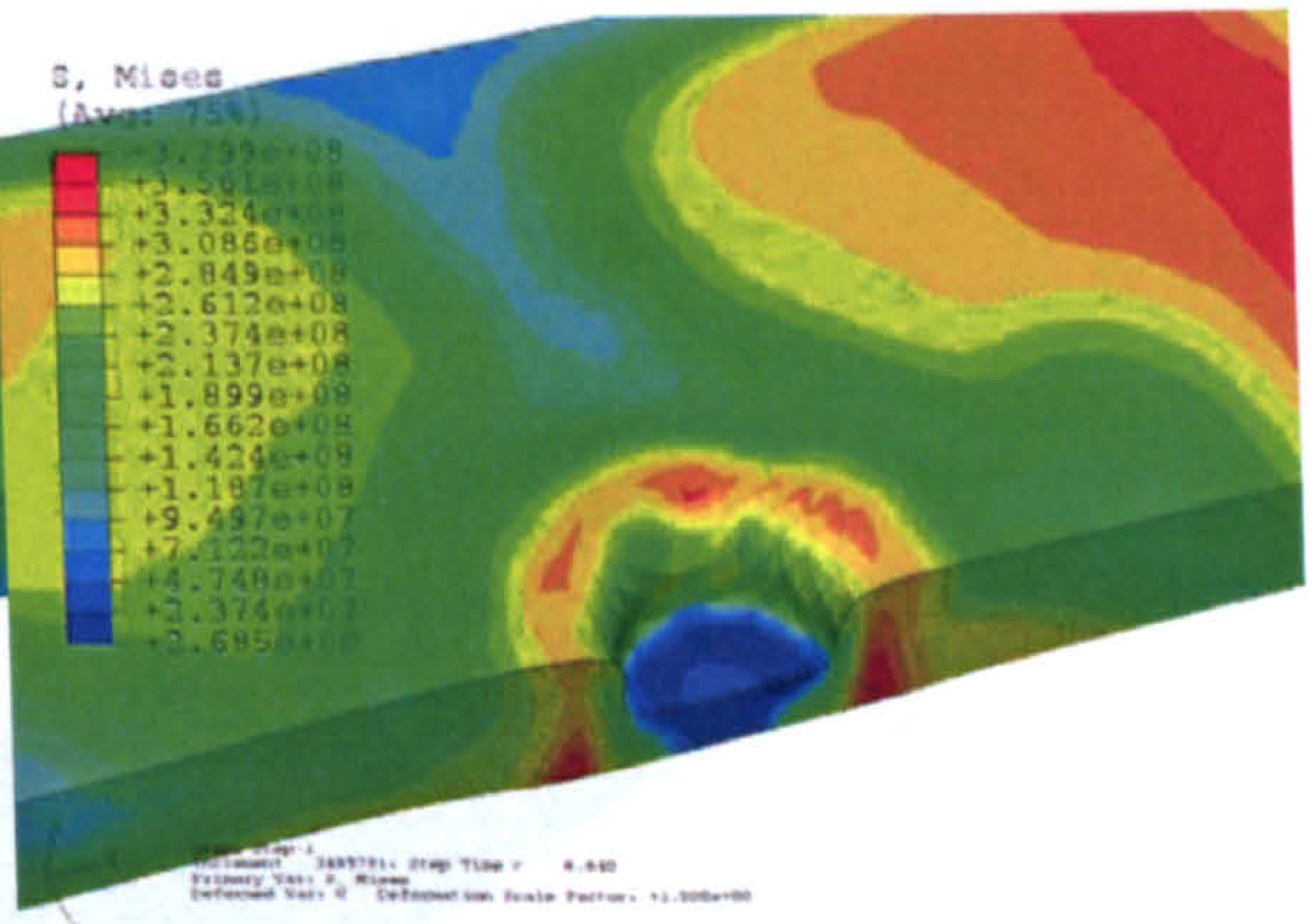

6.6s

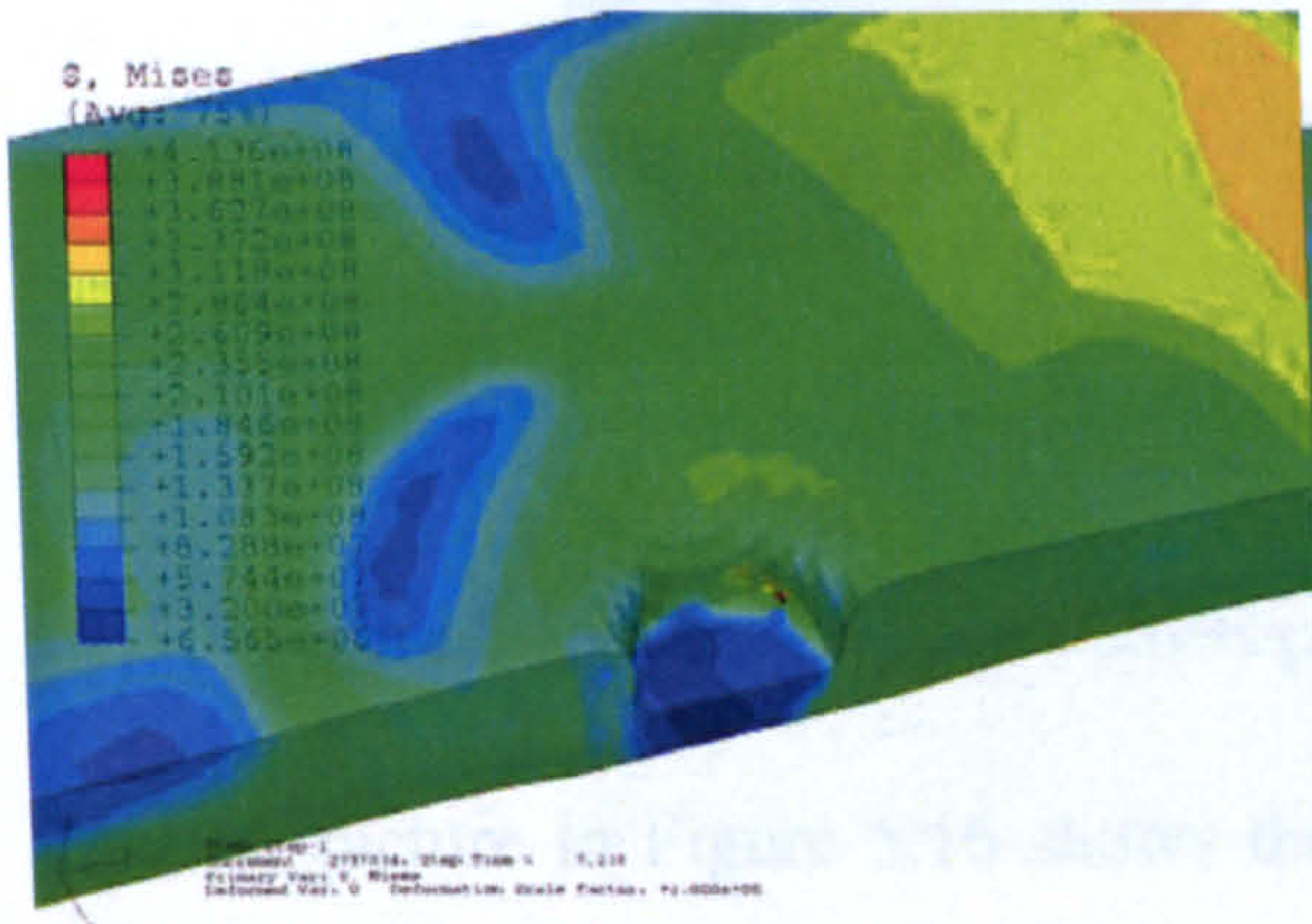

7.1s

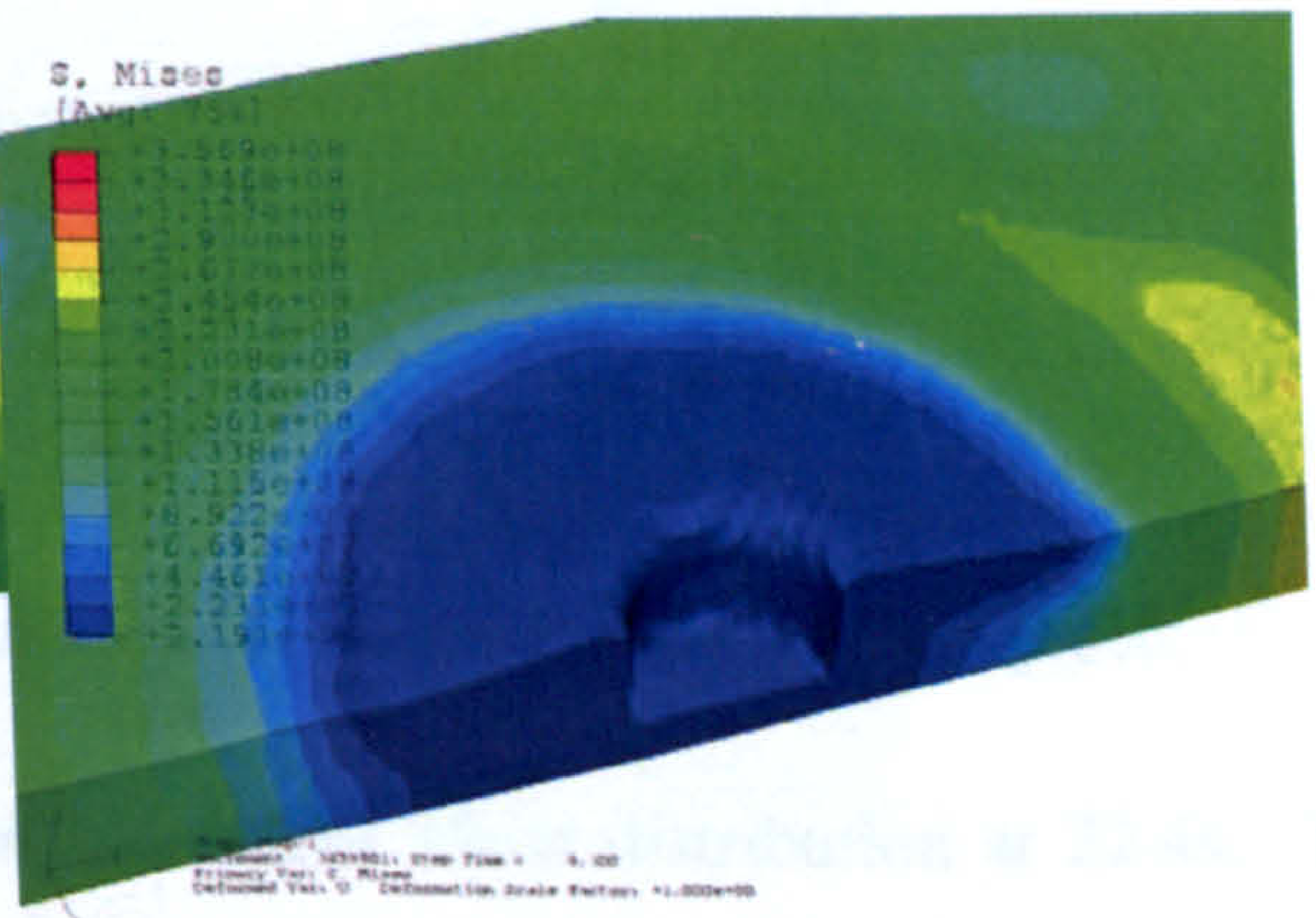

8.3s

(Continued from the previous page)

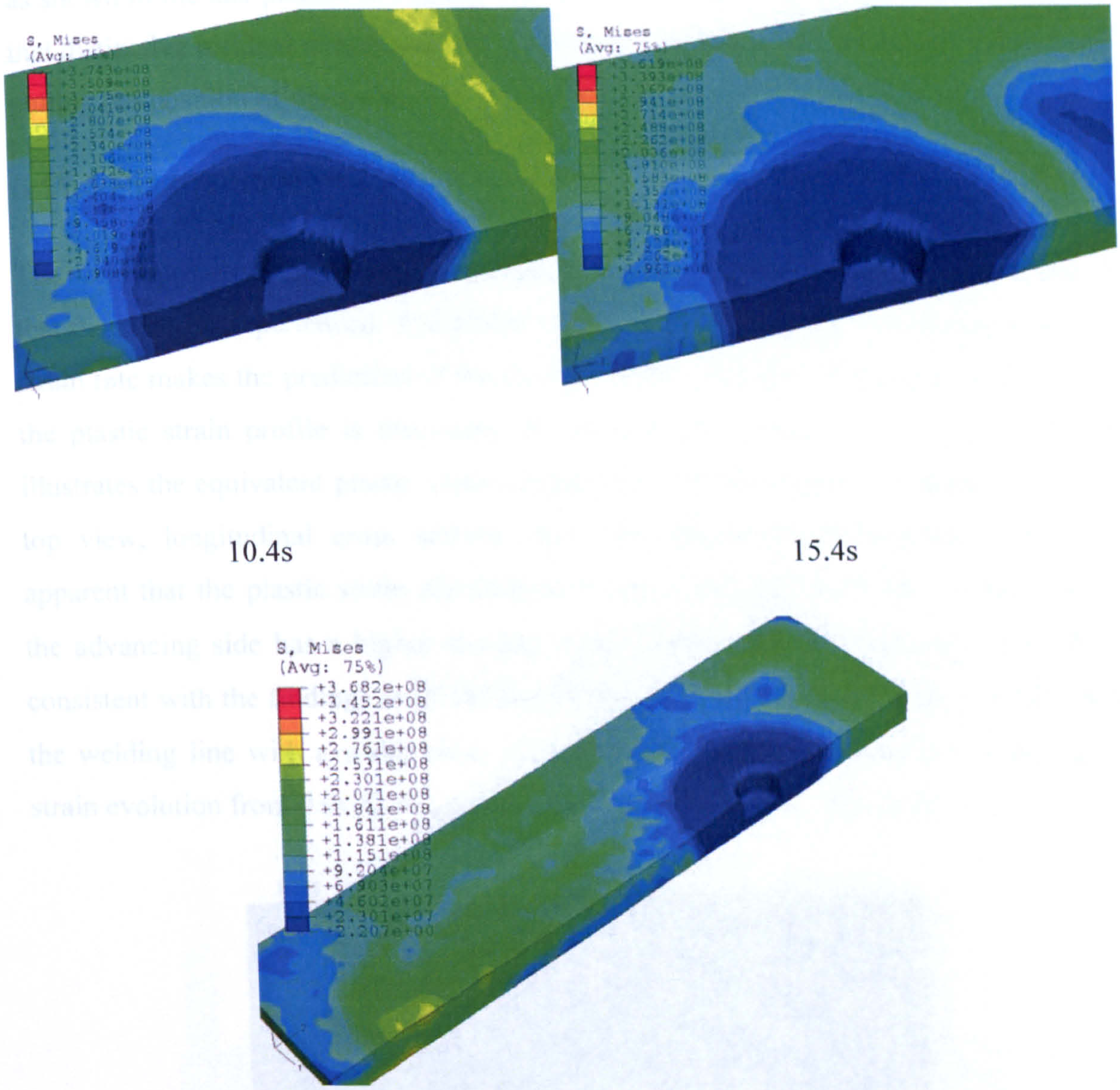

10.4s 15.4s

22.4s

Figure 5.16 The von Mises stress plot at various time point for workpiece.

The last picture in Figure 5.16 shows the von Mises stress distribution at 22.4s. The maximum von Mises stress in the region close to the starting position of the welding, increased from zero up to 270 MPa. However the stress in the region nearer to the tool was quite low. This could be the result of the small model used which is only 60 mm long and 30 mm wide. The temperature was still very high over the whole plate at 22.4s as shown in the last picture of Figure 5.15. If the workpiece cooled down it is expected that distinctive residual stress could be identified along the welding line towards the tool pulling out position of the weld.

5.11.3 Plastic Strain

The weld microstructure strongly depends on the thermal cycle and plastic deformation that the material experienced. The ability of the model to calculate the plastic strain and strain rate makes the prediction of the microstructure possible. In the present study only the plastic strain profile is discussed. As an example, Figure 5.17 in pages 163-164 illustrates the equivalent plastic strain contour at 13.4s from three perspectives, namely, top view, longitudinal cross section view and transverse cross-section view. It is apparent that the plastic strain distribution is not symmetric about the joining line and the advancing side has a higher average plastic strain than the retreating side. This is consistent with the findings in [5.18] and [5.19]. The highest plastic region is still along the welding line with a width close to the pin diameter. The animation of the plastic strain evolution from 0 to 22.4s can be found in file PEEQ.avi, Appendix B.

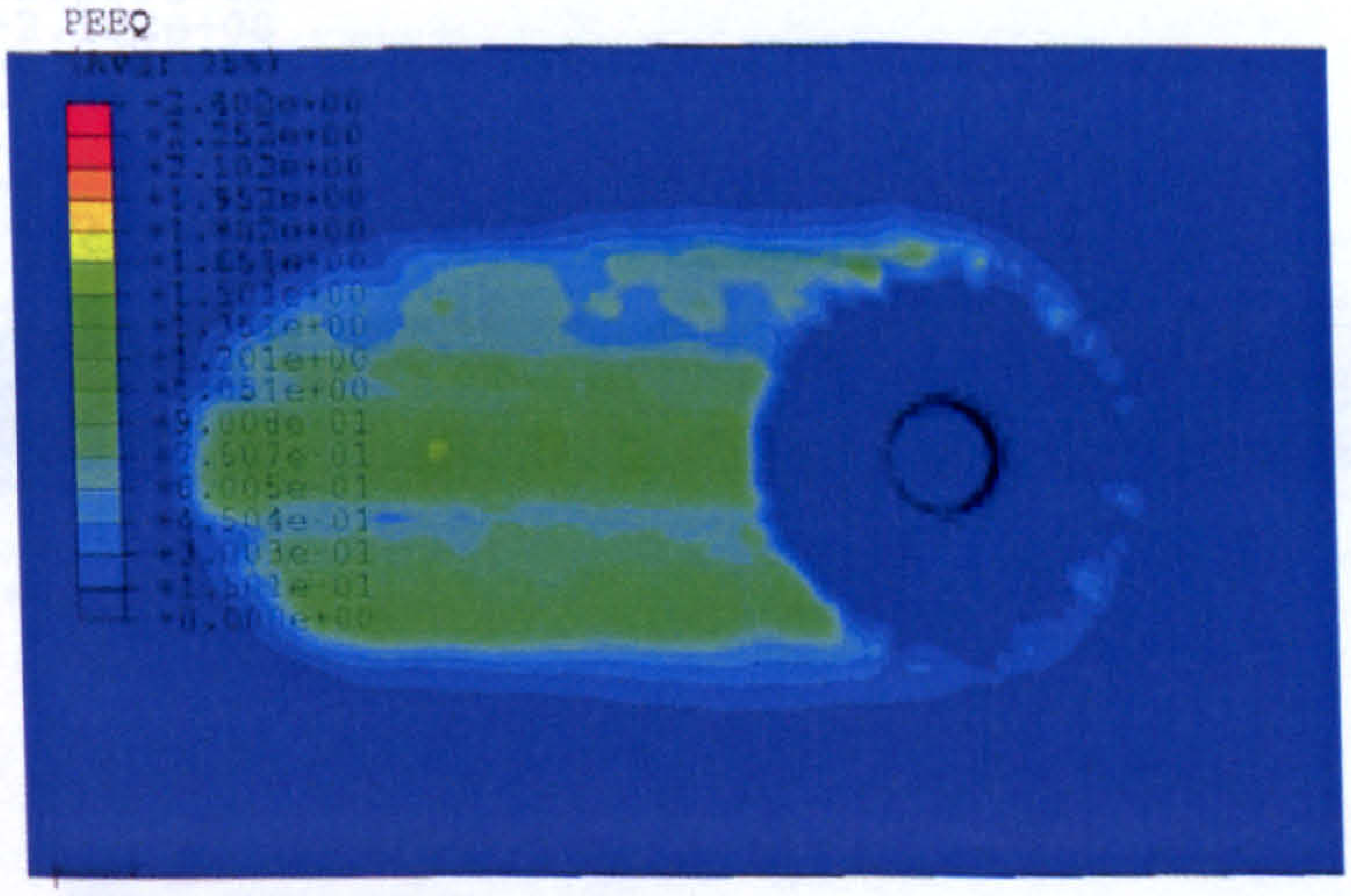

(a) Top view

(Continued from the previous page)

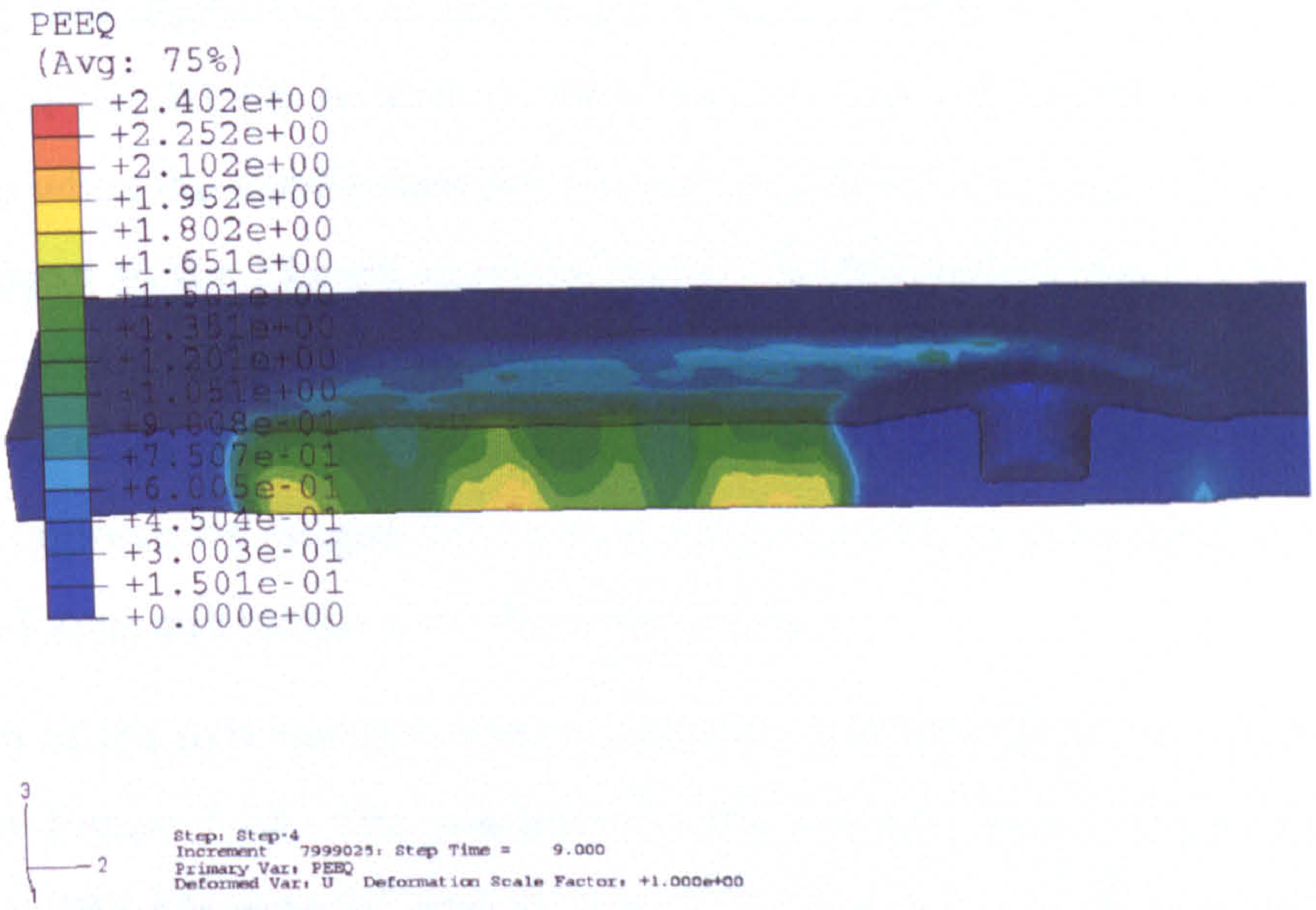

(b) Longitudinal cross-section view

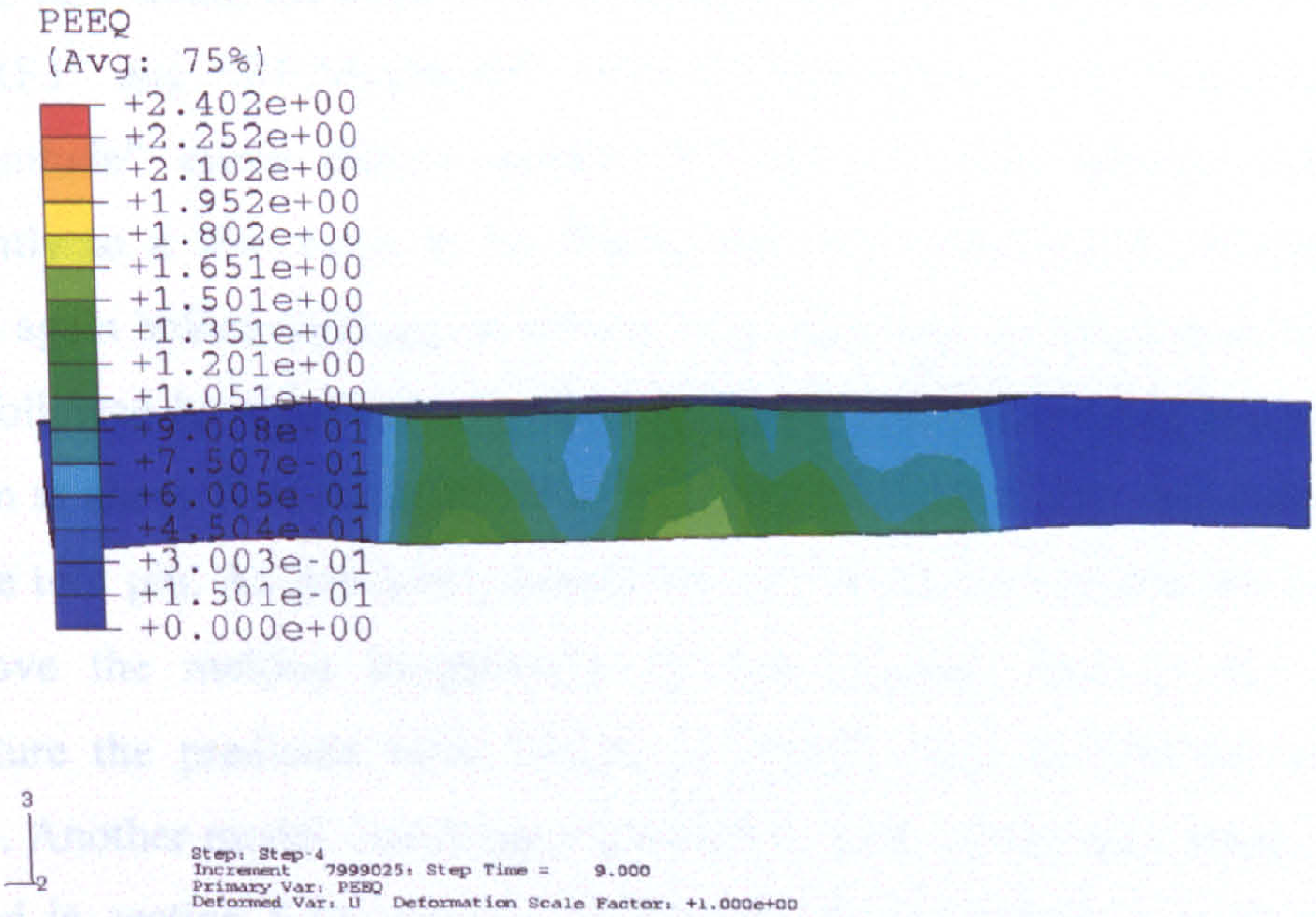

(c) Transverse cross-section view

Figure 5.17 Equivalent plastic strain contour plots at 13.4s.

5.11.4 Tool Reaction Force and Torque

Predicting the tool reaction force and torque is another distinctive feature of the current model. Most of the 3D FE models in the literature can only compute the force in the welding stage when the steady state has been established. However it is well known that the pin is subject to the highest reaction forces in the plunge stage, as revealed in the experimental work [5.20]. The considerable stresses that the pin experienced can cause it to break or be worn off if the mechanical strength is not sufficient. To prevent tool damage and improve its fatigue life, it is necessary to know, reasonably accurately, the tool reaction forces and torque over the whole process.

The variation of the tool reaction forces with time when plunging at a constant speed is illustrated in Figure 5.18. The resultant reaction force magnitude is denoted by the purple curve, "RF:Magnitude" and the reaction axial force in the (Z) direction by the orange curve, "RF3". The other two curves, "RF1" and "RF2" refer to the reaction forces in transverse (X) and longitudinal (Y) directions, respectively. As "RF1" and "RF2" are very small, the axial force component dominates the resultant reaction force, hence "RF3" and "RF:Magnitude" have similar curves with opposite signs. The "RF:Magnitude" curve climbs quickly for the first two seconds and then falls significantly to a low value at 5s. During the next half second the curve suddenly increases again before reaching, at around 7s, a value just below the previous maximum. This is followed by a period of gradual decrease with fluctuation. The deep drop to a minimum at about 5s is thought due to the abrupt local material temperature increment under the tool pin. As previously mentioned, the predicted temperature in the analysis, was above the melting temperature for the material. Due to the overestimated temperature the predicted force history in plunge stage is believed to be not very accurate. Another model, involving a parametric study of the tool shape, which will be described in section 5.12, gives a better temperature prediction correlating well with experimental observation.

Figure 5.19 illustrates the variation of the tool reaction torque with time. "RM1", "RM2" and "RM3" stand for the reaction torque components in X, Y, Z directions, respectively.

The resultant torque is represented by purple curve "RM:Magnitude". The resultant torque curve shows great similarity to the resultant reaction force curve in Figure 5.18 except that at around 6.8s when the tool started to contact the workpiece. At 6.8s the "RM:Magnitude" curve jumped to its peak value which is much higher than the previous maximum before 6.8s. After 8.4s in the dwell and traverse stages the curve gradually decreases with fluctuation.

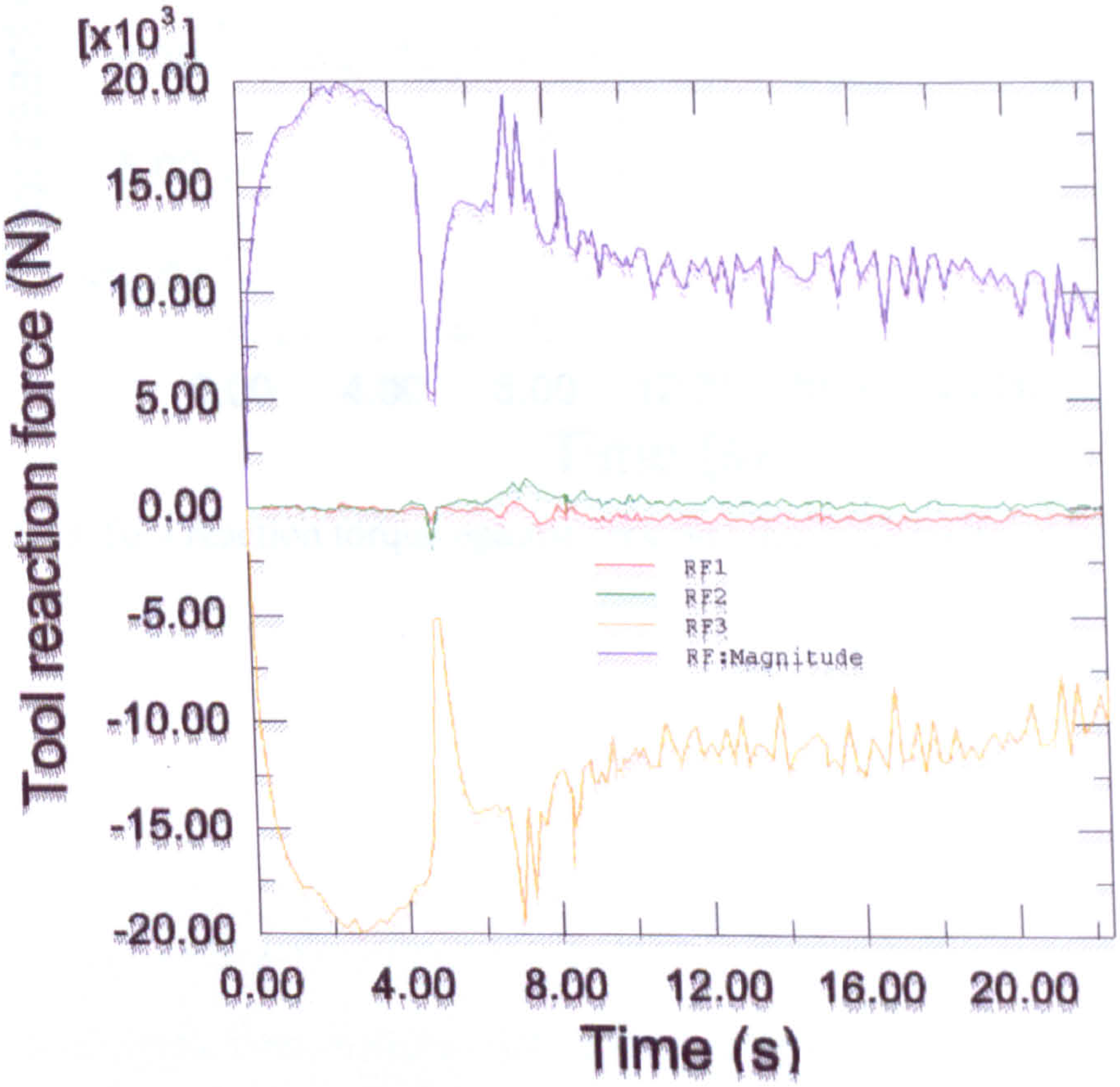

Figure 5.18 Tool reaction forces against time plot during the whole FSW process.

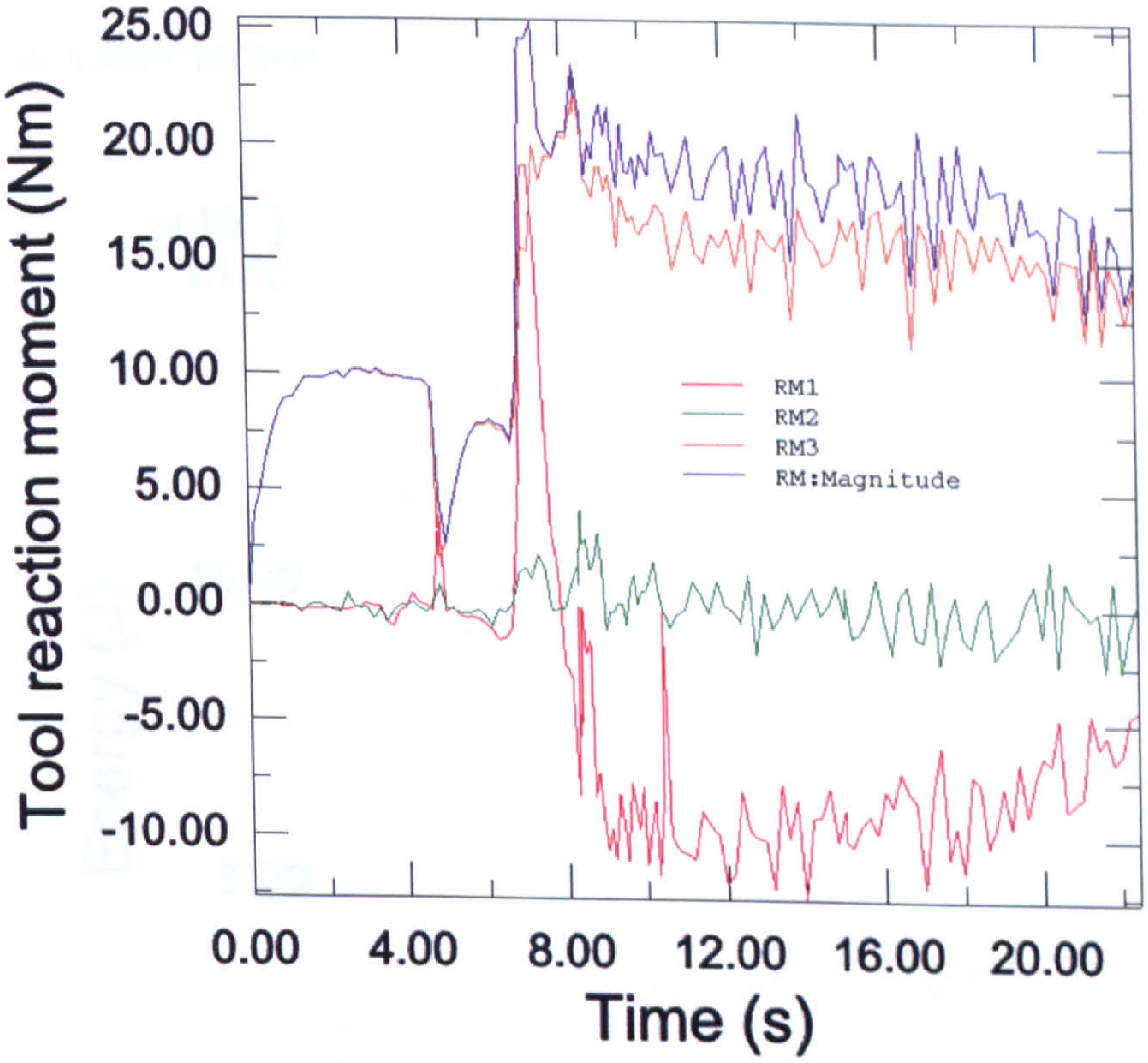

Figure 5.19 Tool reaction torque against time plot during the whole FSW process.

5.11.5 Heat Generation

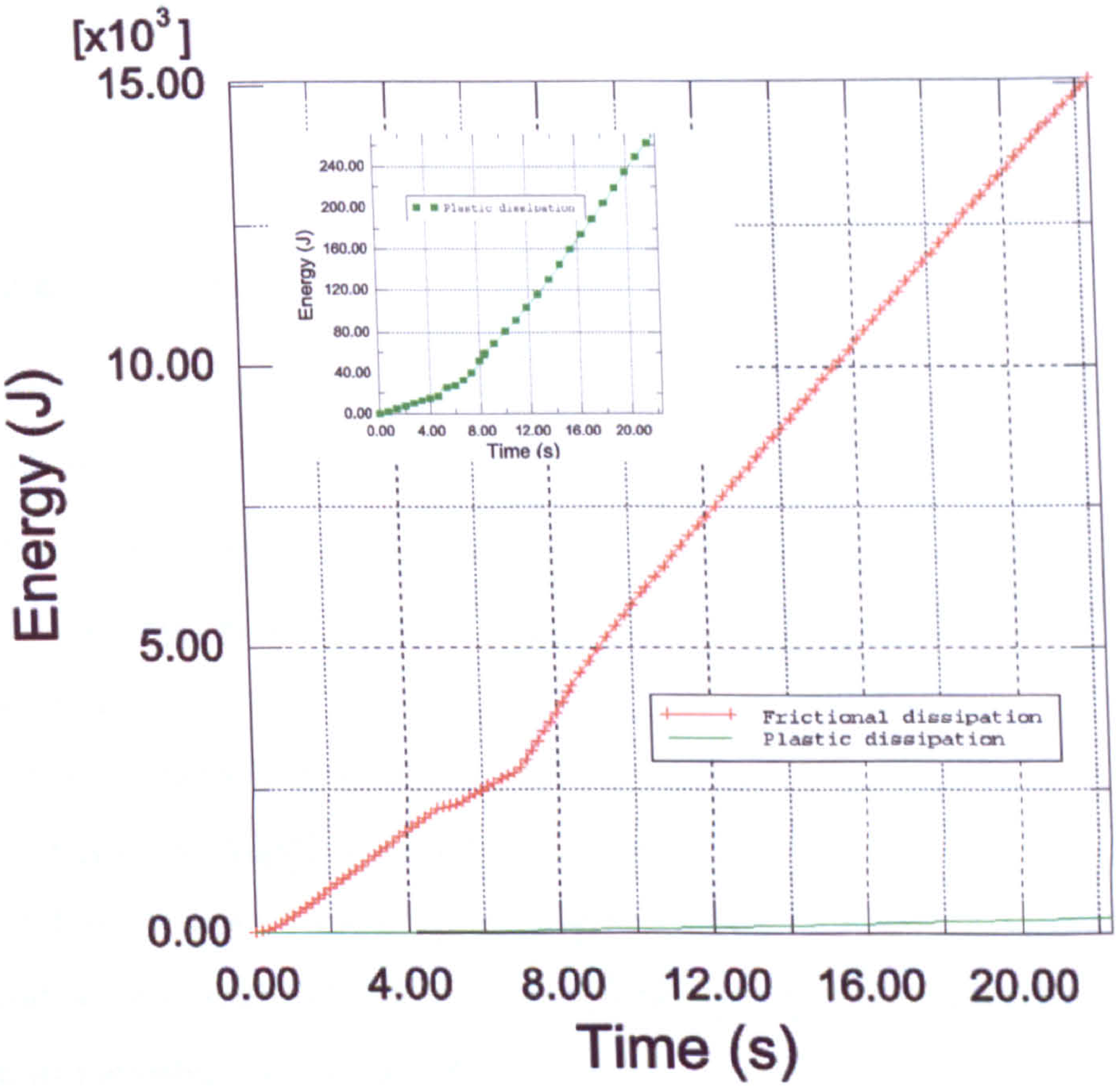

Figure 5.20 Heat generation histories from frictional and plastic dissipation.

Heat generated from both friction and plastic deformation is plotted against time as shown in Figure 5.20. Frictional energy dissipation and plastic dissipation increase in a bilinear manner. There is a smooth transition region around 6s and generation rates become higher after 6.8s. In the current model results, friction was responsible for generating most of the heat need even when full contact condition had established and severe plastic deformation occurred. The model used a constant friction coefficient, 0.3 [5.29] and neglected its temperature dependence. The surface interaction involving contact pressure, friction, temperature dependence etc, is very complicated and not fully understood yet. During the process, the friction force may also exceed the maximum yield shear stress. The current assumed contact condition is far from the real situation.

However due to the uncertainty in the literature as to the nature of the surface interaction, it was decided, as a first step, to keep the contact model definition relatively simple. A more complex model or one that at least considers the temperature effect should give more accurate results, and the percentage of friction generated heat due to frictional effects will be expected to reduce.

5.11.6 Material Movement

The reader is reminded that, for this simulation, the plunge takes 8.3s, a dwell for 0.1s and a traverse occurs in the remainder of the simulation.

The material flow during FSW is complicated and directly influences the properties of a FSW weld. It is of vital importance to understand the deformation process and basic physics of the material flow for optimal tool design. To visualize the material flow phenomenon, tracer particle sets were defined symmetrically, each side, along the welding line to track the material movement at specific locations. Seven tracer particle sets numbered 1 to 7, were used and highlighted by red points in Figure 5.21. Each tracer set includes a few particles in a line or/and in a plane and their initial positions are clearly shown in the different views in Figure 5.21. For the set tracer1 the initial location of each particle also can be found in Figure 5.10.

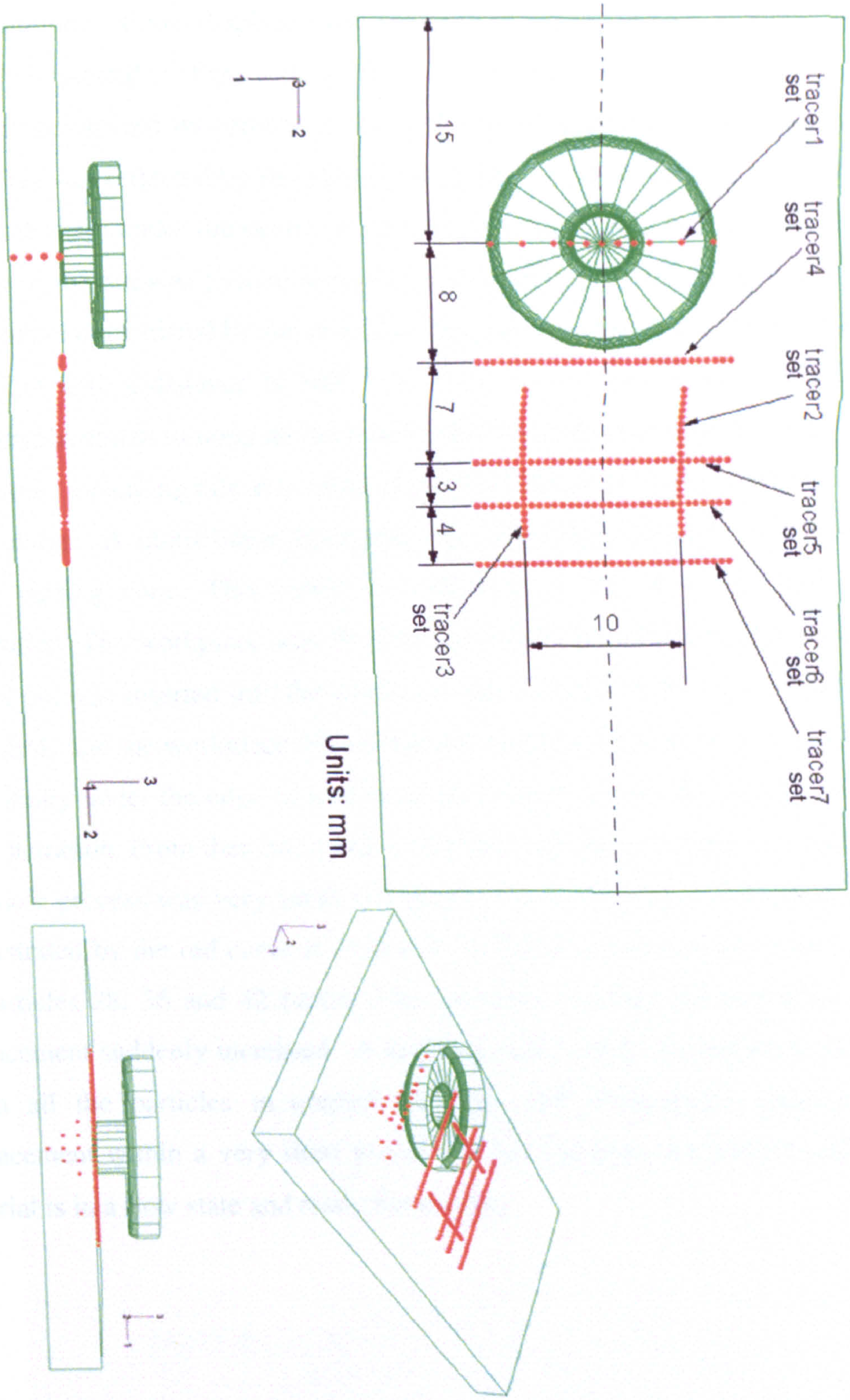

Figure 5.21 Original locations of defined tracer particle sets.

The magnitude of the displacement for several representative particles in tracer set "tracerl" is plotted in Figure 5.22. The selected particles are numbered in the Figure 5.23. The downward movement of the tool was displacement controlled at a constant speed. This was reflected by the plot of the displacement magnitude of tracer particle 30 which is directly under the centre of the tool, having a linear straight line. Particle 28 at the edge of the pin was pushed aside when then pin started plunging hence it had small displacement until stirred by the shoulder. Particle 29 which is also below the pin bottom surface but with a distance of half a tool pin radius from the pin centre experienced largest displacement (among all the tracer particles defined in current model) until about 7.5 seconds, indicating this area of the material suffered most of the stir at the beginning of the plunge. A quasi-linear increment was identified for particles remote from the intense stirring zone. This could be explained as the result of global workpiece deformation. The workpiece was fixed by constraining its bottom edge nodes, so when the tool pin was inserted into the workpiece the material under the tool pin was pushed downwards and the workpiece outside the pin radius bulged upwards. Particle 25, which was initially under the edge of tool shoulder, moved outside the shoulder radius during tool penetration. From then on, it had no contact with the tool, thus its displacement over the whole process was very small and purely due to the global workpiece deformation, as illustrated by the red curve in Figure 5.22. There was no contact with the tool either for particles 28, 36 and 42 before 7.8s, but once touched and stirred by the tool, the displacement suddenly increased. A key time point can be identified at about 8.4s, after which all the particles in contact with the tool experienced significant boost in displacement within a very short period. At this moment, it could be said say that the material is in a flow state and ready for welding.

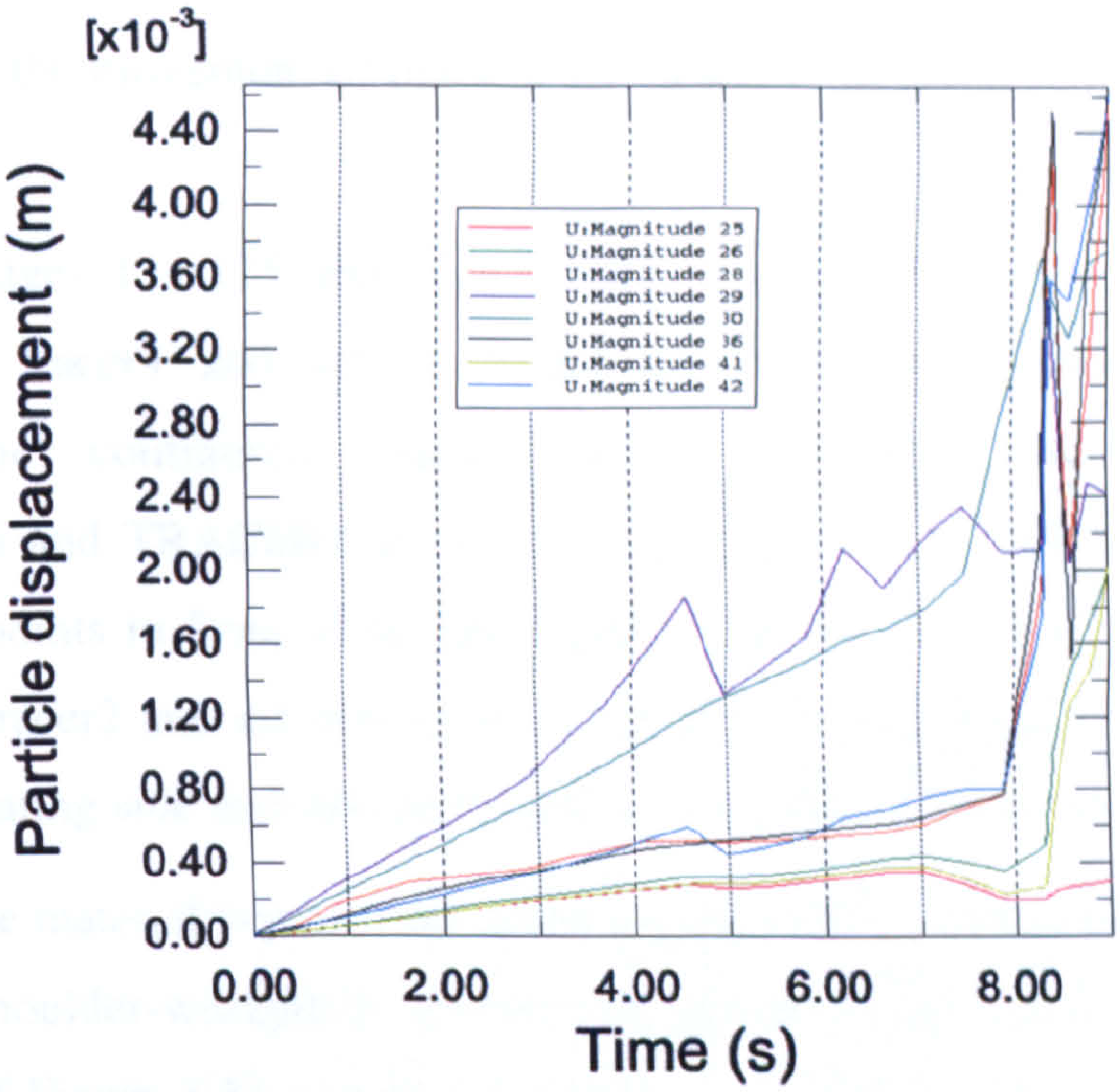

Figure 5.22 Displacement magnitudes for selected particles in tracer particle set "tracer1" from the start of the process up to 9 seconds.

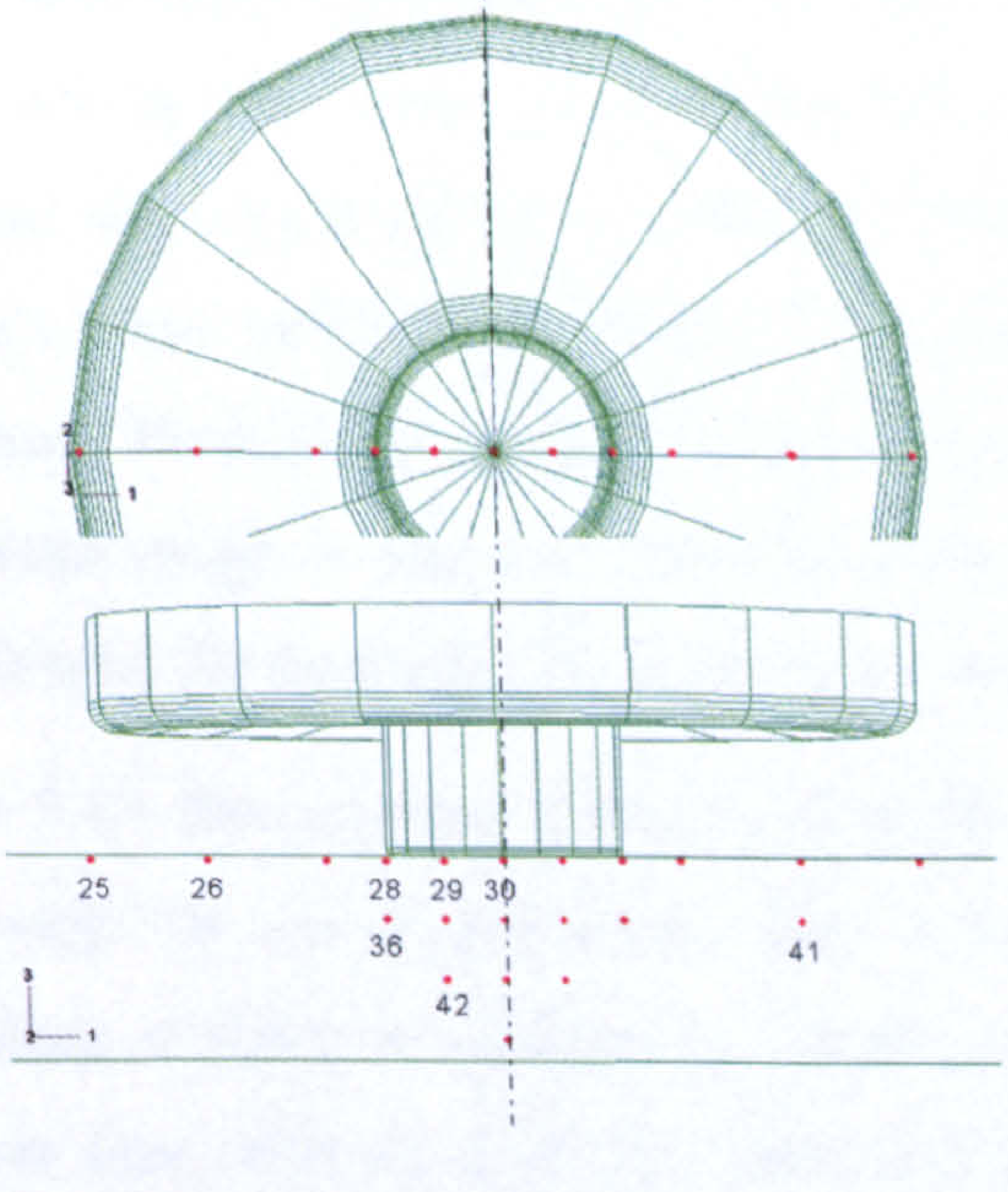

Figure 5.23 Positions of tracer particles of tracer1 at 0s.

The animation of the movement of particle set "tracer1" is given in file TRACER1.avi, Appendix B.

Figure 5.24 in pages 174-175 and Figure 5.25 in page 176 demonstrate the particle locations of set tracer4 and set tracer2&3 at several representative time points, respectively. The continuous tracer particle movement can be found in TRACER2&3.avi and TRACER4.avi of the Appendix B. The particle set tracer4 is a line of material points in front of the tool perpendicular to the joining line (see Figure 5.24). While set racer2 and set tracer3 sit in separate lines along the welding direction, lying on the retreating side and advancing side of the weld, respectively.

For set tracer4 the material points close to the centre line was first touched and sucked in to the conical shoulder-workpiece interface as shown in the pictures (top and cross-section views) of Figure 5.24 at 8.8s (second from the left in top row and second from the right in bottom row). Then the material points from advancing side were forced and squeezed to the retreating side, leading to a non-symmetrical flow field. Most of the particles entering onto the retreating side under the tool shoulder went through several revolutions and dropped off in the wake of the shoulder later on, mainly on the advancing side. There were also some particles, primarily from retreating side, at the contact interface that didn't rotate with the shoulder. They remained on retreating side when left behind by the tool. Finally the material particles formed an arc-shaped strip behind the tool. This banded shape is already well known by numerous experimental studies in the literatures. One of the examples is shown in Figure 5.26 [5.22].

For set tracer2 in Figure 5.25 the particles entered shoulder-workpiece interface and rotated with the shoulder only for a very short time. They were directly pushed back to the wake with the advancing of the tool towards the welding direction. It is noted that the material particles never flew with the tool into the rotational zone. Again in Figure 5.25 tracer3 particles were stirred into the rotational zone at various places and then sloughed off from the welding tool. Those findings are consistent with observations in experiments [5.21-5.24]. Thus the ability of the model to predict the material movement is validated.

However, it should be noted that only a limited number of tracer particles were defined and the flow on the top surface of the workpiece is dominated by the shoulder rather than by the pin. The material has a quite different flow pattern at mid section and the lower part of the pin. To fully track and study the material flow more tracer particles should be defined and seeded.

To investigate the properties or variables accompanying the tracer particles the variable output for the tracer particles should be requested. For field output at tracer particles, displacement is the only valid field request in ABAQUS and the positions or trajectories of the tracer particles at a specific time point can be requested as nodal field output. To gain other field variable at some specific material points will be difficult. Although such data are available at nodal points, in adaptive mesh domains where mesh moves independently from material, the field variable history at these nodes would have no physical meaning. For history output at racer particles, all valid element integration point variable such as temperature can be requested. The displacement, velocity, acceleration and coordinates are the only valid nodal requests.

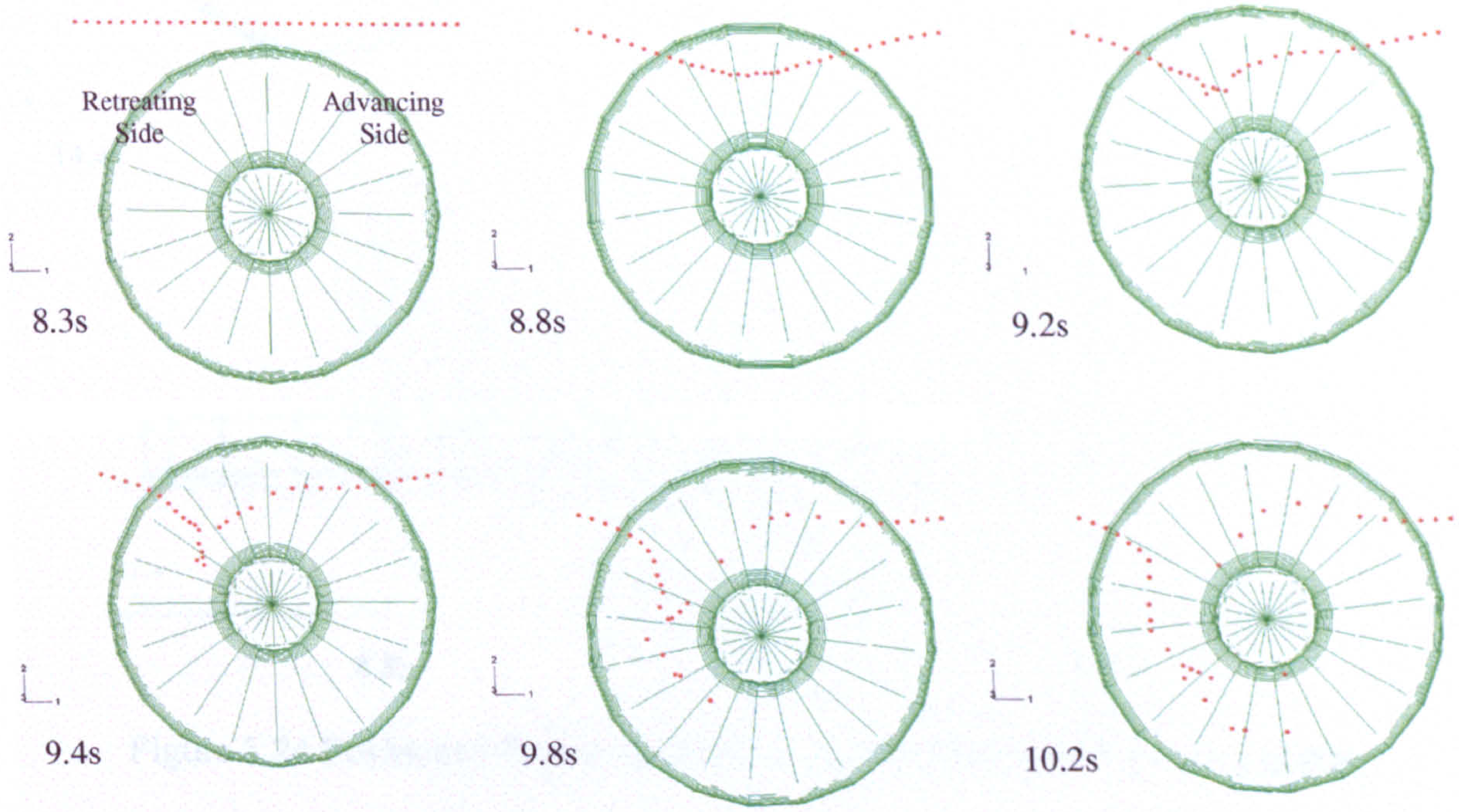

(Continued from the previous page)

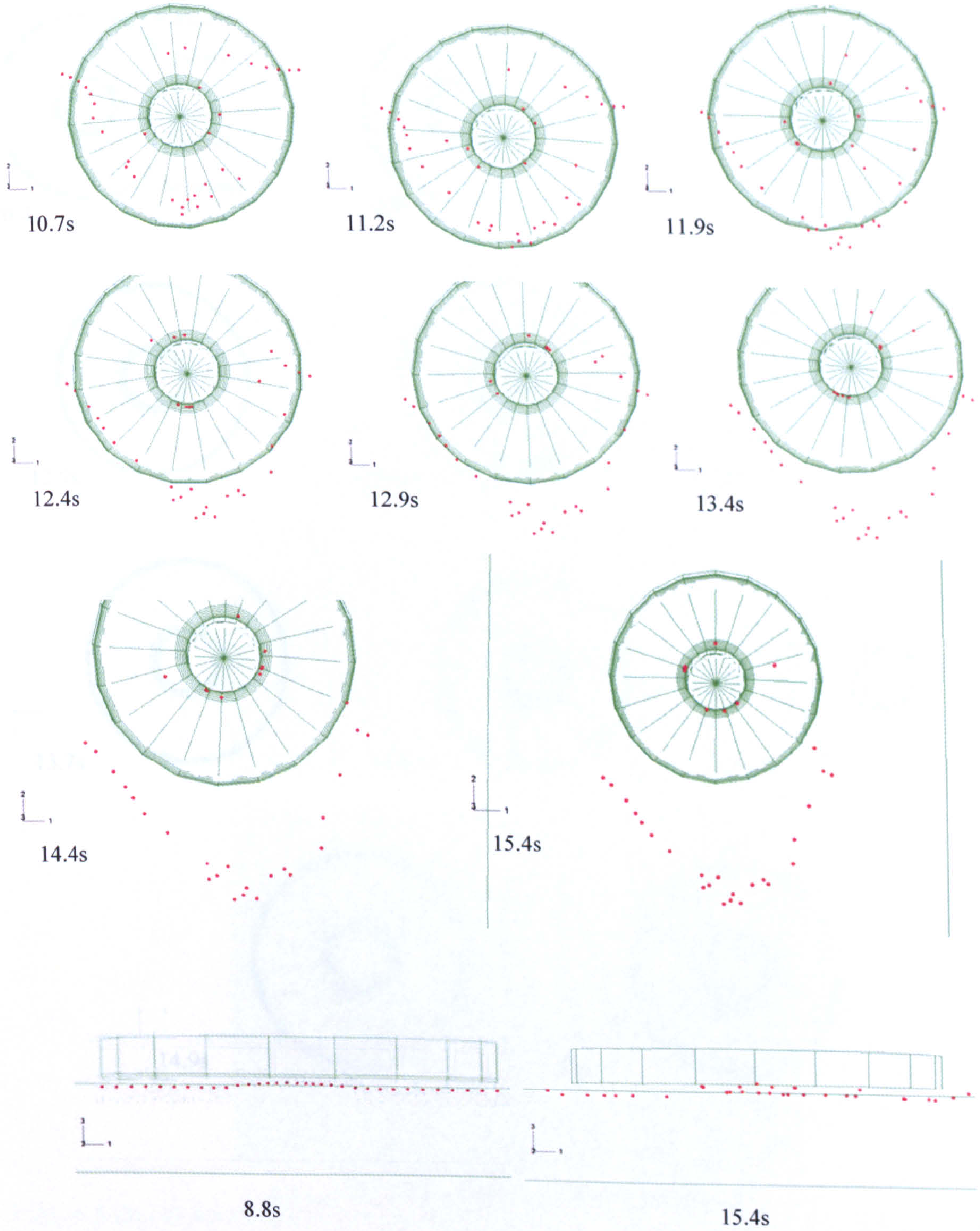

Figure 5.24 Positions of tracer particles of set tracer4 at different time points.

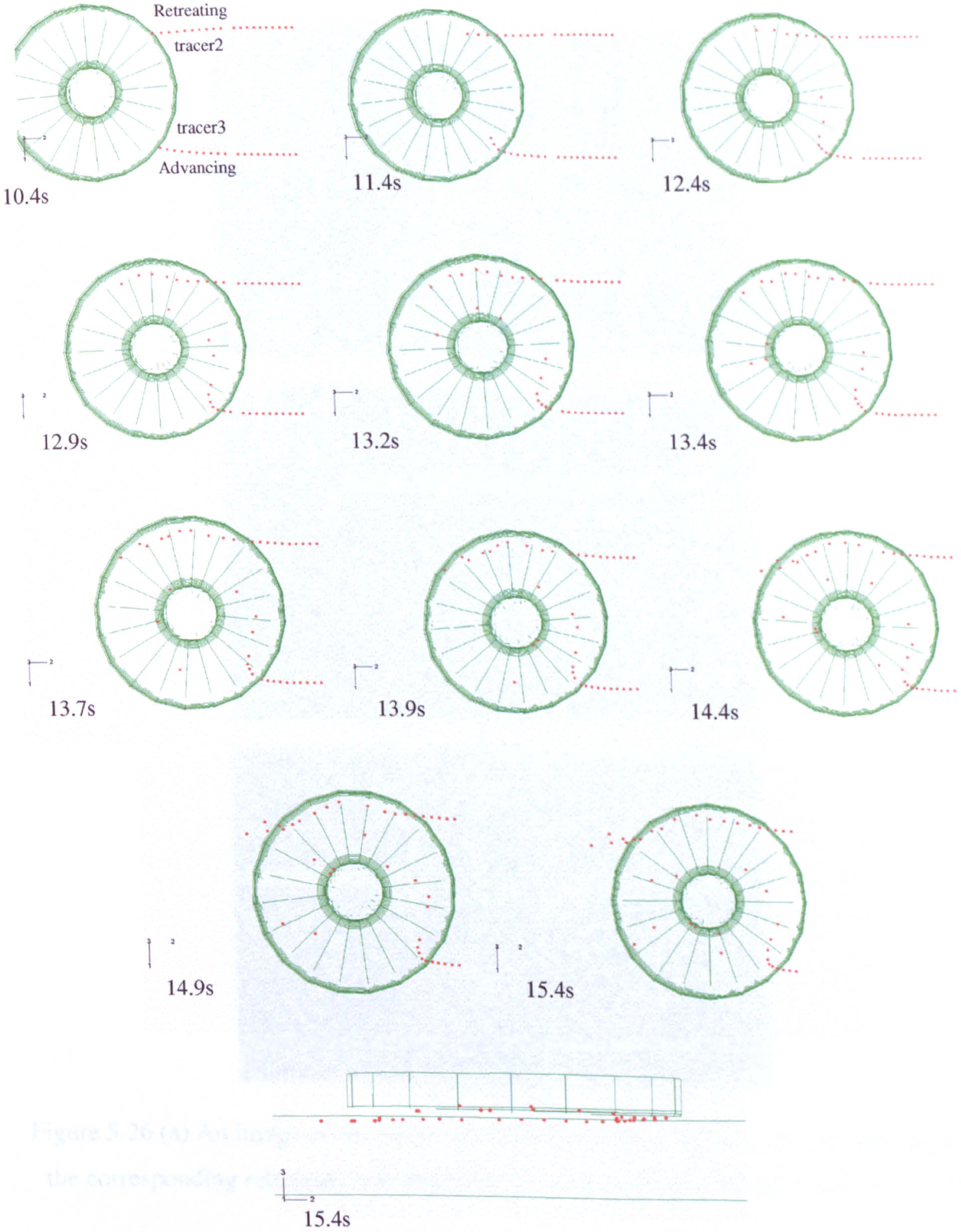

Figure 5.25 Positions of tracer particles of set tracer2 and set tracer3 at different time points.

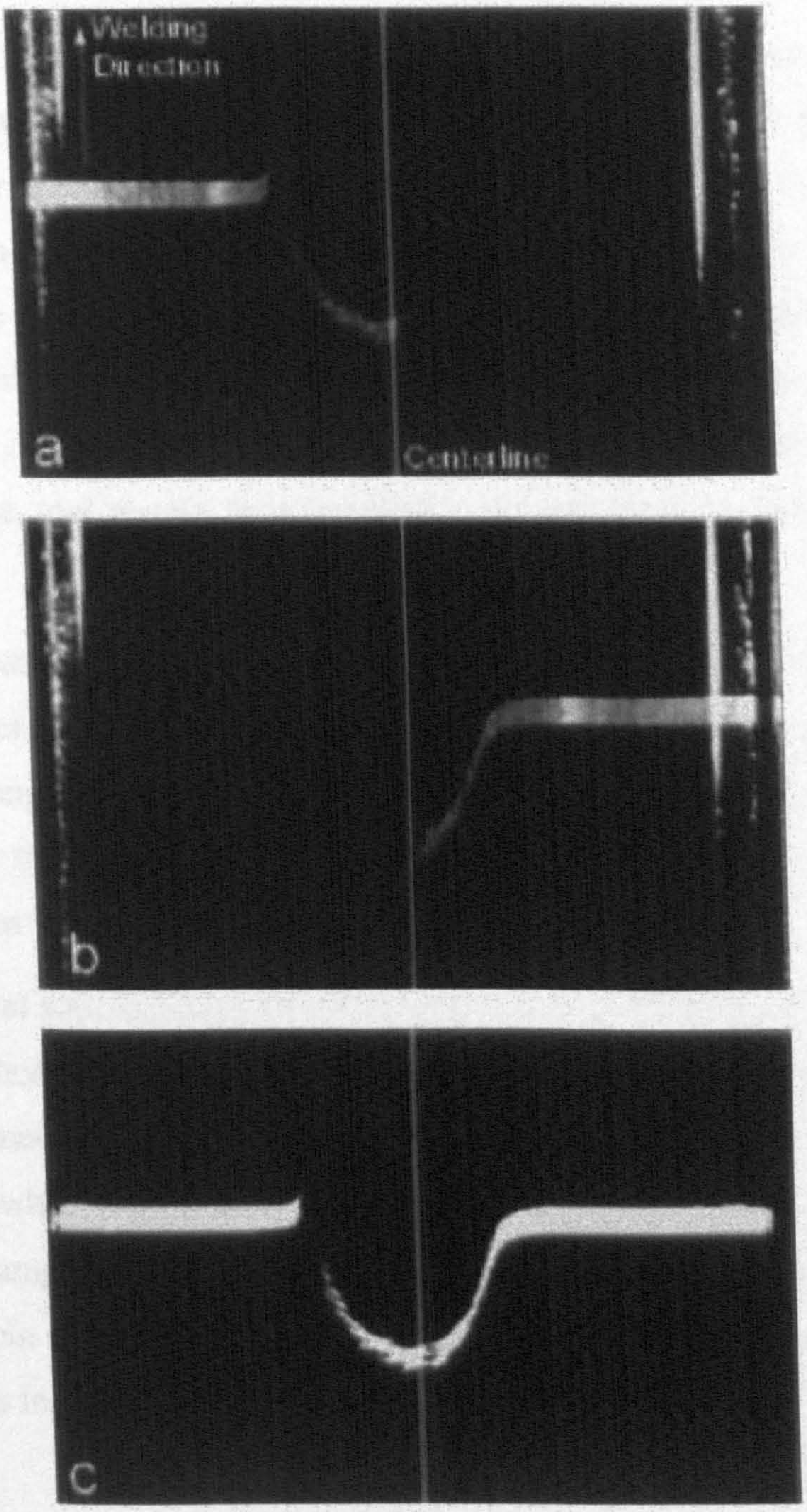

Figure 5.26 (a) An image of the etched markers from the advancing side, (b) an image of the corresponding retreating side markers (c) combined image from (a) and (b) [5.22].

5.12 Effect of Tool Shape in Plunge Stage

The welding tool is the key part of the friction stir welding process. It is well known from literature that the shoulder of the tool is the main source of heat generation. It confines the material expulsion and moves the material at the contact interface. The pin is the secondary heat source and its main function is to stir and mix the material from both sides of the joining line. The geometry of both the shoulder and pin has a significant influence on the weld formation, weld quality, and weld mechanical properties and so on. This section studies the effect of variation in the tool geometry on tool reaction force, tool torque, heat generation, temperature distribution and size of the weld zone.

Due to the limitation of computation time a new model, which uses the speeded-up welding parameters stated in Section 5.8.4.2, was created to investigate the effect of the tool shape in plunge stage. The reason of only considering the plunge stage is that the tool experiences the highest and most unstable forces in this stage. It is the stage in which the tool has the highest possibility to break.

A concave conical smooth shoulder surface and a cylindrical pin surface were chosen for current study. There is no standard rule for choosing the size of the tool. A collection of typical tool geometries, in the literature, used for aluminium alloy is shown in Table 5.5. The pin height, which varies from 1.5 to 7.9, depends much on the required weld depth. The concavity angles are in the range of 0°-10°. The ratios of the shoulder radius, $R_{shoulder}$, to the pin radius, R_{pin}, $R_{shoulder}/R_{pin}$ are close to 3, ranging from 2.6 to 4. For the previous models in this chapter, a tool with a ratio of 2.8 was used (R_{pin}= 5mm, $R_{shoulder}$= 14mm).

Table 5.5 Typical tool geometries used in the literature.

Reference	**Material**	**Pin Height (mm)**	**R_{pin} (mm)**	**$R_{shoulder}$ (mm)**	**$R_{shoulder}/R_{pin}$**	**α_{tool}**
Buffa [2.18]	AA6061	2.8	1.5	5.0	3.3	0.0°
Colegrove [2.26]	AA5083	6.2	4.0	12.5	3.1	7.0°
Seidel [5.22]	AA7075	7.9	5.0	12.7	2.6	7.0°
Chen [2.27]	AA6061	--	3.0	12.0	4.0	--
Moataz [2.28]	AA2095	1.5	1.9	5.0	2.6	--
Schmidt [5.21]	AA2024	--	3.0	9.0	3.0	10.0°

In the parametric study, Figure 5.27 shows the tool design utilized, five different shoulder surface angles, α_{tool} and four different pin radii, R_{pin} were considered:

α_{tool} =0°, 2°, 5°, 8° and 10°

R_{pin} =1 mm, 1.5 mm, 2 mm and 2.5 mm

The rest of the geometry parameters, shoulder radius, $R_{shoulder}$, and pin depth were kept unchanged. All the cases utilized the same procedure and process parameters (rotation speed and plunge speed). For each shoulder surface angle, α_{tool}, four separate models with different pin radii, R_{pin} were generated and solved. This gave a total number of twenty different models each taking typically 50 hours to solve.

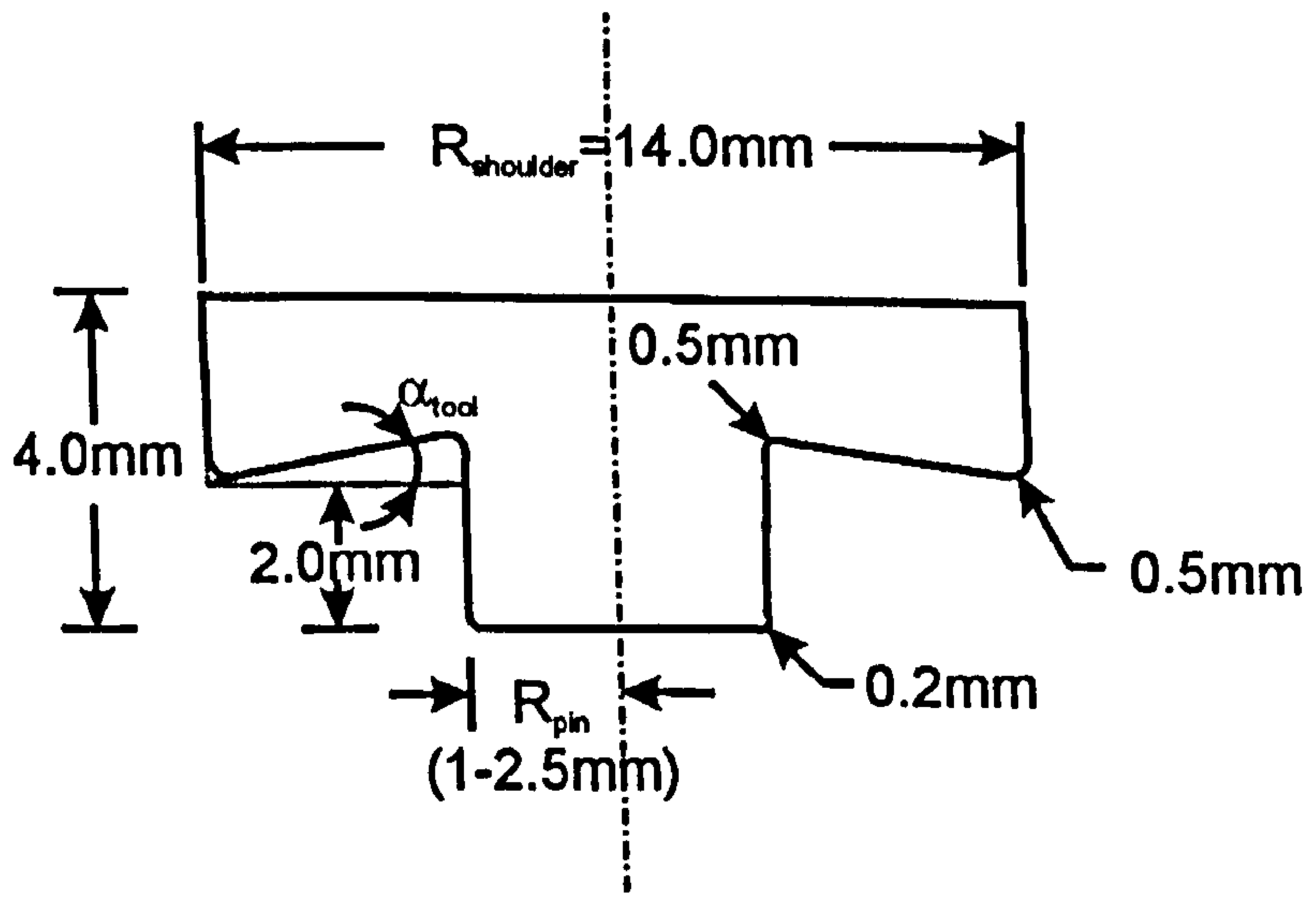

Figure 5.27 tool design used for effect of tool shape study.

The mesh of the model is shown below in Figure 5.28, which is specially designed for simulating plunge stage.

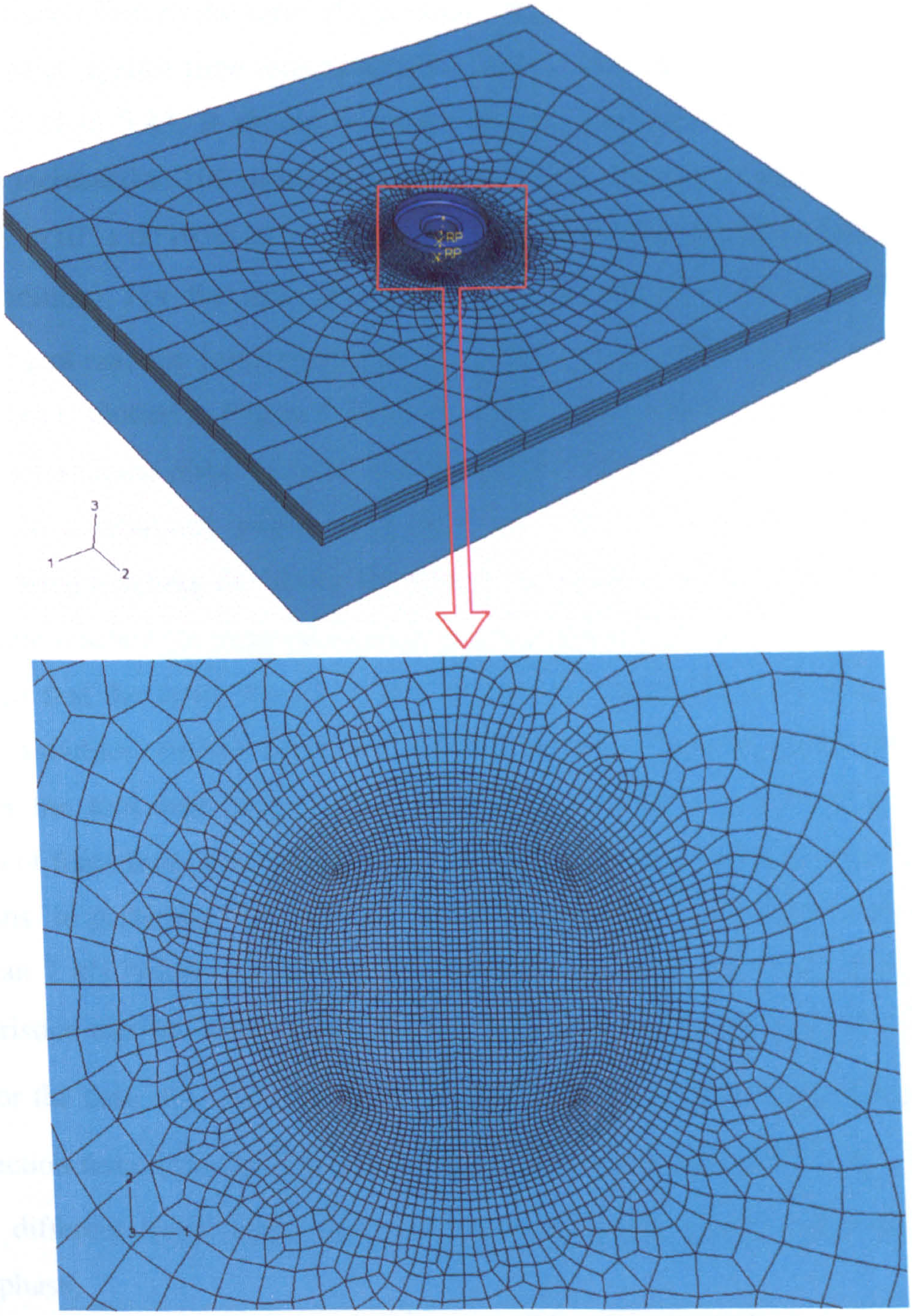

Figure 5.28 The FE model for studying the effect of tool shape.

5.12.1 Effect of Tool Shape on Tool Reaction Force and Torque

To look into the effect of the ratio of pin radius, R_{pin}, to shoulder radius, $R_{shoulder}$, graphs of reaction force against time were plotted for each of the analysis runs, these are shown in Figures 5.29 to 5.33. It should be noted that the tool rotating speed and plunging speed were increased to 100 times of their normal value. The maximum scale of the time X-Axis is 8.6×10^{-2} s or 10.6×10^{-2}s (in some cases, longer time needed to establish the full contact condition). For the case of α_{tool} =0°, i.e. the shoulder has a flat surface, the variation of tool reaction force magnitude with time for four different R_{pin} values, 1, 1.5, 2 and 2.5 mm is plotted in Figure 5.29. At the beginning of the plunge, only the pin was in the contact with the plate. In each of the graphs in Figure 5.29, the axial force climbed from zero to a relatively stable value at about 0.02s. After a short time when the shoulder started touching the plates, the force was suddenly rising again in a fluctuating manner, then reached the peak value when the tool were in full contact with the plates. It is observed that the larger the pin radius R_{pin} is the higher force the tool experiences before the shoulder contacts the plates and the lower peak force during the whole plunge stage. For the tool with a pin radius R_{pin} of 2.5 mm there is a relatively smoother transition of force from only pin contact to shoulder contact compared with other smaller radius pins. In particular, the tool that has a 0.1mm radius pin carried a reaction force lower than 7 kN before 7.2s but the force jumped up to about 57 kN at 8.2s. Similar characteristics can be found for cases α_{tool} =2° (Fig. 5.30) and α_{tool} =5° (Fig. 5.31). While for the case α_{tool} =8° (Fig. 5.32) all the tools with different pin radius reached a peak reaction force close to each other. Figure 5.33 shows the curve for α_{tool} =10° with a slightly different trend; larger pin tool always produces greater force for the whole plunge phase.

To further examine the effect of the shoulder surface angle, α_{tool}, the graphs of tool reaction force against time were plotted in a different form, as shown in Figures 5.34-5.37. In each figure the pin radius R_{pin} is fixed and the variation of tool reaction force against time is plotted for five different shoulder surface angle, α_{tool} values, 0 °, 2 °, 5 °, 8

° and 10 °. As expected the shoulder surface angle, α_{tool} has no effect before the shoulder touches the plates. The initial parts of all curves in each figure are almost coincident although there is a larger fluctuation in the case of R_{pin} =2.5 mm (Fig. 5.33). When the shoulder is in contact with the workpiece, smaller shoulder surface angle tends to give larger peak reaction force as shown in Figure 5.34 (R_{pin} =1 mm) and Figure 5.35 (R_{pin} =1.5 mm). While for R_{pin} =2 mm (Fig. 5.36) and R_{pin} =2.5 mm (Figure 5.37), similar peak forces were found for all the shoulder angles. It is also observed that the tool with smaller shoulder angle always reaches the peak force value earlier.

When full contact is established all the curves are expected to approach a similar force magnitude although following different paths. This is due to the reason that the shoulder radius, $R_{shoulder}$, remains constant and the projected area of the tool on horizontal plane remains the same as well. Therefore the axial force required for a specific sinking depth should be the same theoretically. In reality, the temperature and stress distributions were different for the same tool sinking depth during the plunge stage. Hence the tool reaction forces were different as shown in Figures 5.34-5.37. However when in the steady welding stage, it is expected that, for all the cases, the tool reaction forces will be close to each other. A similar parametric study including the dwell and transverse periods will be part of future work.

The variation of tool torque with time plots for the purpose of examining the effect of pin radius, R_{pin}, and shoulder surface angle, α_{tool}, is shown in Figure 5.38 (a-e) and Figure 5.39 (a-d), respectively. All the curves in these figures demonstrate very similar trends to the curves shown in Figure 5.29 to 5.33 and Figure 5.34 to 5.37. This is reasonable as the Coulomb friction law was specified in the model. The tool torque is roughly proportional to the tool axial force.

When full contact is established (including the dwell and transverse periods), it is also expected that, similar to the tool reaction force, the same tool reaction torque can be obtained for all the cases considered here, as long as the shoulder radius and tool pin height are kept constant.

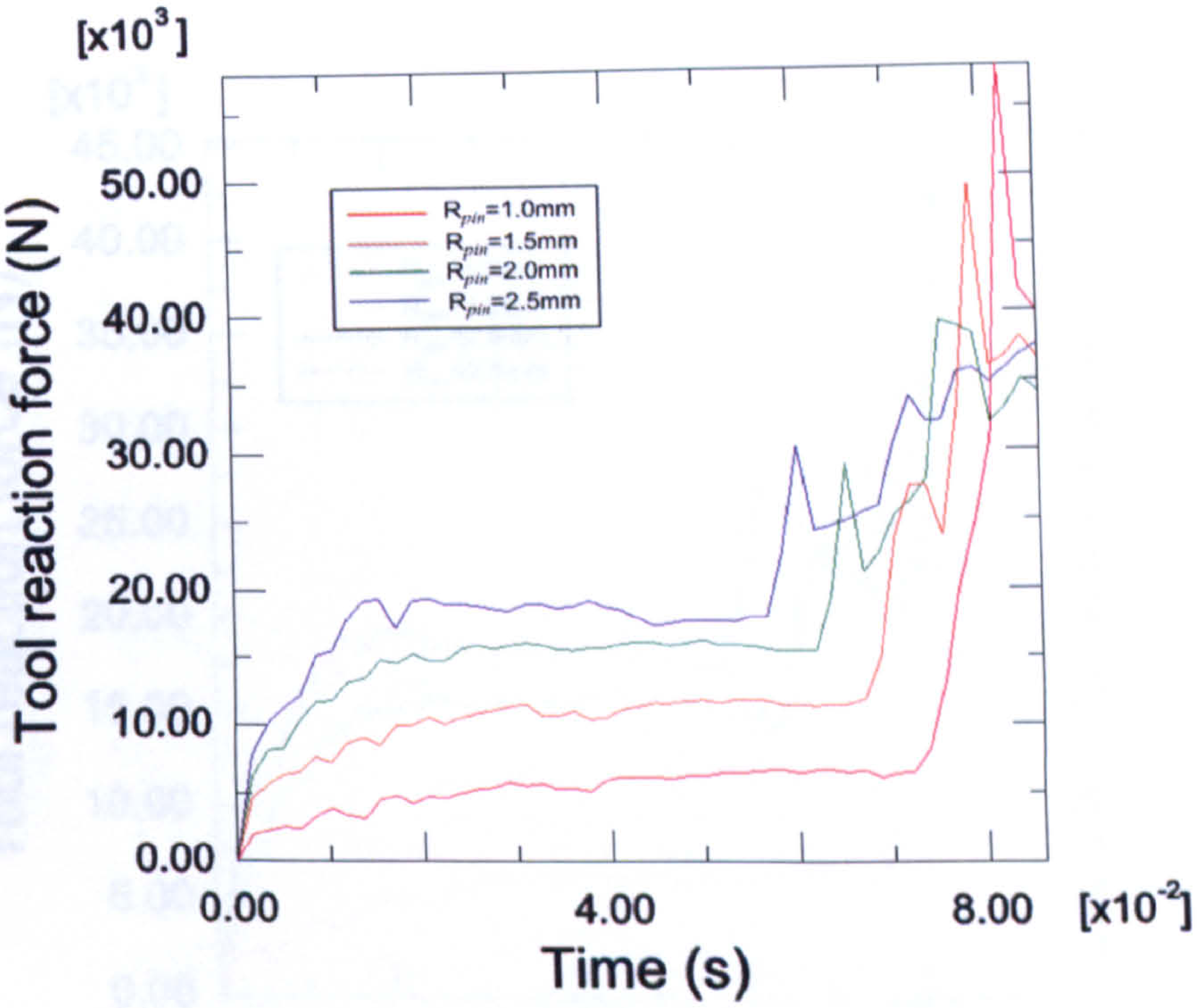

Figure 5.29 Plots of tool reaction force against time in plunge stage, α_{tool} =0°, for R_{pin}= 1, 1.5, 2 and 2.5 mm.

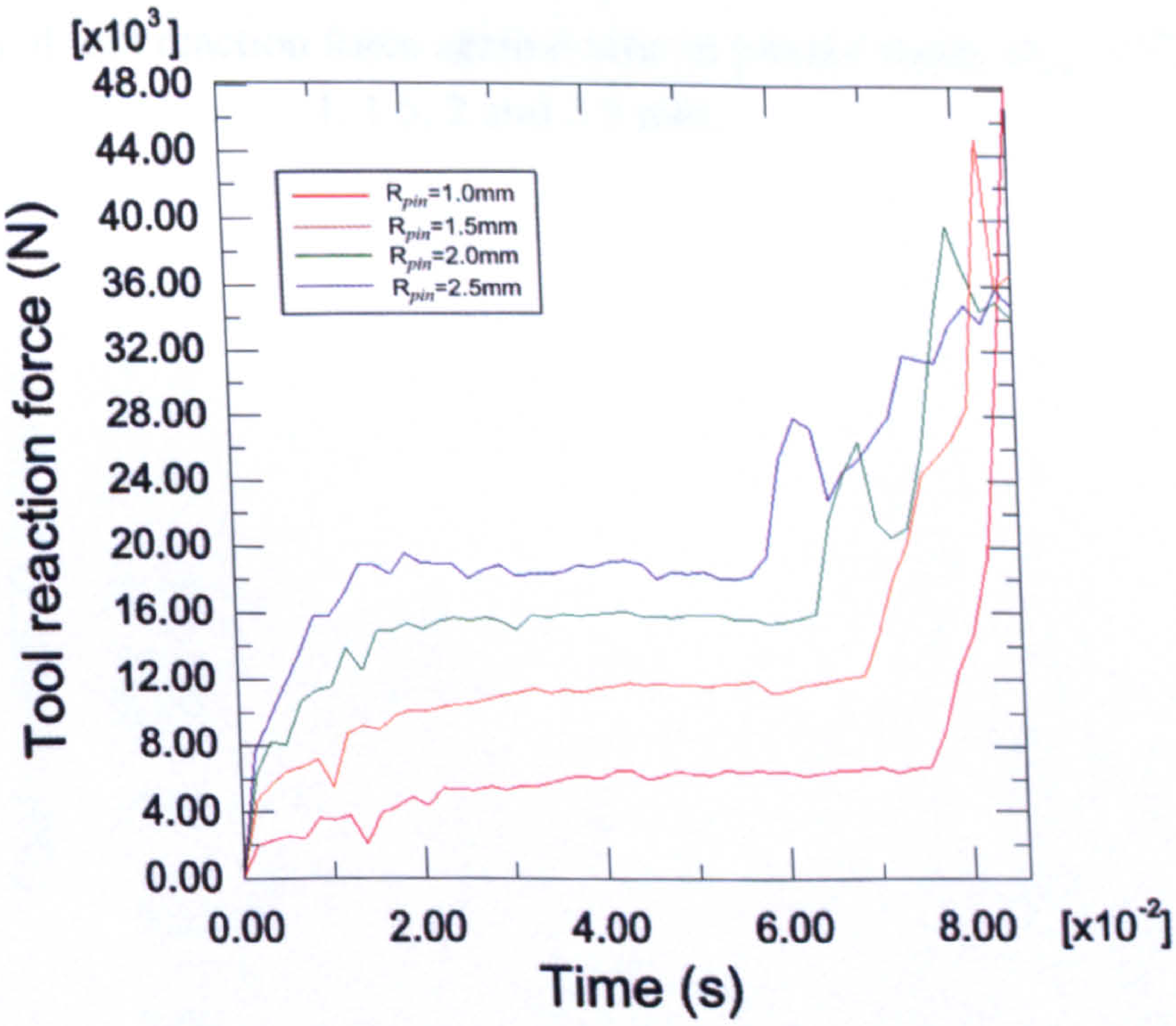

Figure 5.30 Plots of tool reaction force against time in plunge stage, α_{tool} =2°, for R_{pin}= 1, 1.5, 2 and 2.5 mm.

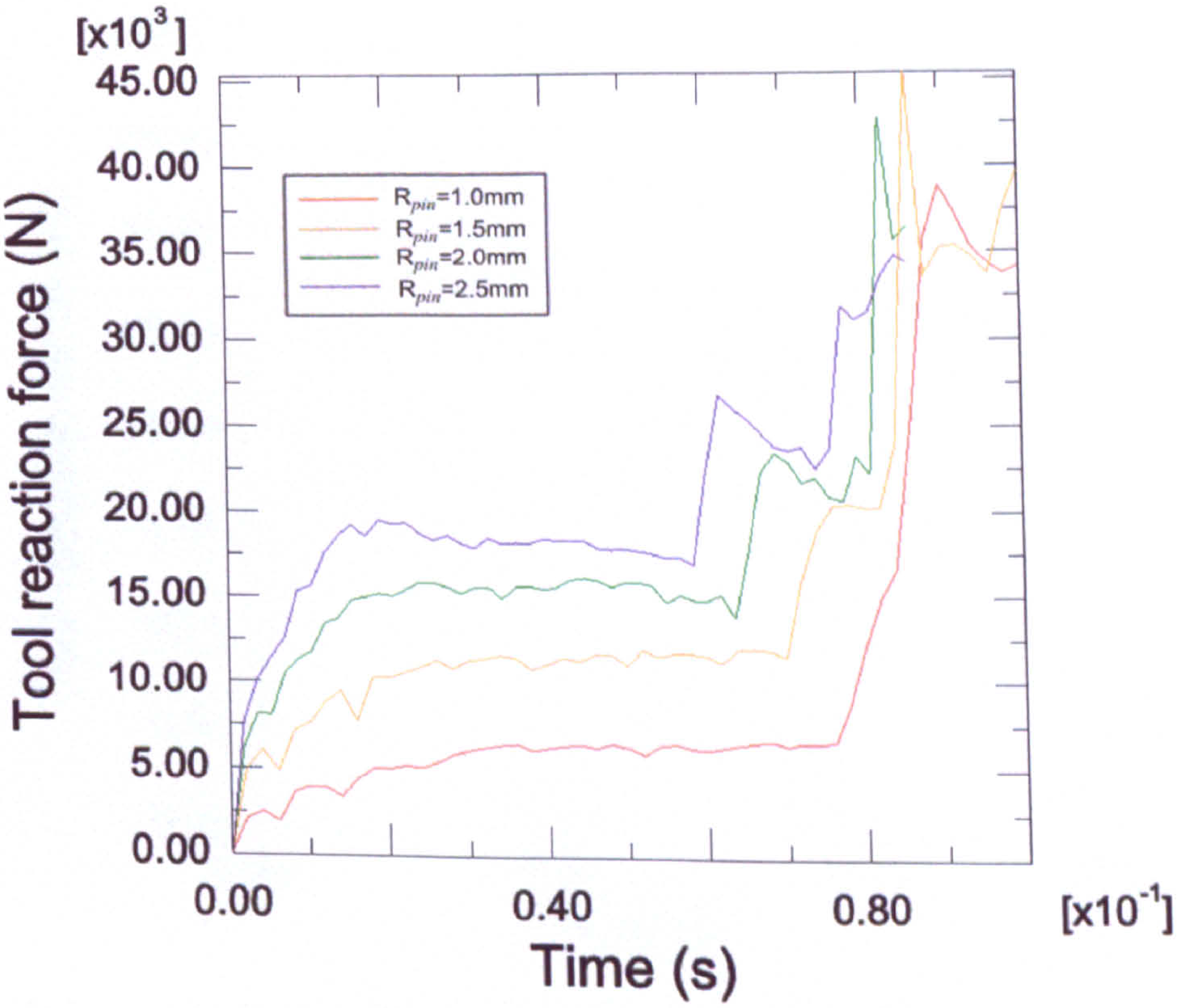

Figure 5.31 Plots of tool reaction force against time in plunge stage, α_{tool} =5°, for R_{pin}= 1, 1.5, 2 and 2.5 mm.

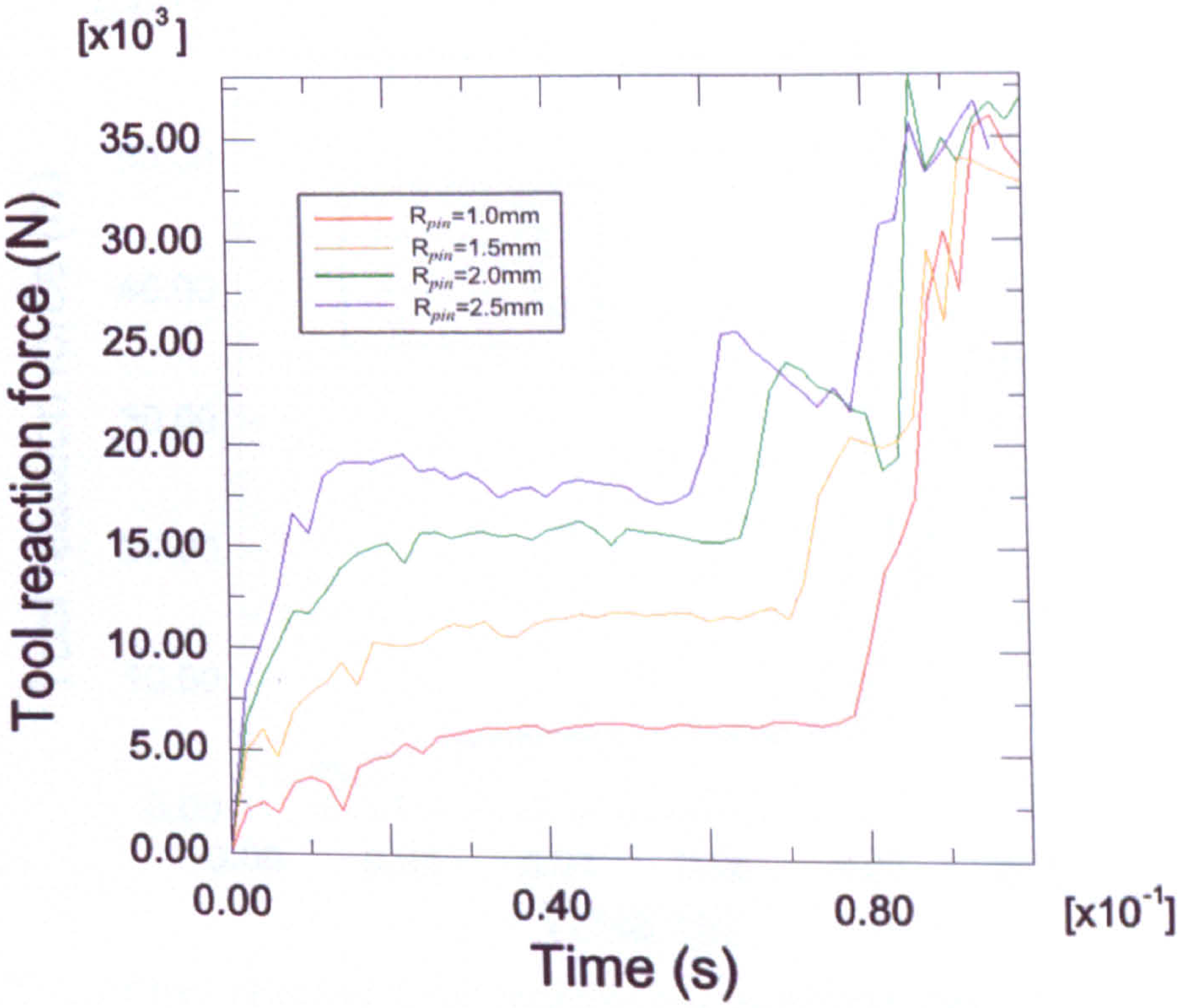

Figure 5.32 Plots of tool reaction force against time in plunge stage, α_{tool} =8°, for R_{pin}= 1, 1.5, 2 and 2.5 mm.

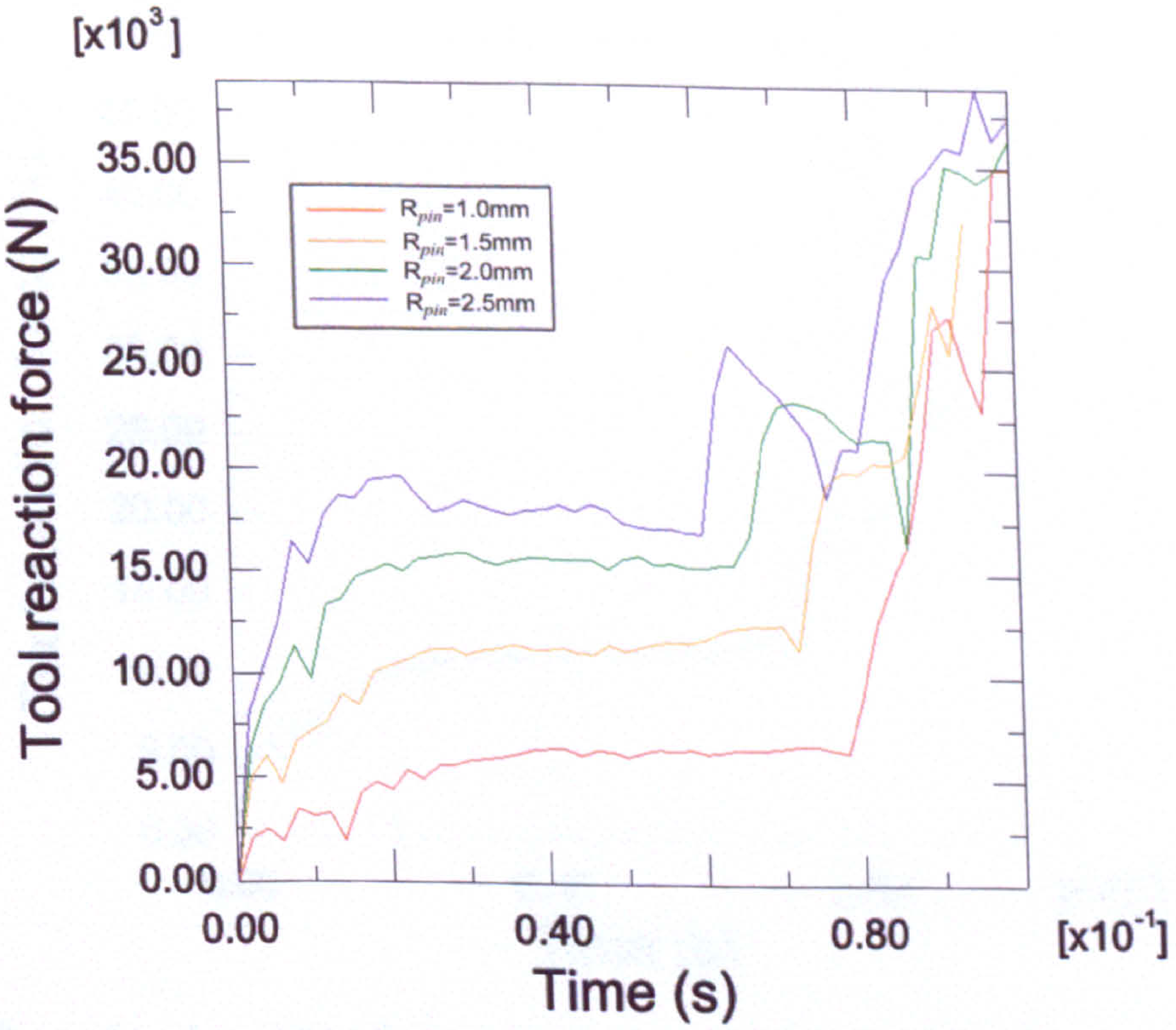

Figure 5.33 Plots of tool reaction force against time in plunge stage, α_{tool} =10°, for R_{pin}= 1, 1.5, 2 and 2.5 mm.

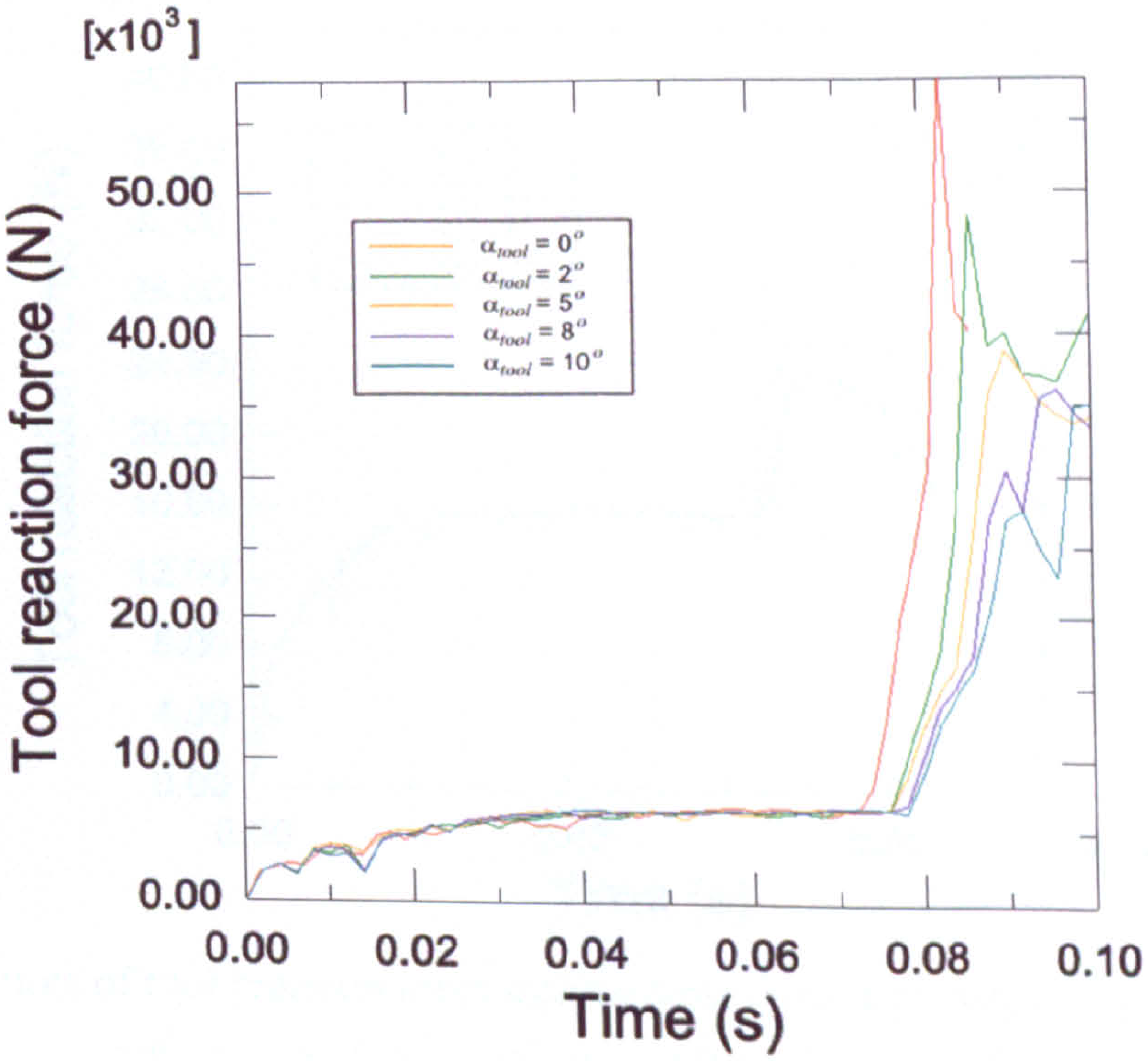

Figure 5.34 Plots of tool reaction force against time in plunge stage, R_{pin}= 1, for α_{tool} =0°, α_{tool} =2° α_{tool} =5° α_{tool} =8° and α_{tool} =10°.

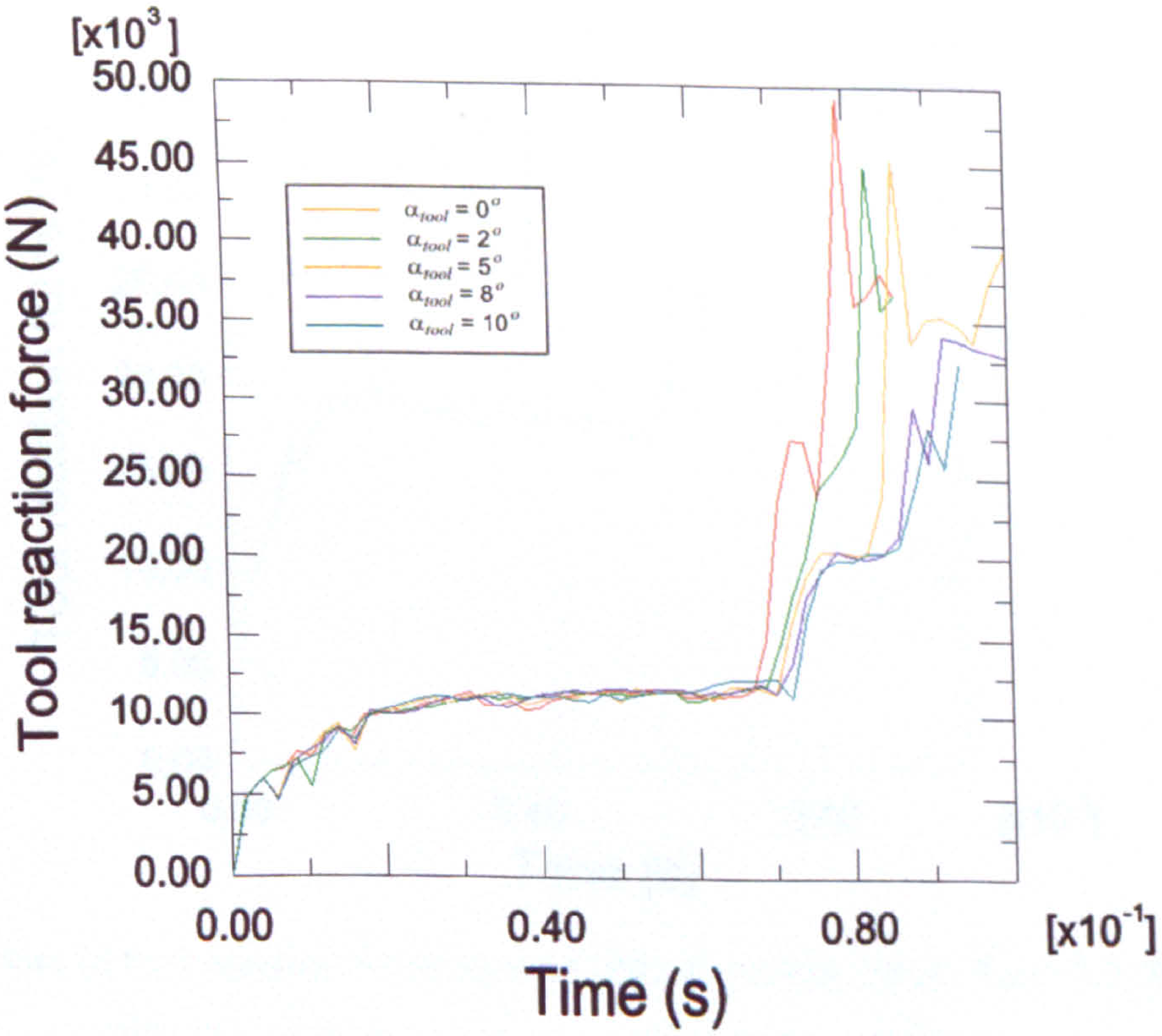

Figure 5.35 Plots of tool reaction force against time in plunge stage, R_{pin}= 1.5, for α_{tool} =0°, α_{tool} =2° α_{tool} =5° α_{tool} =8° and α_{tool} =10°.

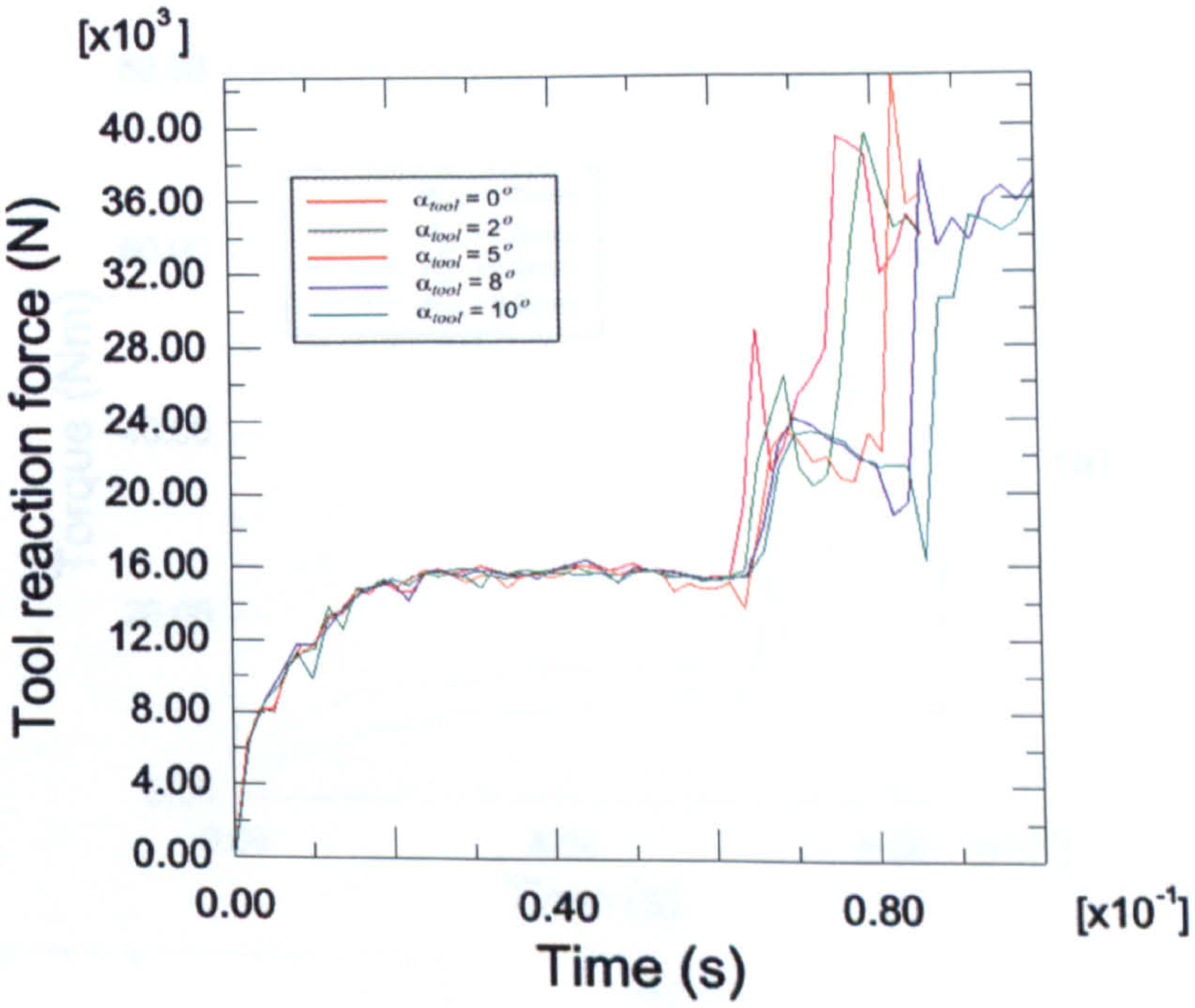

Figure 5.36 Plots of tool reaction force against time in plunge stage, R_{pin}= 2, for α_{tool} =0°, α_{tool} =2° α_{tool} =5° α_{tool} =8° and α_{tool} =10°.

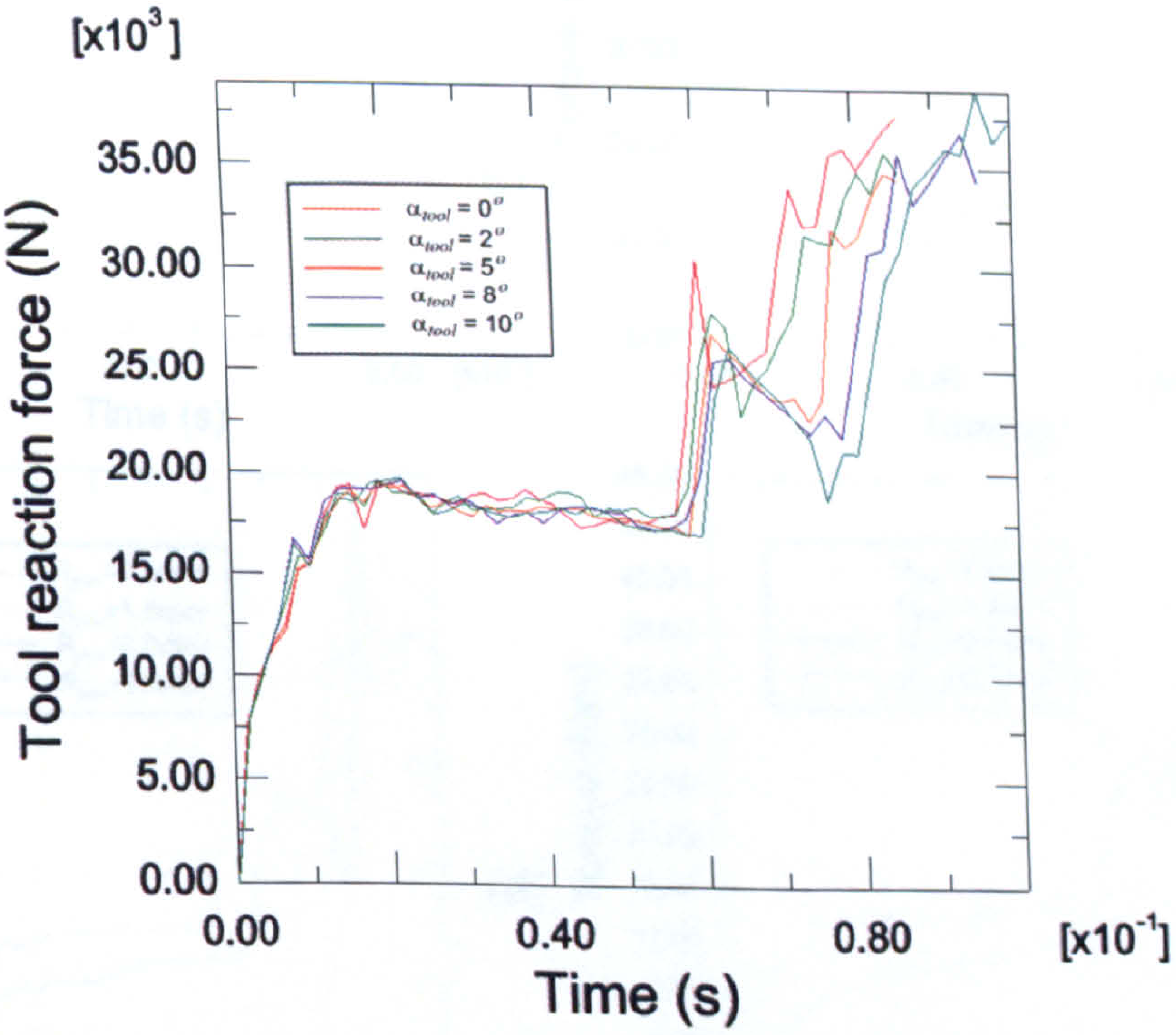

Figure 5.37 Plots of tool reaction force against time in plunge stage, R_{pin}= 2.5, for α_{tool} =0°, α_{tool} =2° α_{tool} =5° α_{tool} =8° and α_{tool} =10°.

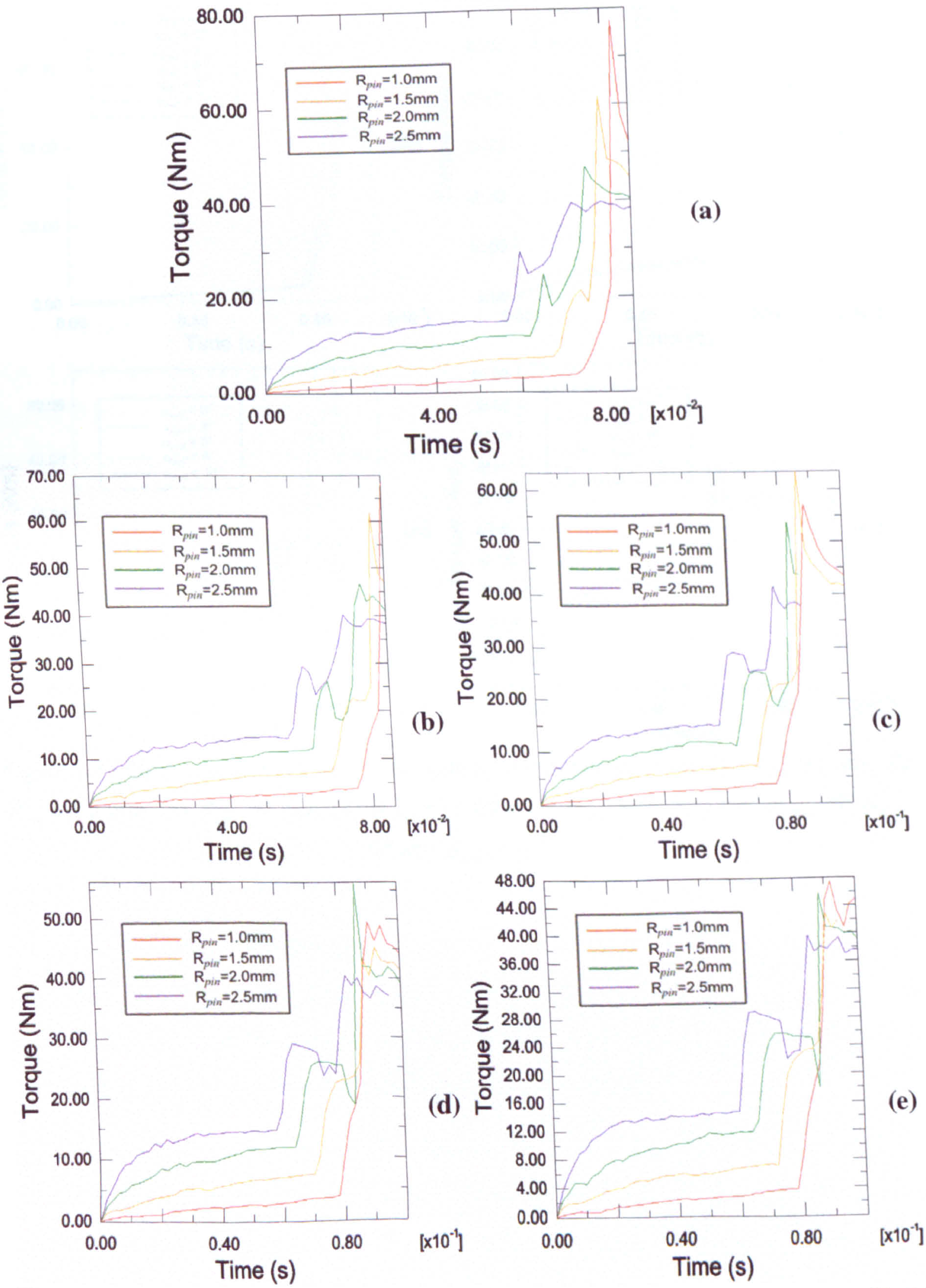

Figure 5.38 Plots of tool reaction torque against time in plunge stage, (a) α_{tool} =0°, (b) α_{tool} =2°, (c) α_{tool} =5°, (d) α_{tool} =8°, (e) α_{tool} =10° for R_{pin}=1, 1.5, 2 and 2.5 mm.

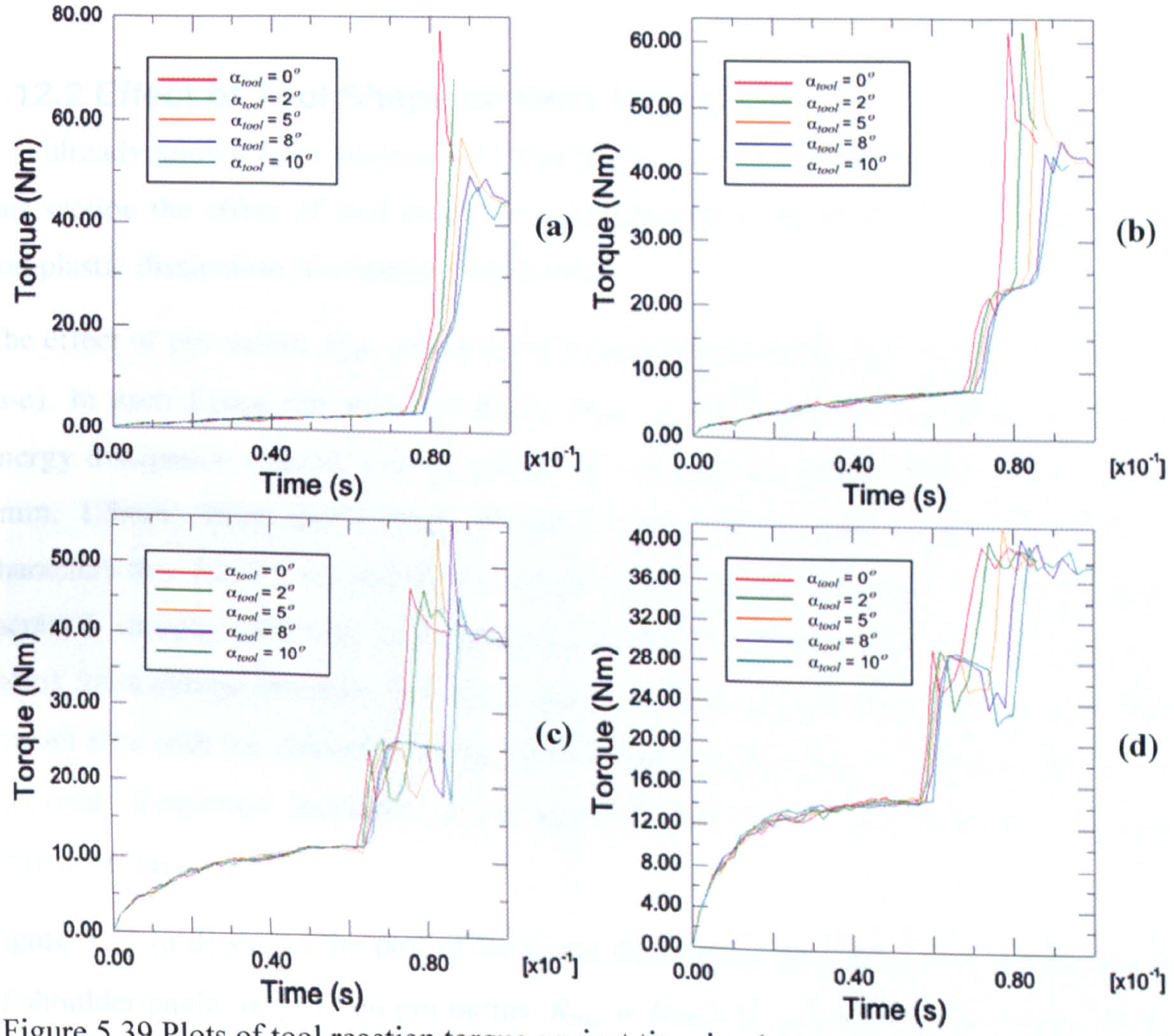

Figure 5.39 Plots of tool reaction torque against time in plunge stage, (a) R_{pin} =1 mm, (b) R_{pin} =1.5 mm, (c) R_{pin} =2 mm, (d) R_{pin} =2.5 mm: for α_{tool} =0°, α_{tool} =2° α_{tool} =5° α_{tool} =8° and α_{tool} =10°.

5.12.2 Effect of Tool Shape on Heat Generation

It is already known from Section 5.11 that the friction dominates the heat generation. In this section the effect of tool shape on heat generation caused by frictional dissipation and plastic dissipation is evaluated separately.

The effect of pin radius, R_{pin}, on frictional energy dissipation is illustrated in Figure 5.39 (a-e). In each figure the shoulder angle, α_{tool}, is fixed and the variation of frictional energy dissipation against time is plotted for four different pin radius, R_{pin}, values of 1mm, 1.5mm, 2mm and 2.5mm. In all the five figures the curves exhibit similar characteristics. Before the shoulder contacts the plates, the frictional energy dissipation increases linearly with time with different slopes for different pin radii. The larger pin radius tools always provide greater energy increment rates because they have a bigger contact area with the workpiece. When the shoulder is in contact with the workpiece, the frictional dissipation increases in an approximately linear manner but with higher increment rate.

Figure 5.41 (a-d) shows the plot of frictional dissipation against time to study the effect of shoulder angle, α_{tool}, when pin radius, R_{pin}, is fixed. It is clear from the figures that all the curves are very close to each other, especially for tools with larger ratio of pin radius to shoulder radius (i.e. Figure 41(c), R_{pin}=2, and Figure 41(d), R_{pin}=2), indicating the surface angle has little effect on the frictional heat generation.

For the plastic energy dissipation, as shown in Figure 5.42 (a-d), the shoulder surface angle, α_{tool}, only affects the time at which the turning point on the curves occur. After the turning point, regardless of the shoulder surface angle, all the curves in each figure have the very similar plastic energy dissipation increment rate.

The effect of pin radius, R_{pin}, is illustrated in Figure 5.43 (a-e). The largest amount of plastic dissipation (purple curve) was generated by the tool with the biggest pin radius, R_{pin} =2.5mm and the smallest amount of plastic dissipation (red curve) corresponds to the smallest pin radius, R_{pin} =1mm. For all the curves, there exists a turning point where the curve slope increases suddenly, which may be attributed to the shearing action of the tool shoulder.

The amount of total energy dissipation is mainly dependent on the size of the pin before full contact between the tool and workpiece forms. This is very obvious when only the pin in contact with workpiece. But once full contact is established, neither the pin radius nor the shoulder surface angle has much effect on the total heat generation.

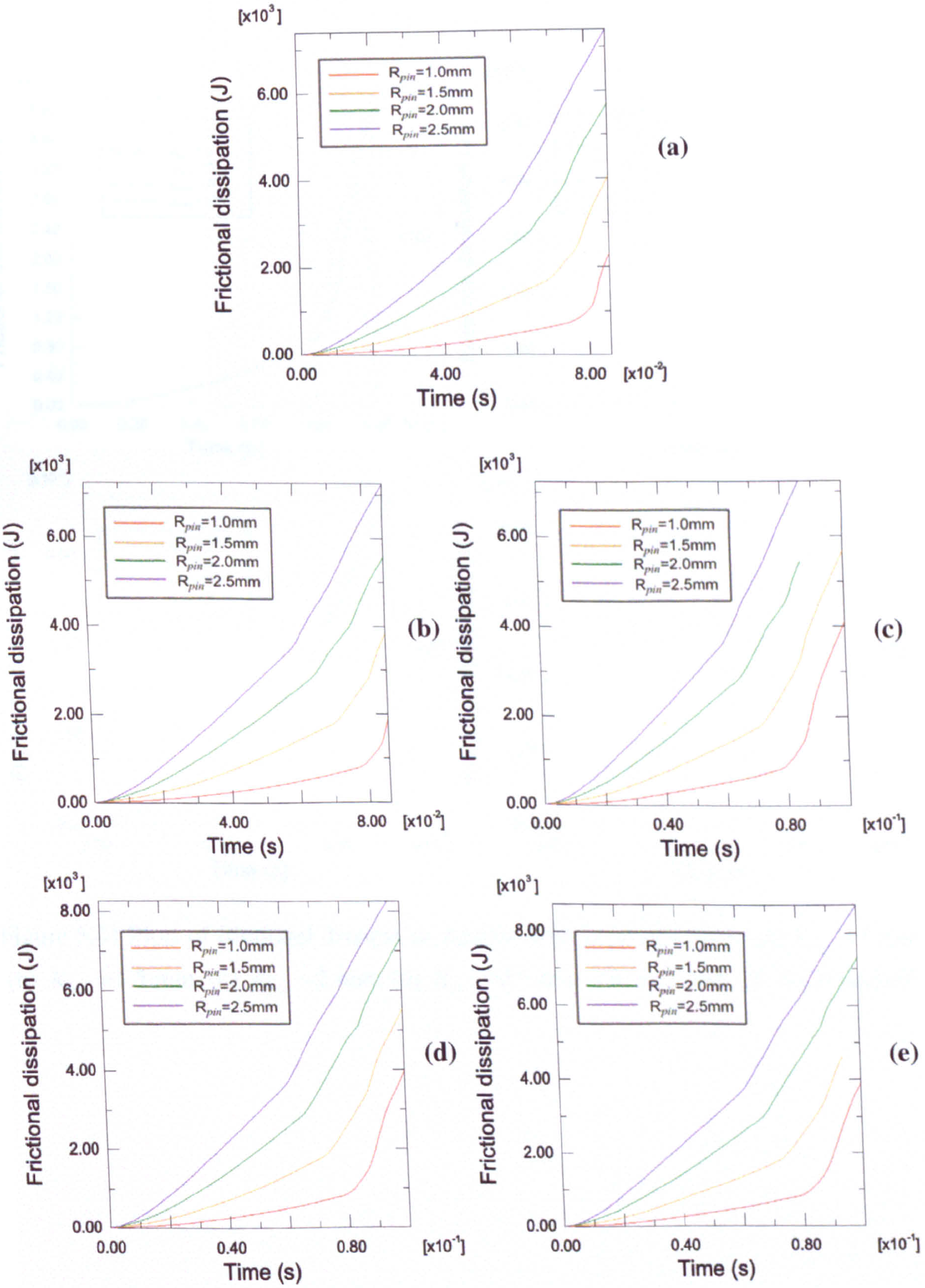

Figure 5.40 plots of frictional dissipation against time in plunge stage, (a) α_{tool} =0°, (b) α_{tool} =2°, (c) α_{tool} =5°, (d) α_{tool} =8°, (e) α_{tool} =10°: for R_{pin}= 1, 1.5, 2 and 2.5mm.

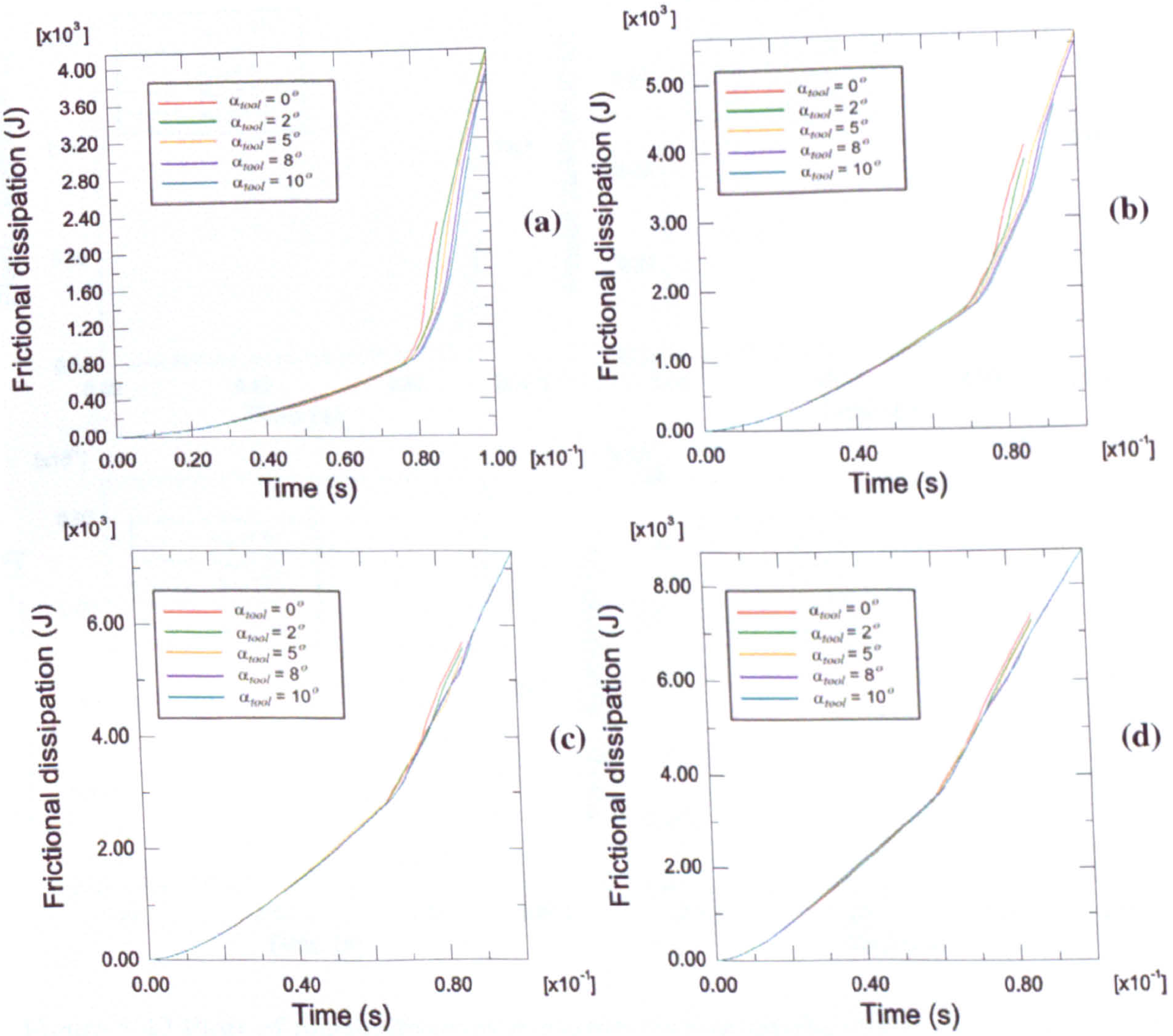

Figure 5.41 Plots of frictional dissipation against time in plunge stage (a) R_{pin} =1 mm, (b) R_{pin} =1.5 mm, (c) R_{pin} =2 mm, (d) R_{pin} =2.5 mm: for α_{tool} =0°, 2°, 5°, 8° and10°.

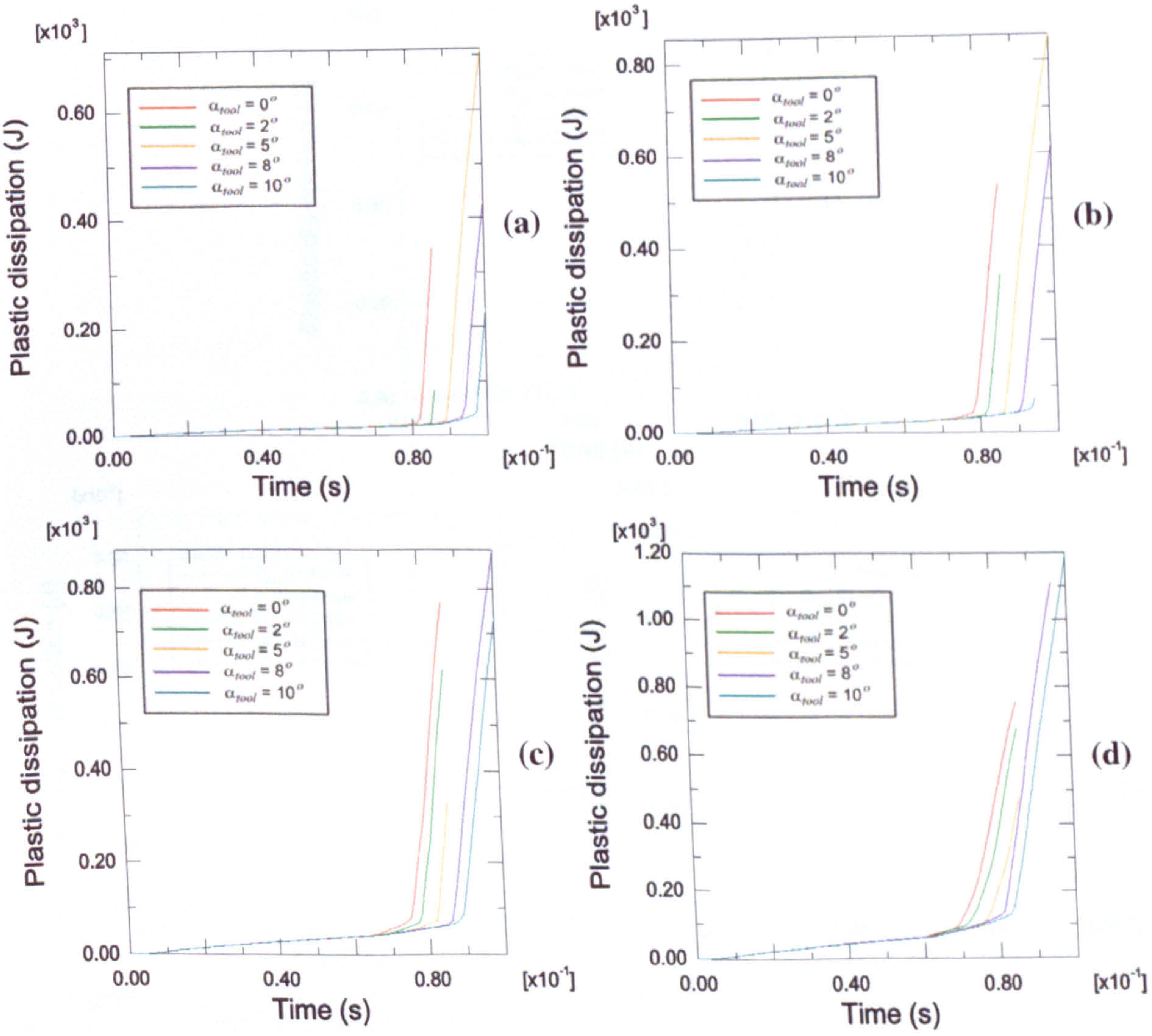

Figure 5.42 Plots of plastic dissipation against time in plunge stage for (a) R_{pin} =1 mm, (b) R_{pin} =1.5 mm, (c) R_{pin} =2 mm, (d) R_{pin} =2.5 mm: for R_{pin} =0°, 2°, 5°, 8° and10°.

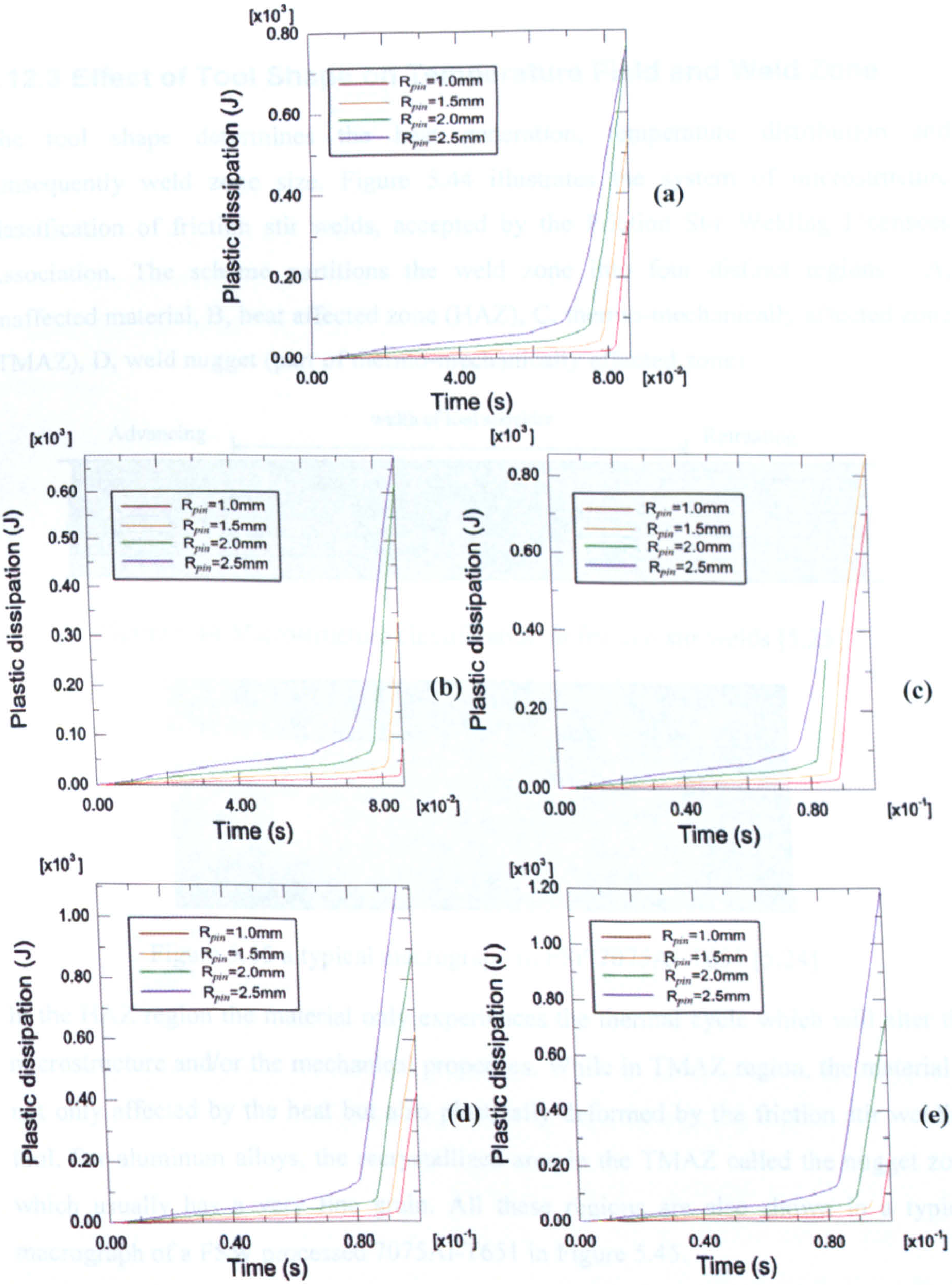

Figure 5.43 Plots of plastic dissipation against time in plunge stage, (a) α_{tool} =0°, (b) α_{tool} =2°, (c) α_{tool} =5°, (d) α_{tool} =8°, (e) α_{tool} =10°: for R_{pin}= 1, 1.5, 2 and 2.5mm.

5.12.3 Effect of Tool Shape on Temperature Field and Weld Zone

The tool shape determines the heat generation, temperature distribution and consequently weld zone size. Figure 5.44 illustrates the system of microstructure classification of friction stir welds, accepted by the Friction Stir Welding Licensees Association. The scheme partitions the weld zone into four distinct regions: A, unaffected material, B, heat affected zone (HAZ), C, thermo-mechanically affected zone (TMAZ), D, weld nugget (part of thermo-mechanically affected zone).

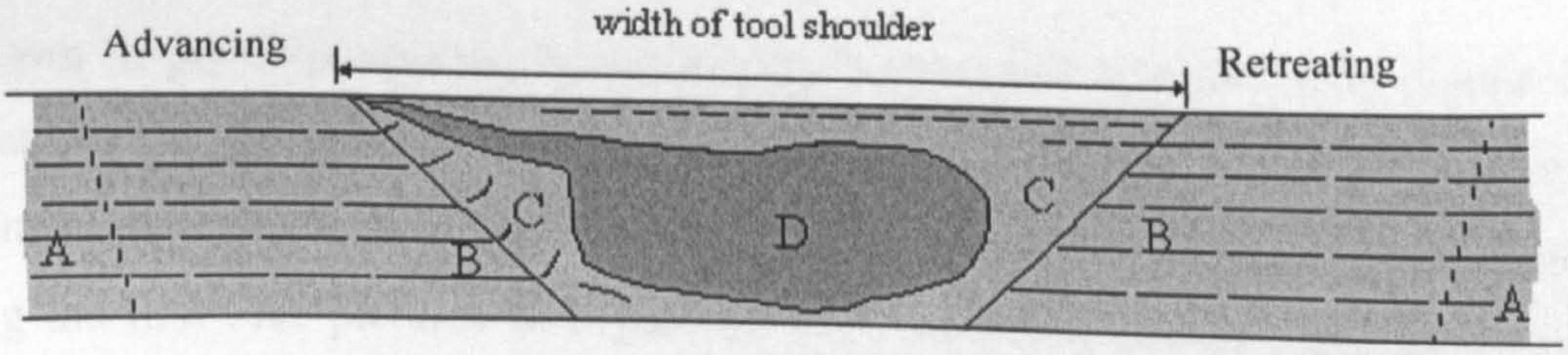

Figure 5.44 Microstructure classification of friction stir welds [5.25].

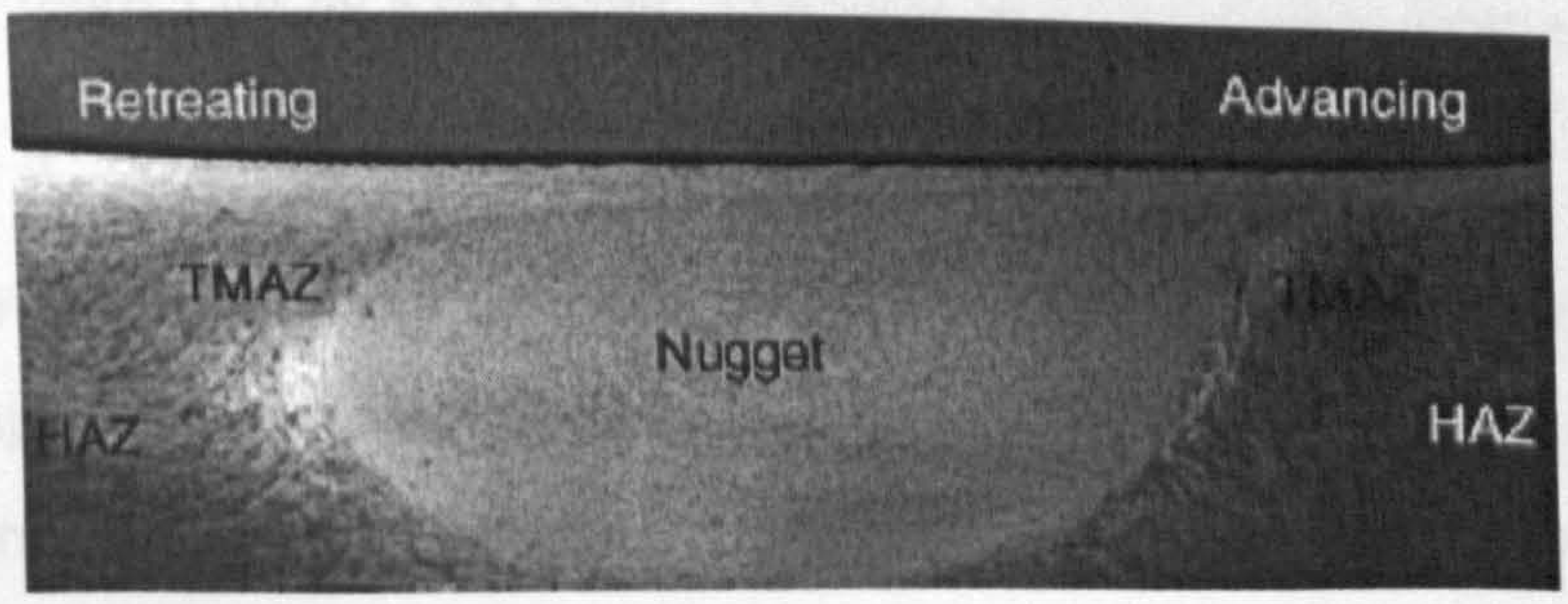

Figure 5.45 a typical macrograph in FSP 7075Al-T651 [5.24].

In the HAZ region the material only experiences the thermal cycle which will alter the microstructure and/or the mechanical properties. While in TMAZ region, the material is not only affected by the heat but also plastically deformed by the friction stir welding tool. For aluminum alloys, the recrystallized area in the TMAZ called the nugget zone which usually has a very fine grain. All these regions are also shown in a typical macrograph of a FSW processed 7075Al-T651 in Figure 5.45.

Figure 5.46 in pages 199-200 and 5.47 in page 201 present the temperature distributions produced by the 20 different tools when full contact forms between the tool and workpiece in the plunge stage. In Figure 5.46 the temperature distributions are given for tools with shoulder angles, α_{tool}= 0°, 2° and 5°. In Figure 5.47 the temperature distribution for α_{tool}= 8°, 10° The tool specification for each case is written in grey texts on the corresponding picture of the Figure 5.46 and 5.47. The first line of the texts indicates the pin radius, R_{pin} used and the second line signifies the shoulder surface angle, α_{tool}.

As shown in previous section, in the plunge stage more frictional and plastic energy dissipations are generated by the tool with larger pins. This can be verified by checking the temperature value at a specific point of the workpiece using different tool pins. Taking the first four pictures in Figure 5.46 for example, all the tools have the same shoulder angle, α_{tool} =0°. The selected material point of the workpiece is shown on the first picture in Figure 5.46 by a red point. The temperatures at this point for R_{pin} =1 mm, R_{pin} =1.5 mm, R_{pin} =2 mm and R_{pin} =2.5 mm are about 80 °C, 120 °C, 160 °C and 200 °C, respectively. Under the same plunging time larger radius pins heat the material point to a higher temperature. It is also found that the maximum temperatures in each of these four pictures are around 520 °C and very close to each other. This means that there is a higher thermal gradient around the tool in the workpiece for the case of smaller pin radius. A higher temperature gradient will lead to higher thermal stress and consequently higher deformation. The above findings are valid for all the shoulder surface angles considered here, not just 0°, which could be examined by looking at the rest of pictures in Figure 5.46 and 5.47. The detailed results are not included here for brevity.

The shoulder surface angle has little effect on the heat generation. Therefore, it is expected that it doesn't have much effect on temperature distribution as well. From inspection of a set of the pictures in Figures 5.46 and 5.47 which have the same pin radius, the discrepancy among them is very small. The slightly higher temperature at the sample point for bigger shoulder surface angle is due to the reason that the tool with bigger shoulder surface takes a slightly longer time to establish the full contact with the plates.

The shape of the reddest (hottest) part of workpiece in each picture also changes with different pins. Normally increasing the pin radius will enlarge the shape of this part, in particular towards the bottom surface of the workpiece. Hence it is safe to say that the pin radius will also affect the size of the weld zone.

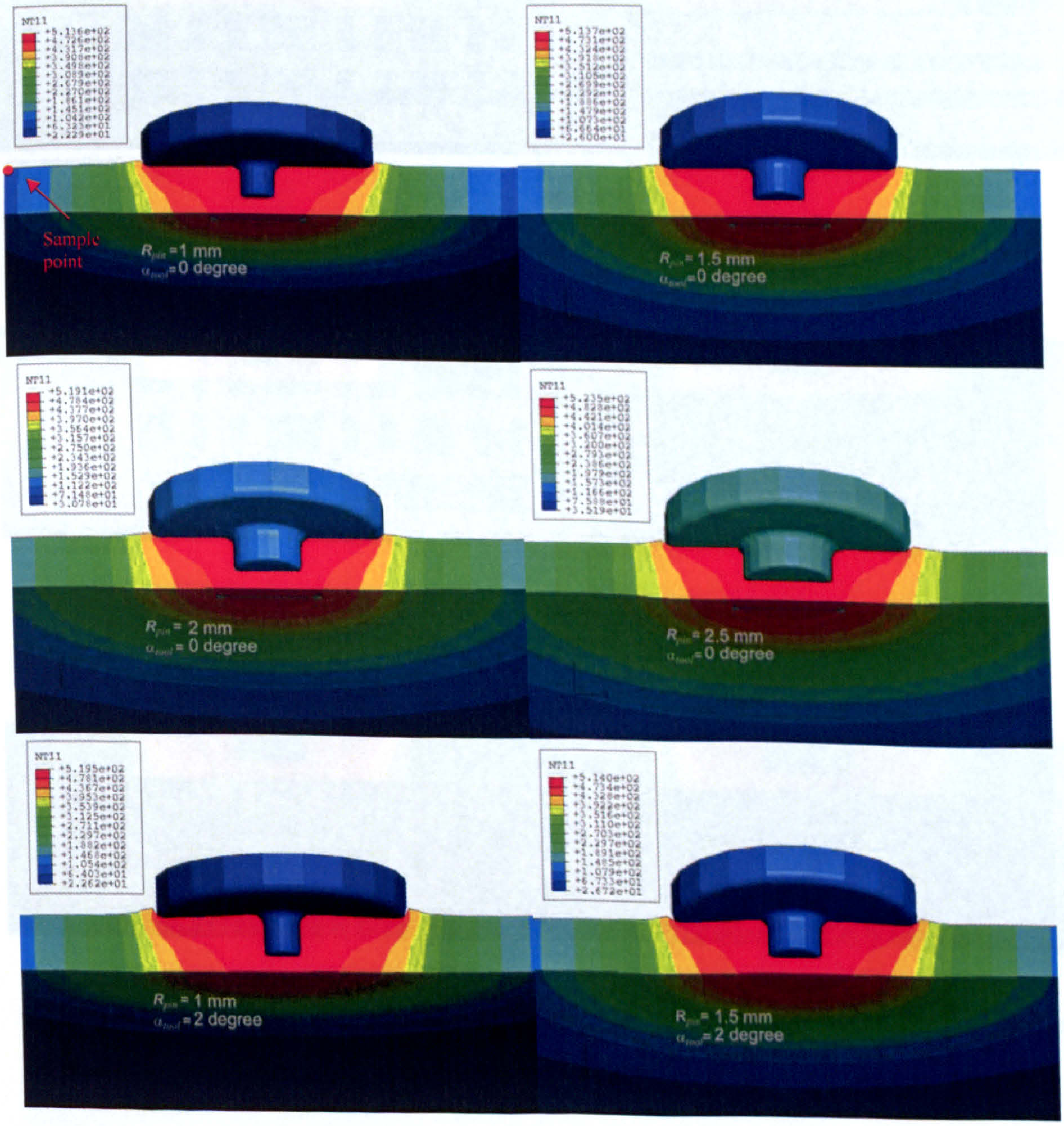

(Continued from the previous page)

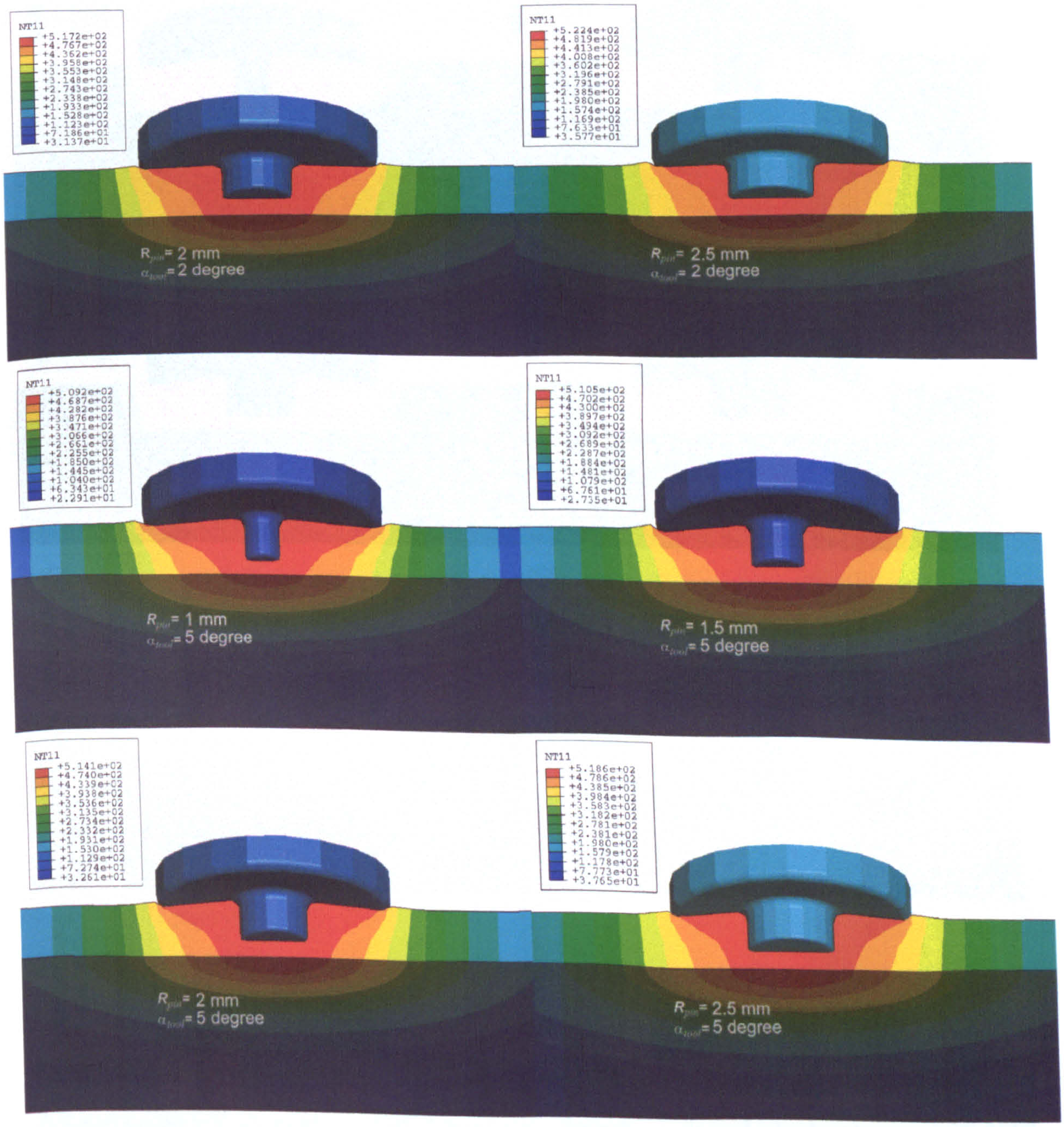

Figure 5.46 Temperature distributions around the tools with α_{tool}= 0°, 2° and 5°, when full contact forms in the plunge stage.

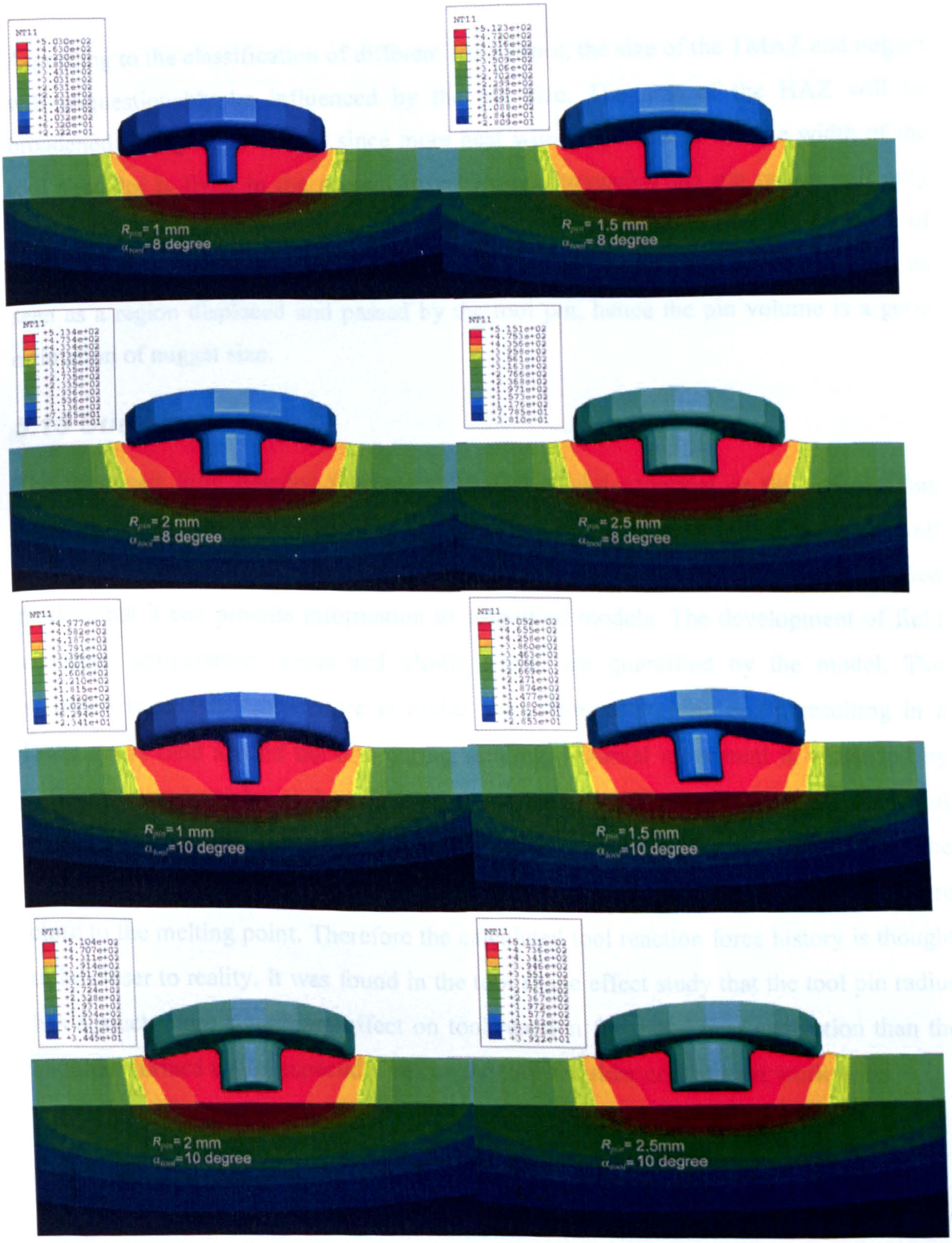

Figure 5.47 Temperature distributions around the tools with α_{tool}= 8° and 10°, when full contact forms in the plunge stage.

According to the classification of different weld zones, the size of the TMAZ and nugget will unquestionably be influenced by the pin size. The size of the HAZ will be broadened if larger pin is used since more heat will be generated. As the width of the tool shoulder is fixed in the present investigation, increasing the pin radius will only expand the TMAZ downwards inside the plates. This is consistent with the variation of the hottest zone shape shown in Figures 5.46 and 5.47. A large part of nugget could be seen as a region displaced and passed by the tool pin, hence the pin volume is a good estimation of nugget size.

5.13 Summary

The improved fully coupled thermo-mechanical model proposed in this chapter has successfully simulated the following friction stir welding process stages: plunge, dwell and traverse stages. The model doesn't need as much input information as simplified models, but it can provide information to simplified models. The development of field variables: temperature, stress and plastic strain, are quantified by the model. The predicted maximum temperature is higher than material melting point, resulting in a lower stress field around the tool during welding. Material movement is visualized by defining tracer particles at the locations of interest. The numerically computed material flow patterns are in very good agreement with the general findings in experiments. The model used for investigating the tool geometry effect predicted a maximum temperature close to the melting point. Therefore the calculated tool reaction force history is thought to be closer to reality. It was found in the tool shape effect study that the tool pin radius has a much more significant effect on tool reaction force and heat generation than the shoulder surface angle, especially before the tool shoulder contacts the workpiece.

5.14 References

[5.1] G. R. Johnson, W. H. Cook, "A constitutive Model and Data for Metal Subjected to Large Strains, High Strain Rates and High Temperatures", *Proceedings of 7th international Symposium on Ballistics*, The Hague, The Netherlands, pp. 541-547, 1983.

[5.2] G. R. Johnson and T. J. Holmquist, "Evaluation of Cylinder-Impact Test Data for Constitutive Model Constants", *Journal of Applied Physics*, Vol. 64, No. 8, pp. 3901-3910, 1998.

[5.3] G. R. Johnson and W. H. Cook, "Fracture Characteristics of Three Metals Subjected to Various Strains, Strain Rates, Temperatures and Pressures," *Engineering Fracture Mechanics*, Vol. 21, No. 1, pp. 31-48, 1985.

[5.4] F. J. Zerilli and R. W. Armstrong, "Dislocation-Mechanics-based Constitutive relations for Material Dynamics Calculations," *Journal of Applied Physics*, Vol. 61, No. 5, pp.1816-1825, 1987.

[5.5] F. J. Zerilli and R. W. Armstrong, "Description of Tantalum Deformation Behavior by Dislocation Mechanics Based Constitutive Equations," *Journal of Applied Physics*, Volume 68, No. 4, pp. 1580-1591, 1990.

[5.6] F. J. Zerilli and R. W. Armstrong, "The Effect of Dislocation Drag on the Stress-Strain Behavior of FCC Metals," *Acta Metallurgica et Materialia*, Vol. 40, No. 8, pp. 1803-1808, 1992.

[5.7] D. J., S. G. Cochran, and M. W. Guinan, "A Constitutive Model for Metals Applicable at High-Strain Rate," Lawrence Livermore National Laboratory, UCRL-80465, Revision 2, 1979.

[5.8] P. S. Follansbee and U. F. Kocks, "A Constitutive Description of the Deformation of Copper Based on the use of the Mechanical Threshold Stress as an Internal State Variable," *Acta Metallurgica*, Vol. 36, pp. 81-93, 1988.

[5.9] ABAQUS Theoretical Manual, Version 6.1, 2006.

[5.10] Donald Lesuer, "Experimental Investigation of Material Models for Ti-6Al-4V and 2024-T3," *FAA Report DOT/FAA/AR-00/25*, September 2000.

[5.11] Jaspers, S. P. F. C. and Dautzenberg, J. H., "Material Behavior in Conditions Similar to Metal Cutting: Flow Stress in the Primary Shear Zone," *Journal of Materials Processing Technology*, Vol. 122, Issues 2-3, pp. 322-330, 2002.

[5.12] Cinnamon, John D. and Brar, N. S., "Johnson-Cook Strength Model Constants for VascoMax 300 and 1080 Steels", *American Physical Society, 14th APS Topical Conference on Shock Compression of Condensed Matter*, July 31-August 5, 2005, abstract #Z3.006.

[5.13] B. Langrand, P. Geoffroy, J. -L. Petitniot, J. Fabis, E. Markiewicz and P. Drazetic, "Identification technique of constitutive model parameters for crashworthiness modelling", *Aerospace Science and Technology*, Vol. 3, Issue 4, pp. 215-227, June 1999.

[5.14] ABAQUS Analysis User's Manual, Version 6.1, 2006.

[5.15] A. Oliphant, "Numerical Modelling of Friction Stir Welding: A Comparison of Alegra and Forge3", Unpublished thesis, Brigham Young University, Provo, UT, 2004.

[5.16] M.J. Lasley, "A Finite Element Simulation of Temperature and Material Flow in Friction Stir Welding", Unpublished thesis, Brigham Young University, Provo, UT, 2005.

[5.17] S. Mandal, J. Rice, A.A. Elmustafa, "Experimental and Numerical Investigation of the plunge stage in friction stir welding", *Journal of Materials Processing Technology*, accepted.

[5.18] G. Buffa, J. Hua, R. Shivpuri, L. Fratini, 'A Continuum Based Fem Model for Friction Stir Welding-Model Development', *Material Science and Engineering A*, Vol. 419, Issues 1-2, pp. 389-396, 2006.

[5.19] Heurtier, P., C. Desrayaud, & F. Montheillet, "A Thermomechanical Analysis of the Friction Stir Welding Process", *Materials Science Forum*, Vol. 396, 4, pp. 1537-1542, 2002.

[5.20] BY T. J. Lienert, W. L. Stellwag, JR., B. B. Grimmett and R. W. Warke, "Friction Welding Studies on Mild Steel", *Supplement to the Welding Journal*, 82(1), pp. 1s-9s, 2003.

[5.21] H.N.B. Schmidt, T.L. Dickerson, and J.H. Hattel, "Material flow in butt friction stir welds in AA2024-T3", Acta Materialia, Vol. 54, pp.1199-1209, 2006.

[5.22] T.U. Seidel and A.P. Reynolds, "Visualization of the Material Flow in AA2195 Friction-Stir Welds Using a Marker Insert Technique", *Metallurgical and materials Transactions A*, 32, p. 2879, 2001.

[5.23] A.P. Reynolds, "Visualisation of material flow in autogenous friction stir welds", *Science and Technology of Welding & Joining*, Vol. 5, Number 2, pp. 120-124, April 2000.

[5.24] R.S. Mishra and Z.Y. Ma, "Friction stir welding and processing", *Materials Science and Engineering: R: Reports*, Vol. 50, Issues 1-2, pp. 1-78, 2005.

[5.25] http://www.twi.co.uk/j32k/unprotected/band_1/fswqual.html

[5.26] Paul A. Colegrove and Hugh R. Shercliff, "3-Dimensional CFD modelling of flow round a threaded friction stir welding tool profile", *Journal of Materials Processing Technology*, Vol. 169, Issue 2, pp. 320-327, 2005.

[5.27] C.M. Chen, R. Kovacevic, "Finite Element Modelling of Friction Stir Welding-Thermal and Thermomechanical analysis", *International Journal of Machine Tols and Manufacture*, Vol. 43, pp. 1319-1326, 2003.

[5.28] Moataz M. Attallaha and Hanadi G. Salem, "Friction stir welding parameters: a tool for controlling abnormal grain growth during subsequent heat treatment", *Materials Science and Engineering A*, Vol. 391, Issues 1-2, 25, pp. 51-59, 2005.

[5.29] H. Schmidt and J Hattel, 'A Local Model for the Thermo-mechanical Conditions in Friction Stir Welding', *Modelling and Simulation in Materials Science and Engineering*, Vol. 13, pp. 77-93, 2005

Chapter 6

Conclusion and Future Work

Thermo-mechanical modeling of the Friction Stir Welding (FSW) process has been studied in the thesis with the purpose of providing a computational tool to investigate the field variable evolutions and effect of process parameters during the FSW process. Creating a fully representative FSW model is challenging and at the limits of current finite element analysis capability. Due to the multi-physics nature of the system, there is a complex interplay between different physical phenomena that change the simulation results noticeably throughout this process.

In the thesis two levels of simulation were considered. One model fully simulates the FSW process and can predict heat generation, temperature, stress, strain, deformation, tool reaction force, tool reaction torque and material movement. It also has the potential to be used to compute microstructure evolution but it is unable to detect flaws. This model is the most comprehensive yet developed and still under development and has not yet been experimentally validated. The other seeks to predict only the deformation, stress and temperature histories in a cheaper and quicker manner.

The conclusions and recommended future works are presented as below in four parts. The last part is the summarized suggestions for future work discussed in the first three parts: simplified model, fully coupled model and effect of process parameter study.

6.1 Simplified Model

The focus of simplified model is on the externally applied heat source which determines the temperature evolution and stress field distribution. The stirring effect of the tool was not included in the model and the workpiece remains as a solid piece of plate without being penetrated. The torque approach was implemented in the model to calculate the total power input.

Comparison with the experimental work on AISI8018 steel showed the simplified model predicts temperature history in good agreement with measured results.

The mechanical interaction between the contacting surfaces was modelled with contact elements. For the model without contact pairs, it was assessed with the experimental work on Al6061. Large stress disagreement was found in longitudinal direction possibly because of the unreleased workpiece fixture.

The contact pressure and temperature dependent heat transfer coefficient significantly affect the thermal analysis. It was found that the proposed adaptive convective boundary condition algorithm is well suited to represent the varying thermal contact conductance at the backing plate-workpiece interface. However the success of this algorithm depends on whether the contact pressure can be accurately obtained.

6.2 Fully Coupled Thermo-mechanical Model

Considering the characteristics of friction stir welding process, ABAQUS/EXPLICIT with ALE formulation was employed to create a numerical model performing an explicit solution of the coupled thermo-mechanical analysis.

The computed temperature contour plot was almost symmetric along the joint line on both retreating and advancing sides, implying the rotating direction has little influence on the temperature distribution. The maximum temperature was found to be greater than melting point, but only a small layer of material at the interface has such a high temperature, all the rest of the materials are in solid state.

The stress field was found to be greatly dependent on the temperature distribution. At steady state, very low stress was observed in most of the material under the tool where high temperature was located. The residual stress was increasing as the temperature was decreasing in the material stirred and left behind by the tool. During the welding stage no obvious variation in the stress field around the tool was found.

Consistent with experimental observations, the plastic strain distribution was not symmetric about the joining line and the advancing side had a higher average plastic strain than the retreating side. The highest plastic strain region is still along the welding line with a width close to the pin diameter.

Based on results from limited number tracer particles, there were some useful findings which are consistent with experiments. The material from the advancing side was stirred onto the retreating side by the tool, and then dropped off in the wake of the shoulder mainly on the advancing side, possibly after several revolutions. While most of the material from the retreating side that didn't rotate with the shoulder was left behind by the tool.

From the predicted tool reaction force and torque results, it was found that the pin was subject to the highest and rapidly changing forces in the plunge stage.

6.3 Effect of Process Parameters Study

Due to the time limitation only the effects, in plunge stage, that the tool geometry (tool shoulder concavity angle and tool pin radius) has on tool reaction force, tool torque, heat generation, temperature distribution and size of the weld zone were studied.

It was found that, before the shoulder contacted the plates, the larger the pin radius was, the higher force the tool experiences. The effect of shoulder surface angle was put into action only when the shoulder was in contact with the workpiece, increasing shoulder surface angle will decrease the peak reaction force for small radius pin tools (R_{pin} =1 mm and R_{pin} =1.5 mm). For larger radius pin tools (R_{pin} =2 mm and R_{pin} =2.5 mm), the shoulder surface angle has little effect on the peak forces. The tool with smaller shoulder angle always reaches the peak force value earlier, indicating less time required for plunge stage.

The effect of tool shape on tool reaction torque is very similar to that on tool reaction force due to an approximately proportional relationship between them.

In plunge stage the pin radius played an import role in both frictional dissipation and plastic dissipation. The greater the pin, more heat generated. The heat energy increases nearly linearly with time, with a small increment rate before shoulder contacting workpiece and a much greater increment rate thereafter. The shoulder angle has very little effect on energy dissipation as well as little effect on temperature distribution. It is also found that increasing pin radius will increase the size of HAZ, TMAZ and nugget zone.

6.4 Summary of Suggested Further Study

The coupled-field model can simulate full FSW process: plunge, dwell, travel and withdraw. In future work, the link between the simplified model and coupled-field model would be established. The latter can be used to calculate input data, such as heat input, for the former. Because the fully coupled models are more complex and don't need as much input information as the simplified model.

For both simplified and fully coupled model, a sensitivity study on radiation and temperature dependent young's modulus should be performed. They were not included in the proposed models but have an impact on the predicted temperature and stress distribution.

Simplified Model

For simplified models, due to contact convergence difficulties, stated in previous section, the future work will concentrate on the contact modeling, probably in another FE code, such as ABAQUS, which has more powerful contact modeling capability.

The common assumption for presented models is that two separate plates to be welded are modeled as one complete piece. This assumption avoids discontinuity difficulty which is insurmountable in a classical finite element method. The material joining process can be seen as an inverse cracking problem. In the simplified model, birth and death element can be introduced to model the joining process. Other approaches such as the Partition of Unity Method (PUM) could be attempted to include the plate interface in a numerical model. The PUM and its siblings, eXtended Finite Element Method (XFEM) and Enriched mesh free methods allow the discontinuities to be mesh-independent by adding appropriate functions into the standard approximation spaces.

For the thermal boundary conditions, constant heat transfer coefficient was used as in other similar models in literature review. The predicted temperature will be improved if the contact pressure dependent coefficient is used. Thus the next future work for simplified thermo-mechanical modelling is to apply adaptive thermal boundary conditions in the model.

Coupled model

The foremost model improvement work will be lowering the predicted maximum temperature values, by changing boundary conditions, mass scaling factors, heat partition between the tool and workpiece. Also the temperature dependent Young's modulus, friction coefficient and shear stress limit can lead to better temperature predictions.

The rigid, isothermal tool can be replaced by a deformable solid body and thus appropriate boundary conditions can be applied and temperature distributions for both tool and workpiece could be achieved.

For present models, both friction coefficient and shear stress limit were kept constant. This is not sufficient to simulate the complex surface interaction, the core of the FSW process. The tool and workpiece should satisfy the condition that the maximum frictional shear stress is lower or equal to the shear yield stress. When the temperature increases, the shear yield stress decreases and may be less than the frictional shear stress if friction coefficient remain constant, resulting in incorrect acceleration and wrong predicted variables in material. So sensitivity study should be carried out to investigate the effect of these parameters.

Future work, therefore, could be focused on the interface interaction considering the balance condition stated above with the help of ABAQUS subroutine VUINTER which can provide the entire definition of the mechanical and thermal interaction between the contacting surfaces.

The workpiece was assumed to be isotropic elastic-plastic hardening material which was described by Johnson-Cook (JC) material law. Identifying the JC model constants remains to be difficult and requires a series of tests. However due to the need of the model to simulate various materials, the direct tabular material data points input could be used in place of JC material to express the strain-yield stress relationship, thus avoiding material model implementation problems. The Sente software company has developed a software program called JMatPro to provide such material property data in a format compatible to the FE code.

To further study the material movement behavior at the tool-workpiece interface, more tracer particles need to be seeded.

More parametric studies of process parameters and workpiece materials need carried out such as tool rotation speed, welding speed, spindle tilt angle and so on.

Although the present model with ALE meshing technique can successfully model the whole FSW welding process, it is still interesting to simulate the welding process in an adaptive remeshing scheme and compare the models' performance.